Fluid-Structure Interaction Studies on the Cardiovascular Hemodynamics of a Mitral Valve

by

Ahmad Moghaddaszade Kermani
B.A.Sc, University of Kerman, 1999
M.A.Sc, Sharif University of Technology, 2002

A Dissertation Submitted in Partial Fulfillment of the
Requirements for the Degree of

DOCTOR OF PHILOSOPHY

in the Department of Mechanical Engineering

Fluid-Structure Interaction Studies on the Cardiovascular Hemodynamics of a Mitral Valve

by

Ahmad Moghaddaszade Kermani
B.A.Sc, University of Kerman, 1999
M.A.Sc, Sharif University of Technology, 2002

Supervisory Committee

Dr. Afzal Suleman, Co-Supervisor
(Department of Mechanical Engineering)

Dr. Peter Oshkai, Co-Supervisor
(Department of Mechanical Engineering)

Dr. Alexandre Brolo, Outside Member
(Department of Chemistry)

Supervisory Committee

Dr. Afzal Suleman, Co-Supervisor
(Department of Mechanical Engineering)

Dr. Peter Oshkai, Co-Supervisor
(Department of Mechanical Engineering)

Dr. Alexandre Brolo, Outside Member
(Department of Chemistry)

ABSTRACT

The thesis presents a fluid-structure interaction studies on the hemodynamics of blood flow in the left ventricle and through the mitral valve. The virtual model consists of a mathematical model of the left ventricle coupled with a complex and structurally flexible bi-leaflet valve representing the mitral opening. The mitral valve is a bicuspid valve with anterior and posterior leaflets and it regulates unidirectional blood flow from the left atrium to the left ventricle in the diastole phase. The leaflets are made of chordae, annulus and papillary muscles. The goal of this study is to provide biomedical engineers and clinical physicians with a virtual laboratory tool to understand the dynamics of blood flow in a diseased heart and aid in the design of novel artificial heart valves. To this end, the simulation studies present an increasingly complex model of the heart to evaluate the vortex ring formation and evolution of the diastole phase in the left ventricle; and to characterize the septal-anterior motion in a diseased heart with obstructive hypertrophic cardiomyopathy. Finally, in collaboration with an industrial partner, the fluid-structure modeling framework was used to evaluate the performance of a new accelerated artificial valve tester.

Contents

Supervisory Committee **ii**

Abstract **iii**

Table of Contents **iv**

List of Tables **viii**

List of Figures **ix**

Acronyms **xvii**

Acknowledgements **xix**

Dedication **xx**

1 Introduction **1**

1.1 Heart Structure 1

1.2 Heart Function 1

1.2.1 Atrial Contraction (Mitral and Tricuspid Valves: Open; Plumunary and Aortic Valves: Closed) 2

1.2.2 Isovolumetric Contraction (All Valves: Closed) 2

1.2.3 Rapid Ejection (Aortic and Pulmonary Valves: Open; Mitral and Trycuspid Valves Remain Closed) 2

1.2.4 Reduced Ejection: Aortic and Pulmonary Valves Open; Mitral and Trycuspid Valves Remain Closed 2

1.2.5 Isovolumetric Relaxation: All Valves Closed 3

1.2.6 Rapid Filling: Mitral and Trycusoid Valves Open 3

1.2.7 Reduced Filling: Mitral and Trycuspid Valves Remain Open . 3

1.3 Diseases in Heart 3

1.3.1 Hypertrophic Cardiomyopathy . . . 3
1.3.2 Congestive Cardiomyopathy . . . 4
1.3.3 Restrictive Cardiomyopathy . . . 4
1.3.4 Mitral Valve Stenosis . . . 4
1.4 Background and Motivation . . . 4
1.5 Previous Works . . . 5
1.6 Literature Review Conclusion . . . 16
1.7 Contributions . . . 17
1.8 Building Blocks of the Thesis . . . 18
1.9 Objectives . . . 20

2 Hemodynamics of the Left Ventricle with Prescribed Boundary Conditions 21
2.1 Parametric Model of the LV . . . 21
2.1.1 Model Construction Method . . . 22
2.1.2 Measurement of the Model Parameters Using MR Images . . . 24
2.2 Characterizing Left Ventricular Motion During A Cardiac Cycle . . . 26
2.3 Limitations of the Model . . . 28
2.4 Lump Model For The Boundary Conditions of the Left Ventricle . . . 29
2.4.1 Arterial System Model . . . 29
2.4.2 Pulmonary Circulation Model . . . 30
2.4.3 Lump Model Results . . . 31
2.5 Fluid-Structure Modeling of The Blood Inside The Normal LV . . . 35
2.5.1 Boundary Conditions . . . 38
2.5.2 Computational Algorithm . . . 39
2.6 Results and Discussion . . . 41
2.6.1 Vortex Ring Formation and Evolution . . . 41
2.6.2 Ventricular Pressure During Diastole . . . 43
2.6.3 Effect of Heart Rate . . . 44
2.6.4 Effect of The Stroke Volume . . . 47
2.7 Chapter Synopsis . . . 51

3 FSI Simulation of The Mitral Valve Within Normal Left Ventricle 53
3.1 Introduction . . . 53
3.2 Chapter Objectives . . . 53

3.3 Parametric Geometry of the Mitral Valve 54
3.4 Geometry of Mitral Valve and Left Ventricle and Boundary Conditions 56
3.5 Finite Element Model of the Mitral valve 58
3.6 Fluid-Structure Interaction Module 59
3.6.1 Fluid-Structure Interaction Framework 60
3.6.2 Method of Generating Geometry of The Deformed Mitral Valve and Left Ventricle 62
3.7 Boundary Conditions 66
3.8 Coaptation and Deformation Analysis 66
3.9 Stress Analysis 67
3.10 Chordae Force 68
3.11 Flow Dynamics in Early Systole 79
3.12 Flow Dynamics During Mid and Late Systole 80
3.13 Vortex Ring Formation During Early Diastole 83
3.14 Vortex Ring Formation During Mid and Late Diastole 83
3.15 Vortex Ring Formation Analysis 87

4 FSI Simulation of The Mitral Valve In A Diseased Left Ventricle with Obstructive Hyperthrophic Cardiomyopathy 97
4.1 Introduction 97
4.2 Geometry of The Left Ventricle With OHCM and Boundary Conditions 97
4.3 Results and Discussion 98
4.3.1 Mitral valve Closure 98
4.3.2 Systolic Anterior Motion Analysis 99

5 Fluid-Structure Interaction Analysis of a New Accelerated Durability Tester for Prosthetic Heart Valves 109
5.1 Introduction 109
5.2 Objectives 110
5.3 Conceptual Design of the Apparatus 110
5.4 Geometry of the Valve 112
5.5 Fluid-Solid Interaction Procedure 112
5.6 Computational Fluid Dynamics (Computational Fluid Dynamic (CFD)) 113
5.7 Mesh Movement 114
5.8 Boundary Conditions 115

5.9 Immersed Solid Method for Modeling the Interaction impeller with Fluid 116
5.10 Computational Structural Dynamics (Computational Structural Dynamic (CSD)) for Modeling the Interaction of the Valve Leaflets with Fluid 117
5.11 Proposed Algorithm 118
5.12 Results and Discussion 121
5.12.1 Initial configuration 121
5.12.2 Effect Having More Impellers 124
5.12.3 Effect Installing the Impeller Close to the Valve 126
5.12.4 Full Fluid Structure Interaction (FSI) Simulation 129
5.13 Conclusion 142

6 Conclusions and Future Work 144
6.1 Conclusions 144
6.1.1 Two-Way Fluid-Structure Interaction Simulation of the Mitral Valve 146
6.1.2 Two-Way Fluid-Structure Interaction Simulation of Septal-Anterior Motion of the Mitral Valve in Obstructive Hypertrophic Cardiomyopathy 148
6.1.3 Accelerated Heart Valve Durability Tester 149
6.2 Study Limitations 149
6.3 Future Work 149

Bibliography 153

A Time History Results of Chapter 2 164

B Time History Results of Chapter 3 187

C Time History Results of Chapter 5 208

D Permission Letter For Copyright Material 230

List of Tables

Table 2.1 Left ventricular dimensions measured from MR images. 24

Table 3.1 Human and porcine mitral valve measurements taken by Kunzelman *et.al.*[57] 55
Table 3.2 Material properties of Mitral Valve used for simulation[56]. . . . 59
Table 3.3 Maximum principal stresses (kPa) at point B, C, D and E. . . . 67
Table 3.4 Value of the parameters used for calculation of FN during diastole, HR=60 bpm, SV=60 mL 89

Table 5.1 y and z component of forces applied to the leaflets. case 1: one impeller, case 2: three impellers, case 3: impeller installed close to the valve. 143

List of Figures

Figure 1.1 Flow chart of the models which have been developed in this work 19

Figure 2.1 Top view of the LV: Septum and free walls are simulated using half ellipses whose dimensions are measured from MR images. b and d are septum-free wall and anterior-posterior short axes; d is free wall radii of curvature at mid point of free wall. 22

Figure 2.2 Side view of the LV. a: long axis and h: height of truncation . . 23

Figure 2.3 Side view of a male volunteer's heart which was used to measure the model parameters 25

Figure 2.4 Long axis, short axis, h and c_i were measured. 25

Figure 2.5 Geometrical description of the LV wall motion (front view). j, k and m are the short and long axes of the ellipses. 26

Figure 2.6 Geometrical description of the LV wall motion (side view). s and m are the short and long axes of the ellipses. 27

Figure 2.7 Three element Windkessel model to simulate peripheral system [102]. R_L and C_L represent the resistance and capacitance of the peripheral vessels and R_{AO} represents the resistance of the aorta. 29

Figure 2.8 Alexander model [3] to simulate the pulmonary system. P_p is the pulmonary source of pressure, R_3 resistance of pulmonary source, C_4 pulmonary venous capacitor, R_4 pulmonary resistor, L_4 pulmonary inertance, R_5 antroventricular resistor, L_5, antroventricular inertance, Q_p pulmonary venous flow rate, Q_{LV} left ventricular blood flow, V_p volume of the pulmonary venous and V_{LA} volume of the left atrium 30

Figure 2.9 Left ventricular flow rates applied to the lump model for the heart rate of 60 bpm. LVE: left ventricular ejection, LVPF: left ventricular passive filling, LAE: left atrial ejection 33

Figure 2.10Left ventricular volume (LVV) for a cardiac cycle with the heart rate of 60 bpm. SLVV: systolic left ventricular volume, DLVV: diastolic left ventricular volume. 33
Figure 2.11The pressure profile of the left ventricle, aorta and left atrium during a cardiac cycle with the heart rate of 60 bpm. LVSP: left ventricular systolic pressure, AOIVCP: aortic isovolumetric pressure, IVCP: left ventricular isovolumetric pressure, LASP: left atrial systolic pressure, LADP: left atrial diastolic pressure, AODP: aortic diastolic pressure, IVRP: left ventricular isovolumetric relaxation pressure. 35
Figure 2.12Every left ventricular point moves toward the center of the ellipse. 37
Figure 2.13Windkessel and Alexander models were used to simulate the boundary conditions for the aortic and mitral orifice respectively. 39
Figure 2.14One way FSI algorithm used for the simulation. 40
Figure 2.15Mesh density used for the CFD model. the average volume of the elements is 0.37 mm^3 41
Figure 2.16Maximum vorticity on the long axis and antrio-posterior planes. 42
Figure 2.17Circulation on the long axis (symmetry) plane during diastole. . 43
Figure 2.18Pressure at the apex and mitral valve orifice during the diastole. 44
Figure 2.19Left ventricular flow rate at the heart rates of 60 (blue), 65 (green), 70 (red), 75 (cyan)and 80 (black) 45
Figure 2.20Left ventricular, aortic and left atrial pressures at heart rates of 60 (blue), 65 (green), 70 (red), 75 (cyan)and 80 (black). SV=60 mL 46
Figure 2.21Circulation in the long axis plane at heart rates of 60 (red), 65 (green), 70 (blue), 75 (purple)and 80 (orange). SV=60 mL . . . 46
Figure 2.22Max Vorticity in the long axis plane at heart rates of 60 (red), 65 (green), 70 (blue) and 75 (purple). SV=60 mL 47
Figure 2.23Left ventricular flow rate at the stroke volumes of 60 mL (blue), 65 mL (green), 70 mL (red), 75 mL (cyan)and 80 mL (black) . . 48
Figure 2.24Left ventricular, aortic and left atrial pressures at Stroke volumes of of 60 mL (blue), 65 mL (green), 70 mL (red), 75 mL (cyan)and 80 mL (black). HR=60 bpm 48

Figure 2.25Circulation in the long axis plane at stroke volumes of 60 mL (red), 65 mL (green), 70 mL (blue), 75 mL (purple)and 80 mL (orange). HR=60 bpm 49
Figure 2.26Max Vorticity in the long axis plane at stroke volumes of 60 mL (red), 65 mL (green), 70 mL (blue) and 75 mL (purple. HR=60 bpm 49
Figure 2.27Velocity vectors in the long axis (symmetry) view. SV=60 ml, HR=60 bpm. 50

Figure 3.1 A: Anterior annular length; B: posterior annular length; C: Anterior annular length; D: posterior annular length; E: anterior edge length; F: posterior edge length; G: anterior leaflet height; H: posterior leaflet height [57]. 55
Figure 3.2 The anterior and posterior leaflets were created by drawing partial circles with radius of 15 mm and 13.9 mm on the planes which have the angles of 15 and 101 degree with basal plane. The half circles were initiated from the distance of 5.14 mm to the base. 56
Figure 3.3 Four views of the constructed Mitral valve 57
Figure 3.4 Constructed model of the left ventricle with mitral valve 58
Figure 3.5 General framework of the partitioned FSI method. 61
Figure 3.6 Time marching approach in the partitioned method. 61
Figure 3.7 Deformed geometry of the mitral valve in three time steps. . . . 63
Figure 3.8 Method of Generating Geometry of The Deformed Mitral Valve and Left Ventricle. N and M are the total number of solid and surface element respectively. 64
Figure 3.9 Fluid-Structure Interaction algorithm used for the simulation of the mitral valve within a beating normal left ventricle 65
Figure 3.10Windkessel and Alexander models used to simulate the boundary conditions for the aortic and mitral orifices, respectively. 66
Figure 3.11Demonstration of the points of interest 67
Figure 3.12displacement of the points A and F during a cardiac cycle. . . . 68
Figure 3.13Chordae forces of 3 samples from anterior and posterior leaflets. 69
Figure 3.14First principal stress, view: Symmetry Plane. SV=60 ml, HR=60 bpm. 70

Figure 3.15First principal stress, view: basal Plane. SV=60 ml, HR=60 bpm. 75
Figure 3.163D streamline of the blood flow in early systole. SV=60 ml, HR=60 bpm. 81
Figure 3.17Mass flow in and out of the left ventricle during a cardiac cycle 82
Figure 3.18Velocity at different points along a streamline which is started from apex and ended in mid aortic aperture 82
Figure 3.19Position of minimum velocity along a streamline which is started from apex and ended in mid aortic aperture 83
Figure 3.203D streamline of the blood flow in early diastole. SV=60 ml, HR=60 bpm. 85
Figure 3.213D streamline of the blood flow in mid diastole at $t = 600ms$ from three views. SV=60 ml, HR=60 bpm. 86
Figure 3.22Z coordinate of vortex core position during diastole. 87
Figure 3.23X coordinate of vortex core position during diastole. 87
Figure 3.24Formation Number (FN) during diastole. 90
Figure 3.25Circulation verses Formation Number (FN) during diastole. . . 90
Figure 3.26Vortex Energy verses Formation Number (FN) during diastole. 91
Figure 3.27Left ventricular Flow Rate verses Formation Number (FN) during diastole. 92
Figure 3.28Velocity contours in the long axis (symmetry) Plane. SV=60 ml, HR=60 bpm. 93

Figure 4.1 Assembly of LV with OHCM and Mitral Valve with chordaes . 98
Figure 4.2 Average pressures on the surfaces of mitral valve. 100
Figure 4.3 Average contact pressure during systole 101
Figure 4.4 Shear stress. ALV: LV side of anterior leaflet, ALA: Atrial side of anterior leaflet, PLV: LV side of posterior leaflet, PLA: Atrial side of posterior leaflet 101
Figure 4.5 Maximum velocity in the outflow track. 102
Figure 4.8 Velocity vectors at different time steps during systole 105
Figure 4.8 Velocity vectors at different time steps during systole 106
Figure 4.8 Velocity vectors at different time steps during systole 107

Figure 5.1 Assembly of the new accelerated durability equipment 111
Figure 5.2 (a) Oblique view of the geometry of the bi-leaflet prosthetic valve, (b) and (c) valve closed and open respectively. 112

Figure 5.3 Weak Coupling Fluid-Structure Interaction Procedure. 113
Figure 5.4 (a) Hexahedral and (b) Thetrahedral elements will be used to mesh the fluid domain. 114
Figure 5.5 Angular velocity and displacement of the impeller during one period with the frequency of 5 Hz. 116
Figure 5.6 Boundary conditions for CFD simulation. 117
Figure 5.7 Proposed algorithm extracted from [99]. 120
Figure 5.8 Pressure on the surfaces of the valve in one cycle(0.4 Sec). P1: pressure on the top surface of the leaflet 1, P2: pressure on the top surface of the leaflet 2, P3: pressure on the bottom surface of the leaflet 1, P4: pressure on the bottom surface of the leaflet 2.122
Figure 5.9 Sum of Fz on the leaflets in one cycle(0.4 Sec).RT: top surface of right leaflet, RB: bottom surface of right leaflet, LB: bottom surface of left leaflet, LT: top surface of left leaflet 123
Figure 5.10Sum of Fy on the leaflets in one cycle(0.4 Sec).RT: top surface of right leaflet, RB: bottom surface of right leaflet, LB: bottom surface of left leaflet, LT: top surface of left leaflet 123
Figure 5.11Pressure on the surfaces of the valve in one cycle(0.4 Sec). RT: right top, RB: right bottom, LB: left bottom, LT: left top . . . 124
Figure 5.12Total Pressure on the surfaces of the valve in one cycle(0.4 Sec). RT: right top, RB: right bottom, LB: left bottom, LT: left top . 125
Figure 5.13Sum of Fz on the leaflets in one cycle(0.4 Sec) in the system with 3 impellers installed.RT: top surface of right leaflet, RB: bottom surface of right leaflet, LB: bottom surface of left leaflet, LT: top surface of left leaflet 125
Figure 5.14Sum of Fy on the leaflets in one cycle(0.4 Sec) in the system with 3 impellers installed.RT: top surface of right leaflet, RB: bottom surface of right leaflet, LB: bottom surface of left leaflet, LT: top surface of left leaflet 126
Figure 5.15Pressure on the surfaces of the valve in one cycle(0.4 Sec). . . . 127
Figure 5.16Sum of Fz on the leaflets in one cycle(0.4 Sec).RT: top surface of right leaflet, RB: bottom surface of right leaflet, LB: bottom surface of left leaflet, LT: top surface of left leaflet 128

Figure 5.17Sum of Fy on the leaflets in one cycle(0.4 Sec).RT: top surface of right leaflet, RB: bottom surface of right leaflet, LB: bottom surface of left leaflet, LT: top surface of left leaflet 128
Figure 5.18Velocity contours at mid surface(0.02 Sec). 130
Figure 5.19Velocity contours at mid surface(0.04 Sec). 130
Figure 5.20Velocity contours at mid surface(0.06 Sec). 131
Figure 5.21Velocity contours at mid surface(0.06 Sec). 131
Figure 5.22Velocity contours at mid surface(0.08 Sec). 132
Figure 5.23Velocity contours at mid surface(0.1 Sec). 132
Figure 5.24Velocity contours at mid surface(0.12 Sec). 133
Figure 5.25Velocity contours at mid surface(0.14 Sec). 133
Figure 5.26Velocity contours at mid surface(0.16 Sec). 134
Figure 5.27Velocity contours at mid surface(0.18 Sec). 134
Figure 5.28Velocity contours at mid surface(0.2 Sec). 135
Figure 5.29Velocity contours at mid surface(0.22 Sec). 135
Figure 5.30Velocity contours at mid surface(0.24 Sec). 136
Figure 5.31Velocity contours at mid surface(0.26 Sec). 136
Figure 5.32Velocity contours at mid surface(0.28 Sec). 137
Figure 5.33Velocity contours at mid surface(0.30 Sec). 137
Figure 5.34Velocity contours at mid surface(0.32 Sec). 138
Figure 5.35Velocity contours at mid surface(0.34 Sec). 138
Figure 5.36Velocity contours at mid surface(0.36 Sec). 139
Figure 5.37Velocity contours at mid surface(0.38 Sec). 139
Figure 5.38Velocity contours at mid surface(0.4 Sec). 140
Figure 5.39Leaflet angle during a period. The left leaflet closes slightly sooner than the right one. 141
Figure 5.40Y component of the force applied by fluid to the top and bottom surfaces of the leaflets during a period. RT: right top, RB: right bottom, LB: left bottom, LT: left top 141
Figure 5.41Z component of the force applied by fluid to the top and bottom surfaces of the leaflets during a period. RT: right top, RB: right bottom, LB: left bottom, LT: left top 142
Figure 5.42Z component of the velocity (w) at the mid point of the valve . 142

Figure 6.1 Overview of the project. 145

Figure A.1 Velocity vectors in the long axis (symmetry) view. SV=60 ml, HR=60 bpm. 165
Figure A.2 Velocity vectors in the Anterio-Posterior view. SV=60 ml, HR=60 bpm. 167
Figure A.3 Streamlines of the flow in the Basal view. SV=60 ml, HR=60 bpm. 169
Figure A.4 Velocity contours in the long axis (symmetry) view. SV=60 ml, HR=60 bpm. 171
Figure A.5 Velocity contours in the Antrio-Posterior view. SV=60 ml, HR=60 bpm. 173
Figure A.6 Pressure contours in the long axis view. SV=60 ml, HR=60 bpm. 175
Figure A.7 Vorticity contours in the long axis (symmetry) view. SV=60 ml, HR=60 bpm. 177
Figure A.8 Vorticity contours in the Antrio-Posterior view. SV=60 ml, HR=60 bpm. 179
Figure A.9 Velocity contours in the mitral valve orifice. SV=60 ml, HR=60 bpm. 181
Figure A.10 Velocity vectors in the long axis (symmetry) view. SV=30 ml, HR=60 bpm. 183
Figure A.11 Velocity vectors in the Anterio-Posterior view. SV=30 ml, HR=60 bpm. 185

Figure B.1 First principal stress, view: basal Plane. SV=60 ml, HR=60 bpm. 188
Figure B.2 First principal stress, view: Symmetry Plane. SV=60 ml, HR=60 bpm. 193
Figure B.3 Velocity contours in the long axis (symmetry) Plane. SV=60 ml, HR=60 bpm. 198
Figure B.4 Velocity contours in the long axis (symmetry) Plane. SV=60 ml, HR=60 bpm. 202
Figure B.5 Vorticity contours in the long axis (symmetry) Plane. SV=60 ml, HR=60 bpm (cont.). 206

Figure C.1 3D streamlines, colored with velocity at $t = 0.1$ Sec in which the impeller is at its pick velocity. 208
Figure C.2 2D streamlines, colored with velocity at different time steps. . . 209
Figure C.3 Velocity vectors at $t = 0.1$ Sec. 211

Figure C.4 Velocity contours at different time steps. 212
Figure C.5 Velocity contours at different time steps. 215
Figure C.6 Velocity contours at different time steps for the case of installing the impeller close to the valve. 218
Figure C.7 Streamlines for the case of full FSI. 221
Figure C.8 Pressure contours for the case of full FSI. 224
Figure C.9 Velocity vectors for the case of full FSI. 227

Acronyms

ADT Accelerated Durability Tester

ALC antero-lateral commissure

AO Aorta

AV Aortic Valve

CFD Computational Fluid Dynamic

CSD Computational Structural Dynamic

HCM Hypethrophic Cardiomyopathy

FE Finite Element

FSI Fluid Structure Interaction

FDA Food and Drug Administration

FW Free Wall

IVC Isovolumetric Contraction

IVR Isovolumetric Relaxation

IS Immersed Solid

ISO International Standard Organization

LA Left Atrium

LAP Left Atrial Pressure

LV Left Ventricle

LVEDP Left Ventricular End Diastolic Pressure

LVESP Left Ventricular End Systolic Pressure

LVOT Left Ventricular Outflow Tract

LVP Left Ventricular Pressure

LVV Left Ventricular Volume

MV Mitral Valve

OHCM Obstructive Hypethrophic Cardiomyopathy

PHV Prosthetic Heart Valve

PMC postero-medial commissure

SAM Systolic Anterior Motion

ACKNOWLEDGEMENTS

I would like to thank Dr Suleman for providing me an opportunity to come to Canada and finish Ph.D under his supervision and in his group.

Also, I would like to thank David Mester, president of ViVitro Labs Inc, for giving me a chance to work in his lab and allowing me to include the work I did for him in my thesis.

I appreciate my wife, Ellahae Keshmiri, for her enormous help, encouragement, support and love throughout my project during past six years. I could not complete this project without her support.

I also would like to thank Manouchehr Hadian, Shohreh Hadian, Sandra Makosinski and my parent-in-laws Dr. Mahdi Keshmiri and Narges Malaeke for supporting me throughout this project.

I also thank my brother and sister for helping throughout my education. My brother always supported my studies when I was student in Iran.

Most importantly, I would like to thank my mom who taught me to pursuit and protect my goals and never give up. Her prays have always worked for me in the most difficult circumstances.

DEDICATION

To my mother Zahra, my wife Ellahae and my father Ali

Chapter 1

Introduction

1.1 Heart Structure

The human heart is a natural pump causing circulation of blood inside the human body. Heart consists of four chambers, called left and right atriums and ventricles. The atriums receive the blood from the tissues while the Ventricles send the blood into the tissues. Two valves are installed on each ventricle to guaranty the unidirectional flow through the heart and consequently through the body, one at the inlet and one at the outlet. The inlet valves are tricuspid and the mitral. The outlet valves are the pulmonary and the aortic.

1.2 Heart Function

The cardiac cycle can be divided in seven phases:

- Atrial Contraction
- Isovolumetric Contraction
- Rapid Ejection
- Reduced Ejection
- Isovolumetric Relaxation
- Rapid Filling
- Reduced Filling

1.2.1 Atrial Contraction (Mitral and Tricuspid Valves: Open; Plumunary and Aortic Valves: Closed)

In this phase the atriums contract to push the blood into the ventricles. During this process the pressure in the atriums rises until it exceeds the ventricular's pressure. At this point the valves (mitral and tricuspid) open and let the blood rushes into the ventricles. This phase is associated with the p wave in the electricardiogram (ECG) wave. Depolarization of the atriums causes the contraction of the muscles.

The atrial pressure begin to drop after the contraction is completed. This causes the mitral leaflets to move toward the atrium before the closure. This point is the end diastolic volume (EDV) when the left ventricle is at its maximum volume. The S4 peak in the sound wave is related to atrial contraction due to vibration of the ventricular wall.

1.2.2 Isovolumetric Contraction (All Valves: Closed)

In this phase, the depolarization of the ventricular muscle leads to contraction which causes rapid increase in ventricular pressure without increase in volume since the aortic valve is closed.

The rapid pressure increase leads to sudden closure of the mitral valve since the left ventricular pressure exceeds the atrial pressure. During the mitral valve closure the papillary muscles contract to prevent the prolapse of the mitral leaflets into the atrium. S1 sound is related with the MV closure at this phase.

1.2.3 Rapid Ejection (Aortic and Pulmonary Valves: Open; Mitral and Trycuspid Valves Remain Closed)

When the ventricular pressure exceeds the aortic pressure the aortic valve opens and let the blood rushes into the aorta and plumonary artrey. In this phase the blood flow out of the ventricles is high.

1.2.4 Reduced Ejection: Aortic and Pulmonary Valves Open; Mitral and Trycuspid Valves Remain Closed

In this phase, due to re-polarization of the ventricles the tension of the myocardium reduces and the ventricular pressure begins to drop down. Also, the atrial pressure starts to increase due to return of blood from lungs and organs.

1.2.5 Isovolumetric Relaxation: All Valves Closed

When the ventricular pressure reaches bellow the aortic pressure the aortic and pulmonary valves close, causing the S2 hear sound. After the aortic closure the myocardium starts to relax causing the left ventricular pressure continue decreasing.

1.2.6 Rapid Filling: Mitral and Trycusoid Valves Open

Ventricular pressure continues to decrease until it reaches bellow the atrial pressure. At this point the mitral and trycuspid valves open and let the blood fill the ventricles. Also, the atrial pressure drops suddenly at onset of the opening of the mitral and trycuspid valves.

1.2.7 Reduced Filling: Mitral and Trycuspid Valves Remain Open

s the ventricles continue being filled the ventricular pressure increases and the flood flow rate from atrium to the ventricle reduces.

1.3 Diseases in Heart

Heart disease is one of the leading causes of death in North America and more than 2.6 million people have heart disease in Canada [38]. In this section we briefly describe four types heart diseases.

1.3.1 Hypertrophic Cardiomyopathy

Hypertrophic Cardiomyopathy is a genetic disease in which the muscle mass of the left ventricle is larger than it is supposed to be, causing the Mitral valve touching the muscle dividing two sides of the heart (this muscle is called Septum). The effect is a narrowing passage that can block or reduce the blood flow out the left ventricle to the aorta which is called "outflow tract obstruction" [77]. In this condition ventricle must pump harder to overcome the narrowing or blockage. When the outflow tract is narrowed, blood rushing through the passageway drags the leaflets of the Mitral valve. Moreover, the Mitral valve normally functions to keep blood flowing in one direction from the left atrium to the left ventricle. However, the increased force of blood pulls the valve open and may cause blood to leak backward (called regurgitation) into the left atrium.

The following issues exist with the Hypertrophic Cardiomyopathy which were studied in this thesis:

- Outflow obstruction

- Shear stress applied to the Mitral valve
- Leakage of blood from the left ventricle to the left atrium

1.3.2 Congestive Cardiomyopathy

Congestive cardiomyopathy is a condition where the heart has become weakened and is not able to squeeze as well as it should and in an attempt to compensate for this weakness it enlarges. The most common identifiable cause of congestive cardiomyopathy is widespread coronary artery disease (CAD). CAD can lead to inadequate blood supply to the heart muscle. The healthy heart muscle stretches to compensate for the lost pumping action.

1.3.3 Restrictive Cardiomyopathy

Restrictive cardiomyopathy refers to a group of disorders in which the heart chambers are unable to be filled with blood properly because of stiffness of the heart. In restrictive cardiomyopathy, the heart is normal in size or only slightly enlarged, but it cannot relax normally during diastole (that is, the time between heartbeats in which the blood returns from the body to the heart). Later in the disease, the heart may not pump blood efficiently. Restrictive cardiomyopathy may affect either or both ventricles and may or may not be associated with a disease of the heart muscle.

1.3.4 Mitral Valve Stenosis

Mitral stenosis is a condition in which the mitral valve leaflets become thickened and the commissures fused along with thickening and shortening of the chordae tendineae. The normal area of the mitral valve orifice is 4-6 sq. cm. When this orifice is reduced to 2 sq.cm, increased left atrial pressure (LAP) is necessary for normal transmitral flow. Critical mitral stenosis occurs when the opening is reduced to 1 sq. cm. At this stage, elevated left atrial pressure (LAP) is required to maintain a normal cardiac output [49].

1.4 Background and Motivation

Fluid-Structure Interaction (FSI) is the coupling of fluid flow and structure motion, and it has recently become one of the foremost researches in the field of computational mechanics. The fluid-structure interaction (FSI) problem has been studied by many researchers using different techniques but only recently, with the significant advances in computational resources power, researchers has been able to study real world applications. One of the interesting applications of the FSI is modeling of the motion

of the heart valves interacting with the blood. The proposed research will focus on fluid-structure interaction dynamics related to the mitral valve. The goal is to provide insight into the physics of the flow and to develop engineering methods to predict the success of surgical plan. The development of a computer simulation tool of a human heart which is capable of reproducing the hemodynamic characteristics of the blood flow through the left ventricle and mitral valve will allow significant progress to be made towards an optimum design of surgical plan. Moreover, the ability to simulate a wide range of design parameters in terms of hemodynamic performance will provide clinicians with a tool for quantitative estimation of the benefits of valve replacement operation.

1.5 Previous Works

In the mid to late 1990s, the computer resources available to the heart valve researchers developed to the point at which three-dimensional and fluid-structure interaction simulations of heart valves could be performed. Au Greenfield [2] predicted the steady flow through a disk-caged valve. They performed FSI simulation in which the disk has rigid motion from closed position to full open position. They tried to predict thrombosis formation in laminar flow at Re = 100, which is a volumetric flow much lower than physiological values. They solved vorticity equations for the fluid flow and the discretization scheme is finite difference. They observed a jet at the edge of disk when the disk is almost at closet position. Also they investigated shear stress in the blood at different positions of the disk. Underwood and Mueller [32, 33] employed the same method to predict the separation of the blood downstream of the disk valve for Reynolds numbers from 20 to 1300. Their model included the sinus of aorta and aorta. They presented stream functions, vorticity and shear and normal stress plots. They investigated that the maximum value of the shear stress occurs on the upstream corner of the disk. They identified the separated or reverse flow regions. To predict two-dimensional fluid-structure interactions, Peskin et al. [88] developed an immersed boundary method to couple the blood flow to the structure of the heart and its valves. They used the method to predict the flow through a mitral valve mounted in a straight tube connected to the left ventricle [31]. They also applied the method to predict the flow through prosthetic valves [72]. The early version of the immersed boundary method was limited to very low Reynolds numbers. Peskin and McQueen [83] extended the method to larger Reynolds and the results were improved between the flow at Re = 20 and Re = 200.

Idelsohn et al. [96] simulated steady flow of the blood through three common types of prosthetic heart valves using finite element method. The velocity, pressure and stress contours were obtained for the disk-type, tilting-disk and ball-type prosthetic heart valves in the aortic positions with Reynolds numbers up to 900, 1500 and 2000 respectively. The accelerated flow, recirculation and stagnation areas were presented in detail. The flow characteristics and performance for each valve were compared and the results were presented in terms of energy loss and maximum shear stress.

Stevenson et al. [22], [21] performed numerical simulation of steady turbulent blood flow through trileaflet tissue valve. They used a curvilinear formulation of the vorticity-stream-function form of the Navier-Stokes equations to overcome the problem with Cartesian grids. They also used model with the wall function method for turbulence. The was picked since they realized this model has better performance comparing with the lower order turbulence models. The above methods were limited to two-dimensional or axisymmetric flow.

More recently Huang et al. [42] performed time-accurate two-dimensional simulations of a tilting disk heart valve using a grid resolution of over 90,000 nodes, much larger than any previous heart valve simulation, for Re between 10 and 1000.

King et al. [75] performed a steady two-dimensional finite element simulation of a bileaflet heart valve at Re = 3000. Also, King et al. [74], [76] modeled one quarter of the bileaflet valve geometry using fluid-structure interaction technique during first half of systole. They used a sinusoidally varying inlet velocity to model the acceleration phase of systole with a peak Re = 3000. Flow was assumed to be Newtonian and laminar. The peak systolic Reynolds number was 1500. They did both experiment (using laser Doppler anemometry) and CFD modeling and compared the results. They observed that a vortex was shed from the valve leaflets and as systole progressed the two major orifice jets were directed towards the aortic walls and the a weaker central jet was seen in both experimental and CFD models. Also large vortices were created on either side of central orifice jet in the sinus area of the aorta.

Kiris et al. [54] used a multi block method with approximately 22,000 nodes to predict the three-dimensional flow in a fixed tilting-disk valve. They used the full three-dimensional geometry for steady flow and varied the Reynolds from 2000 to 6000.

Krafczyk et al. [66] used the Lattice-Boltzmann method with over 5 million particles to predict the flow in a full three-dimensional model of a fixed bileaflet valve at different opening angles using a pulsating inflow with a peak Re = 1800. The focus

of their study was investigating 3D flow pattern and shear stress downstream of the valve. They observed that shear stress remained in similar size (as was observed at the entrance of the valve) far away from walls because of very steep velocity gradients due to vortex-jet interactions.

Aluri and Chandran [87] and Lai et al. [59] numerically studied the effect of valve closure on the cavitations formation for mechanical mitral [87] and aortic [59] valves. To avoid complexity and focus on the detail of flow patterns near the tips of the leaflets, they also restricted their model to two-dimensional. Their study included leaflet motion towards closure and sudden stop in the closed position. They reported creation of large negative pressure transient downstream of the valve. Also they calculated the stress induced to the leaflet in the sudden stop in the closed position.

Peskin and McQueen [16], [17] used immersed boundary method to perform fluid-structure interaction analysis of heart valves. They successfully computed the flow in the entire heart at a Reynolds number much bellower than physiological range. Their three-dimensional method was also applied to heart valves [18] however difficulties still exist with extending their method to predict the turbulent flow that often occurs in heart valves near pick systole.

Carmody et al [10] simulated 3D left ventricle and aortic valve using finite element package called LS-DYNA since they attempted to implement a complicated geometry which is left ventricle. They simplified their model into two separate sub-models including left ventricle and aortic valve. They modeled the left ventricle separately in order to obtain velocity distribution of the flow delivered by the left ventricle to the aortic valve. This information in the form of time-varying distributions of velocity provides boundary conditions for the aortic valve model. They did not include the Mitral valve due to avoiding more computational efforts. They considered the Mitral aperture as an orifice on which a uniform pressure distribution similar to the atrio-ventricular pressure difference was applied in diastole. The reason for employing this procedure is that the orifice allows the blood flows into the left ventricle when the left ventricle meets a specific pressure difference at each time during the cardiac cycle. Also in systole the aortic aperture was considered as outlet type of boundary condition while the Mitral aperture was closed. They also provided ventricular contraction by decreasing the temperature of the ventricular wall with the time to reach appropriate volume at the end of systole. This procedure was employed to reduce computational efforts because the alternative method is extracting geometry from clinical images at each time step which needs reconstruction of the left ventricle at any time step.

The fluid was considered as laminar and Newtonian since the package can not model turbulent flow regime and we believe including turbulent model will improve accuracy of the results near pick systole the results show that the maximum Reynolds number at pick systole in the middle point of aortic aperture is about 18000.The results from the model of the left ventricle show that the distribution of velocity vectors across the aperture of aortic valve is not symmetric in terms of direction this is an advantage of involving left ventricle in the model. Also the distribution of pressure is not symmetric. The results from the aortic model include the displacements of the aortic valve leaflets and stress distributions in the aortic valve. They reported that theses results are similar in form of magnitude to the experimental studies done by Patterson et al. [80].

Lei et al. [61] simulated a 3D bileaflet valve in the Mitral position. Their first simulation was conducted with the fixed wall ventricle which its tip was cut to perform a pressure inlet to allow the blood flows into the left ventricle. In his second simulation he involved the motion of ventricular wall using 2D MRI data. The fluid was considered laminar, incompressible and Newtonian.

Nakamura et al. [67] simulated blood flow in an integrated model of the left ventricle and the aorta. In their model the aortic valve was considered as an orifice type of boundary condition to avoid fluid-structure analysis of aortic valve. Ventricular wall was moved inward and outward in a normal direction to the wall to model the heart beating process using clinical data. The blood flow was assumed to be laminar, incompressible and Newtonian. They investigated the formation of recirculating flow beneath the aorta valve (AV) during diastole effecting systolic ejection. Also they investigated that blood flow through Aorta orifice creates swirling flow, provoking helical flow in the aorta.

De Hart et al. [20] extended their fictitious domain fluid-structure interaction code to predict the flow and motion of fiber-reinforced bioprosthetic and native aortic valves. Because of the cost of their numerical method, their work was limited to predicting only one sixth of the valve with a limited spatial resolution of the fluid and valve leaflets using only 26,500 degrees of freedom. The flow was considered in laminar regime and Newtonian.

Cheng et al. [107] conducted fluid-structure coupled simulation of the heart by combining the fluid and structure equations as a unified system and solving it simultaneously at every time step. They simulated the left ventricular filling flow in a three-dimensional ellipsoidal thin-wall model geometry of the human heart, based on a

prescribed time-varying Young's modulus. In that work they analyzed the pressure–volume relation of the model ventricle, the spatial and temporal distributions of pressure, transient velocity vectors as well as vortex patterns.

Bernardo Baccani et al. [6] investigated the flow inside the left ventricle during the diastole by numerical solution of the Navier–Stokes equations under the axisymmetric assumption. They analyzed the solution under healthy conditions in terms of vorticity dynamics and they showed that the flow field is characterised by the presence of a vortex wake; it is attached to the mitral valve during the accelerating phase of the E-wave, and it detaches and translate towards the ventricle apex afterwards. Also they reported that In the presence of ventricle dilatation the mitral jet extends farther inside the ventricle, propagation velocity decreases, and the fluid stagnates longer at the apex.

In another work Bernardo Baccani et al. [5] simulated the flow inside a model of left ventricle during filling (diastole) by the numerical solution of the equations of motion under the axisymmetric approximation. A truncated ellipsoid geometry was used for left ventricle and a simple conceptual model was introduced to simulate the presence of the moving mitral valve. The presence of a moving valve was found to produce a non-simultaneous spatial development of the entering bulk flow and a slightly more complex vortex wake structure.

Hiroshi Watanabe et al. [100] developed a threedimensional finite-element-based simulation program incorporating the cellular mechanisms of excitation-contraction coupling and its propagation, and simulated the fluid-structure interaction involved in the contraction and relaxation of the human left ventricle. Thay used the FitzHugh-Nagumo model and four-state model representing the cross-bridge kinetics for cellular model. They simulated dynamics of ventricular filling as well as ejection by using electrical analog of pulmonary circulation and left atrium as a preload and the windkessel model as an afterload.

Sainte-Marie et al. [92] We proposed an approach to model the electromechanical behavior of the heart, and used the model in a data assimilation procedure in order to perform an identification of the parameters and state. The modeling of the heart tissue was based on an electrically activated contraction law formulated via multi scale considerations and was consistent with various physiological and thermomechanical key requirements. For the global heart system also they incorporated a simplified lumped modeling of the blood compartments.

Liang Zhong et al. [108] conducted a study to develop the contractility indices in

terms of the left ventricular ellipsoidal geometrical shape-factor. They expressed the contractility index in terms of the shape factor (the ratio of the minor axis and major axis of the instantaneous left ventricular ellipsoidal model). Also, They developed another contractility index based on how far apart the in vivo shape factor at the start of ejection is from its optimized value. The values of shape factor were calculated from cineventriculographically monitored left ventricular volume, myocardial volume and wall-thickness.

F. Domenichini [23] presented a numerical study of the three-dimensional fluid dynamics inside a model left ventricle during diastole. They modeled the left ventricle as a portion of a prolate spheroid with a moving wall, whose dynamics is externally forced to agree with a simplified waveform of the entering flow. The flow was characterized by a well-defined structure of vorticity that was found to be the same for all values of the parameters, until, at low values of the Strouhal number, the flow developed a weak turbulence.

Rafael Beyar et al. [8] developed a thick wall ellipsoidal model of the left ventricle to describe both the transmural and global features of ventricular contraction. They included fiber oriented in parallel with the well known physiological properties of the muscle fibers. The model described systolic function utilizing the force-length and force-velocity relationship of the fibers. They simulated the local oxygen consumption by assuming a linear relationship with the area of the stress-length loop and the triangle between the loop and the maximum active force formed locally for each fiber. They achieved the transmural distribution of oxygen demand as a function of the loading conditions, and accounted for twist of the left ventricle over its long axis during ejection.

Rumei Dong et al. [24] developed a finite element model of the left ventricle with an axisymmetric geometry to determine left ventricular pressures and volumes.They related regional myocardial contractions defined by the finite elements to the time-varying left ventricular elastance (instantaneous pressure over volume ratio). In their work left ventricular geometry was modeled as a truncated ellipsoid with user defined parameters such as wall thickness, short axis length, and long axis length. They assumed the stress-strain relationship for each element to be linear but with a timevarying Young's modulus. They concluded that the left ventricular ejection fraction and pressure and volume curves are consistent with typical clinical observations.

P. N. Watton et al. [101] used Immersed Boundary Method to model multileaflet elastic structure including the chordae attached to the leaflets and continued through

the leaflet surfaces. In addition, they applied an external surface pressure to the leaflets, enabling the deformations that arise under steady loads to be solved. They validated their model for a model of the native mitral valve under systolic loading and for a prosthetic aortic valve under static loading. Results were compared with those obtained by using the commercial package ANSYS as well as with experimental measurements.

Zhenhua Hu et al. [41] presented an iterative model to estimate the in-vivo myocardium material properties, the active forces generated along fiber orientation, and strain and stress distribution in both ventricles. Using the model, they simulated the mechanical events of a few different heart diseases. Noticeable strain and stress differences were found between normal and diseased hearts.

Jean G. Dumesnil et al. [26] examined the relations that may exist between the geometric variables most frequently used to describe left ventricular contraction. The left ventricle was represented by a thick-walled cylinder contracting both radially and longitudinally. In this model, they showed wall thickening, mid-wall radius shortening and longitudinal axis shortening were uniquely related during contraction. Also, they demonstrated that internal radius shortening was not uniquely related to these variables, but was also determined by the specific geometry of the cylinder, expressed in terms of the mid-wall radius-to-wall thickness ratio of the cylinder.

Ling Xia et al. [106] developed a biventricular model, which coupled the electrical and mechanical properties of the heart, and computer simulations of ventricular wall motion and deformation. In their constructed electromechanical model, the mechanical analysis was based on composite material theory and the finite-element method. They used an electrical heart model to simulate the propagation of electrical excitation and the resulting active forces were used to calculate ventricular wall motion. They calculated Regional deformation and Lagrangian strain tensors during the systole phase. Their simulations showed that during the period of systole, the right ventricular free wall moves towards the septum, and at the same time, the base and middle of the free wall move towards the apex, which reduces the volume of the right ventricle.

N. J. Tustison et al. [1] estimated both left and right ventricular deformation from tagged cardiac magnetic resonance imaging using volumetric deformable models with a nonuniform rational B-splines (NURBS) basis. They constructed the initial nurbs model from a set of short and long axis images by fitting two surfaces with the same parameterization to the set of epicardial and endocardial contours from which a

volumetric model was created. Using displacement information derived from tag line and contour data, they solved for the optimal homogeneous coordinates, in a least-squares sense, of the nurbs model at a later time point using quadratic programming.

Jacques M. Huyghe et al. [43] described an axisymmetric model for myocardial tissue as a spongy anisotropic viscoelastic material. It included torsion around the axis of symmetry of the ventricle, transmural variation of fiber angle, and redistribution of intracoronary blood in the myocardial wall.

Ronald F. Janz et al. [46] used a finite-element model to analyze the mechanical behavior of the left ventricle. They treated the ventricle as a heterogeneous, linearly elastic, thick walled solid of revolution. The inner third of the ventricular wall was assumed to be transversely isotropic and in the outer wall two-thirds of the ventricular wall of the myocardium was assumed to be isotropic. They simulated the valvular ring at the base of the ventricle by a homogeneous layer cf collagen. The endocardial surface resulted in significantly lower axial and circumferential stresses in this region than were present in a homogeneous, isotropic model. The presence of a simulated valvular ring resulted in a concentration of relatively large stresses near the base of the ventricle.

A Bosnjak et al. [44] presented a segmentation method of volumetric echocardiographic images, using a 3D front propagation initialized as a small sphere that grows until arriving to the walls of the left ventricle, adjusting the parameters to the model. They developed the project in three modules called ; acquisition, segmentation and Visualization. The images acquisition of volumetric sequences of the left ventricle was obtained in an echocardiographic test. The segmentation was divided in three parts. First segmentation method 2D to 3D. They used a fiont propagation method initialized with a circle that grows inside the acquired volume. In the second segmentation method, a 3D front propagation initialized with a small sphere placed in the interior of the left ventricle, which began to grow occupying part of the ventricle cavity. In the third segmentation method The surface obtainedpreviously was parameterized.

Richard G Wise [105] developed a quantitative analysis and model for the differences in left ventricular dynamics in normal and spontaneously hypertensive rats, as determined using non-invasive magnetic resonance imaging (MRI). They emerged with a characterization of the geometrical changes in the left ventricle resulting from hypertension. In addition, the techniques they used are potentially applicable to the study of other disease models for important human cardiac pathologies. A gradient-echo multislice imaging sequence (echo time 4.3 ms) achieved complete image coverage

of the heart at high time resolution (13 ms) through the cardiac cycle. An ellipsoidal figure of revolution offered an effective description of the three-dimensional left ventricular geometry throughout the cardiac cycle in both normal and diseased animals. The model successfully characterized both the dynamic changes in the shape of the left ventricle through the cardiac cycle and the pathological alterations resulting from spontaneous hypertension. The elliptical model also formed the basis of a simple stress distribution analysis. Such parametric descriptions thus provided a useful alternative to more complex finite element analyses of cardiac function.

Norberto Malpica [68] propsed contrast echocardiography as an indicator of myocardial perfusion in a non-invasive way. They obtained the reperfusion curves by destroying all the microbubbles using an ultrasound pulse with high mechanical index and acquiring images during the reperfusion process. To analyze the complete myocardium, they proposed a method for the simultaneous segmentation and tracking of endocardium and epicardium in myocardial contrast echocardiography sequences. Their model consisted of two active contours, guided by optical flow estimates. The evolutions of the two contours were coupled geometrically using a novel scheme that imposes stability in wall thickness, to deal with low contrast regions in the epicardial contour. The model was evaluated with experimental and clinical sequences, comparing the results with manual segmentations carried out by an expert.

Elie H. Karam [50] presented a model of the left ventricle derived based on nonlinear stress-length myocardial characteristics integrated over truncated ellipsoidal geometry, and second-order dynamic mechanism for the excitation-contraction coupling system. The results of the model described the effects of the viscoelastic damping element of the electromechanical coupling system on the hemodynamic response. They considered different heart rates to study the pacing effects on the performance of the left-ventricle against constant preload and afterload conditions under various damping conditions. Their results indicated that the pacing process of the left ventricle has to take into account, among other things, the viscoelastic damping conditions of the myofilament excitation-contraction process.

Helene A. Simon et al. [95] evaluated the hinge flow dynamic of the 23 mm St. Jude Medical (SJM) Regent and the 23 mm CarboMedics (CM) valves under aortic conditions and compared these results with previous findings under mitral conditions. They captured velocity and Reynolds shear stress fields using two-component laser Doppler velocimetry. As reults, they found that under aortic conditions, both the SJM and CM hinge flow fields exhibited a strong forward flow pattern during systole

and two main leakage jets during diastole. In addition, they showed that aortic and mitral flow patterns within the two hinges were similar, but with a more dynamic flow during the forward flow phase under aortic conditions. Velocity magnitudes and shear stresses measured under mitral conditions were generally higher than those obtained in the aortic position, which may explain the higher rates of thromboembolism in the mitral implants when compared with the aortic implants.

Morten O. J. Jensen et al. [47] developed an in vitro model that allowed quantification of the papillary muscle spatial position and quantification of the three dimensional force vector applied to the left ventricular wall by the papillary muscles. This system allowed for the quantification of the global force exerted on the posterior left ventricular wall from the papillary muscles during simulation of normal and diseased conditions. In this paper, the effects of papillary muscle (PM) position are investigated with reference to changes in the PM forces. When we look at the normal PM position for the fresh valves, an interesting relationship between the normal position of the posteromedial PM and the anterolateral PM became evident. The normal position of the posteromedial PM was located further towards the apex than the anterolateral PM in 67 percent of all the valves.

Ling Chen et al. [12] performed experimental measurements of mitral valve leaflet deformation under quasi-static pressure loading on isolated porcine hearts. Biplane video images of markers placed on the anterior leaflet surface were used to reconstruct the 3D position of the markers at several pressure levels over the physiological range. They used a least-squares finite element. method to fit parametric models to the markers and to calculate the deformation over the surface. Their results showed that the leaflet deformations were anisotropic, exhibiting a large nonhomogeneous radial stretch and a small circumferential stretch. This information can be used to better understand how the valve deforms under physiological loading, and to help design treatments for valve problems, such as mitral regurgitation.

Jun Liao [62] compared the stress relaxation properties of different types of chordae and relate their variation to structural features. Fifty chordae from eight hearts were subjected to stress relaxation tests in this study. The percent stress relaxation and the relaxation rates were found to increase in the order of marginal, basal, and strut chordae. They quantified the collagen, elastin, and glycosaminoglycan (GAG) content in chordae using hydroxyproline assay, fastin elastin assay, and fluorophore-assisted carbohydrate electrophoresis, respectively.

Ling Chen [11] conducted experimental measurements of mitral valve deformation

under quasi-static pressure loading on isolated pig hearts before and after transecting both strut chordae. Theu used biplane video images of markers placed on the anterior leaflet surface to reconstruct the 3D position of the markers. The 2D nonhomogeneous deformations in the anteriorv leaflet were calculated by least squares fit to the 3D marker coordinates in successive pressure loading states. they showed that the anterior leaflet undergoes large, anisotropic and nonhomogeneous deformation, with a significant radial stretch gradient and smaller, uniform circumferential stretch. They osereved that a gradient in the circumferential stretch as an increase from the annulus toward the coaptation line. In addition thay showed that without the support provided by the strut chordae, the center portion of the anterior leaflet experienced a substantial change in shape in response to the systolic pressure, altering the load-bearing mechanism in the valvular structure.

Jorge Hernan Jimenez et al. [48] investigated the effects of annular motion/flexibility and papillary muscle displacement on chordal force and mitral valve function. They studied six human mitral valves in a left heart simulator using a flexible annular model. The monitored mitral flow, trans-mitral pressure and chordae tendineae tension online in normal and pathophysiologic papillary muscle positions. They observed that the flexible annulus model showed a significant increase in mitral regurgitation volume when compared to static annuli models. They also saw there was a significant increase of force on the basal chords compared to the force present with the static annuli models.

S. Aluri et al. [4] performed a computational fluid dynamic simulation of a mechanical heart valve closing dynamics in the mitral position in order to delineate the fluid induced stresses in the closing phase. They computed the pressure and shear stress fields in the clearance region and near the inflow (atrial) side of the valve during the mitral heart valve closure. Three separate numerical simulations were performed. The atrial chamber pressure was assumed to be zero in all the simulations. The first simulation was steady flow through a closed mitral valve with a ventricular pressure of 100 mm Hg. In the second simulation, the leaflet remained in the closed position while the ventricular pressure increased from 0 to 100 mm Hg at a rate of 2000 mm Hg/s. In the third case, the leaflet motion from the fully open position to the fully closed position was simulated for the same ventricular pressure rise (simulating the normal closure of the mechanical valve).

M. S. Sacks et al. [91] presented a detailed study of the surface strains in the anterior leaflet in the functioning of mitral valve (MV). They determined the three di-

mensional spatial positions of markers placed in the central region of the MV anterior leaflet in a left ventricle-simulating flow loop over the cardiac cycle. They demonstrated that during valve closure the anterior leaflet experienced large, anisotropic strains with peak stretch rates of 500-1000 percent. This rapid stretching was followed by a plateau phase characterized by relatively constant strain state. They also hypothesized that the presence of this plateau phase was a result of full straightening of the leaflet collagen fibers upon valve closure. This hypothesis suggested that the MV collagen fibers are designed to allow leaflet coaptation followed by a dramatic increase in stiffness to prevent further leaflet deformation, which would lead to valvular regurgitation.

Jonathan S. Grashow et al. [36] explored the effects of strain rate on the biaxial mechanical properties of the native mitral valve anterior leaflet (MVAL). They developed a novel high-speed biaxial testing device, capable of achieving in vitro strain rates reported for the MVAL. The resulting loading stress–strain responses were found to be remarkably independent of strain rate. The hysteresis, defined as the fraction of the membrane strain energy between the loading and unloading curves tension-areal stretch curves, was low and did not vary with strain rate. They indicated that the MVAL tissues exhibit complete strain rate insensitivity at and below physiological strain rates under physiological loading conditions.

Mario G et al. [97] developed a three dimensional coupled fluid-structure dynamic model of the mitral valve, in order to determine the stress-strain distribution in the valve, as well as the blood flow patterns. The valve leaflets were represented by orthotropic non-linear elements and the chordae were represented by linear elements (LS-DYNA). They computed the structural solution using a Lagrangian method. They applied physiologic pressure wave profiles input for both diastole and systole. They demonstrated that physiologic opening and closing of the valve, and time to leaflet closure was 30 mSec after the onset of systole. Stress was highest in the anterior leaflet 825 kPa, the maximum flow velocity was 500mm/sec, and peak systolic pressure was 120 mmHg.

1.6 Literature Review Conclusion

The ongoing researches in the cardiovascular field can be categorized in the following items:

- **Cardiovascular Imaging:** In this field the researches attempted to construct patient specific time dependent 3D left ventricular geometry. This geometry is

used in the FSI model specified for the patient.

- **Experimental Hemodynamics:** In this field researches use In Vivo and In Vitro data to investigate the left ventricular and trans-valvular blood flow.
- **Computational Hemodynamics Using FSI:** In this field the strong and partitioned FSI methodologies are used to investigate the ventricular and trans-valvular blood flow.
- **Lump Models:** In this field the researches develop and implement electrical circuit and simulate the cardiovascular circulatory systems.
- **Structural Models of Tissue:** In this field the researches develop finite element models to calculate the structural behavior of myocardium and heart valves.

1.7 Contributions

The following contributions to the state of the art in the area of computational fluid dynamics and fluid-structure interaction have been accomplished:

- **Development of a flexible and computationally efficient fluid-structure interaction (FSI) framework:** The mitral valve experiences large deformations relative to its size. To accommodate this requirement, the FSI model for the mitral valve allows for large mesh deformations. All the current FSI frameworks reported in the literature for the modelling of heart valves employ the strong form of the FSI methodology where the structural and fluid equations are solved together using the finite element method. This approach is not practical in terms of convergence and this is there reason that in all of the previous works, a coarse mesh has been used to allow the computational iterations to achieve convergence. On the other hand, the partitioned method is much more practical and is widely used in industry. However, it is not capable of handling large deformations that is required for FSI modeling of a mitral valve. Here, we have developed a FSI framework with re-meshing capabilities to overcome the large deformation challenge.
- **Modeling of the Mitral Valve Closure:** One of the important physiological features of the mitral valve function is the coaptation of the leaflets in the

systole which requires a complete closure of the valve. The existing partitioned FSI frameworks are not able to model the complete closure of the mitral valve. This issue has been addressed and resolved.

- **Investigation of the Diastolic Flow:** Using the proposed FSI framework, we conducted the FSI simulation of the mitral valve for the complete cardiac cycle. We also used the vortex ring formation theory to characterize the diastolic blood flow and left ventricular efficiency in diastole. Since the complete closure of the mitral valve has been achieved in the simulations, several interesting characteristics have been observed the early diastolic flow pattern.
- **Simulation of the Systolic Anterior Motion in the Obstructive Hyperthrophic Cardiomyopathy:** The FSI framework was used to simulate the venturi and drag mechanisms which are believed to be the cause of SAM in OHCM.
- **FSI Simulation of Flow in a New Accelerated Heart Valve Durability Tester:** Also, for an industrial application, the FSI framework was used to simulate the flow circulating in a new accelerated durability tester for heart valves.

1.8 Building Blocks of the Thesis

The models which have been developed to reach the objectives of the thesis are presented in the figure 1.1. We first developed a simple parametric model for the geometry of the left ventricle. Next, we developed a lump model to calculate the functioning parameters of the left ventricle such as left ventricular volume, pressure and flow rate with respect to time. Next, the motion of the left ventricle was parametrized. This information were used as boundary conditions for the CFD simulation. Next, we performed the CFD simulation of the blood flow inside the left ventricle without the mitral valve. Next, we developed a parametric geometrical model for the mitral valve. Next, structural simulation of the mitral valve using the data from lump model as structural boundary conditions was performed. Next, we created the left ventricular geometry with mitral valve and finally, we performed two-way fluid-structure simulation of the mitral valve in a beating left ventricle. Also, as an extra work, I applied the full FSI methodology which was developed to handle large deformation for an industrial application. In this work, I simulated the flow inside a new concept of a prosthetic heart valve fatigue tester.

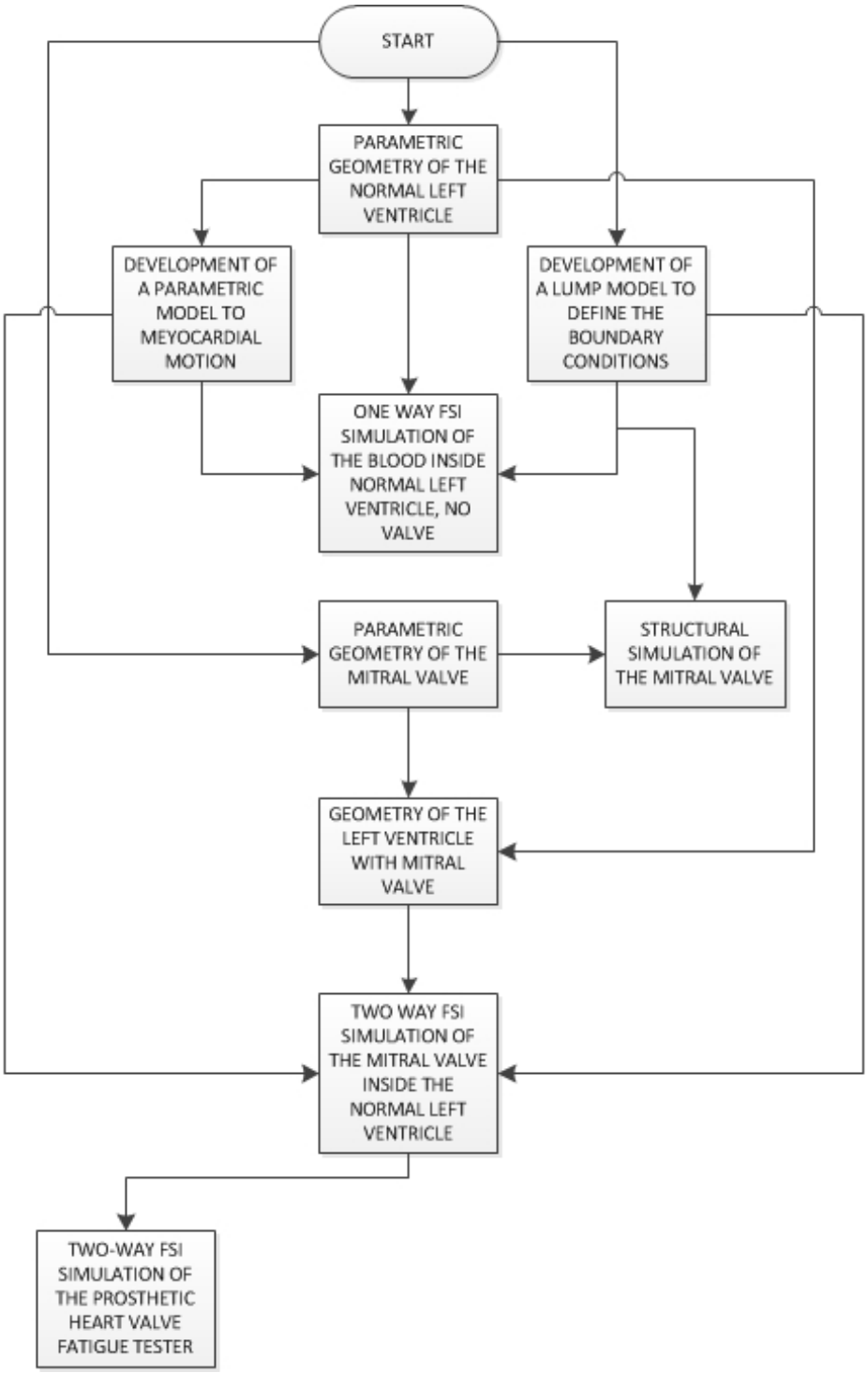

Figure 1.1: Flow chart of the models which have been developed in this work

1.9 Objectives

The objectives of this work are the followings:

- Developing parametric geometrical models for the left ventricle and natural mitral valve.
- Performing structural analysis of the mitral valve.
- Developing a fluid-structure technique to be able to handle large deformation.
- Developing a computational model for the fluid-structure interaction simulation of the natural and prosthetic mitral valve.
- Investigation of the blood flow in the diastole phase using the above model.

Chapter 2

Hemodynamics of the Left Ventricle with Prescribed Boundary Conditions

2.1 Parametric Model of the LV

The first component of the fluid-structure interaction modeling framework consists of constructing a parametric mathematical model of the left ventricle (LV). In the early days, scientists used mathematical models to fit the cavity of LV. In 1969, Dieuddoe [65] was one of the first researchers to make an analogy between the LV and a truncated eggshell in which the aortic and mitral openings are mounted on a truncated base surface. In this work, the LV wall was assumed to have a varying thickness by having the largest thickness at the circumference plane and being thin at the apex in the bottom. The inner (endocardium) and outer (epicardium) surfaces were shaped as confocal ellipsoids of revolution. Later, Streeter [45] experimentally validated this model by comparing the model to a dog's heart and proposed some improvements to the model.

More recently, technological developments in imaging technologies such as x-ray, ultrasound and Magnetic Resonance (MR) provided scientists with a tool to more accurately construct the four-dimensional (3D + time) geometry of the LV. In one of the most complete works documented in the open literature, Lorenz [64] describes a method to generate a cardiovascular model including the coronary arteries using MR images. However, the segmentation technique used is manually intensive and time consuming.

In another work, Michael R. Kaus [51] presented an automated technique for myocardium segmentation using 4D MR images. Although his method is automated and fast,the final model resulted in surface discontinuities such as small holes and bumps

which hindered automatic finite element and computational fluid dynamic meshing techniques. To overcome these issues, the surfaces required manual intervention which made it cumbersome and time consuming, as well. This is particularly critical when it is intended to create the geometry of LV at different time steps during a cardiac cycle.

Here, we have developed a geometrical parametric model for the LV by using measurements from documented MR images. The main advantage of the proposed method is that the LV can be constructed in an automated and computationally efficient manner at every time step of the simulation cycle.

2.1.1 Model Construction Method

In this model, the septum and free wall are simulated as half ellipsoidal volumes where the dimensions are extracted from MR images. Figures 2.1 and 2.2 show the top and side views of the model. The dimensions b and d are septum-free wall and anterior-posterior short axes. The dimension d is the free wall radii of curvature at mid point of the free wall. Also, the dimension a is the LV long axis.

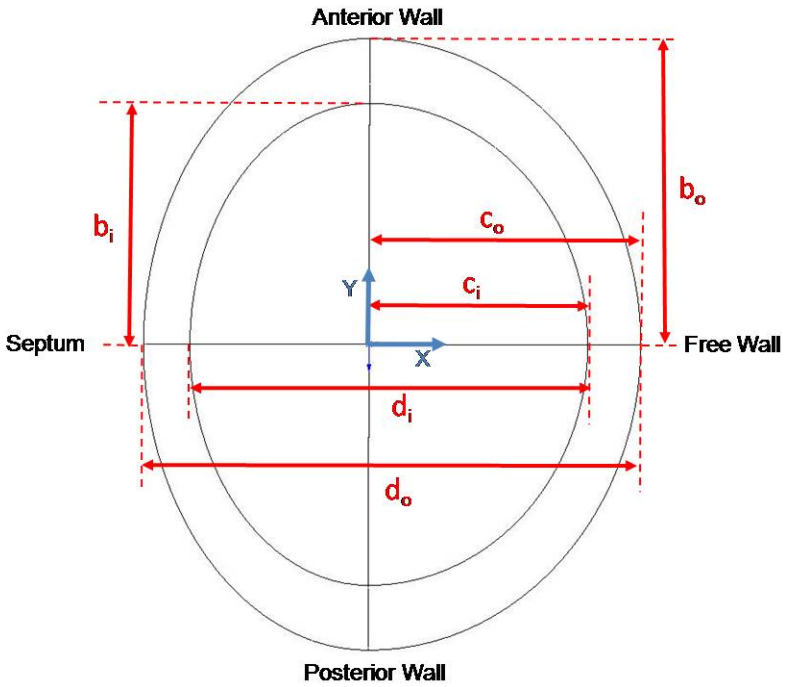

Figure 2.1: Top view of the LV: Septum and free walls are simulated using half ellipses whose dimensions are measured from MR images. b and d are septum-free wall and anterior-posterior short axes; d is free wall radii of curvature at mid point of free wall.

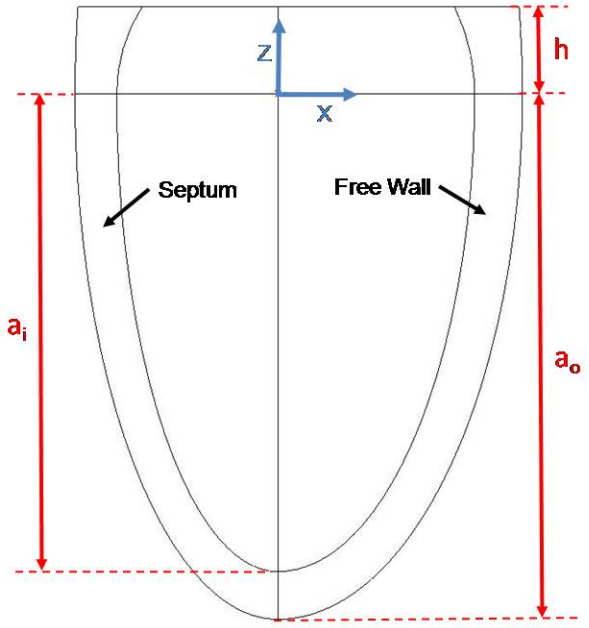

Figure 2.2: Side view of the LV. a: long axis and h: height of truncation

The septal ellipsoidal volume is calculated by integrating the septal segment parallel to the basal plane from base to apex.

$$\forall_S = \int_{-a_i}^{h} \frac{1}{2}\pi xy dz \tag{2.1}$$

x is obtained from the equation of an ellipse in the xz plane:

$$\frac{x^2}{(d_i - c_i)^2} + \frac{z^2}{a_i^2} = 1 \tag{2.2}$$

Also, y is obtained from the equation of ellipse in the yz plane:

$$\frac{y^2}{b_i^2} + \frac{z^2}{a_i^2} = 1 \tag{2.3}$$

Substituting x and y from equations (5.2) and (2.3) into the integral (5.1), we obtain:

$$\forall_S = \int_{-a}^{h} \frac{\pi}{2}\left(\frac{d-c}{a}\right)\left(\frac{b}{a}\right)\left(a^2 - z^2\right) dz \tag{2.4}$$

By solving the integral (2.4), we obtain the $\forall_s$ as:

$$\forall_S = \frac{\pi}{2}\frac{b_i(d_i - c_i)}{a_i^2}\left[a_i^2(h + a_i) - \frac{1}{3}\left(a_i^3 + h^3\right)\right] \tag{2.5}$$

Similarly, we derived a formula for free wall segment of the LV ($\forall_{FW}$):

$$\forall_{FW} = \frac{\pi}{2}\frac{b_i c_i}{a_i^2}\left[a_i^2(h + a_i) - \frac{1}{3}\left(a_i^3 + h^3\right)\right] \tag{2.6}$$

The volume of LV ($\forall_{LV}$) is the summation of the septal and free wall volumes, given as:

$$\forall_{LV} = \forall_S + \forall_{FW} = \frac{\pi}{2}\frac{b_i d_i}{a_i^2}\left[a_i^2(h + a_i) - \frac{1}{3}\left(a_i^3 + h^3\right)\right] \tag{2.7}$$

Also, the volume of the myocardium is calculated as follows:

$$\forall_{MY} = \frac{\pi}{2}\frac{b_o d_o}{a_o^2}\left[a_o^2(h + a_o) - \frac{1}{3}\left(a_o^3 + h^3\right) -\right] \frac{\pi}{2}\frac{b_i d_i}{a_i^2}\left[a_i^2(h + a_i) - \frac{1}{3}\left(a_i^3 + h^3\right)\right] \tag{2.8}$$

2.1.2 Measurement of the Model Parameters Using MR Images

MR images of a volunteer, 29-year old male, obtained from the open literature, were analyzed and the parameters of the above model were measured. Figure 2.4(1) shows the mid section, and the side view of the heart at the end of diastole. In this figure, the LV cavity, myocardium, left atrium, septum, base, apex and papillary muscles are visible. Figures 2.4(1) to 2.4(4) show the other measurements which are summarized in the table 2.1.

Table 2.1: Left ventricular dimensions measured from MR images.

Parameter	Units	Endocardium	Epicardium
a	mm	77	87
b	mm	34	46
c	mm	33	41
d	mm	60	75
h	mm	14.5	14.5

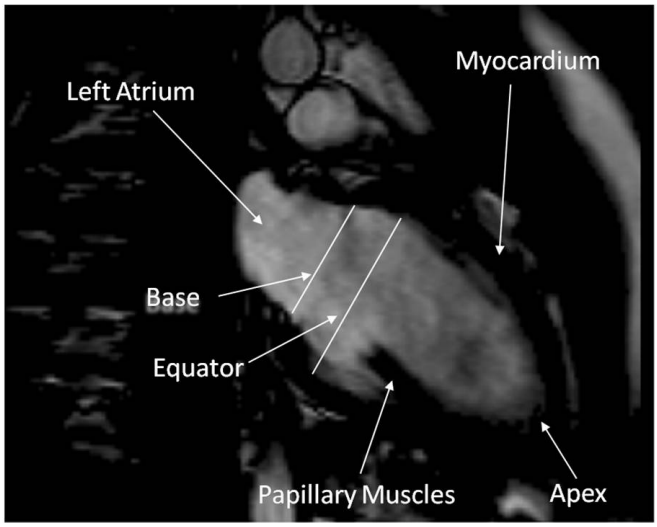

Figure 2.3: Side view of a male volunteer's heart which was used to measure the model parameters

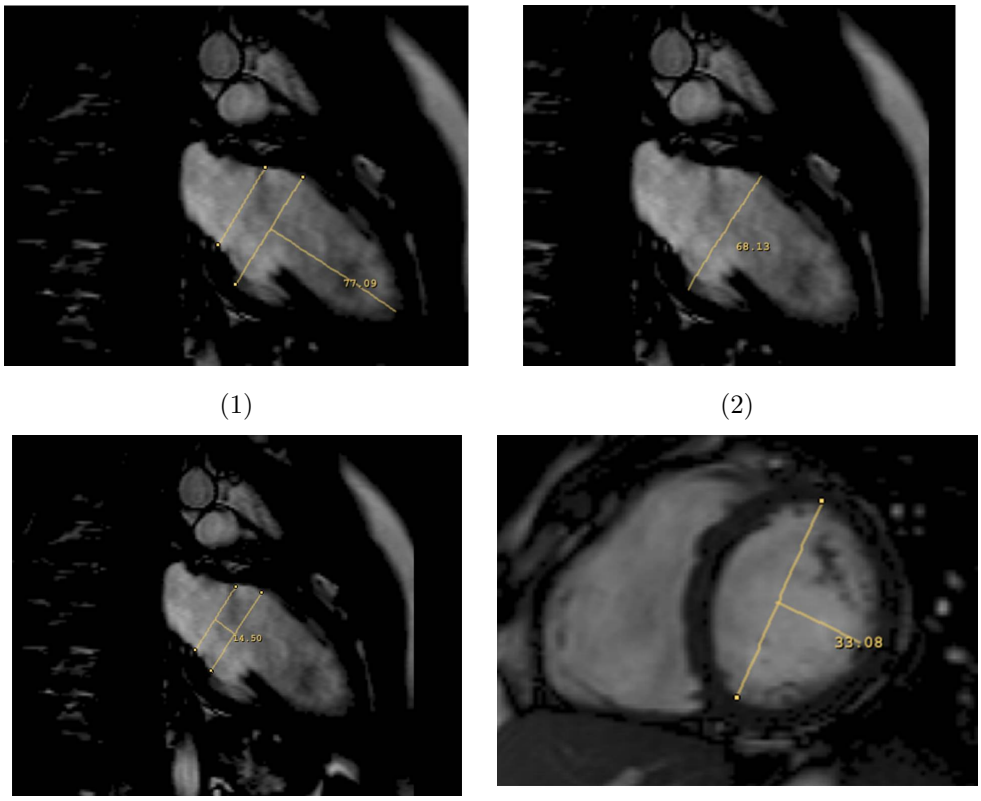

(1) (2)

(3) (4)

Figure 2.4: Long axis, short axis, h and c_i were measured.

2.2 Characterizing Left Ventricular Motion During A Cardiac Cycle

Here, a mathematical formulation for the motion of the LV wall is presented. This model satisfies the temporal variation of the volume profile of the LV. This formulation will be subsequently used as a boundary condition for fluid dynamic simulations of the model in the fluid-structure interaction studies.

In this model, we assume that the LV wall maintains its ellipsoidal shape during the motion. Therefore, the goal here is to formulate the equations of the ellipsoid at any time during a cardiac cycle. To do this, we defined ellipses whose centers have been shifted up as the shape deforms from the initial stage. Also, these ellipses pass through the fixed points A, B and C. Figures 2.5 and 2.6 detail the geometrical description of the model.

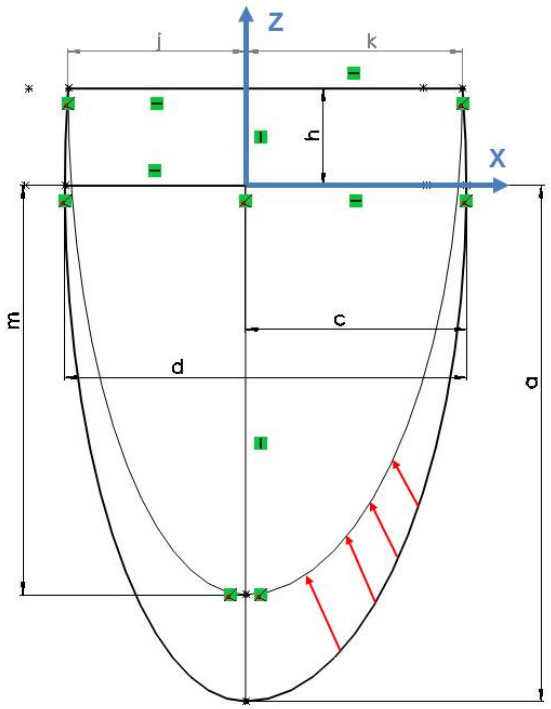

Figure 2.5: Geometrical description of the LV wall motion (front view). j, k and m are the short and long axes of the ellipses.

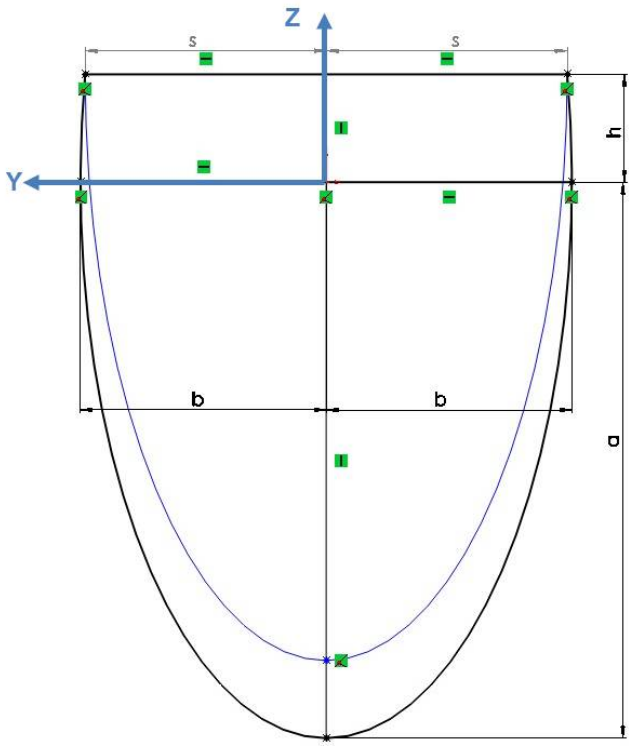

Figure 2.6: Geometrical description of the LV wall motion (side view). s and m are the short and long axes of the ellipses.

In this model, the parameters: $j = 26.52mm$, $k = 32.41mm$, $s = 33.35mm$ fixed and m is variable. To obtain m, we first calculate the volume of the deformed LV using the following integral:

$$\forall_{FW} = \int_{-m}^{h} \pi xydz \tag{2.9}$$

From the equation of the free wall in xz plane, we obtain x in terms of z:

$$\frac{(z-h)^2}{(m+h)^2} + \frac{x^2}{k^2} = 1 \tag{2.10}$$

Also, from the equation of the free wall in the zy plane, we obtain y in terms of z:

$$\frac{(z-h)^2}{(m+h)^2} + \frac{y^2}{s^2} = 1 \tag{2.11}$$

Substituting Eqs. 2.10 and 2.11 into the Eq. 2.9, we obtain:

$$\forall_{FW} = \frac{\pi}{2} \int_{-m}^{h} \frac{ks}{(m+h)^2} \left[(m+h)^2 - (z-h)^2 \right] dz \tag{2.12}$$

After calculating the integral 2.12, the $\forall_{FW} becomes$:

$$\forall_{FW} = \frac{\pi}{3} ks(m+h) \tag{2.13}$$

Similarly, $\forall_S is calculated as followed$:

$$\forall_S = \frac{\pi}{3} js(m+h) \tag{2.14}$$

Finlay, $\forall_{LV} becomes$:

$$\forall_{LV} = \frac{\pi}{3} (k+j)s(m+h) \tag{2.15}$$

After obtaining the LV volume, $\forall_{LV}$, as a function of time, we can calculate m at each time step. Next, we have implemented an existing lump model which calculates the left ventricular volume and pressure, aortic pressure and systolic flow rate at each time step during the complete cardiac cycle.

2.3 Limitations of the Model

The proposed left ventricular model (LV geometry and motion) has the following limitations:

- **Sharp Edges:** The proposed LV geometry contains sharp edges at the base including the intersection of the basal plane with the LV wall and the Mitral and Aortic apertures. These sharp corners may add some features to the left ventricular flow in the systole when the blood is striking toward the base. These features could appear as separation of flow at the sharp edges. We predict that the sharp edges will not have any significant impact on the main features of the flow such as left ventricular vortex ring in the diastole since in this phase the blood is flowing away from the basal sharp edges.

- **Maximum Apical Displacement:** In this model, the left ventricular motion is highest at the apex and zero at the base. Therefore the apex moves significantly during cardiac cycle.

2.4 Lump Model For The Boundary Conditions of the Left Ventricle

To introduce accurate boundary conditions to the aortic and mitral orifices for the fluid dynamics model, we simulated the arterial and pulmonary circulations using the Windkessel [102] and Alexander [3] models for aortic and mitral boundary conditions, respectively.

2.4.1 Arterial System Model

The arterial tree was modeled using the three element Windkessel model introduced by Westerhof *et. al.* [102]. As illustrated in Figure 2.7, the arterial vessels were simulated using a resistor and capacitor which represent the resistance and elastic capacity of the vessels, respectively. Also, the resistance of the aorta was simulated using another element. In this model, R_L and C_L represent the resistance and compliance of the peripheral system and R_{AO}, represents the resistance of the aorta.

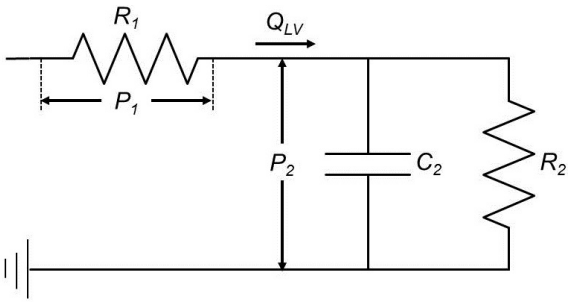

Figure 2.7: Three element Windkessel model to simulate peripheral system [102]. R_L and C_L represent the resistance and capacitance of the peripheral vessels and R_{AO} represents the resistance of the aorta.

The model is represented by the following equations:

$$\frac{dP_2}{dt} = \frac{1}{C_2}\left(Q_{LV} - \frac{P_2}{R_2}\right) \tag{2.16}$$

$$Q_{LV} = \frac{P_1}{R_1} \tag{2.17}$$

$$P_{LV} = P_1 + P_2 \tag{2.18}$$

2.4.2 Pulmonary Circulation Model

An electrical circuit was proposed by Alexander *et. al.* [3] to model the behavior of the left atrium and the pulmonary system (figure 2.8). In this model, P_p is the pulmonary source of pressure, R_3 resistance of pulmonary source, C_4 pulmonary venous capacitor, R_4 pulmonary resistor, L_4 pulmonary inertance, R_5 antroventricular resistor, Q_p pulmonary venous flow rate, Q_{LV} left ventricular blood flow, V_p volume of the pulmonary venous and V_{LA} volume of the left atrium. Similar to the left ventricle, the left atrium is characterized by a reservoir where the elastance, K_{LA} changes with time.

The following ODE's represent the pulmonary model:

$$\frac{dV_p}{dt} = \frac{1}{R_3}\left(P_p - \frac{V_p}{C_4}\right) - Q_p \tag{2.19}$$

$$\frac{dV_{LA}}{dt} = Q_p - Q_{LV} \tag{2.20}$$

$$\frac{dQ_p}{dt} = \frac{1}{L_4}\left(\frac{V_p}{C_4} - R_4 Q_p - K_{LA} V_{LA}\right) \tag{2.21}$$

$$\frac{dQ_{LV}}{dt} = \frac{1}{L_5}\left(K_{LA} q_{LA} - R_5 Q_{LV} - P_{LV}\right) \tag{2.22}$$

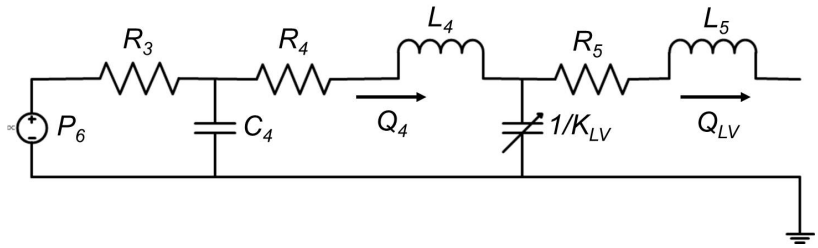

Figure 2.8: Alexander model [3] to simulate the pulmonary system. P_p is the pulmonary source of pressure, R_3 resistance of pulmonary source, C_4 pulmonary venous capacitor, R_4 pulmonary resistor, L_4 pulmonary inertance, R_5 antroventricular resistor, L_5, antroventricular inertance, Q_p pulmonary venous flow rate, Q_{LV} left ventricular blood flow, V_p volume of the pulmonary venous and V_{LA} volume of the left atrium

2.4.3 Lump Model Results

In this simulation, three sinusoidal waves have been used for the left ventricular systolic ejection, left ventricular passive filling and left atrium ejection flow rates in the lump model:

Left ventricular ejection:

$$QLV_s(t) = QLV_sMax \times \sin\left[\pi\left(\frac{t - T_{bs}}{T_{es} - T_{bs}}\right)\right] \tag{2.23}$$

Left ventricular passive filling (E wave):

$$QLV_{d1}(t) = QLV_{d1}Max \sin\left[\pi\left(\frac{t - T_{bd}}{T_{d1} - T_{bd}}\right)\right] \tag{2.24}$$

Left atrial ejection (A wave):

$$QLV_{d2}(t) = QLV_{d2}Max \sin\left[\pi\left(\frac{t - T_{d2}}{T_{ed} - T_{d2}}\right)\right] \tag{2.25}$$

T_{bs}, T_{es}, T_{bd}, T_{d1}, T_{d2} and T_{ed} are the beginning of the systole, end systole, beginning of the diastole, end of left ventricular passive filling and beginning of the left atrial ejection, respectively. Hirschfeld *et. al.* [40] reported that the isovolumetric contraction time (ms) obeys the following linear relation with the heart rate (bpm):

$$IVCT = T_{bs} = 53 - 0.22HR \tag{2.26}$$

The left ventricular ejection duration (ms) (LVET) obeys the following relationship with the heart rate according to the Lance *et. al.* [60] investigations:

$$LVET = 264.25 - 1.2HR \tag{2.27}$$

Therefore, T_{es} is calculated as $T_{es} = T_{bs} + LVET$. Chung *et. al.* [13] investigated that the diastolic duration (ms) (DD: beginning to end diastole) is estimated according the following equation:

$$DD = -549 + 2.13HR + \frac{61500}{HR} \tag{2.28}$$

Therefore, the T_{bd} is calculated as:

$$T_{bd} = \left(\frac{1}{HR}\right) - DD \tag{2.29}$$

Also, Chung et. al. [13] reported that left ventricular passive filling (E_{dur}), the duration of the diastasis ($D_{diastasis}$: end of passive filling to the beginning of the left atrial ejection) and the left atrial duration (A_{dur}) are estimated as functions of heart rate by:

$$E_{dur} = 313 - 0.957HR \tag{2.30}$$

$$D_{diastasis} = -1150 + 4.4HR + \frac{65500}{HR} \tag{2.31}$$

$$A_{dur} = 166 - 0.454HR \tag{2.32}$$

Thus, the T_{d1} and T_{d2} are calculated as:

$$T_{d1} = T_{ed} - D_{diastasis} - A_{dur} \tag{2.33}$$

$$T_{d2} = T_{ed} - A_{dur} \tag{2.34}$$

where, T_{ed} is $1/HR$. Also, the QLV_sMax is calculated by equalizing the area under the left ventricular ejection wave to the specified stroke volume (SV):

$$QLV_sMax = \frac{\pi\, SV}{2\,(T_{es} - T_{bs})} \tag{2.35}$$

If we know the fraction of the hight of E wave to A wave as EAR, we calculate the $QLV_{d1}Max$ by equalizing the sum of the areas under E and A waves to the stroke volume:

$$QLV_{d2}Max = \frac{\pi\, SV}{2\,((T_{d1} - T_{bd}) + EAR\,(T_{ed} - T_{d2}))} \tag{2.36}$$

and

$$QLV_{d1}Max = EAR\,(QLV_{d2}Max) \tag{2.37}$$

Figure 2.9 shows the left ventricular ejection, E and A waves calculated with the heart rate of 60 bpm and stroke volume of 60 mL. In this case the cardiac phases timings were calculated as: $T_{bs} = 39.8\,ms$, $T_{es} = 232.1\,ms$, $T_{bd} = 396.2\,ms$, $T_{d1} = 655.6\,ms$, $T_{d2} = 861.2\,ms$ and finally $T_{ed} = 1000\,ms$. Figure 2.10 shows the left

ventricular volume during a cardiac cycle calculated from the flow rate wave.

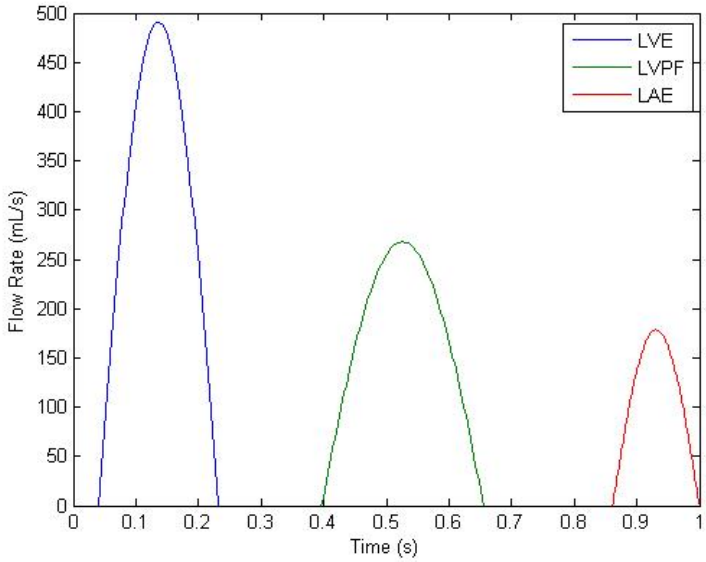

Figure 2.9: Left ventricular flow rates applied to the lump model for the heart rate of 60 bpm. LVE: left ventricular ejection, LVPF: left ventricular passive filling, LAE: left atrial ejection

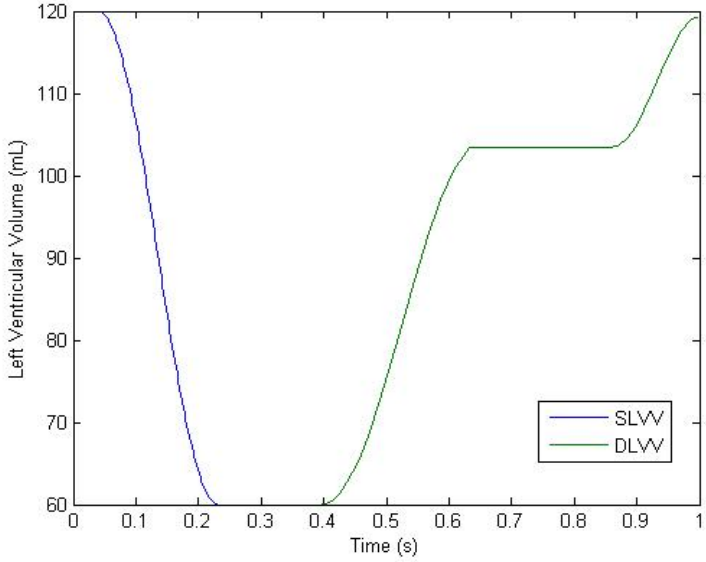

Figure 2.10: Left ventricular volume (LVV) for a cardiac cycle with the heart rate of 60 bpm. SLVV: systolic left ventricular volume, DLVV: diastolic left ventricular volume.

During the isovolumetric contraction the Windkessel model is disconnected from left ventricle i.e. $Q_{LV} = 0$. Therefore, from equations 2.16 and 2.18 PAO_{ivc} is calculated as:

$$PAO_{ivc} = PAO_{ed}\, e^{\left(\frac{t}{R_2 C_2}\right)} \tag{2.38}$$

Since the left ventricle is isolated in the isovolumetric contraction, it has been assumed that the pressure rises rapidly from 0 to T_{bs} according the following exponential equation:

$$PLV_{ivc} = PLV_{ed}\, e^{C_{ivc}\, t} \tag{2.39}$$

C_{ivc} is calculated by equalizing the left ventricular pressure to the aortic pressure, computed from equation 2.38 at $t = T_{bs}$.

$$C_{ivc} = \left(\frac{1}{T_{bs}}\right) \ln\left(\frac{PAO_{bs}}{PLV_{ed}}\right) \tag{2.40}$$

For the systolic phase the QLV_s from equation 2.23 was fed to the ODE of 2.16 and this ODE was solved for the systolic duration (T_{bs} to T_{es}) using the Rung-Kutta order 4. Then, the calculated P_2 was used in the equation 2.18 to compute the systolic left ventricular pressure. The following values were used for the Windkessel parameters [100]: $R_1 = 10^6\ Pa\, s^3$, $R_2 = 150 \times 10^6\ Pa\, s^3$, $C_2 = 0.016 \times 10^{-6}\ m^{3/Pa}$.

The left atrial pressure from 0 to T_{bd} is calculated first, by setting the Q_{LV} to 0 and solving the system of ODEs of 2.19, 2.20 and 2.21 using Rung-Kutta order 4. Then, the multiplying the computed V_{LA} by the left atrial elastance (K_{LA}):

$$PLA_{0tobd} = K_{LA}\, V + LA \tag{2.41}$$

The following values were used for the parameters of the model: $P_p = 1600\ Pa$, $R_3 = 333 \times 10^3\ Pa\, s/m^3$, $C_4 = 0.0525 \times 10^{-6}\ m^3/Pa$, $R_4 = 12 \times 10^6\ Pa\, s/m^3$, $L_4 = 133 \times 10^3\ Pa$, $R_5 = 3.47 \times 10^6\ Pa\, s/m^3$, $L_5 = 267 \times 10^3\ Pa$.

We also assumed that the left ventricular pressure falls according the following exponential function rapidly from T_{es} to T_{bd}:

$$PLV_{ivr} = PLV_{es}\, e^{-C_{ivr}\,(t - T_{es})} \tag{2.42}$$

Where, $\mathrm{C}_{ivr} is calculated from \mathrm{PLV}_{ivr} = PLA_{ivr} @ t = Tbd$ as follows:

$$C_{ivr} = \left(\frac{1}{(T_{bs} - T_{es})}\right) \ln\left(\frac{PLV_{es}}{PLA_{bd}}\right) \tag{2.43}$$

In the diastolic phase, we insert the specified E and A waves (equations 2.24 and 2.25) into the system of ODEs 2.19, 2.20 and 2.21 and solve it with the Rung-Kutta order 4 from T_{bd} to T_{ed}. Then, we use equation 2.22 to calculate PLV_d.

Figure 2.11 shows the results of the lump model with the input left ventricular flow rate shown in the figure 2.9.

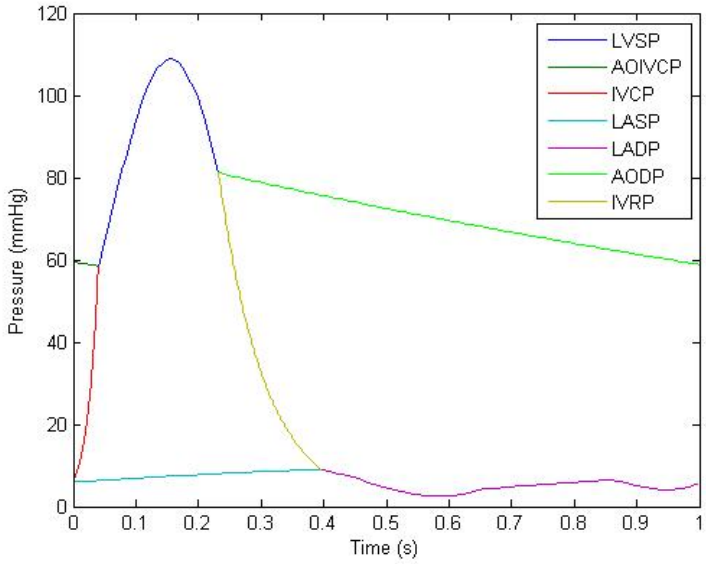

Figure 2.11: The pressure profile of the left ventricle, aorta and left atrium during a cardiac cycle with the heart rate of 60 bpm. LVSP: left ventricular systolic pressure, AOIVCP: aortic isovolumetric pressure, IVCP: left ventricular isovolumetric pressure, LASP: left atrial systolic pressure, LADP: left atrial diastolic pressure, AODP: aortic diastolic pressure, IVRP: left ventricular isovolumetric relaxation pressure.

2.5 Fluid-Structure Modeling of The Blood Inside The Normal LV

In this section, the blood flow in the diastolic phase inside the normal left ventricle has been simulated. The model consists off the normal left ventricle with initial volume of 117 mL and stroke volume of 60 mL. This means that the deformation of the myocardium (simulated as a moving wall) is very high: about 60 percent of the initial geometry. Currently, all of the commercially available computational tools can

handle only low deformation relative to the entire computational domain. The reason behind it is that there is a need to move the mesh at every coupling time step which degrades the mesh gradually until it becomes unusable by the fluid dynamics solver. To overcome this issue, we have implemented a method which can be used for high deformation FSI problems and it includes the following steps at every coupling time step:

1. Extract the geometry from the deformed structure.
2. Change the fluid geometry with the new deformed structure.
3. Re-mesh the new fluid geometry.
4. Interpolate the previous solution to the new mesh.
5. Calculate and apply the momentum sources on the FSI surfaces.

In this case, we do not have any structure and only the myocardium wall moves according to the model which we described in the section 2.2.

To calculate the momentum effect of the left ventricular wall on the fluid we used the following method. Figure 2.12 demonstrates how a node A with the Cartesian coordinate of $x(t_n)$, $y(t_n)$, $z(t_n)$ moves between the two time steps of t_n and t_{n+1}. In the figure 2.12, the left ventricular long axis has shortened from $m(t_n)$ to $m(t_{n+1})$. To calculate the magnitude and direction of the velocity of the node A we calculated the $x(t_{n+1})$, $y(t_{n+1})$, $z(t_{n+1})$ as followed:

The point A on the left ventricular wall belongs to the ellipse which is radiated out from the origin with the angle of θ from X axis. This point moves toward the center of the ellipse (origin) at each time step. Therefore, we find it the line which connects this point to the origin. As you see on the figure 2.12, θ and α are calculated as:

$$\theta = \arctan\left[\frac{y(t_n)}{x(t_n)}\right] \tag{2.44}$$

$$\alpha = \arctan\left[\frac{\sqrt{x(t_n)^2 + y(t_n)^2}}{z(t_n)}\right] \tag{2.45}$$

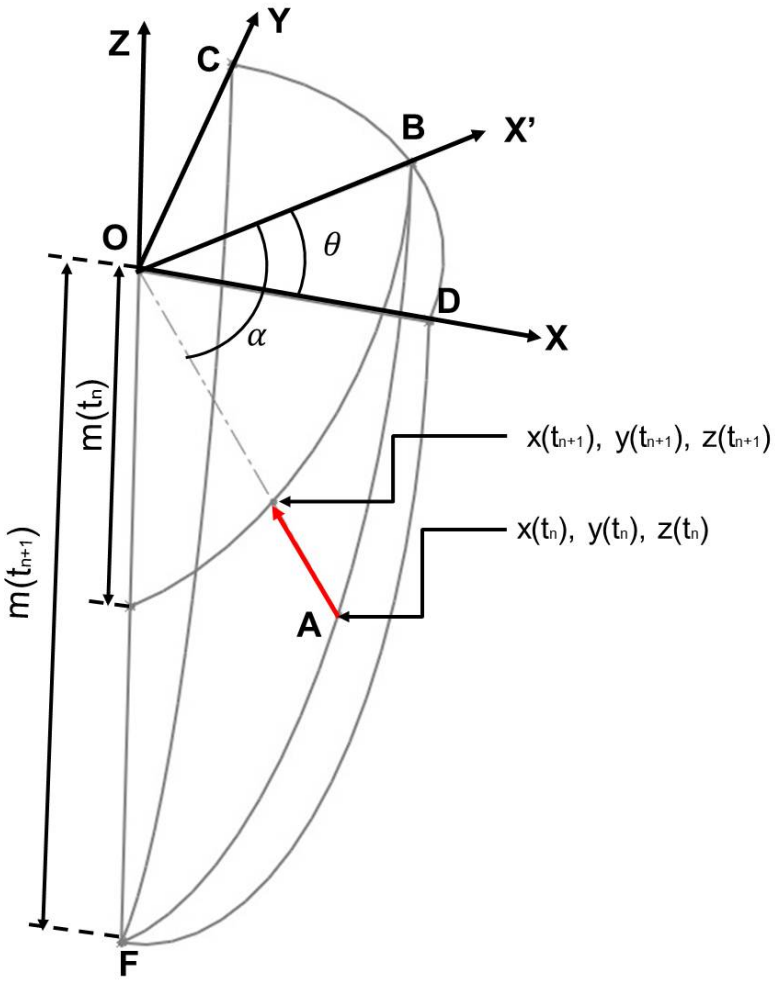

Figure 2.12: Every left ventricular point moves toward the center of the ellipse.

In the basal plane:

$$p^2 = OB = \frac{j^2 s^2}{s^2 \cos^2\theta + j^2 \sin^2\theta} \tag{2.46}$$

Where, j and s are OD and OC respectively. Also, we know:

$$\frac{z(t_{n+1})^2}{m(t_{n+1})^2} + \frac{\acute{x}(t_{n+1})^2}{p(t_{n+1})^2} = 1 \tag{2.47}$$

and

$$z(t_{n+1}) = (\tan\alpha)\,\acute{x}(t_{n+1}) \tag{2.48}$$

From the equations 2.47 and 2.48 we calculate the $z(t_{n+1})$ as:

$$z(t_{n+1}) = \frac{p\, m(t_{n+1}) \tan\alpha}{[p^2 \tan^2\alpha + m(t_{n+1})^2]^{\frac{1}{2}}} \tag{2.49}$$

Consequently,

$$x(t_{n+1}) = \acute{x}(t_{n+1}) \cos\theta = \frac{p\, m(t_{n+1}) \cos\theta}{[p^2 \tan^2\alpha + m(t_{n+1})^2]^{\frac{1}{2}}} \tag{2.50}$$

and

$$y(t_{n+1}) = \acute{y}(t_{n+1}) \sin\theta = \frac{p\, m(t_{n+1}) \sin\theta}{[p^2 \tan^2\alpha + m(t_{n+1})^2]^{\frac{1}{2}}} \tag{2.51}$$

Therefore, by having the $x(t_{n+1})$, $y(t_{n+1})$, $z(t_{n+1})$ we calculated the velocity of the point A as:

$$U_A = \sqrt{[x(t_{n+1}) - x(t_n)]^2 + [y(t_{n+1}) - y(t_n)]^2 + [z(t_{n+1}) - z(t_n)]^2}/\Delta t \tag{2.52}$$

2.5.1 Boundary Conditions

The lump model developed in Section 2.4 was used to introduce the boundary conditions at the mitral and the aortic orifices (3.10). For the diastolic phase, we closed the aortic orifice (wall) and we introduced the diastolic pressure, calculated using the lump model (figure 2.11), to the mitral orifice. In the systolic phase, we closed the mitral orifice and we used the aortic pressure for the aortic orifice (2.11). The ventricular wall was moved according to the model described in the section 2.2.

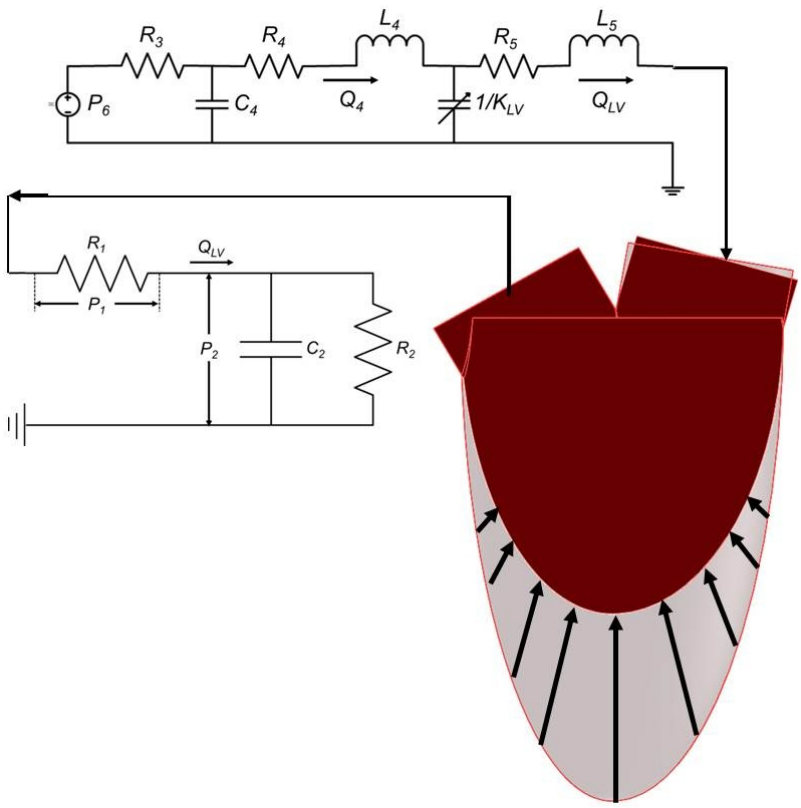

Figure 2.13: Windkessel and Alexander models were used to simulate the boundary conditions for the aortic and mitral orifice respectively.

2.5.2 Computational Algorithm

Figure 2.14 shows the one way fluid-structure interaction algorithm used for the simulation. At every time step, the volume of left ventricle was calculated using the method described in the section 2.4.3 and we created the geometry according the method we explained in the section 2.2. Simulation was started at the beginning of diastole when the left ventricular volume is 57 mL. Then, the blood flow was calculated using the CFD module for one time step. For the next time step, the new left ventricular volume was calculated and we enlarged the left ventricle accordingly. Next, The new geometry was remeshed and the previous results were interpolated to the new mesh as initial conditions. Next, the momentum sources of the left ventricular wall was calculated and applied to the LV wall. Next, the fluid flow was calculated with the new geometry and boundary conditions. This cycle was followed to the end of diastole. Figure 2.15 demonstrates the density of the meshed used for the CFD model. We used 814836 tetrahedral elements with average elemental volume of 0.37

mm^3.

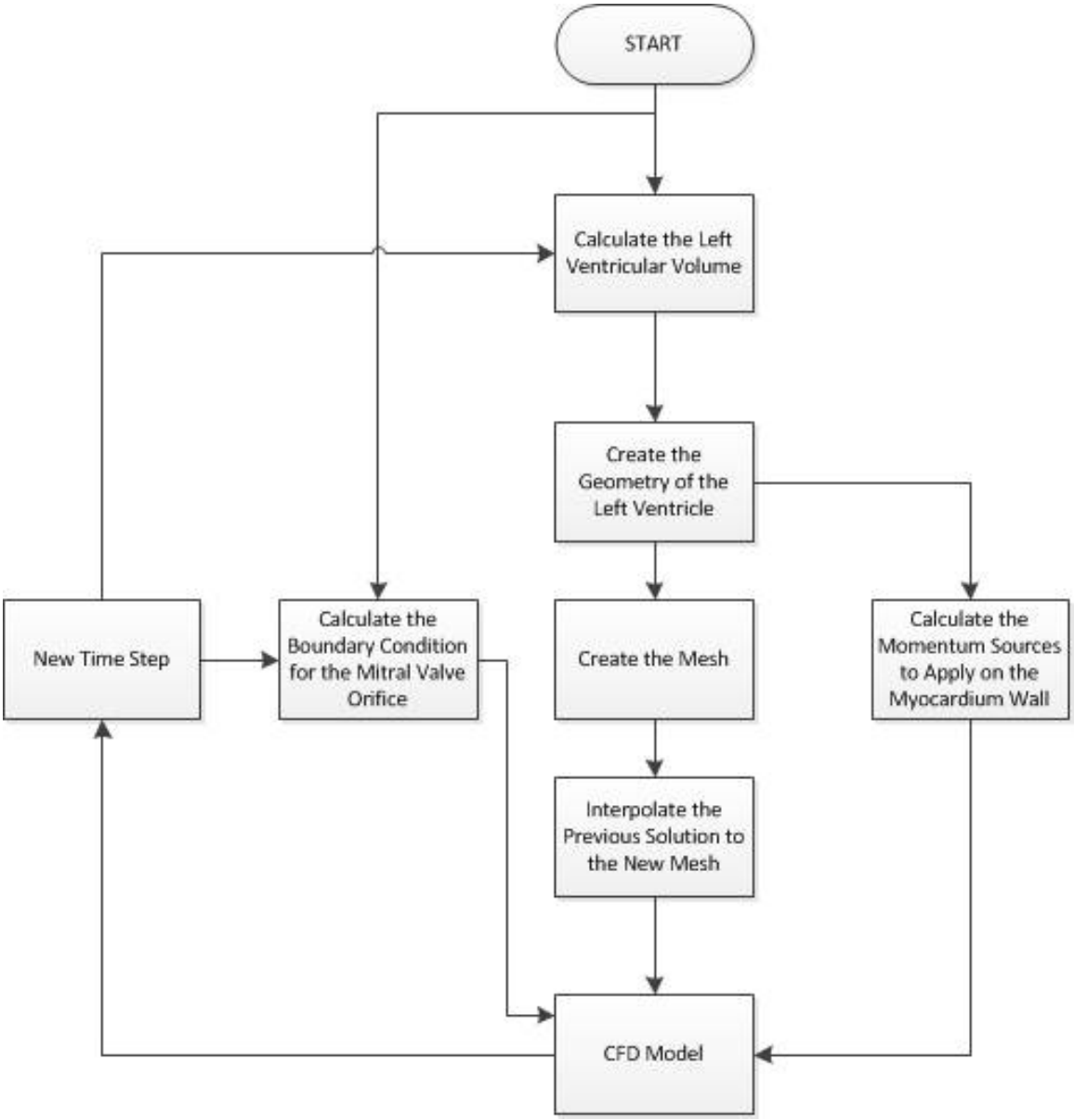

Figure 2.14: One way FSI algorithm used for the simulation.

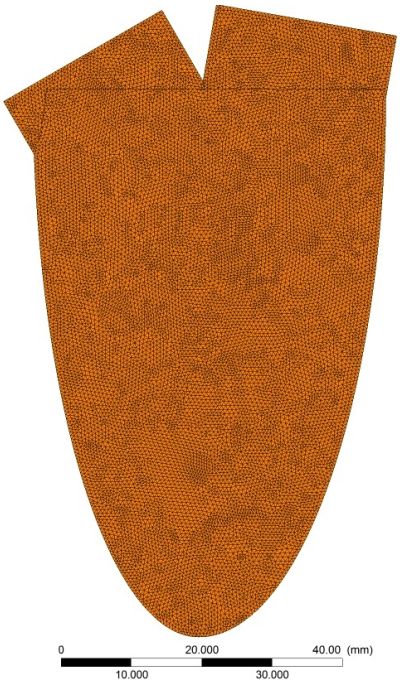

Figure 2.15: Mesh density used for the CFD model. the average volume of the elements is 0.37 mm^3

2.6 Results and Discussion

2.6.1 Vortex Ring Formation and Evolution

The first simulation was conducted with the stroke volume of 60 mL and heart rate of 60 bpm with the end systolic volume of 60 mL. At the onset of the mitral valve opening (beginning of the E wave, $t = 0.00Sec$), a jet of blood flows into the left ventricle at its minimum volume: 60 mL. Figures A.1(1), A.2(1) show this in the long axis and antro-posterior planes. This jet forms an annular vortex which is called the vortex ring and was reported for the first time by Bellhouse *et. al.* in [7]. This vortex ring is smoothly expanding toward the septum as the the rapid filling (E wave) progresses. (figure A.1). Also, as the left ventricle enlarges, this vortex expands toward the anterior and posterior walls as well and becomes an annular ring circumferentially (figure A.3). In the anterio-posterior plane, this vortex ring is symmetric and it is forming twin vortexes initially close to the base (figure A.2(1)) and as the left ventricle enlarges the twin vortexes elongate toward the apex (figure A.2). During the diastasis, the vortex ring decelerates smoothly until the beginning of the A wave when another jet is discharged to the left ventricle figure A.1(13) to A.1(20). The A-

wave jet accelerates the vortex ring and also creates another small vortex ring between the mitral and aortic orifices. Also, it was found that as the diastole proceeds, the high velocity region of the vortex ring moves from mitral orifice toward the apex (see figure A.1(1) to A.1(15)).

Figures A.3(1) to A.3(22) show the streamline colored with velocity viewing downward from basal plane. As it can be observed, the flow starts to recoil circumferentially at about the peak E wave. As the left ventricle expands, this circumferential coil accelerates and becomes more intense.

Figure 2.16 presents the vorticity of the vortex in the long axis and anterio-posterior planes. This graph shows that the vortex ring rotates faster in the long axis and becomes slower on the anterio-posterior plane. The first and second jumps are associated with E and A waves respectively. Figures A.4 show that the vortex is initiated at the circular edge of the mitral orifice.

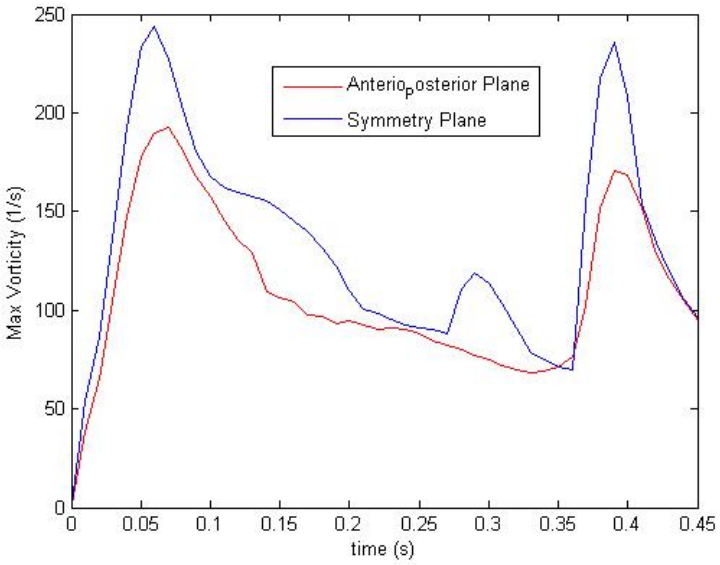

Figure 2.16: Maximum vorticity on the long axis and antrio-posterior planes.

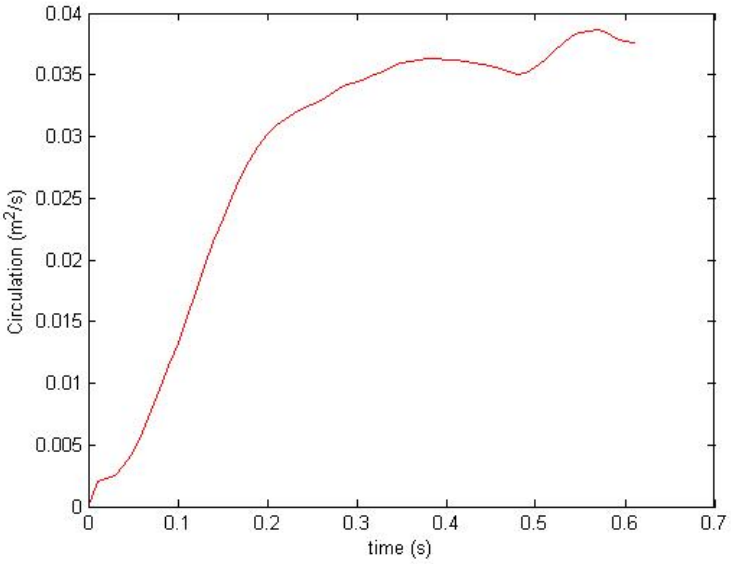

Figure 2.17: Circulation on the long axis (symmetry) plane during diastole.

2.6.2 Ventricular Pressure During Diastole

Figure 2.18, presents the pressure at the mitral orifice and apex during diastole. Once the left ventricle begins to enlarge, a pressure gradient is created between the mitral orifice and apex with the low pressure located in the apex (figure A.6(1)). At this moment, a low pressure region is formed at the center of the vortex ring (figure A.6(2)). As the diastole progresses, this low pressure region moves toward the apex (figures A.6(2) to A.6(17)). Also, the pressure wave reaches the apex within 0.1 s (figure A.6(1) to A.6(5)). At this point, the pressure gradient is reversed with the highest at the apex and lowest at the mitral orifice After, the peak of the E wave, pressure increases as a result of flow deceleration until the end of the E wave (0.28 s). At this point, since the flow rate is near zero, the apical pressure drops quickly and becomes equal to the mitral pressure to accommodate the zero flow rate. The apical pressure follows the mitral pressure until the beginning of the A wave (0.34 s) when the second jet of flow is discharged into the left ventricle causing the drop of the apical pressure. The apical pressure increases during A wave and the pressure gradient is reversed at 0.4 s.

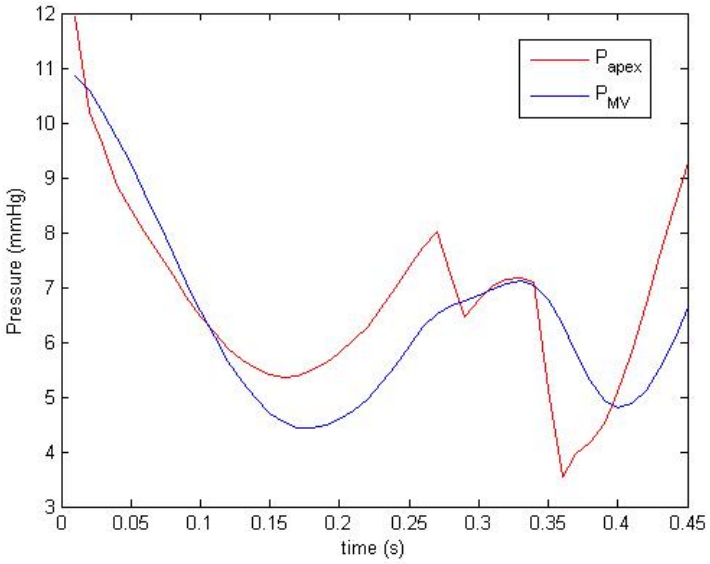

Figure 2.18: Pressure at the apex and mitral valve orifice during the diastole.

2.6.3 Effect of Heart Rate

Here, we investigated the effect heart rate on the left ventricular flow pattern. Figure 2.19 presents the left ventricular flow rate at different heart rates calculated using the method described earlier in the section 2.4.3. These flow rates (left ventricular ejection, E and A waves) were fed into the lump model and the left ventricular pressure was calculated. Figure 2.20 shows the left ventricular, aortic and left atrial pressures with the heart rates of 60, 65, 70, 75, and 80 bpm and the stroke volume 60 mL. It can be seen that, as we increase the heart rate (with the same stroke volume) the peak of left ventricular ejection, E and A waves increases. Also, the A wave is shifted more leftwards than the LV ejection and E waves. The diastolic portion of pressure was used as boundary condition for the mitral orifice in the simulations. Figure 2.21 demonstrates the vortex ring circulation on the long axis plane for different heart rates. This circulation was calculated by integrating the vorticity over the estimated area where the vortex ring is projected in the long axis plane. This graph shows that for the HR=60 bpm, the circulation of the vortex ring initially increases almost linearly during the most of E wave (0 to 0.2 s). After this point, the vortex continues to increase with much smaller rate until it becomes almost fully developed at mid diastasis (0.38 s). The arrival of the A wave discharges more energy to the vortex and makes the circulation of the vortex ring rises to a higher level. The interesting

point is that all of the circulation curves change the slope around 0.2 sec regardless of the heart rate. Figure 2.22 shows the maximum vorticity in the long axis plane during the diastole. It was found that as we increased the heart rate the first peak of the maximum vorticity which is associated with the E wave did not change but the second peak which is associated with the A wave did not change in magnitude but was shifted toward E wave.

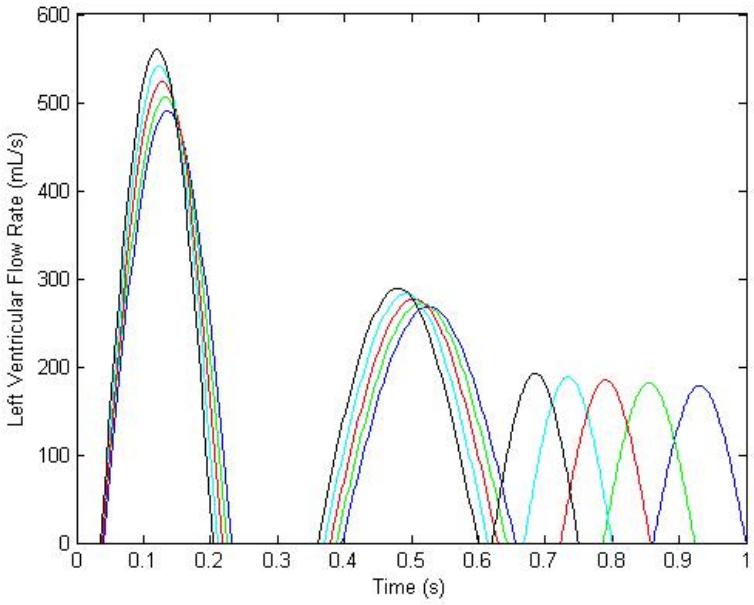

Figure 2.19: Left ventricular flow rate at the heart rates of 60 (blue), 65 (green), 70 (red), 75 (cyan)and 80 (black) .

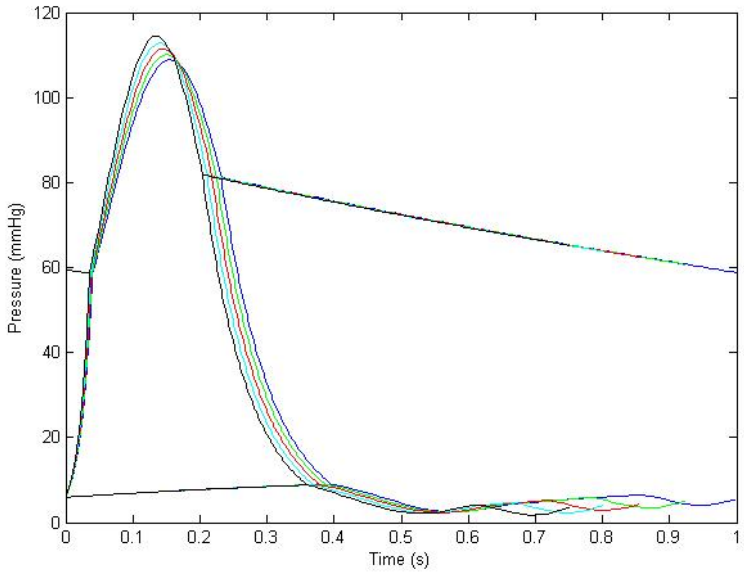

Figure 2.20: Left ventricular, aortic and left atrial pressures at heart rates of 60 (blue), 65 (green), 70 (red), 75 (cyan)and 80 (black). SV=60 mL

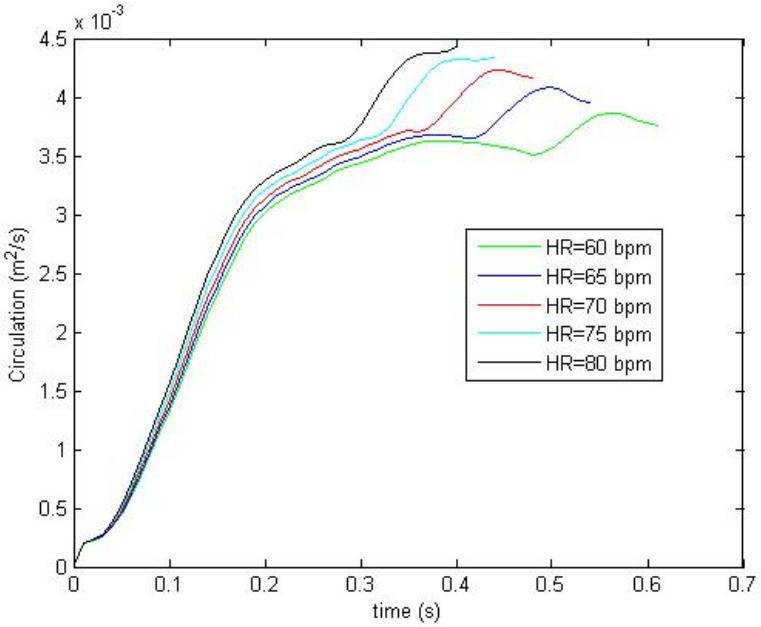

Figure 2.21: Circulation in the long axis plane at heart rates of 60 (red), 65 (green), 70 (blue), 75 (purple)and 80 (orange). SV=60 mL

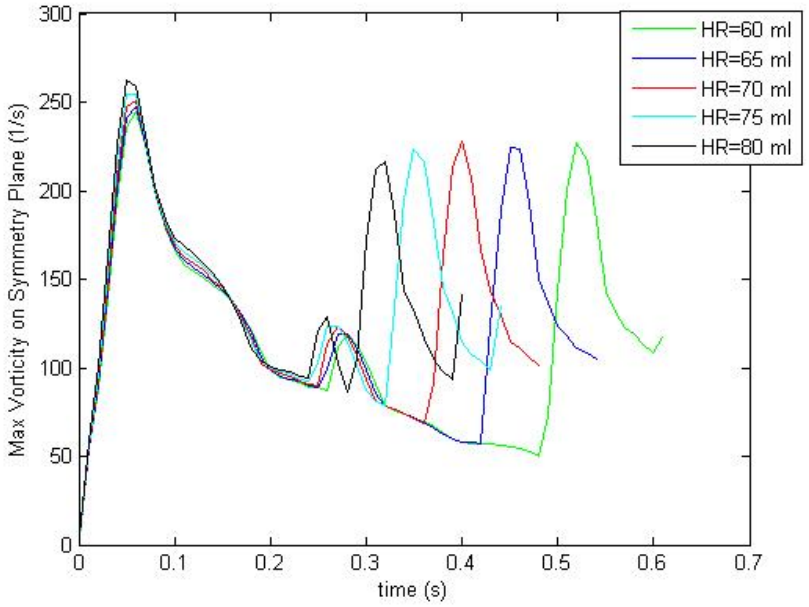

Figure 2.22: Max Vorticity in the long axis plane at heart rates of 60 (red), 65 (green), 70 (blue) and 75 (purple). SV=60 mL

2.6.4 Effect of The Stroke Volume

Next, the effect of stroke volume on the circulation of the vortex ring is investigated. Figure 2.23 presents the left ventricular flow rate at the heart rate of 60 bpm and stroke volumes of the 60, 65, 70, 75 and 80 mL. In this graph, it can be seen that since the heart rate is fixed the E and A wave timings remain constant but the peak A and E waves have increased with stroke volume. The calculated left ventricular pressure is shown in Figure 2.24. The left ventricular pressure in the diastolic phase at the mitral orifice remains almost the same. The circulation in the long axis plane is shown in Figure 2.25. It can be seen that the circulation increases with the increase of the stroke volume but all of them almost pinch off at the same time (0.2 sec). Figure 2.26 shows the maximum vorticity of the fluid in the long axis plane. It was found that as we increased the stroke volume, the maximum vorticity at peak E and A waves slightly moves higher but the interesting point is that all the peaks take place at the same time (0.05 s for the E wave and 0.52 s for the A wave) regardless of the change in the stroke volume.

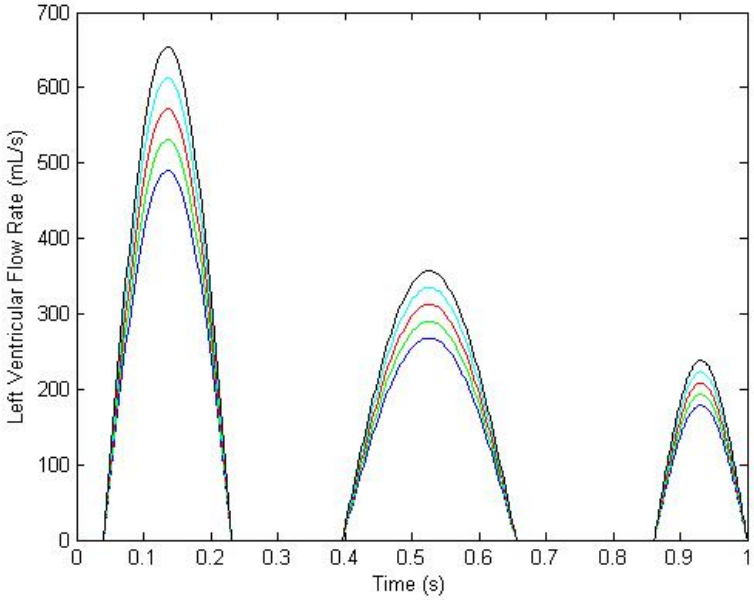

Figure 2.23: Left ventricular flow rate at the stroke volumes of 60 mL (blue), 65 mL (green), 70 mL (red), 75 mL (cyan)and 80 mL (black) .

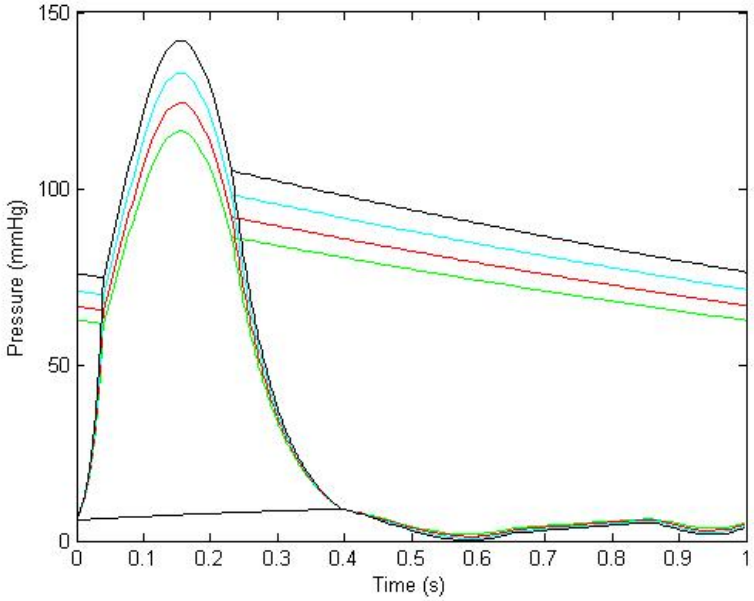

Figure 2.24: Left ventricular, aortic and left atrial pressures at Stroke volumes of of 60 mL (blue), 65 mL (green), 70 mL (red), 75 mL (cyan)and 80 mL (black). HR=60 bpm

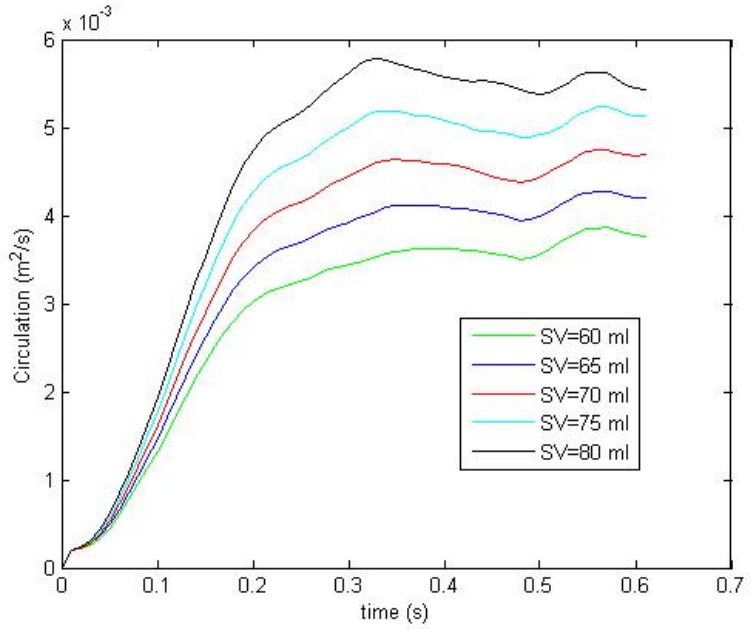

Figure 2.25: Circulation in the long axis plane at stroke volumes of 60 mL (red), 65 mL (green), 70 mL (blue), 75 mL (purple)and 80 mL (orange). HR=60 bpm

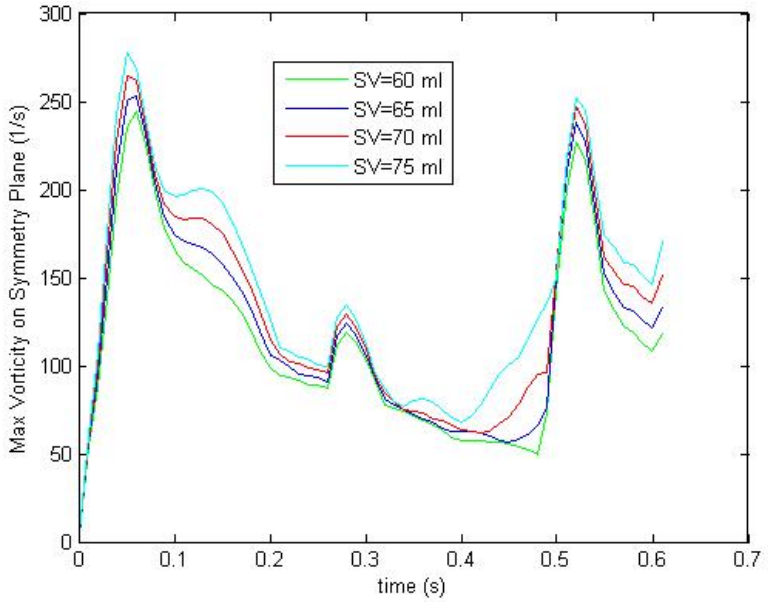

Figure 2.26: Max Vorticity in the long axis plane at stroke volumes of 60 mL (red), 65 mL (green), 70 mL (blue) and 75 mL (purple. HR=60 bpm

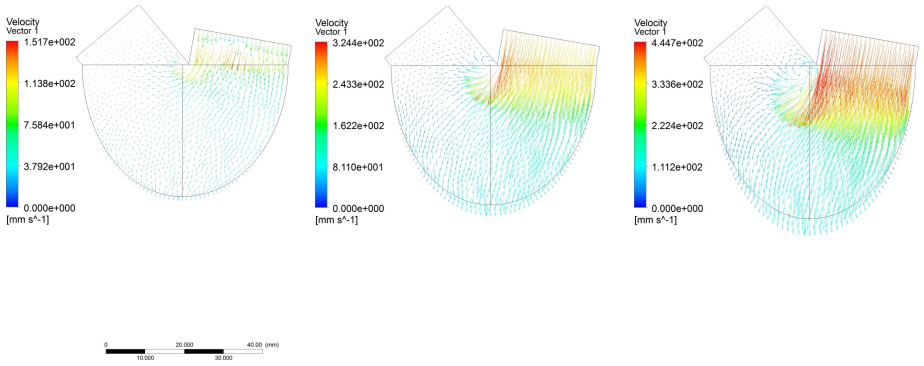

(1) t=0.02 Sec (2) t=0.05 Sec (3) t=0.08 Sec

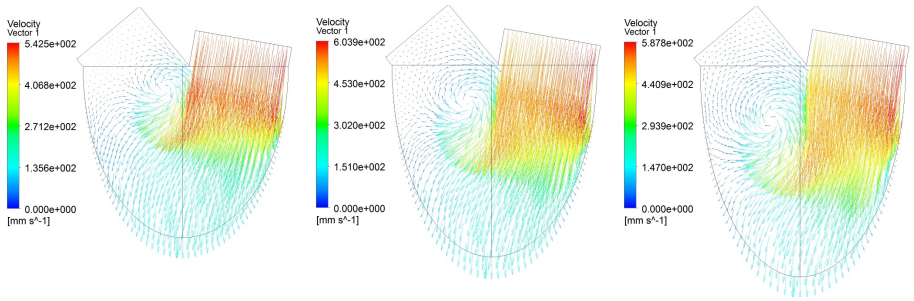

(4) t=0.11 Sec (5) t=0.14 Sec (6) t=0.17 Sec

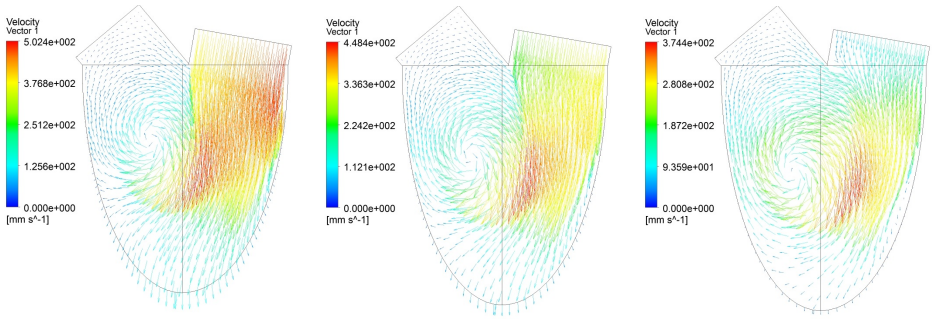

(7) t=0.20 Sec (8) t=0.23 Sec (9) t=0.26 Sec

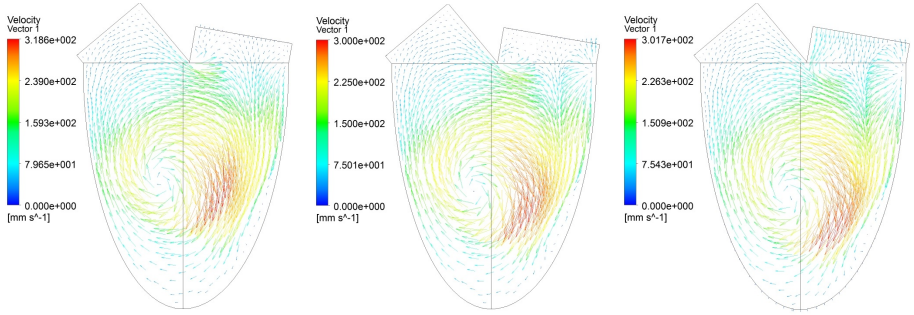

(10) t=0.29 Sec (11) t=0.32 Sec (12) t=0.35 Sec

Figure 2.27: Velocity vectors in the long axis (symmetry) view. SV=60 ml, HR=60 bpm.

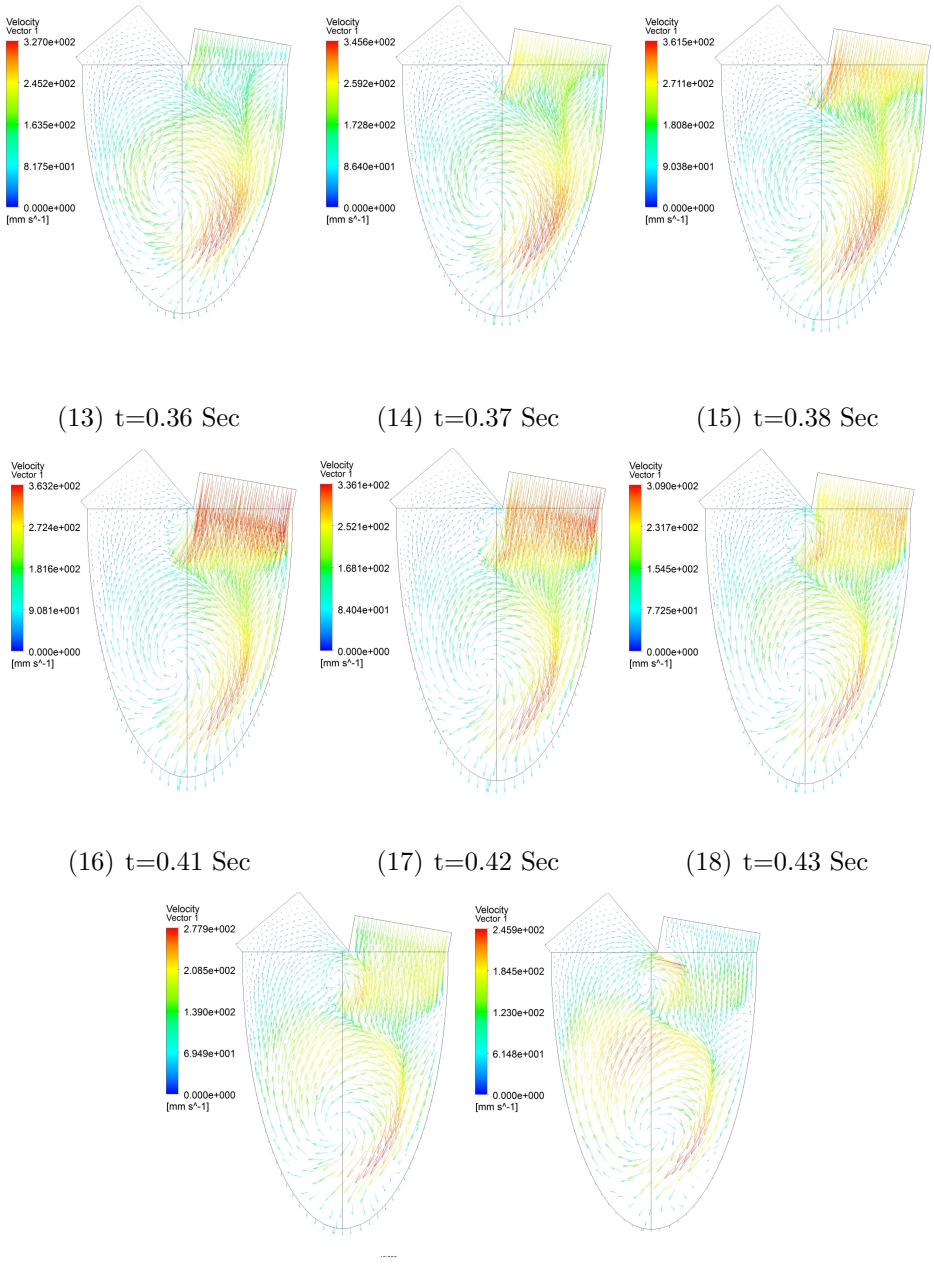

(13) t=0.36 Sec (14) t=0.37 Sec (15) t=0.38 Sec

(16) t=0.41 Sec (17) t=0.42 Sec (18) t=0.43 Sec

(19) t=0.44 Sec (20) t=0.45 Sec

Figure 2.27: Velocity vectors in the long axis (symmetry) view. SV=60 ml, HR=60 bpm(cont).

2.7 Chapter Synopsis

In this chapter, we modeled the blood flow inside the left ventricle in diastole phase. We first developed a mathematical model for the left ventricular wall motion which

satisfies a predefined left ventricular volume. Then, we implemented the Windkessel and Alexander models to provide pressure boundary conditions for the aortic and mitral apertures respectively. Next, we conducted CFD simulation of the blood flow and we investigated the vortex ring formation in diastole phase. At the onset of diastole a jet of blood rushes into the left ventricle and coils back toward the base. This vortex ring is initiated from mitral aperture and is distributed circumferentially with larger diameter near the septum and smaller diameter near the free wall. As the left ventricle becomes larger the vortex ring moves toward the apex, becomes bigger and rotates faster. We also calculated vortex ring circulation and plot it as a function of time. The vortex ring circulation increases sharply during E wave. Then, it goes flat out and reaches its first maximum between E and A waves. The vorticity contours show the vortex ring pinches off at the first maximum of the circulation. At the beginning of the A wave another vortex is initiated from mitral aperture slowly grows until the end of diastole. Also, the effect heart rate on the vortex ring was studied. Our investigations show that as the heart rate increases since the A wave becomes closer to the E wave the vortex ring pinch off disappears at the high heart rates.

Chapter 3

FSI Simulation of The Mitral Valve Within Normal Left Ventricle

3.1 Introduction

The mitral valve controls the blood flow between the left atrium and the left ventricle. The structure of the mitral valve includes anterior and posterior leaflets and annulus, chordae and papillary muscles. The chordae maintain the shape of the leaflets and prevent them from prolapsing during systole when the pressure in the left ventricle is higher than the atrial pressure. Mitral prolapse takes place when the leaflets deform into the left atrium causing regurgitation of the flow to the left atrium [37].

The annulus is the circumference of the mitral valve at the base where the leaflets diverge (Antero-Lateral Commissure (ALC) and Postero-Medial Commissure (PMC)). The anterior annulus and leaflet are adjacent to the aortic valve and the posterior annulus and leaflet are adjacent to the free wall. The posterior leaflet consists of one, two or three scallops but the single one is more common [57]. In this work, we consider the posterior leaflet with a single scallop. Figures 3.1 shows the schematic of the opened mitral valve [57].

3.2 Chapter Objectives

In this chapter, the design and implementation of a full large-deformation fluid-structure interaction hemodynamics of the mitral valve with the left ventricle is presented. A geometric and parametric model for the mitral valve has been developed, and a finite element analysis of the valve using an orthotropic model has been carried out to characterize the structural properties of the valve. The coaption behavior of the valve in a healthy left ventricle was studied and the flow characterization in the systole and diastole phases was achieved where the formation of a vortex ring is of

particular significance.

3.3 Parametric Geometry of the Mitral Valve

The model was started by creating the mitral base. Here, it is assumed that the basal mitral valve does not change during a cardiac cycle, as shown in Figure 3.3(2). The shape of the mitral valve base includes two parts: the posterior base which was created using a half ellipse and the anterior base which was made by a straight line connected by two arcs to the posterior ellipse.

Next, the diverging point of the leaflets (ALC and PMC) was positioned at a height from the basal plane and x and y distances from anterior and posterior corners of the base. Therefore, three design variables are introduced for the ALC and PMC.

The leaflets edges are defined as two arcs laid on the two planes being radiated out from the ALC and the PMC 3.2 at prescribed angles. Also, the leaflets curvature was defined by two arcs on the plane of symmetry from mid base to the mid edges. Thus, an additional six design variables for each leaflet are introduced: the radius of the edges, the angle of the planes where the edges are seated on and the radius of the leaflets curvature. Then, the leaflets were created by lofting the anterior and posterior parts of the base to the edges with the curvature arcs as the guide curves (figure 3.2).

Kunzelman *et.al.*[57] measured the following structural dimensions of porcine and human mitral valves (Figures 3.1):

- Total annular length
- Anterior and posterior annular lengths
- Height of anterior and posterior leaflets
- Edge lengths of anterior and posterior leaflets
- antero-lateral and postero-medial commissural height

Table 3.1 presents these measurements for both human and porcine cases. All the dimensions for both cases were found almost similar except the posterior edge length for porcine was found slightly longer compared to the human heart.

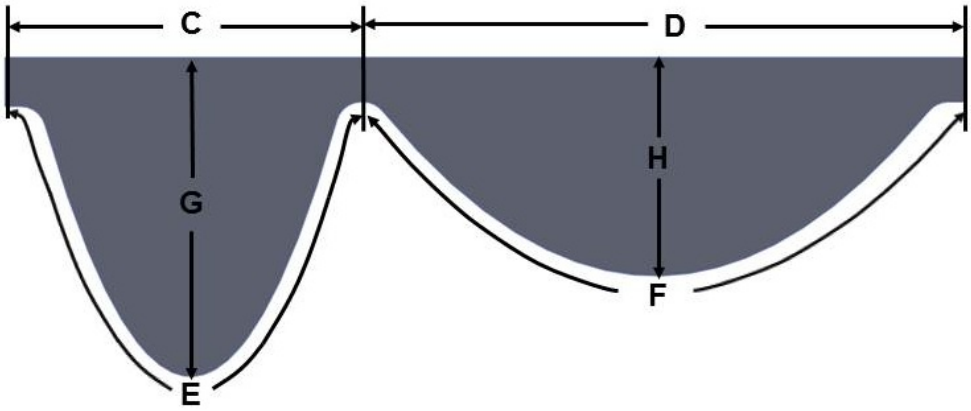

Figure 3.1: A: Anterior annular length; B: posterior annular length; C: Anterior annular length; D: posterior annular length; E: anterior edge length; F: posterior edge length; G: anterior leaflet height; H: posterior leaflet height [57].

Table 3.1: Human and porcine mitral valve measurements taken by Kunzelman *et.al.*[57]

Parameter	Units	Human	Porcine
Total annular length	mm	82	79
Anterior annular length	mm	30	31
Anterior edge length	mm	45	46
Anterior leaflet height	mm	20	20
Anterior commissural height	mm	0.7	0.7
Posterior annular length	mm	52	50
Posterior edge length	mm	75	94
Posterior leaflet height	mm	12	12
Posterior commissural height	mm	0.7	0.7

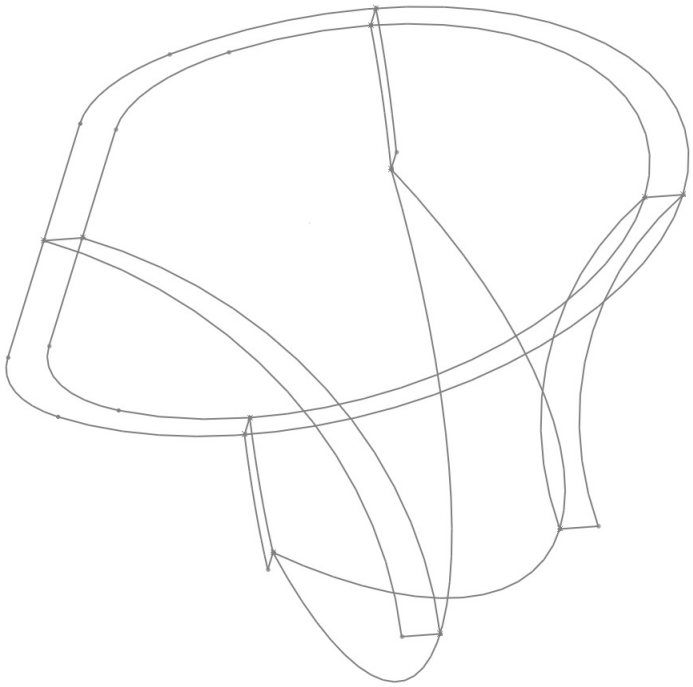

Figure 3.2: The anterior and posterior leaflets were created by drawing partial circles with radius of 15 mm and 13.9 mm on the planes which have the angles of 15 and 101 degree with basal plane. The half circles were initiated from the distance of 5.14 mm to the base.

3.4 Geometry of Mitral Valve and Left Ventricle and Boundary Conditions

To perform the FSI simulations, the two main components of the framework consists of the geometry of the mitral valve, as discussed earlier and the geometry of normal left ventricle, developed in Chapter 2. Figure 3.4 shows the assembly of the left ventricle and the mitral valve. The basal plane of the mitral valve is seated on the basal plane of the left ventricle.

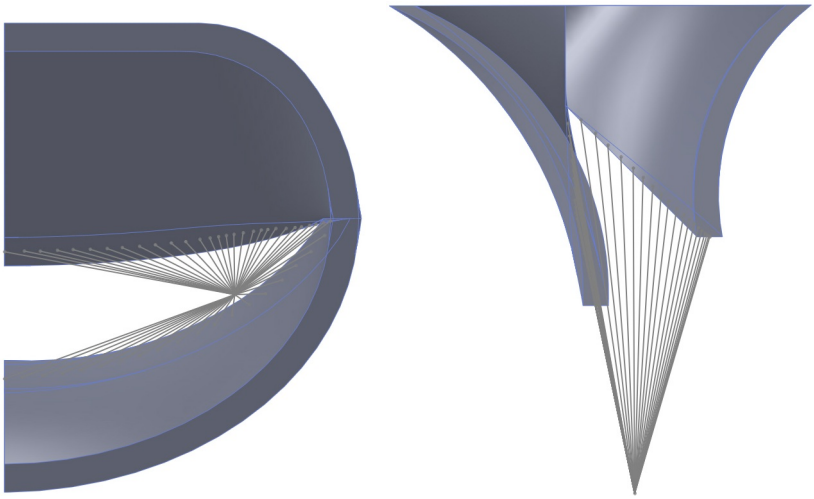

(1) Basal View

(2) Symmetry View

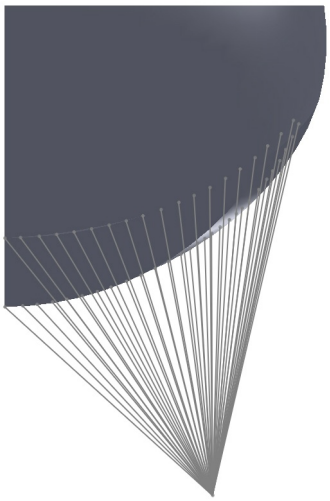

(3) Side View

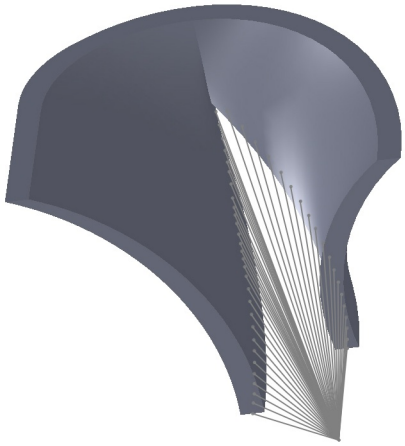

(4) Oblique View

Figure 3.3: Four views of the constructed Mitral valve

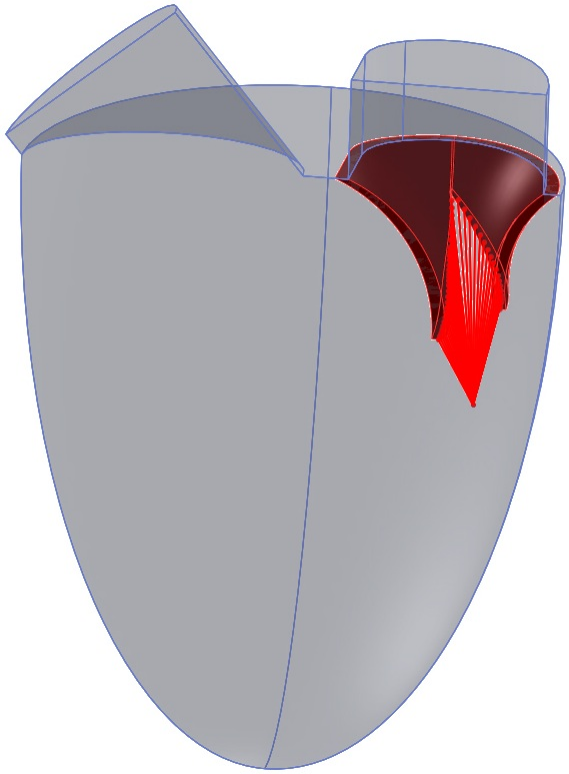

Figure 3.4: Constructed model of the left ventricle with mitral valve

3.5 Finite Element Model of the Mitral valve

The finite element model used for the structural analysis of the mitral valve is discussed next. After creating the undeformed parametric geometry of the mitral valve, the solid model of the valve was meshed using SOLID186 tetrahedral element [ANNSYS REF]. This element has 20 nodes with three degrees of freedom per node. The edges of the leaflets were connected to a fixed point that represents the papillary muscle, and these were modeled using the LINK180 tension only element. This is a cable type of element which only resists against the tension and it becomes passive when it goes under compression.

Most of the soft biologic tissues can be represented by the stress/strain relationship which includes three deformation stages: pre-transition, transition and post-transition [55]. In the pre-transition region, the stiffness of the tissue is low under small loads and in post-transition it is high in order to tolerate high loads. The Mitral tissue presents similar behavior due to the existence of fibers embedded in the tissue. The collagen fibers are responsible for carrying most of the tension loads. Therefore, the

Young's Modulus parallel to the fibers is higher than the perpendicular one. The fibers are orientated primarily along a line from the basal circumference toward the leaflet's edges [14]. In this model, we adjusted the local x-axis of the SOLID186 parallel to fibers and its local y-axis is perpendicular to the fibers. Table 3.2 presents the material properties of the tissue used in our model. Since the bending resistance within the tissue of leaflet is negligible, we selected the lowest allocable magnitude for the E_z in order for the stiffness matrix to be positive definite.

Table 3.2: Material properties of Mitral Valve used for simulation[56].

Property	Units	Anterior Leaflet	Posterior Leaflet	Chordae
E_x	kPa	6233	2087	33000
E_y	kPa	2350	1887	-
G_{xy}	kPa	1369	694	-
ν	-	0.45	0.45	-
ρ_{mv}	kg/m^3	1040	1040	1040
A	mm^2	-	-	0.55

The CONTC175 and TARGE170 elements were also used to model the atrial surfaces of the anterior and posterior leaflets. Since these surfaces are not in contact at the beginning of the simulation, a parameter was setup to measure the distance between the edges of the leaflets at the beginning of each time step. If the distance is less than 1 mm, we activated the CONTAC175 and TARGE170 elements since the leaflets are about to contact in the following time step. The contact was set to be frictionless, meaning that the leaflets can slide on each other.

We also assumed that the mitral valve is symmetric with respect to the long axis (antro-posterior) plane. Therefore, we only simulate half of the mitral valve geometry with symmetry boundary condition at the antero-posterior plane. The basal circumference of the mitral valve is fixed.

3.6 Fluid-Structure Interaction Module

FSI coupling can be done in two ways: monolithic and partitioned. In the monolithic method, the fluid flow (Navier-Stokes) and structural (stress-strain) equations are solved in one system using the finite element method. The monolithic approach has two main disadvantages: first, it is very difficult to solve the Navier-Stokes equations

using the finite element approach. Second, the resulting stiffness matrix is ill conditioned since it contains both fluid and structural stiffness terms which are present different orders of magnitude and this causes stability and convergence issues, specially when we are solving in the structurally nonlinear turbulence regime. On the other hand, the partitioned method is very versatile and practical since here we solve the fluid and structural equations separately (usually finite volume for fluid and finite element for structure) and transfer the load and deformations between the two solvers. Figure 3.5 presents the general framework of the partitioned approach. In this method, first the initial fluid and structural meshes are generated. Then, the fluid solver progresses for one time step (coupling time step). Next, the pressure loads are transferred to the wet surfaces of the structural mesh according to an interpolation scheme. Next, the structural solver progresses for the same time step and finally, the structural displacements are transferred to the wet surfaces of the fluid mesh and the fluid is moved accordingly. The FSI cycle is repeated to the final time step (n=N). Figure 3.6 shows the synchronization of the two solvers in terms of time. As it is shown in this sketch, one solver is always one time step ahead of the other one depending which one starts first. This is the major disadvantage of this method.

3.6.1 Fluid-Structure Interaction Framework

Normally, the partitioned fluid-structure interaction approach in which the fluid mesh is moved every coupling time step (i.e. spring network [28]) is not capable of accommodating large deformations since eventually the fluid mesh becomes distorted at some point. Also, we can not close the mitral valve completely with the regular FSI method because we are not allowed to split the computational domain during the computation. Therefore, we developed a hybrid FSI framework which consists of both moving and regenerating the mesh (re-meshing). Figure 3.9 illustrates this fluid-structure interaction algorithm. Here, we have implemented the FSI module by moving the mesh every coupling time step until the mesh quality becomes unsuitable for the CFD solver. Then we regenerate the deformed geometry of the mitral valve and left ventricle, as described in Chapter 3.6.2 and create a new mesh for both fluid and structural domains. Then, we interpolate the solutions of the old meshes to the new meshes and proceed with the FSI cycle until the next mesh distortion point at which time we repeat the mesh regeneration process. The adopted scheme for the FSI algorithm may be summarized in the following way:

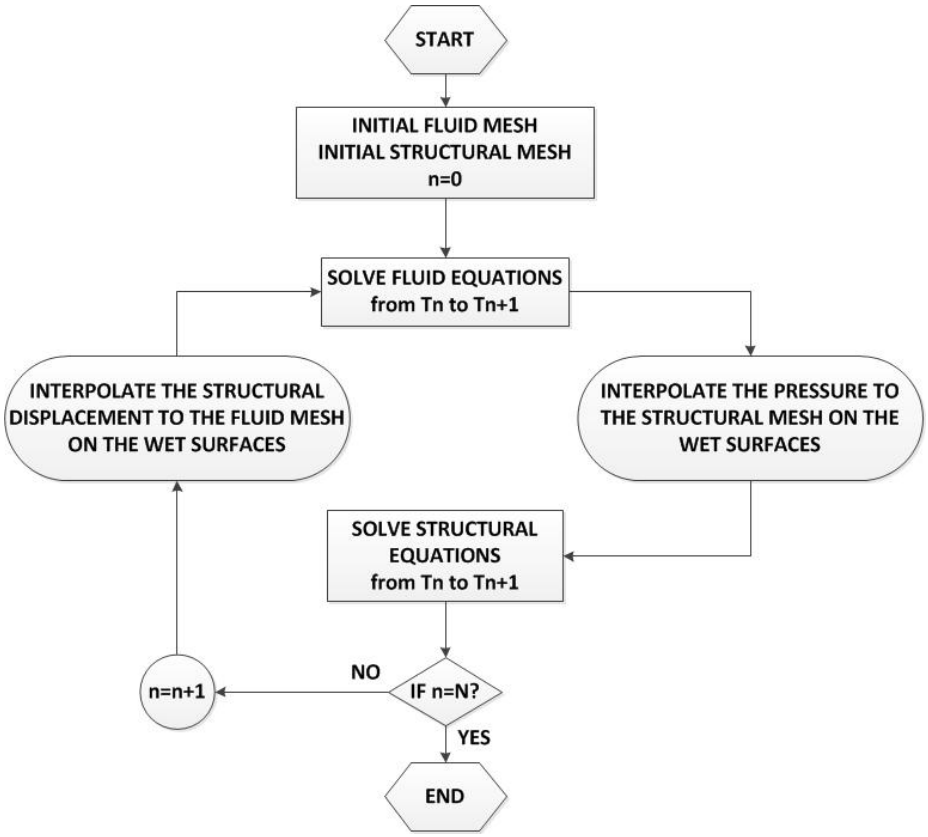

Figure 3.5: General framework of the partitioned FSI method.

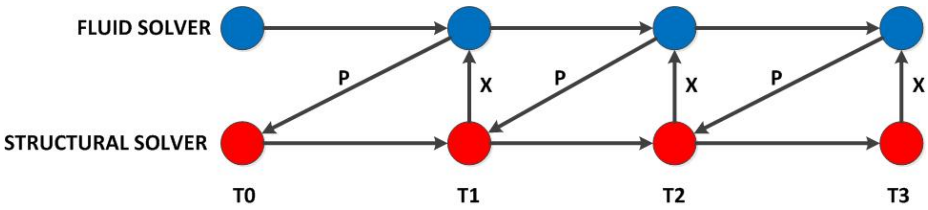

Figure 3.6: Time marching approach in the partitioned method.

1. Create the geometry of the mitral valve and left ventricle at the beginning of the isovolumetric systole.

2. Calculate the boundary conditions.

3. Calculate the velocity of the left ventricular wall.

4. Conduct CFD simulation and calculate the pressures on the FSI interfaces.

5. Relax the pressures by a factor of 0.75.
6. Transfer the relaxed pressures to the FSI interfaces.
7. Perform finite element simulations of the mitral valve.
8. Move the fluid mesh according to the deformation of the mitral valve.
9. Conduct CFD simulation and calculate the pressures on the FSI interfaces.
10. Check if the difference between the pressures of the current sub-step and previous one is less than 0.001 Pa.
11. If No, go back to step 7.
12. If Yes, proceed to the next coupling time step.
13. Check the quality of the mesh.
14. If convergence checks, then go to the step 3
15. if the mesh does not converge, create the deformed geometry of the mitral valve and left ventricle.
16. Create a new mesh for the fluid and structural domains.
17. Interpolate the solution of the old mesh to the new mesh for both structure and fluid. A code in Matlab was written to implement the interpolation.
18. Go to step 3

3.6.2 Method of Generating Geometry of The Deformed Mitral Valve and Left Ventricle

Figure 3.8 depicts the flowchart of the method used to generate geometry of the deformed mitral valve and left ventricle. The method is implemented using APDL (Ansys Parametric Design Language). We begin by selecting the surface nodes of the deformed mesh. Then, we create a surface mesh using these nodes. Next, we convert each surface element (element type: MESH200) to each facet. Finally, we convert the enclosed volume to a part in IGES format. Figure 3.7 shows the IGES geometry of deformed mitral valve in three time steps during systole.

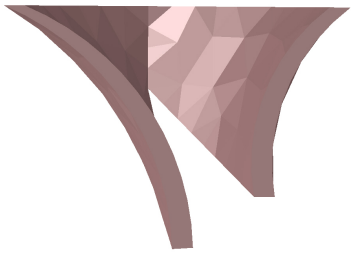

(1) t = 5 ms, Symmetry view

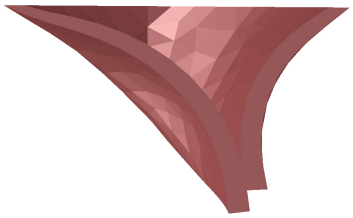

(2) t = 35 ms, Symmetry view

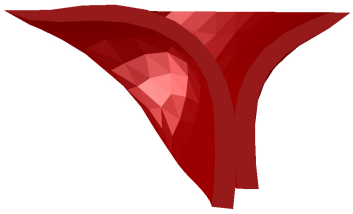

(3) t = 120 ms, Symmetry view

(4) t = 5 ms, Basal View

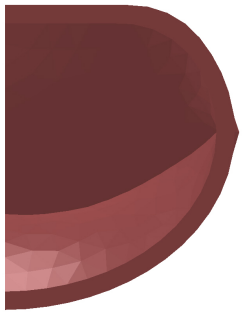

(5) t = 35 ms, Basal View

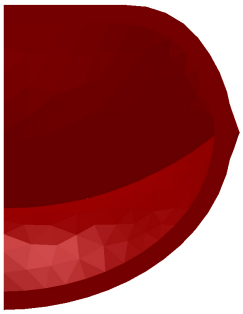

(6) t = 120 ms, Basal View

Figure 3.7: Deformed geometry of the mitral valve in three time steps.

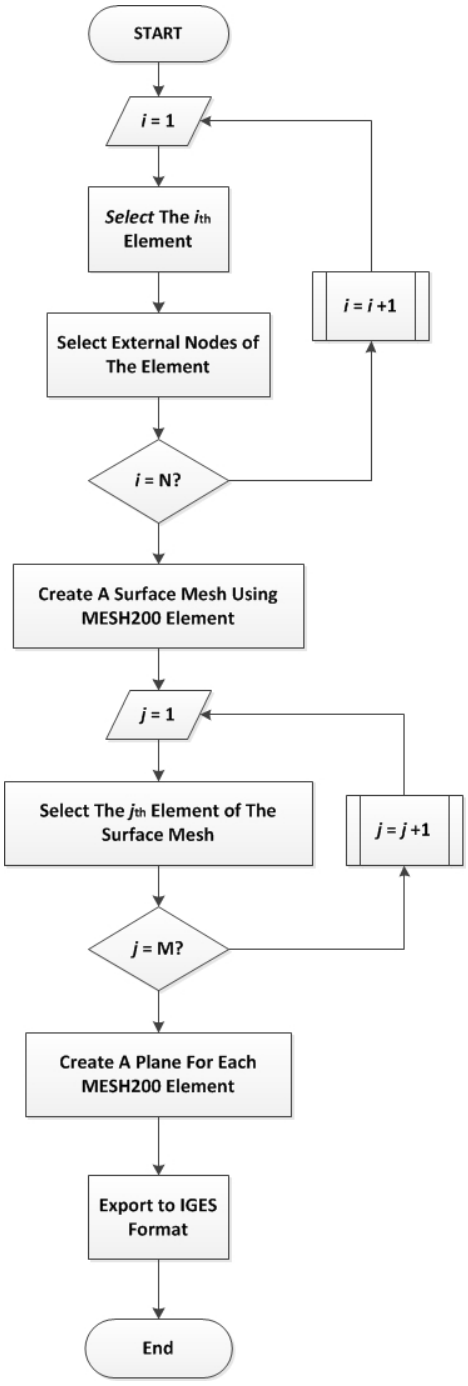

Figure 3.8: Method of Generating Geometry of The Deformed Mitral Valve and Left Ventricle. N and M are the total number of solid and surface element respectively.

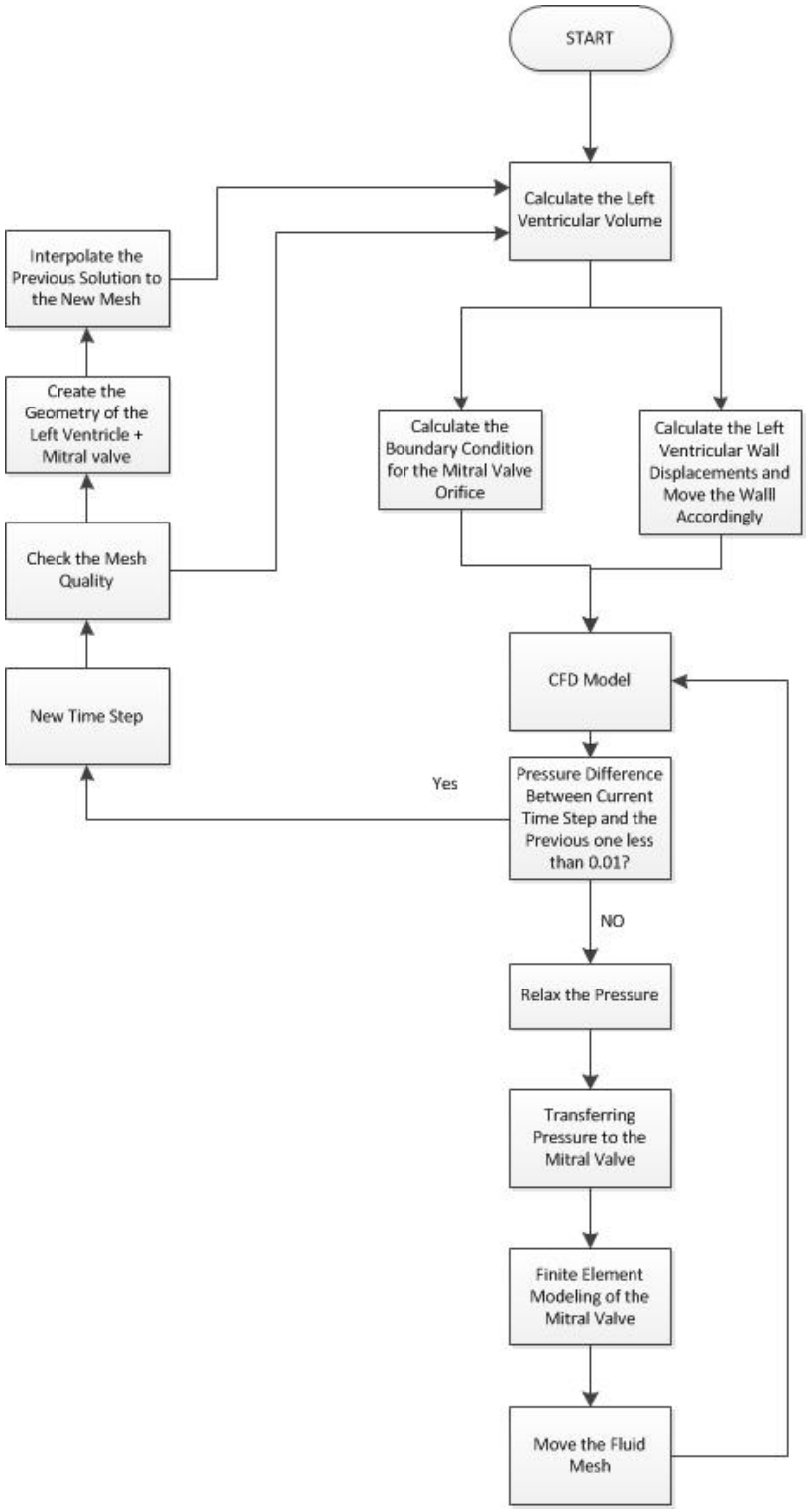

Figure 3.9: Fluid-Structure Interaction algorithm used for the simulation of the mitral valve within a beating normal left ventricle

3.7 Boundary Conditions

chap3$_b cs$

The pressure boundary conditions for the aortic and mitral apertures were calculated using the Alexander and Windkessel models. These were implemented and are described earlier in Chapter 2. Figure 3.10 presents the boundary conditions used for the simulation.

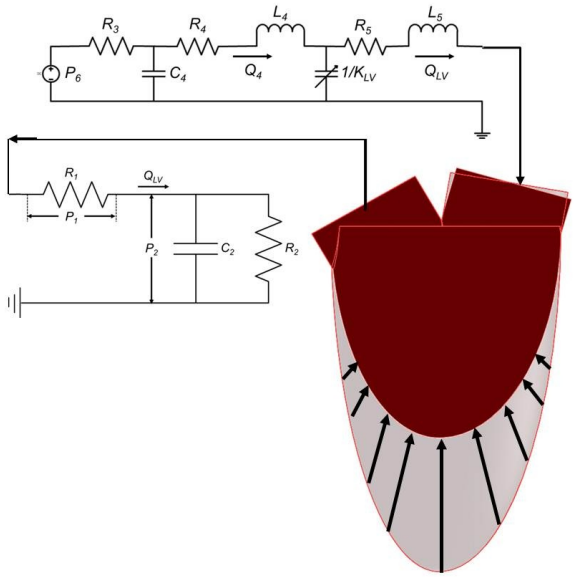

Figure 3.10: Windkessel and Alexander models used to simulate the boundary conditions for the aortic and mitral orifices, respectively.

3.8 Coaptation and Deformation Analysis

Figure 3.12 shows the displacement of point A in Figure 3.11. It can be observed that, from the beginning of the isovolumetric contraction to the point of coaptation, point A displaces linearly. Immediately after the beginning of the coaptation, the posterior leaflet pushes the anterior leaflet back and they reach equilibrium. The full coaptation takes place at the peak systole when the left ventricular pressure is maximum (figures 3.14(29) and 3.15(29)). After this point, as the left ventricular pressure falls, the coaptation begins to reduce until the beginning of the isovolumetric relaxation when the leaflets start to separate from each other. During the isovolumetric relaxation, the valve opens almost linearly. Also, from the beginning to the full coaptation point, the length of the coaptation line (at the symmetry plane) increases but its angle remains almost constant.

3.9 Stress Analysis

The maximum stress is observed at the base since it is clamped during the simulation. Then the stress reduces as it moves toward the edge. Table 3.3 presents the maximum principal stress at two points along each leaflet.

Table 3.3: Maximum principal stresses (kPa) at point B, C, D and E.

State	B	C	D	E
Early IVC	55	117	8	54
Mid IVC	197	343	67	243
End IVC	268	763	126	453
Peak Systole	820	1200	250	580

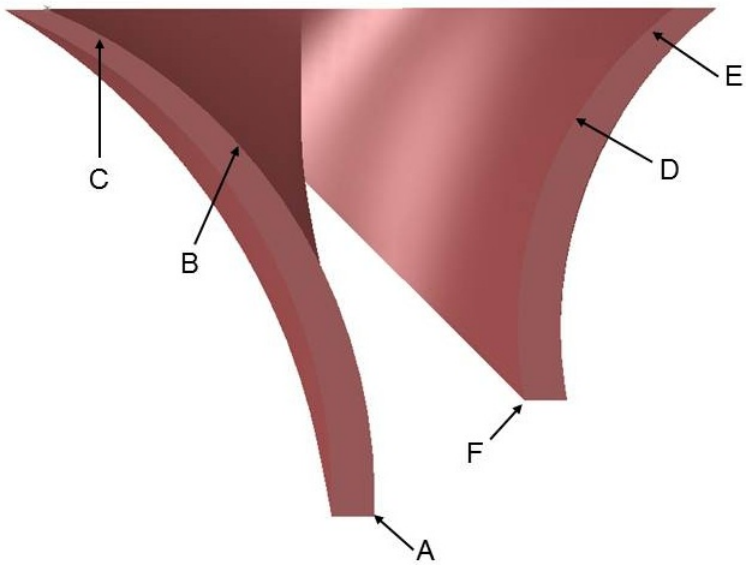

Figure 3.11: Demonstration of the points of interest

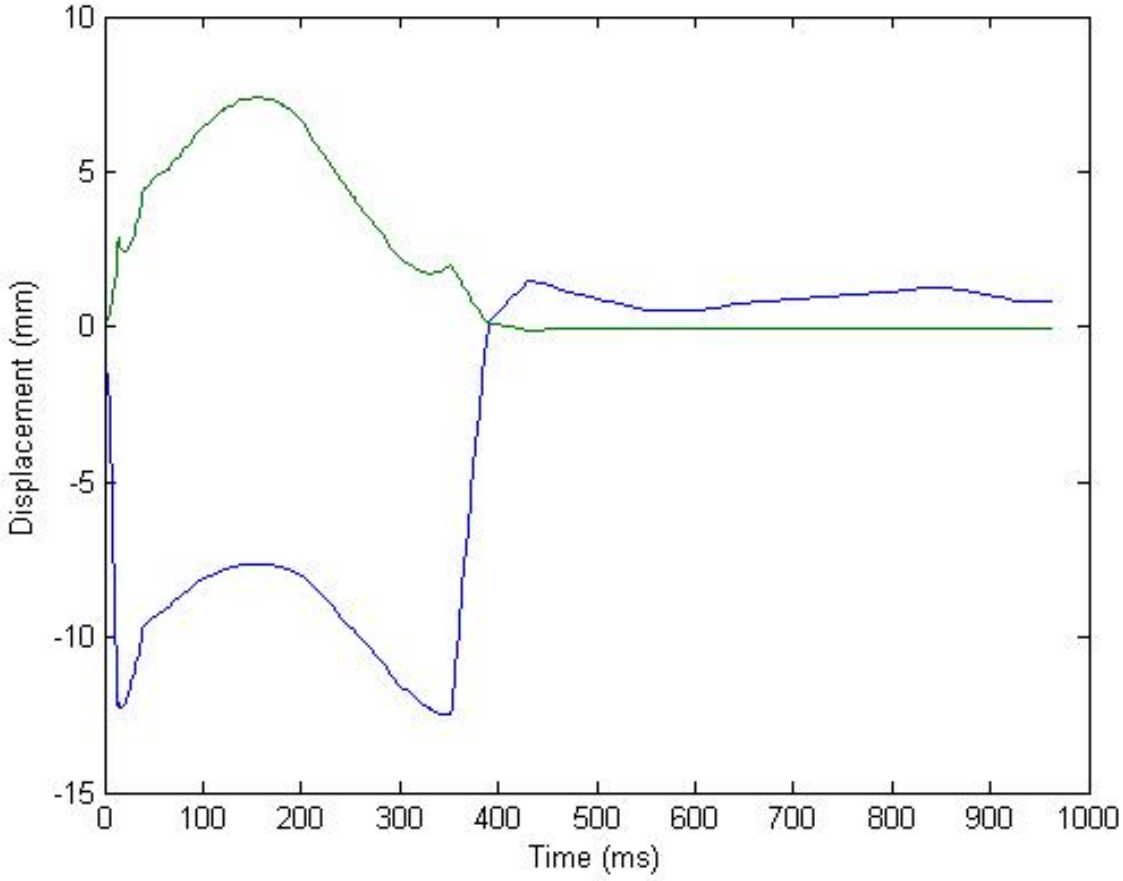

Figure 3.12: displacement of the points A and F during a cardiac cycle.

3.10 Chordae Force

Figure 3.13 exhibits the chordal force as a function of time during a cardiac cycle. Three chordaes were selected from different positions on each leaflets: on the symmetry plane, halfway between the symmetry plane and ALC, and near the ALC. Here, it can be observed that the anterior chordal forces are about 3 time larger than the posterior ones. Also, the force is highest on the symmetry plane and decreases toward the ALC for both leaflets. The break point on the left side of the curves belongs to the beginning of coaptation. As expected, the highest tension takes place at the peak systole which is about 3 N.

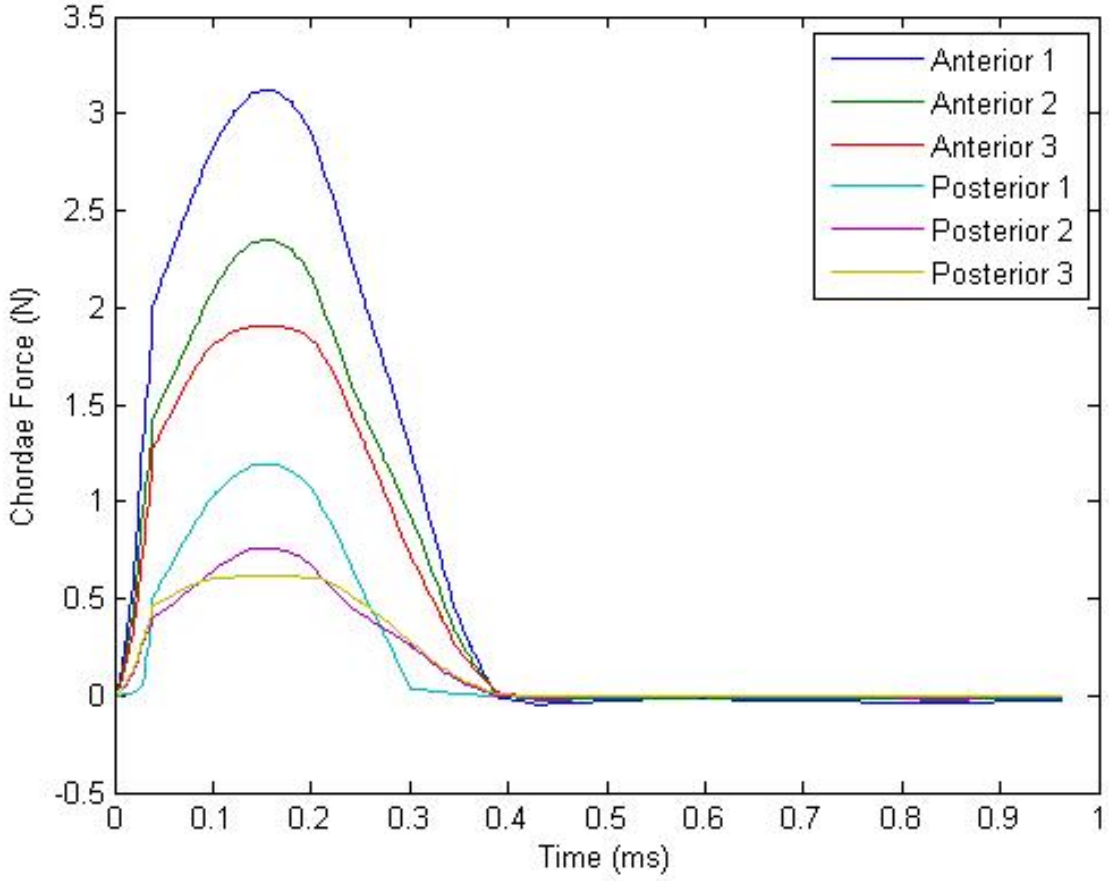

Figure 3.13: Chordae forces of 3 samples from anterior and posterior leaflets.

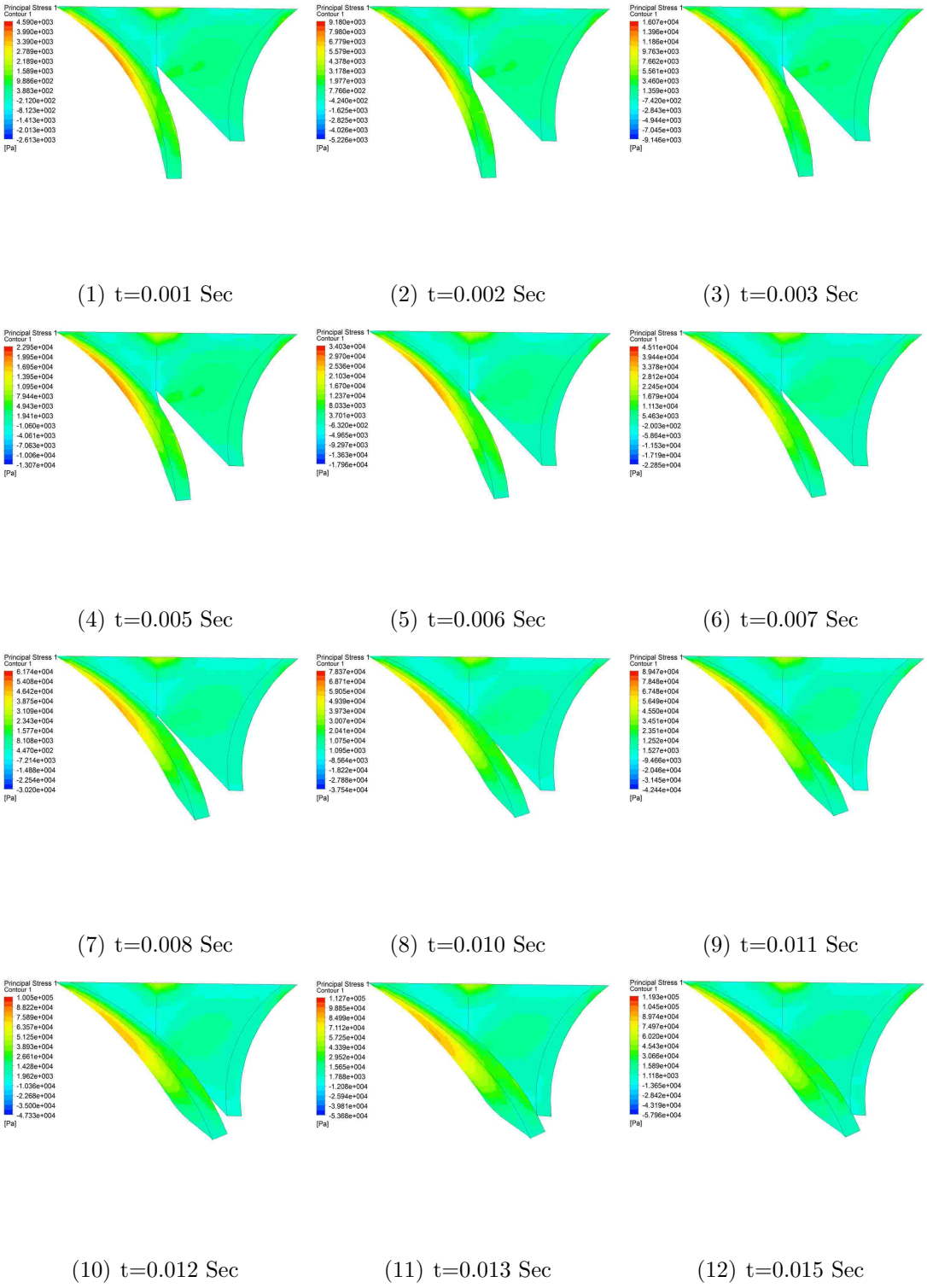

Figure 3.14: First principal stress, view: Symmetry Plane. SV=60 ml, HR=60 bpm.

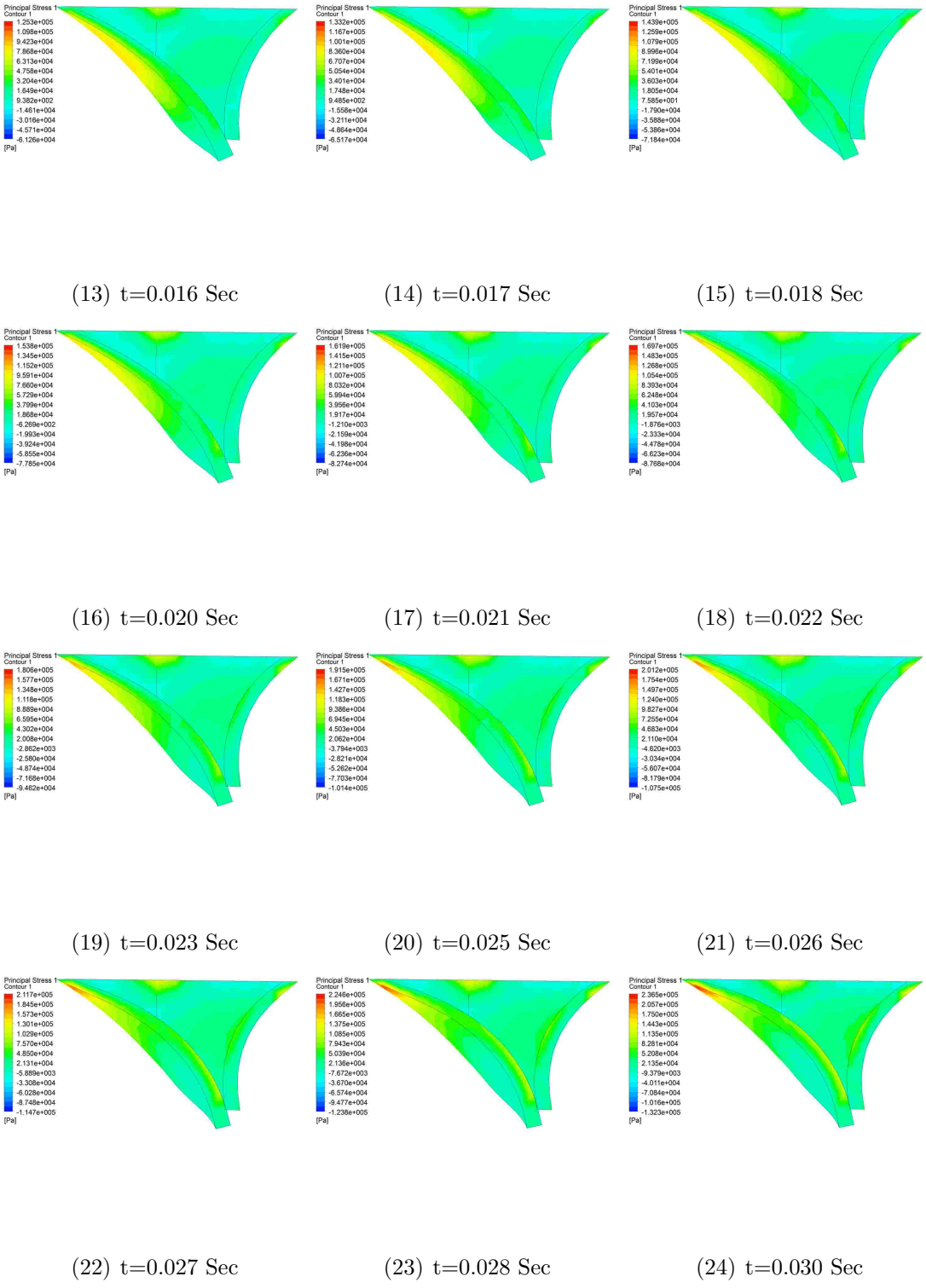

(13) t=0.016 Sec (14) t=0.017 Sec (15) t=0.018 Sec

(16) t=0.020 Sec (17) t=0.021 Sec (18) t=0.022 Sec

(19) t=0.023 Sec (20) t=0.025 Sec (21) t=0.026 Sec

(22) t=0.027 Sec (23) t=0.028 Sec (24) t=0.030 Sec

Figure 3.14: First principal stress, view: Symmetry Plane. SV=60 ml, HR=60 bpm (cont).

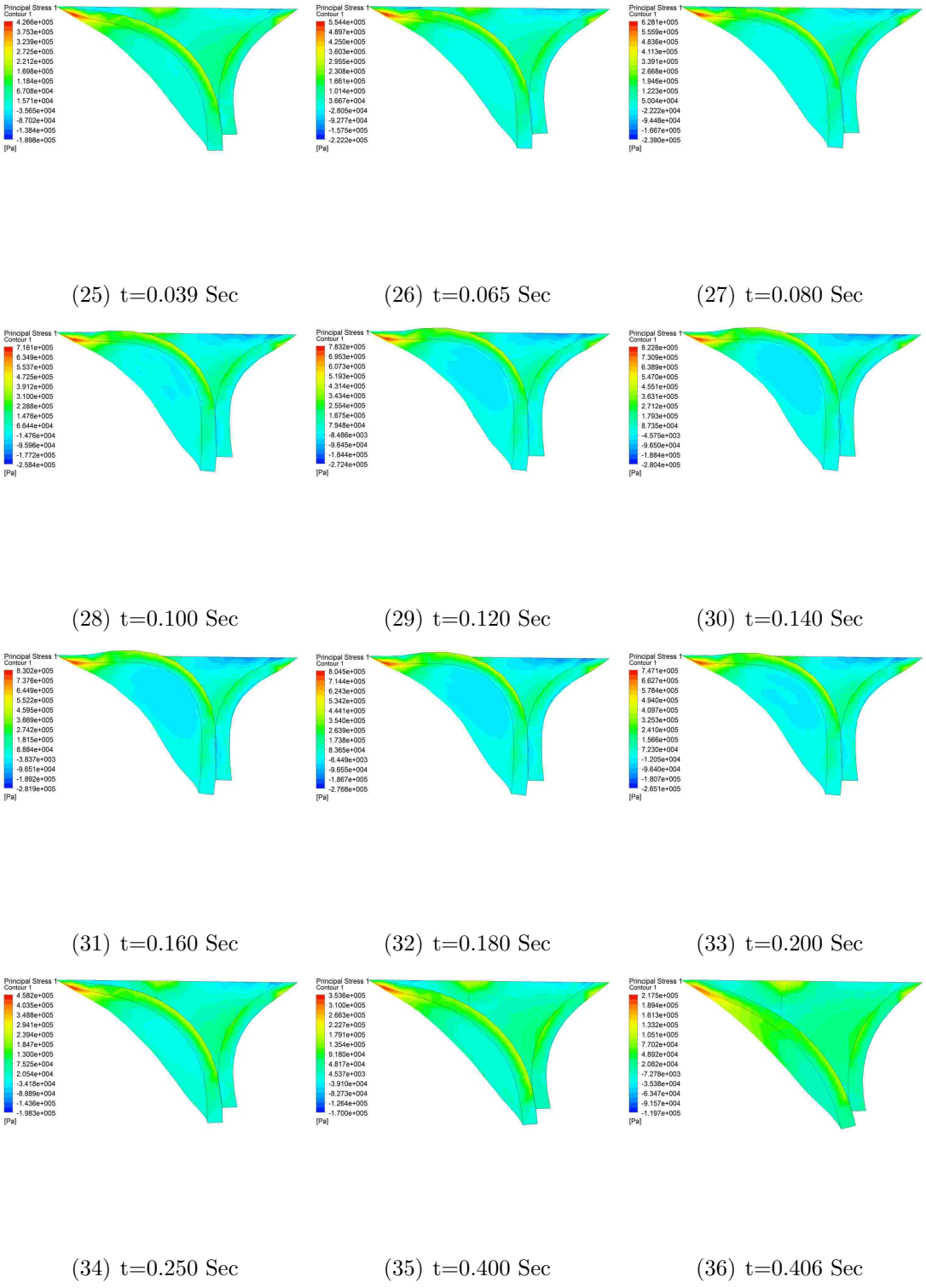

(25) t=0.039 Sec (26) t=0.065 Sec (27) t=0.080 Sec

(28) t=0.100 Sec (29) t=0.120 Sec (30) t=0.140 Sec

(31) t=0.160 Sec (32) t=0.180 Sec (33) t=0.200 Sec

(34) t=0.250 Sec (35) t=0.400 Sec (36) t=0.406 Sec

Figure 3.14: First principal stress, view: Symmetry Plane. SV=60 ml, HR=60 bpm (cont).

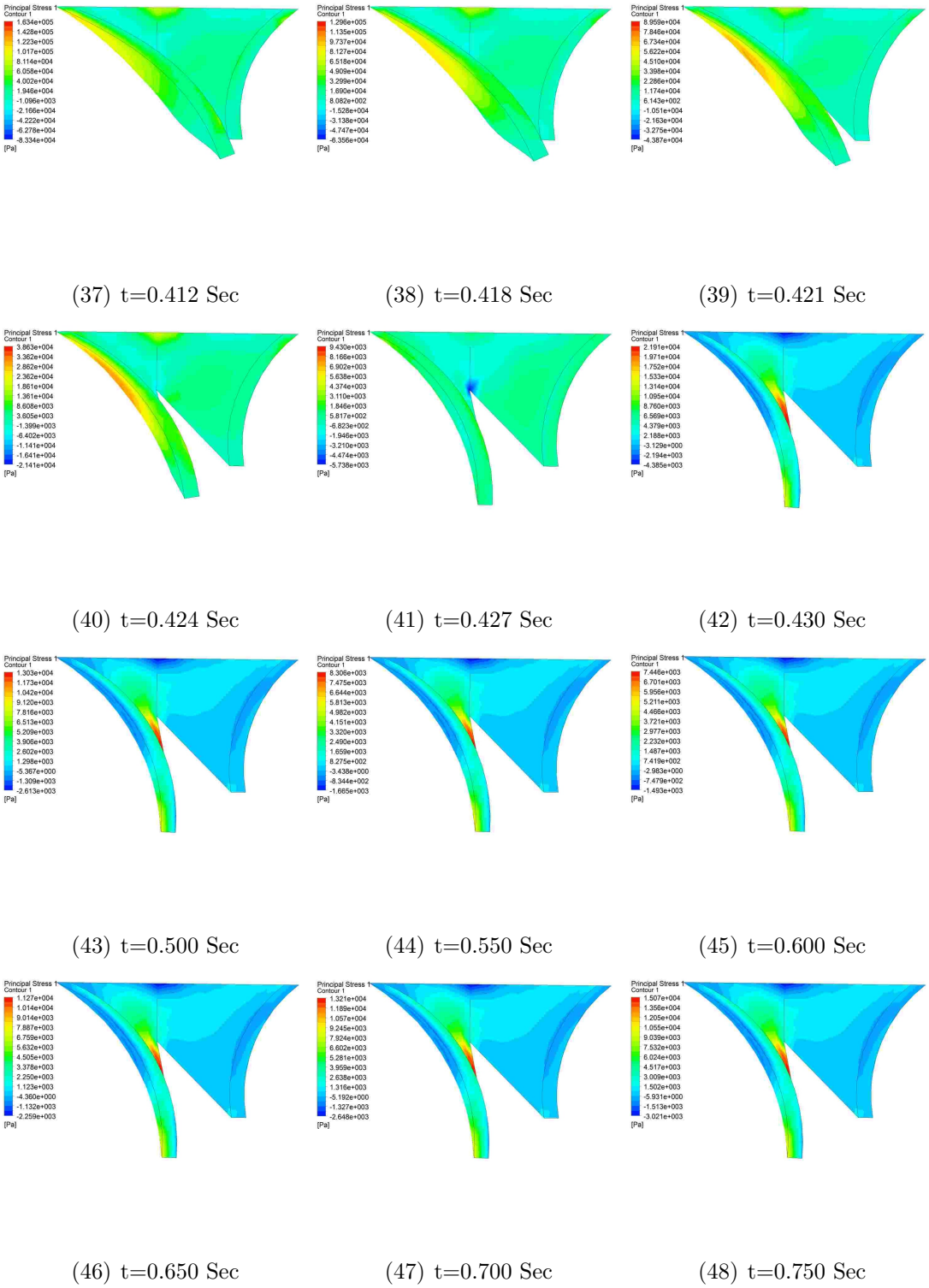

Figure 3.14: First principal stress, view: Symmetry Plane. SV=60 ml, HR=60 bpm (cont).

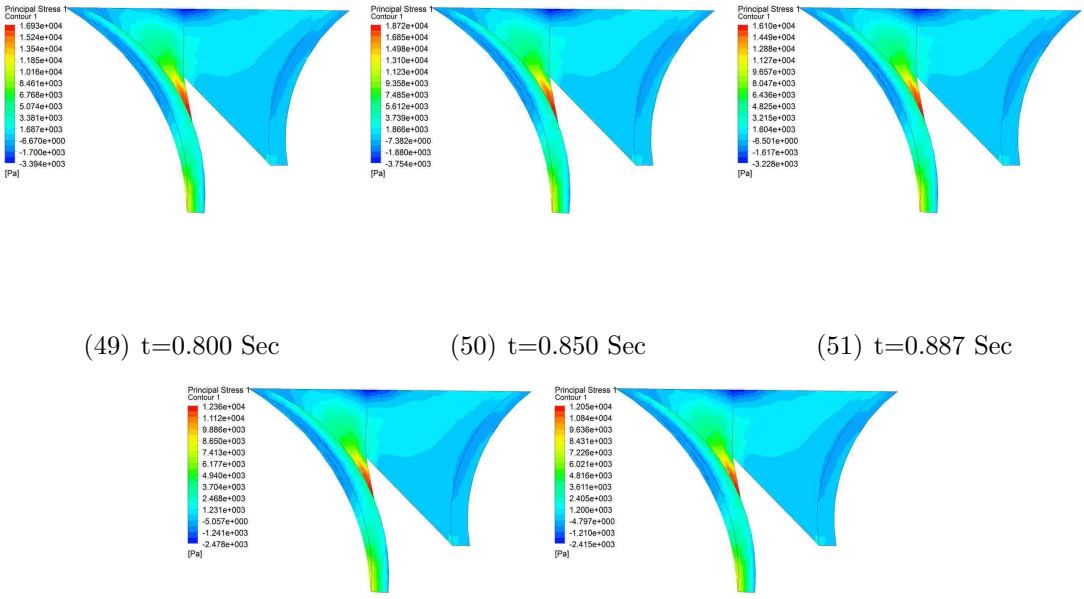

(49) t=0.800 Sec (50) t=0.850 Sec (51) t=0.887 Sec

(52) t=0.925 Sec (53) t=0.962 Sec

Figure 3.14: First principal stress, view: Symmetry Plane. SV=60 ml, HR=60 bpm (cont).

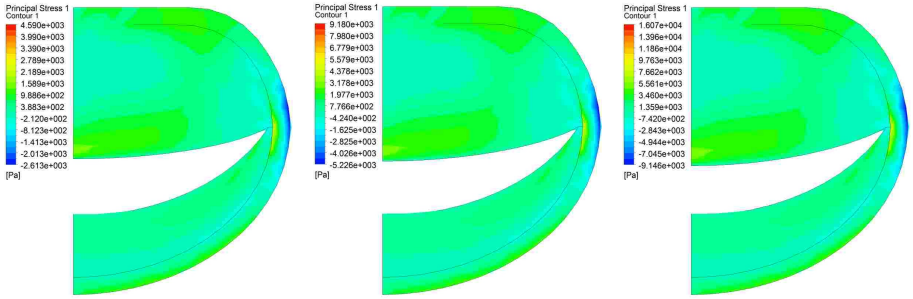

(1) t=0.001 Sec

(2) t=0.002 Sec

(3) t=0.003 Sec

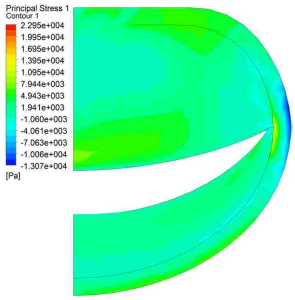

(4) t=0.005 Sec

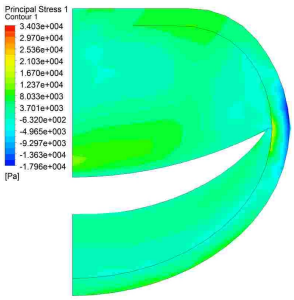

(5) t=0.006 Sec

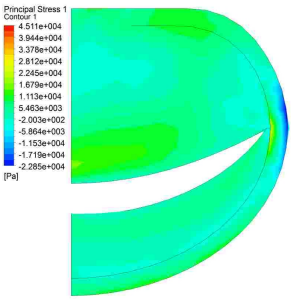

(6) t=0.007 Sec

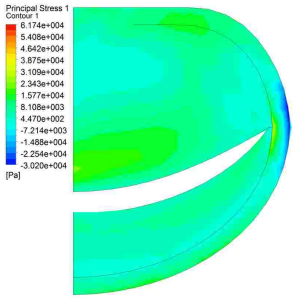

(7) t=0.008 Sec

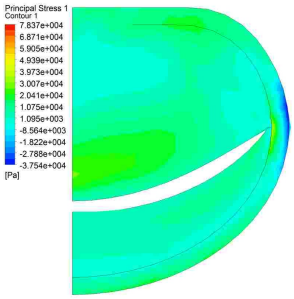

(8) t=0.010 Sec

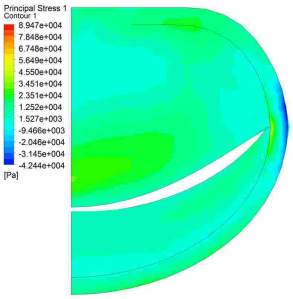

(9) t=0.011 Sec

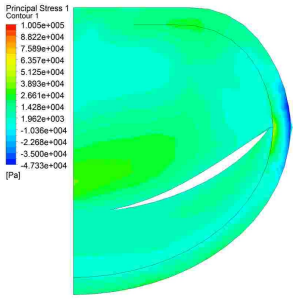

(10) t=0.012 Sec

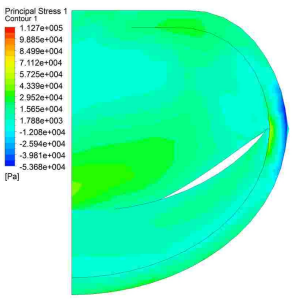

(11) t=0.013 Sec

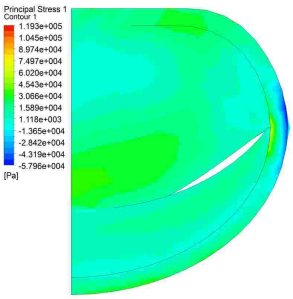

(12) t=0.015 Sec

Figure 3.15: First principal stress, view: basal Plane. SV=60 ml, HR=60 bpm.

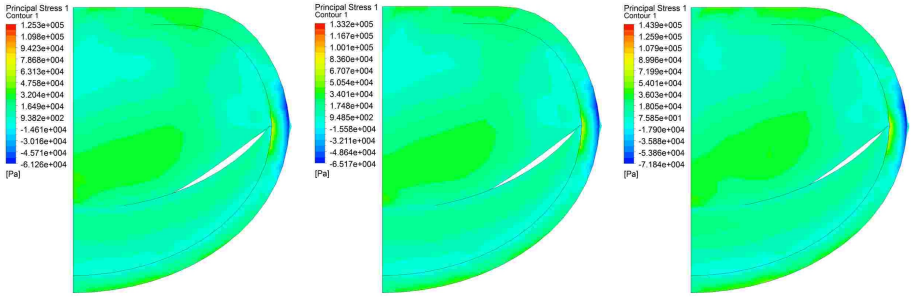

(13) t=0.016 Sec (14) t=0.017 Sec (15) t=0.018 Sec

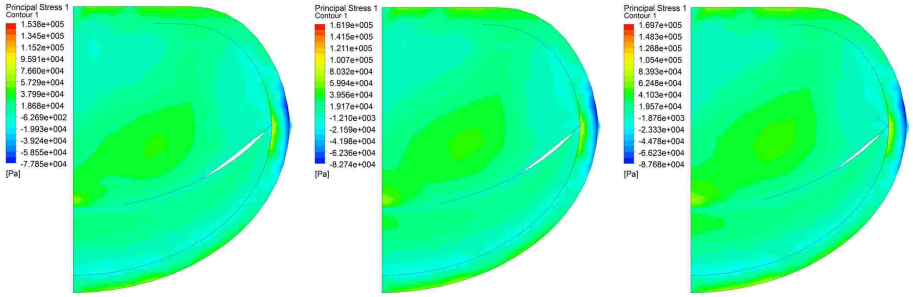

(16) t=0.020 Sec (17) t=0.021 Sec (18) t=0.022 Sec

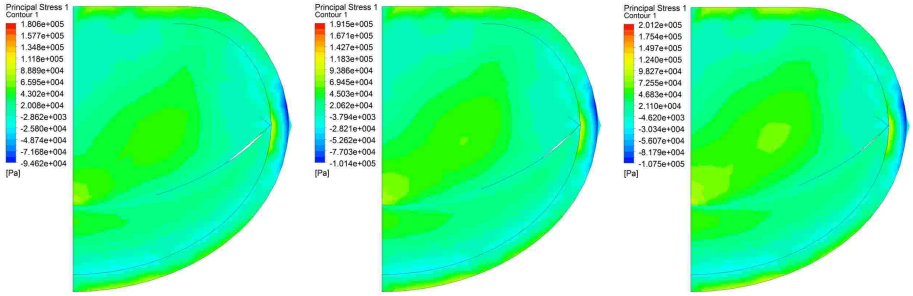

(19) t=0.023 Sec (20) t=0.025 Sec (21) t=0.026 Sec

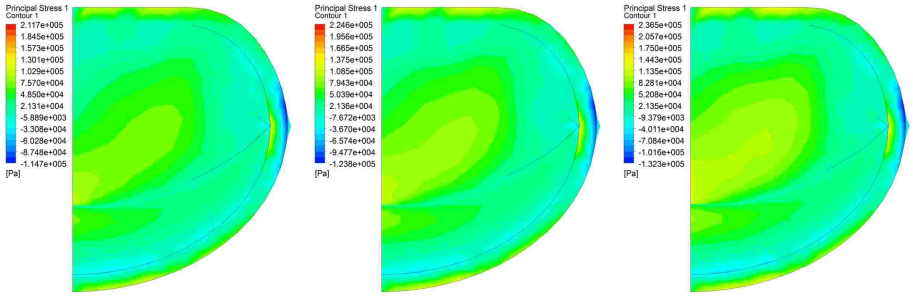

(22) t=0.027 Sec (23) t=0.028 Sec (24) t=0.030 Sec

Figure 3.15: First principal stress, view: basal Plane. SV=60 ml, HR=60 bpm (cont).

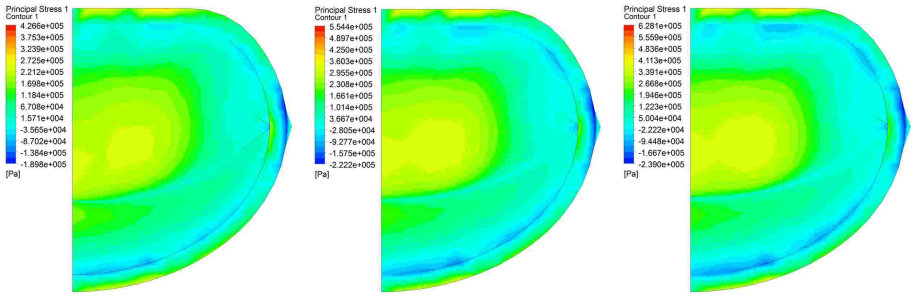

(25) t=0.039 Sec (26) t=0.065 Sec (27) t=0.080 Sec

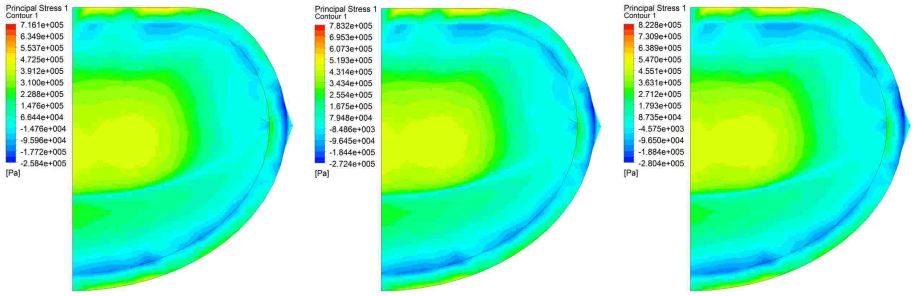

(28) t=0.100 Sec (29) t=0.120 Sec (30) t=0.140 Sec

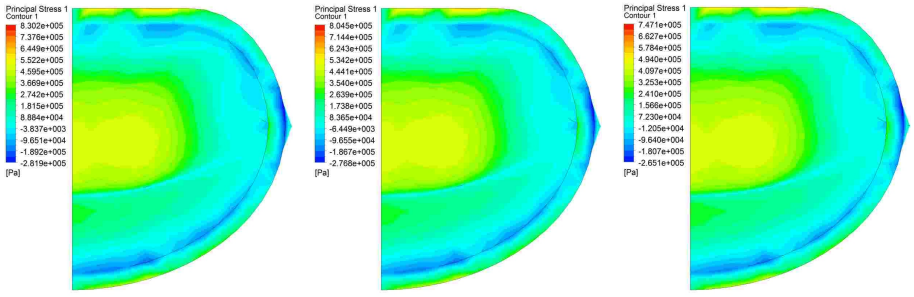

(31) t=0.160 Sec (32) t=0.180 Sec (33) t=0.200 Sec

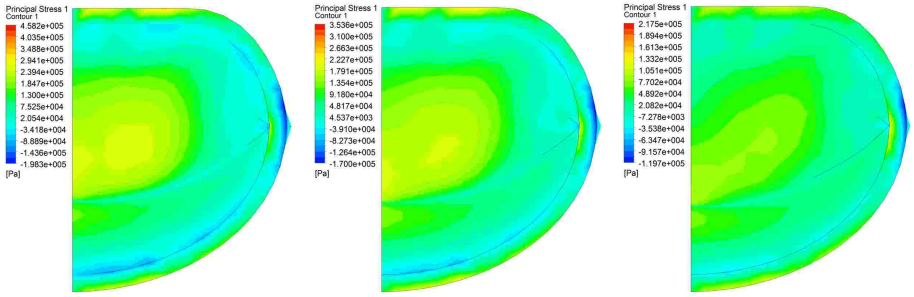

(34) t=0.250 Sec (35) t=0.400 Sec (36) t=0.406 Sec

Figure 3.15: First principal stress, view: basal Plane. SV=60 ml, HR=60 bpm (cont).

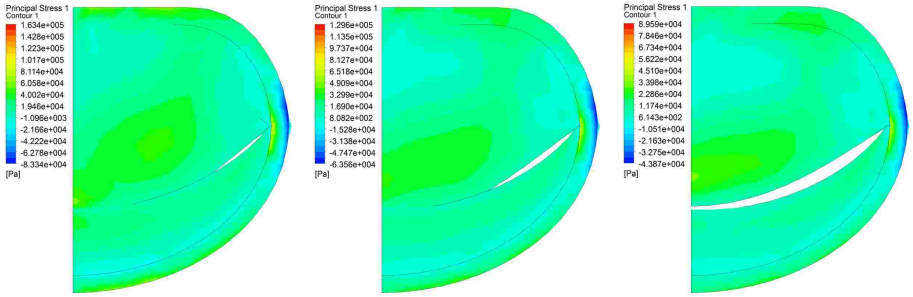

(37) t=0.412 Sec

(38) t=0.418 Sec

(39) t=0.421 Sec

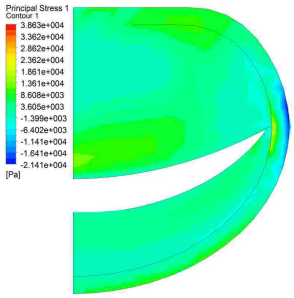

(40) t=0.424 Sec

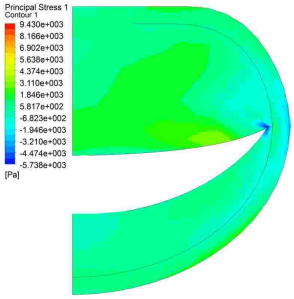

(41) t=0.427 Sec

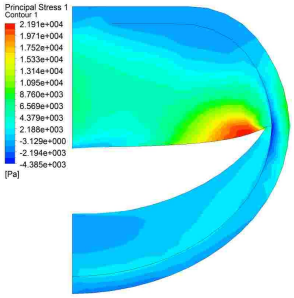

(42) t=0.430 Sec

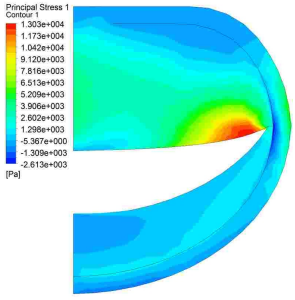

(43) t=0.500 Sec

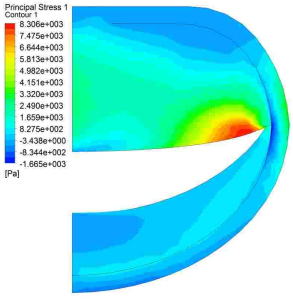

(44) t=0.550 Sec

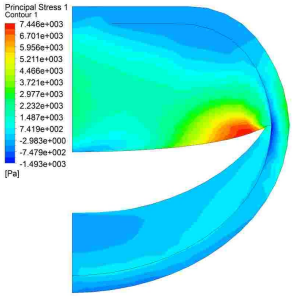

(45) t=0.600 Sec

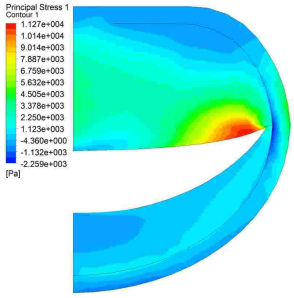

(46) t=0.650 Sec

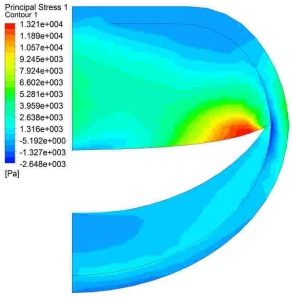

(47) t=0.700 Sec

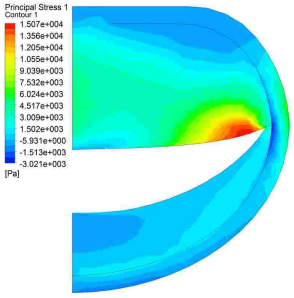

(48) t=0.750 Sec

Figure 3.15: First principal stress, view: basal Plane. SV=60 ml, HR=60 bpm (cont).

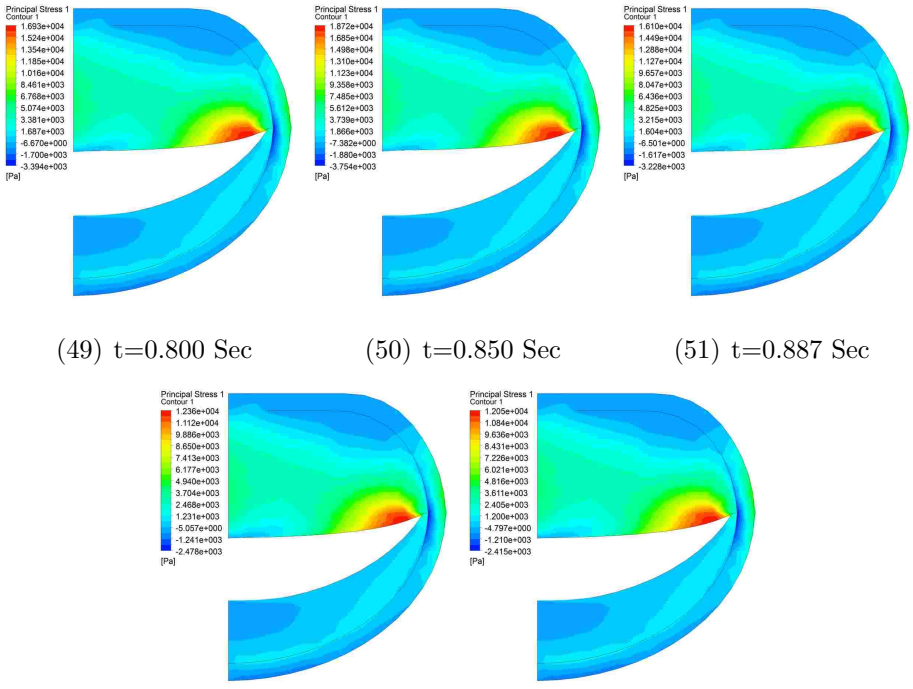

(49) t=0.800 Sec (50) t=0.850 Sec (51) t=0.887 Sec

(52) t=0.925 Sec (53) t=0.962 Sec

Figure 3.15: First principal stress, view: basal Plane. SV=60 ml, HR=60 bpm (cont).

3.11 Flow Dynamics in Early Systole

Figures B.3(1) to 3.28(8) and B.3(1) illustrate the long axis view (looking into the symmetry plane) of the 2D and 3D streamlines of the blood flow in the early systole. Simulation began at the beginning of the left ventricular contraction when the mitral valve is fully open with zero stress. At this point, the left ventricular pressure rises rapidly causing the sudden closure of the mitral valve which is shown in the Figures B.3(1) to 3.28(8). Here, it can be observed that during the mitral valve closure, a regurgitation jet flows into the left atrium with the peak velocity of 7.2 mm/s. Figure 3.17 illustrates the regurgitation flow rate (mL/s) during a cardiac cycle. Here, the first jump is associated with the mitral valve closure. The flow streamlines start perpendicular to the left ventricular wall and converge toward the mitral valve opening (figures B.3(1) to B.3(2)) resulting in a pressure rise and drop in the left ventricle and atrium, respectively. This pressure difference deforms the mitral valve toward the left atrium which reduces the valve's opening, contributing to higher pressure difference and faster closure of the mitral valve.

At the beginning of the systole, when the mitral valve is still wide open (figures

B.3(1) and B.3(2)), the high velocity region is located in the edge of posterior leaflets. The structural simulation shows that the mitral valve begins to close from mid section i.e. the leaflets contact each other at the symmetry. After this initial contact, since the blood flow is blocked at the symmetry plane, a coil is initiated behind the anterior leaflet and is expanded circumferentially. As the mitral valve closes further, this coil becomes larger in the symmetry plane (figures 3.16(3) to 3.16(8)). The contact grows to the antero-lateral and postero-medial commisures and the opening becomes smaller until the complete closure (B.1(1) to B.1(25) and B.2(1) to B.2(25)). Consequently, the high velocity region moves toward the antero-lateral and postero-medial commisures.

3.12 Flow Dynamics During Mid and Late Systole

After the mitral valve is fully closed, the aortic valve opens and lets the flow to rush out of the left ventricle. Figures B.3(5) to B.3(12) show that, the left ventricular wall transfers its momentum to the flow and the streamlines are initiated from the left ventricular wall and converge on the aortic aperture. In this phase, the velocity is higher at the apex and it reduces as we move to the center of left ventricle and it increases as we travel to the aortic aperture. Figure 3.18 presents the velocity profile of a particle traveling from apex to the center of aortic orifice on a streamline. Figure 3.19 presents the vertical position of the minimum velocity on the same streamline. During mid systole, the pressure increases and after peak systole it decreases. This pressure moves the mitral leaflets back toward left atrium and increases the level of coaptation.

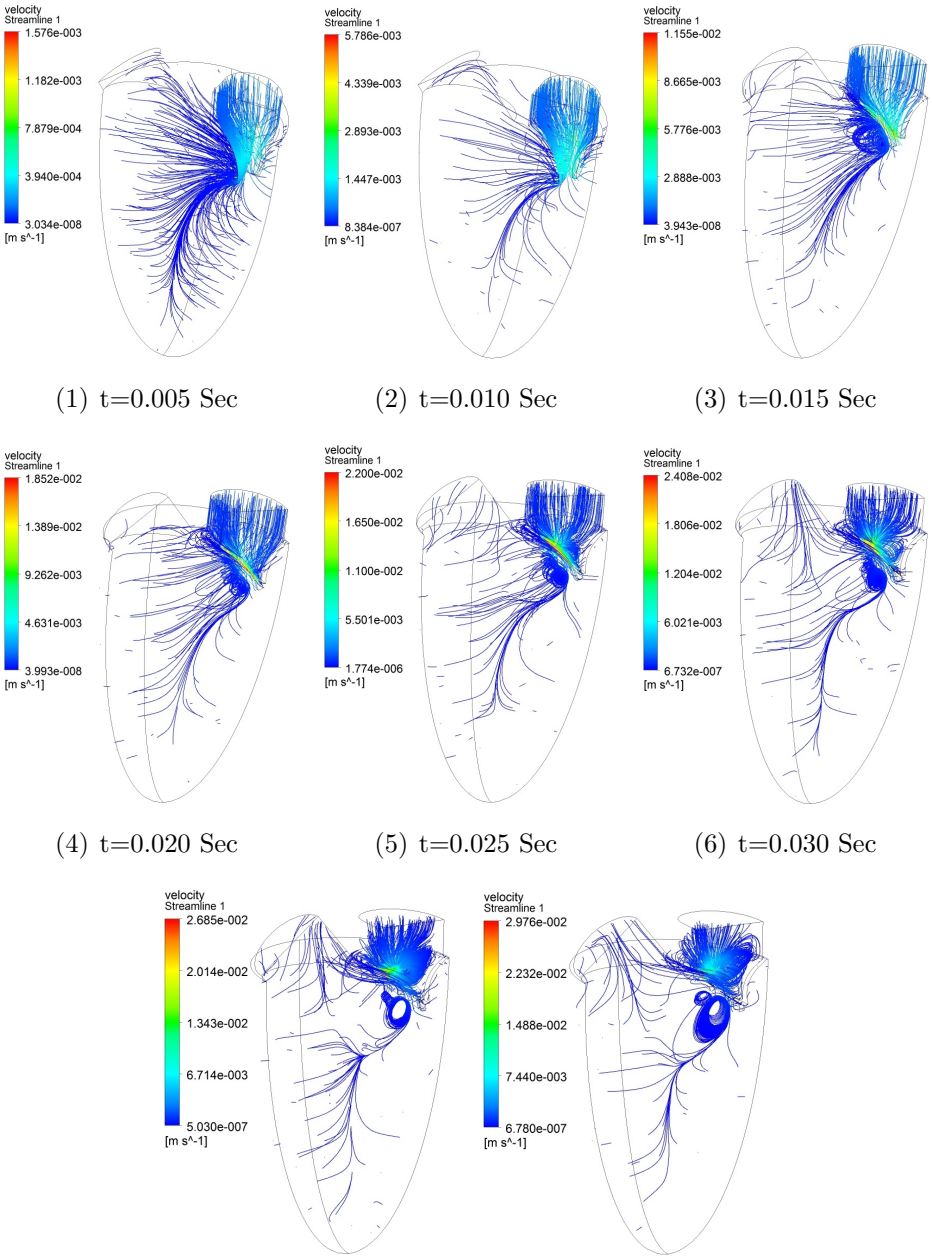

(1) t=0.005 Sec (2) t=0.010 Sec (3) t=0.015 Sec

(4) t=0.020 Sec (5) t=0.025 Sec (6) t=0.030 Sec

(7) t=0.035 Sec (8) t=0.039 Sec

Figure 3.16: 3D streamline of the blood flow in early systole. SV=60 ml, HR=60 bpm.

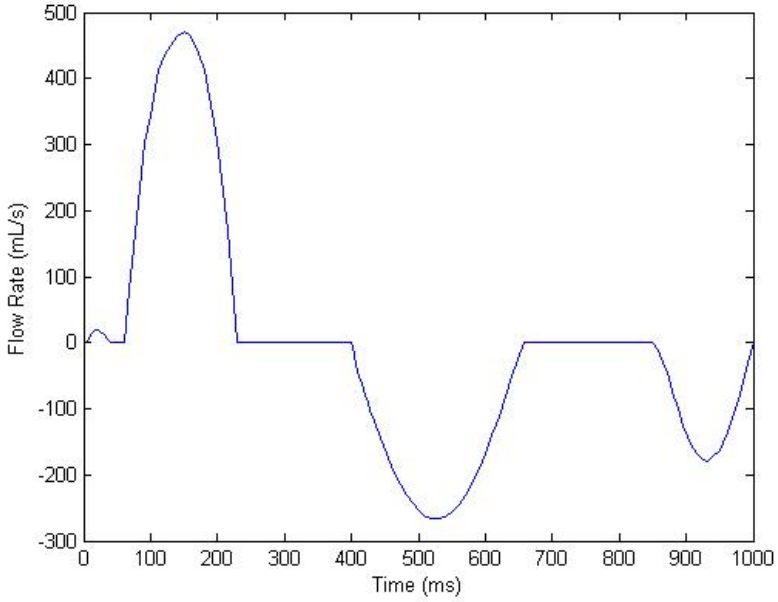

Figure 3.17: Mass flow in and out of the left ventricle during a cardiac cycle

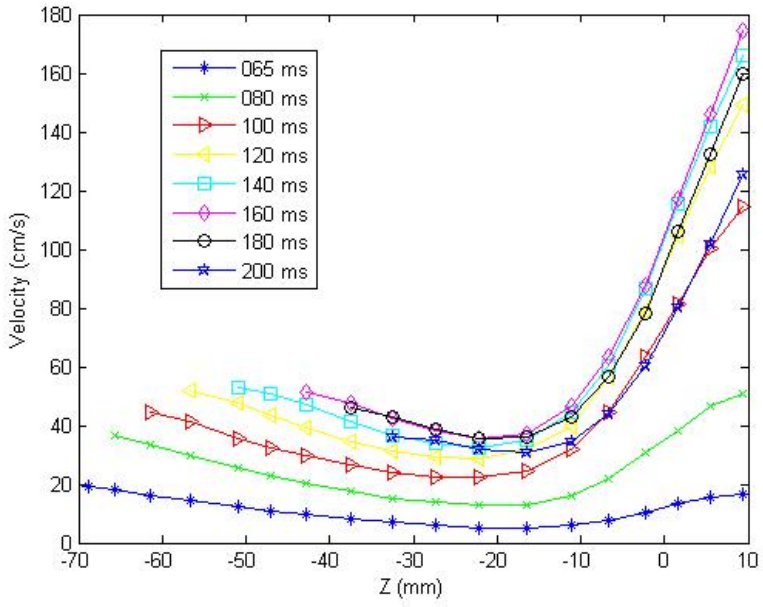

Figure 3.18: Velocity at different points along a streamline which is started from apex and ended in mid aortic aperture

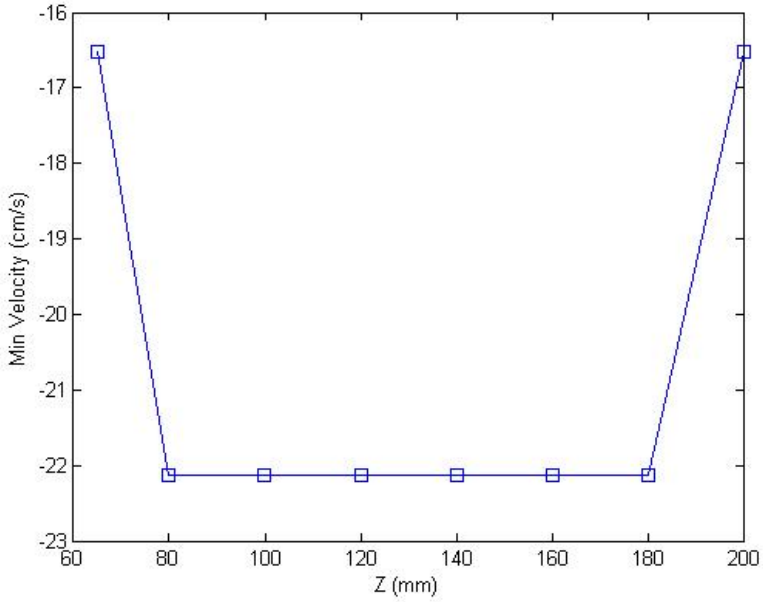

Figure 3.19: Position of minimum velocity along a streamline which is started from apex and ended in mid aortic aperture

3.13 Vortex Ring Formation During Early Diastole

After the isovolumetric relaxation, once the left ventricular pressure drops below the atrial pressure, the mitral valve starts to open (figures B.3(13) to B.3(19)). Figure 3.15(37) shows that the valve begins to open from the antero-lateral and postero-medial corners by formation of two small openings where two jets of blood flow into the left ventricle with velocity of 5.2 cm/sec. However, these jets decay shortly after entering the left ventricle. (about 3 mm below the orifices, their velocity drops to 1 cm/sec). After hitting the opposing wall, these twin jets recoil right below the mitral valve. As the mitral valve progresses its opening, the ALC and PMC orifices expand toward the symmetry plane and the two jets become bigger in size. At the onset of leaflet separation, the jets unify and create a curvy jet sheet stretching from postero-medial to antero-lateral corners of the mitral valve.

3.14 Vortex Ring Formation During Mid and Late Diastole

At the onset of the separation of the leaflets ($t = 421ms$, B.3(16)), the twin coils coalesce and begin to create a vortex ring at the symmetry plane. The resulting jet moves down the left ventricle and recoils back toward the base (B.3(16) to B.3(19)). This vortex ring stretches circumferentially with the larger diameter in the septal side

of the left ventricle and the smaller diameter in the free wall side of the LV. During mid diastole (421 to 430 ms), the vortex core is located near the base (figures B.3(17) to B.3(19)). As the left ventricle expands, the vortex core moves down toward the apex (figures B.3(20) and B.3(21)). Figures B.3(17) to B.3(19) show that at t=424 ms, the high velocity region of the vortex is adjacent to the anterior wall of the left ventricle and it rotates clockwise as we progress to t= 427 ms and t=430 ms. At around t=500 ms, the incoming flow reaches its maximum value and the highest velocity (90 cm/s) at the opening of the valve is observed (figure B.3(20)). Also, Figures 3.21(1) and 3.21(2) show that the vortex core has the largest diameter at the symmetry plane and it becomes smaller toward the left ventricular wall. Moreover, the vortex is oriented to the top left of the left ventricle. Figure 3.21(3) also shows that another vortex exists behind the posterior leaflets with it axis of rotation perpendicular to the posterior leaflet but it later disappears. Figures 3.22 and 3.23 present the Z (long axis) and X (basal axis) position of the vortex core (occupying the left ventricle) during diastole. At the beginning of diastole (start of the twin coils explained in the 3.13), the vortex core moves toward the base. Then, as the mitral valve opens, the vortex core moves down and starts fluctuating up and down during the first wave of the diastole. Between the first and second waves the vortex core moves down slightly. With the start of the second wave, the vortex core position moves toward the apex with the lowest position at around the peak of the second diastolic wave (A wave). After deceleration of flow, the vortex core moves up.

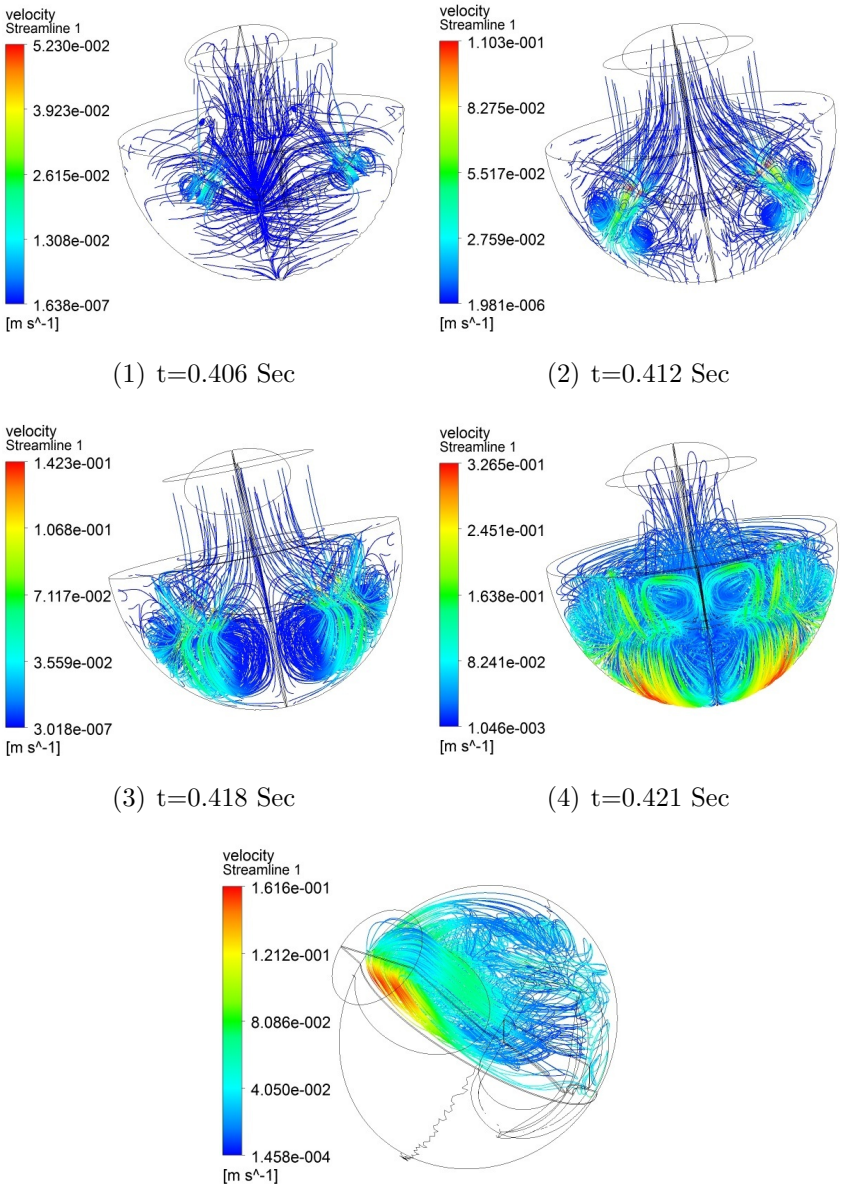

(1) t=0.406 Sec

(2) t=0.412 Sec

(3) t=0.418 Sec

(4) t=0.421 Sec

(5) t=0.424 Sec

Figure 3.20: 3D streamline of the blood flow in early diastole. SV=60 ml, HR=60 bpm.

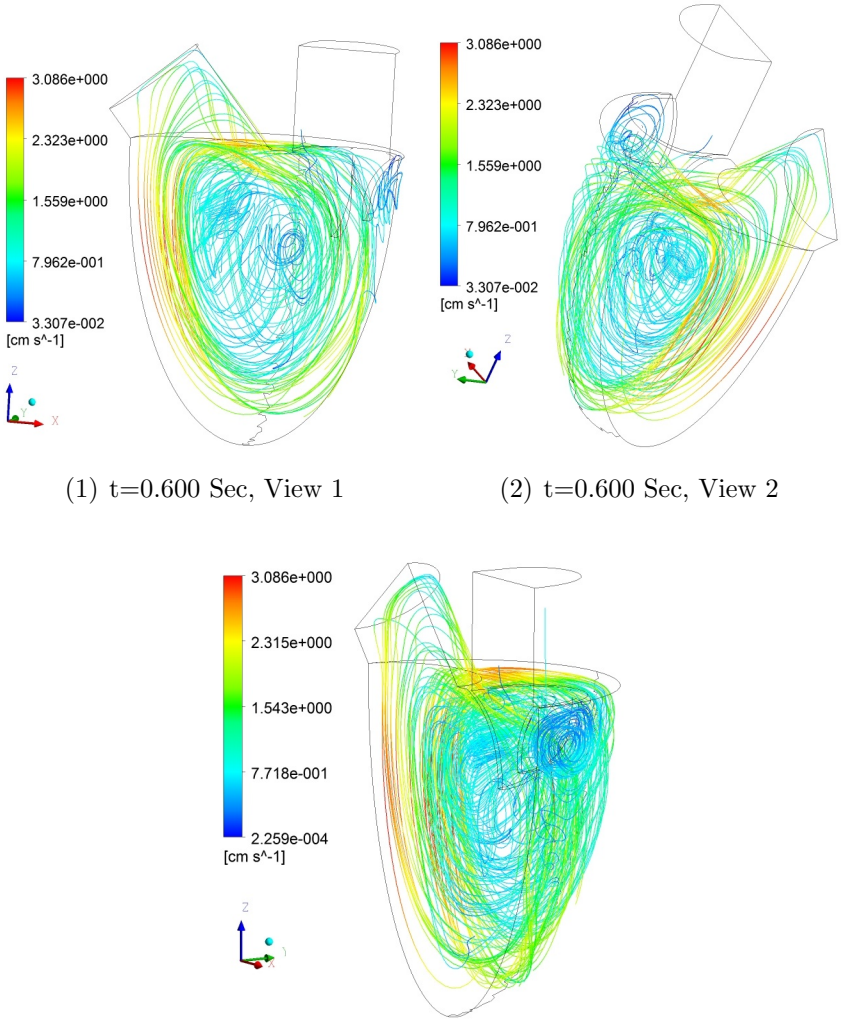

(1) t=0.600 Sec, View 1

(2) t=0.600 Sec, View 2

(3) t=0.600 Sec, View 3

Figure 3.21: 3D streamline of the blood flow in mid diastole at $t = 600ms$ from three views. SV=60 ml, HR=60 bpm.

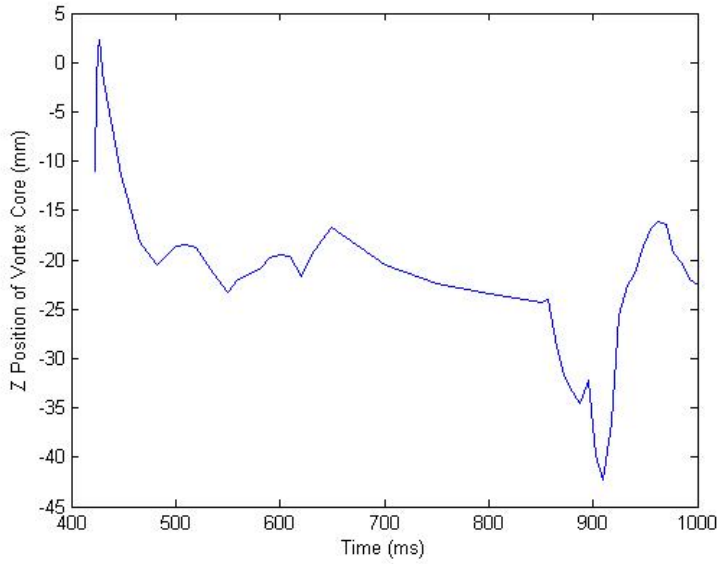

Figure 3.22: Z coordinate of vortex core position during diastole.

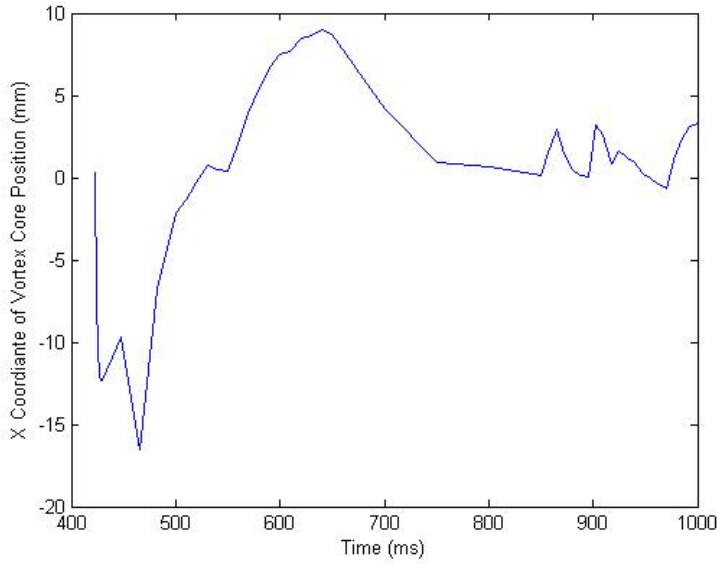

Figure 3.23: X coordinate of vortex core position during diastole.

3.15 Vortex Ring Formation Analysis

The hydrodynamic efficiency of the mitral valve and left ventricular filling based on critical vortex formation number presented by Gharib *et. al.* [35, 86] is further

discussed here. The theory states that the dynamic characteristics of the vortex formation are related to a non dimensional number called Critical Formation Number (FN). At this critical FN, the vortex ring reaches its maximum circulation. After this point, the auxiliary energy exerted on the vortex does not contribute to the size of vortex and it goes to the formation of trailing wakes. The vortex formation in the diastolic phase has been experimentally studied by Pierrakos *et. al.* [84] where they analyzed the efficiency of the mechanical valves. Here, the observations presented by Pierrakos to characterize the natural mitral valve as well as the left ventricular filling have been confirmed by the computational studies presented here.

Slug Flow Model (SFM) was used by Gharib *et. al.* [35, 35] to characterize the dynamics of vortex formation. SFM assumes that the flow is axisymmetric with uniform velocity profile and is incompressible. The vortex generated in the left ventricle is assumed axisymmetric. According to the SFM, the Formation Number is calculated by the following equation:

$$FN\,(t) = \frac{\int_{T_{bd}}^{t} U_{us}\,dt}{D_{MV}} \tag{3.1}$$

Where, U_{us} is the flow velocity upstream of the mitral valve, D_{MV} is the mitral valve diameter and T_{bd} is beginning of diastole time. Mitral flow rate is related to the U_{us} by:

$$Q_{MV} = U_{us}\,A_{MV} \tag{3.2}$$

Where, Q_{MV} and A_{MV} are the mitral flow rate and are respectively. Therefore

$$U_{us} = \frac{4Q_{MV}}{\pi D_{MV}^2} \tag{3.3}$$

Using equations 3.1 and 3.3 we conclude that:

$$FN(t) = \frac{4}{\pi D_{MV}^3}\int_{Tbd}^{t} Q_{LV}\,dt = \frac{4V_{LVd}(t)}{\pi D_{MV}^3} \tag{3.4}$$

Where V_{LVd} is left ventricular volume during diastole. From Chapter 2, we know the following equations for V_{LVd} in first and second waves of the diastole (E and A waves):

$$V_{LVd1} = Q_{LVdMax1}\left[\frac{T_{d1} - T_{bd}}{\pi}\right]\left[1 - \cos\left(\frac{t - T_{bd}}{T_{d1} - T_{bd}}\right)\right] \tag{3.5}$$

$$V_{LVd2} = Q_{LVdMax2}\left[\frac{T_{ed} - T_{d2}}{\pi}\right]\left[1 - \cos\left(\frac{t - T_{d2}}{T_{ed} - T_{d2}}\right)\right] \tag{3.6}$$

T_{bs}, T_{es}, T_{bd}, T_{d1}, T_{d2} and T_{ed} are the beginning of the systole, end systole, beginning of the diastole, end of left ventricular passive filling and beginning of the left atrial ejection. Table 3.4 presents the values of parameters used for calculation of FN. These values are for normal heart with heart rate (HR) of 60 bpm and stroke volume (SV) of 60 mL.

Table 3.4: Value of the parameters used for calculation of FN during diastole, HR=60 bpm, SV=60 mL

Parameter	Unit	Value
T_{bs}	ms	398
T_{es}	ms	232
T_{bd}	ms	396
T_{d1}	ms	655.6
T_{d2}	ms	861.2
T_{ed}	ms	1000
D_{MV}	cm	3.4

Figure 3.24 presents the calculated FN during diastole. According to Equation 3.4, FN exhibits the same trend as the volume curve. From beginning of diastole, the FN rises until the end of first wave. Then stays constant to the beginning of second wave at which starts rising again. The circulation of a vortex is calculated by integrating the vorticity over the area of the vortex:

$$\Gamma_{vortex} = \int_A \omega \, dA \tag{3.7}$$

where Γ_{vortex}, ω and A are the circulation, vorticity and area of the vortex respectively. Figure 3.25 demonstrates the variation of the circulation with FN during diastole. The graph shows the vortex circulation increases until the end of rapid filling at $FN = 1.89$ (first diastolic wave) and between the rapid filling and left atrial contraction the circulation drops down due to energy dissipation and then it increases from the beginning of atrial contraction and continues to increase up to the end of

diastole. Also, this graph shows that there is no maximum in both diastolic waves.

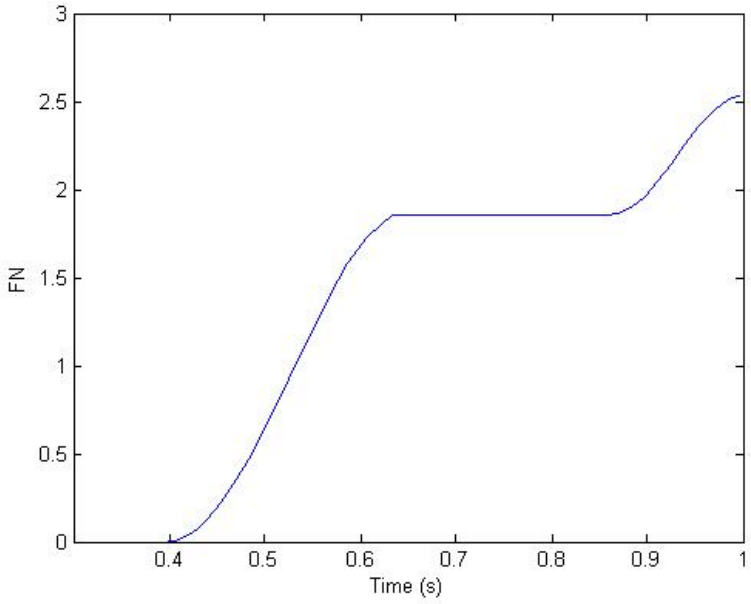

Figure 3.24: Formation Number (FN) during diastole.

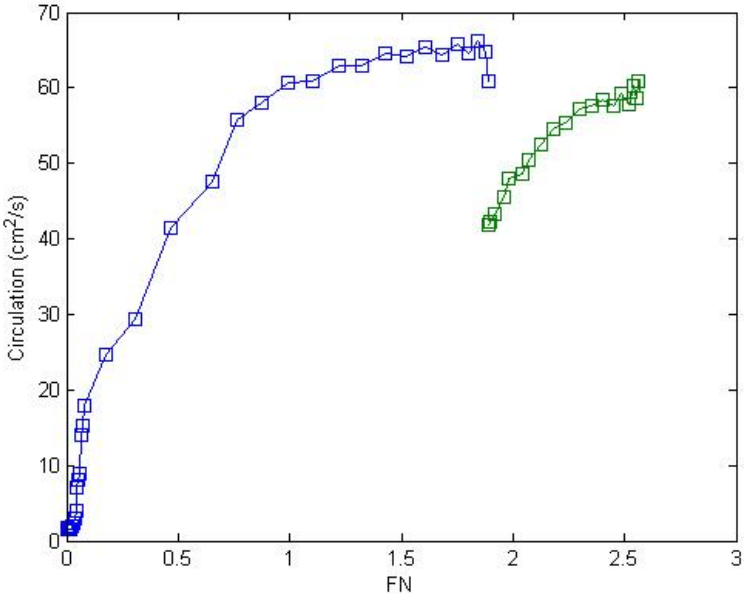

Figure 3.25: Circulation verses Formation Number (FN) during diastole.

The energy of the vortex is calculated from the following equation [94]:

$$E_{vortex} = \frac{1}{2} R \int_A \left(u^2 + v^2\right)\, dA \tag{3.8}$$

Where, E_{vortex}, u, v, A and R are energy, two components of velocity, the area and radius of the vortex in the symmetry plane, respectively. We calculated the energy of vortex on the symmetry plane and Figure 3.26 exhibits this graph as functions of formation number (FN). This figure shows that the vortex energy follows almost the same trend as the circulation graph (figure 3.25). We also presented the graph of diastolic left ventricular flow rate as functions of formation number in the figure 3.27. From analyzing the Figures 3.25, 3.26 and 3.27, it can be concluded that the circulation of the left ventricular vortex ring does not reach its critical capacity corresponding to critical formation number. This is the reason we do not observe any pinch off in the vortex ring during both waves. The only pinch off is between the rapid filling and atrial contraction because the incoming flow (as well as supplying energy) has been stopped temporarily.

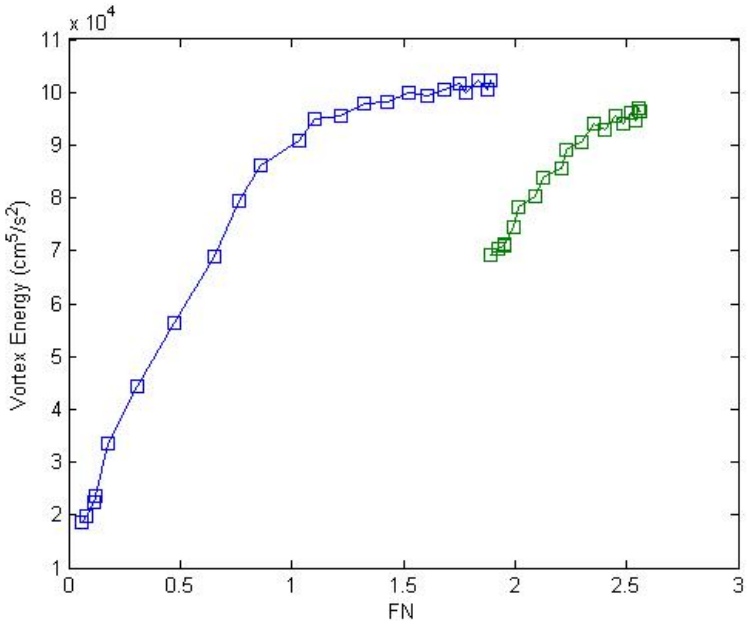

Figure 3.26: Vortex Energy verses Formation Number (FN) during diastole.

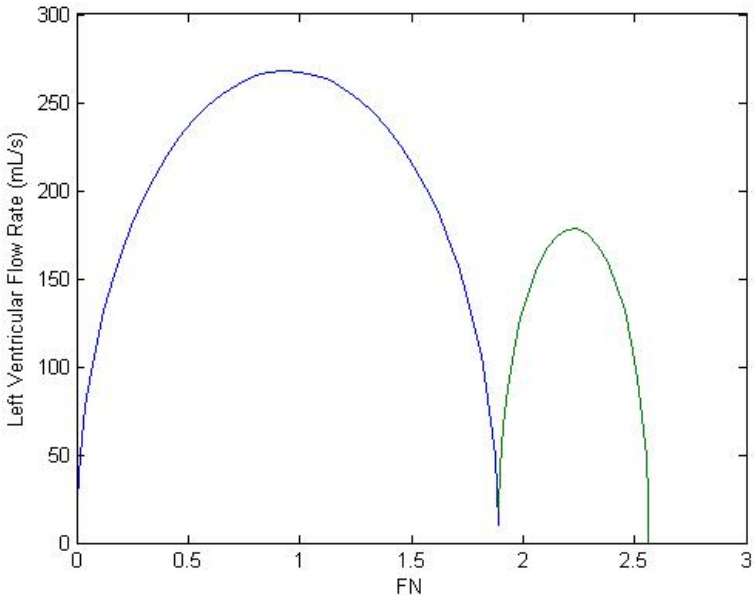

Figure 3.27: Left ventricular Flow Rate verses Formation Number (FN) during diastole.

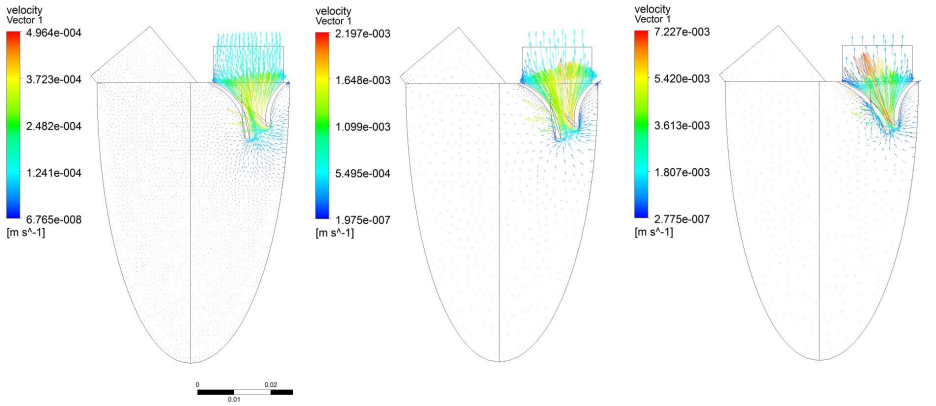

(1) t=0.005 Sec (2) t=0.010 Sec (3) t=0.015 Sec

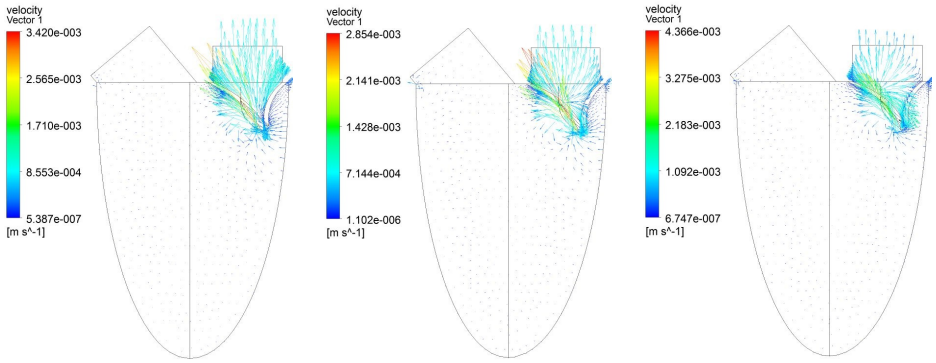

(4) t=0.020 Sec (5) t=0.025 Sec (6) t=0.030 Sec

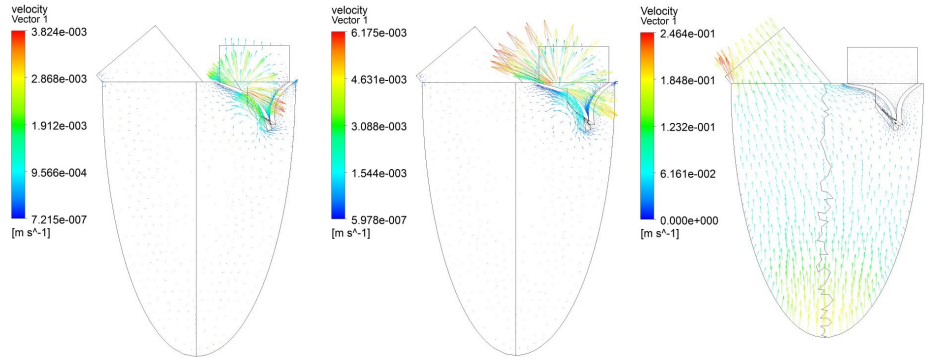

(7) t=0.035 Sec (8) t=0.039 Sec (9) t=0.065 Sec

Figure 3.28: Velocity contours in the long axis (symmetry) Plane. SV=60 ml, HR=60 bpm.

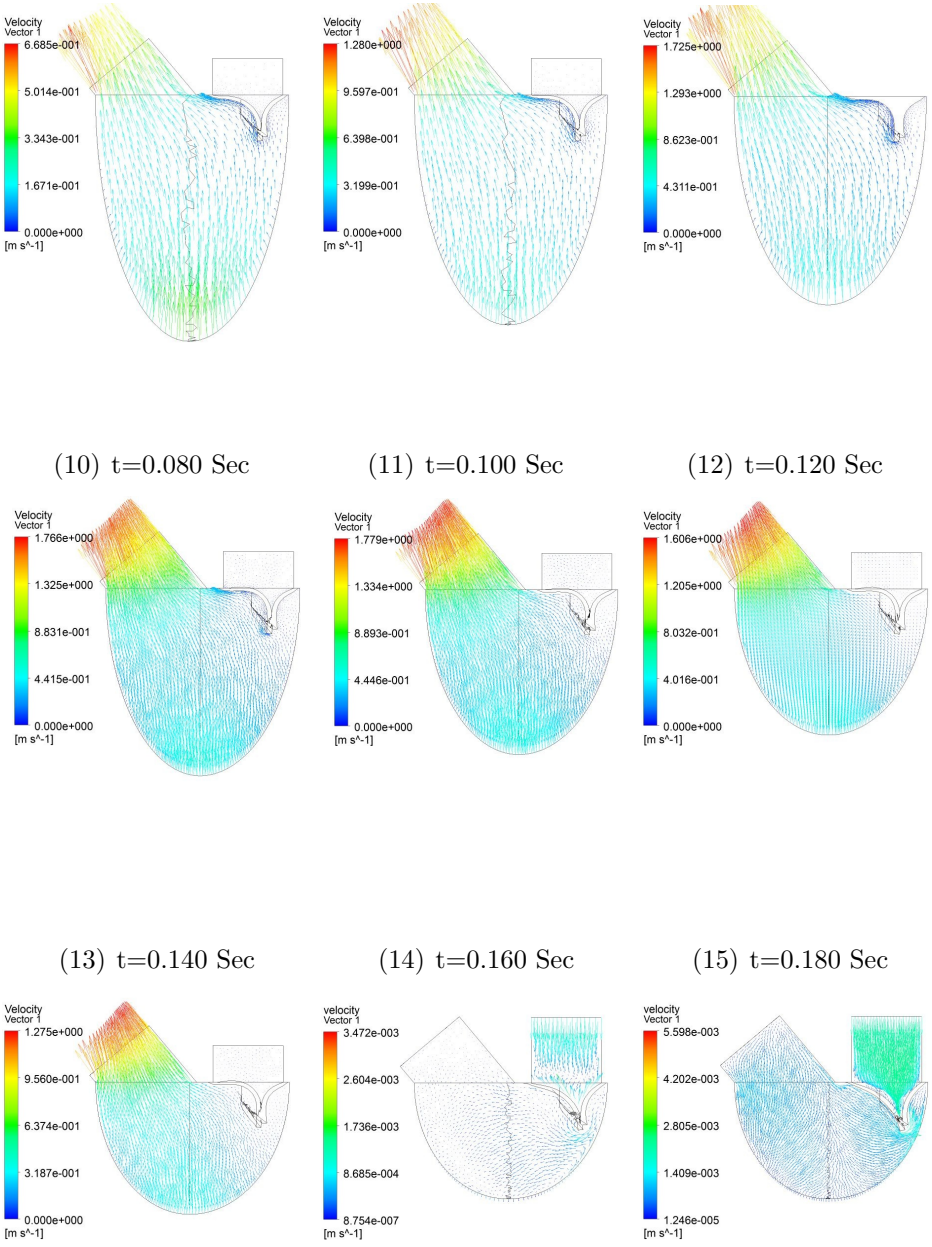

(10) t=0.080 Sec (11) t=0.100 Sec (12) t=0.120 Sec

(13) t=0.140 Sec (14) t=0.160 Sec (15) t=0.180 Sec

(16) t=0.200 Sec (17) t=0.406 Sec (18) t=0.412 Sec

Figure 3.28: Velocity contours in the long axis (symmetry) Plane. SV=60 ml, HR=60 bpm (cont).

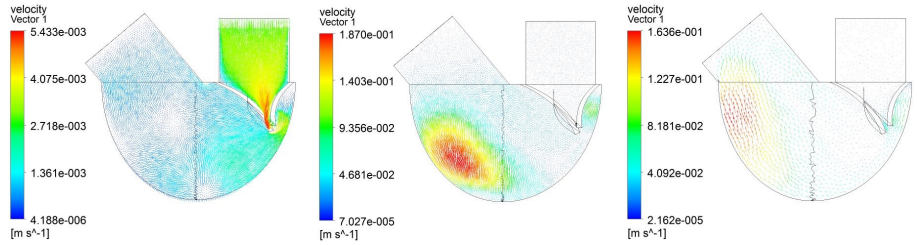

(19) t=0.418 Sec (20) t=0.421 Sec (21) t=0.424 Sec

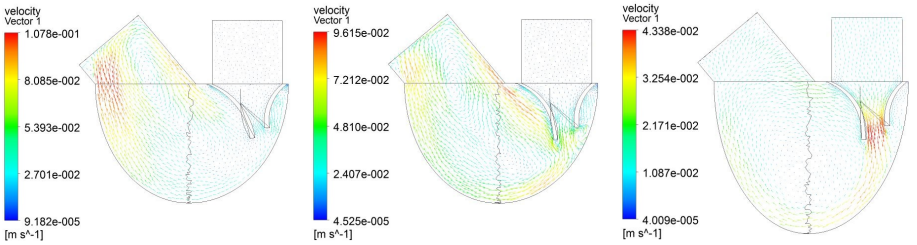

(22) t=0.427 Sec (23) t=0.430 Sec (24) t=0.500 Sec

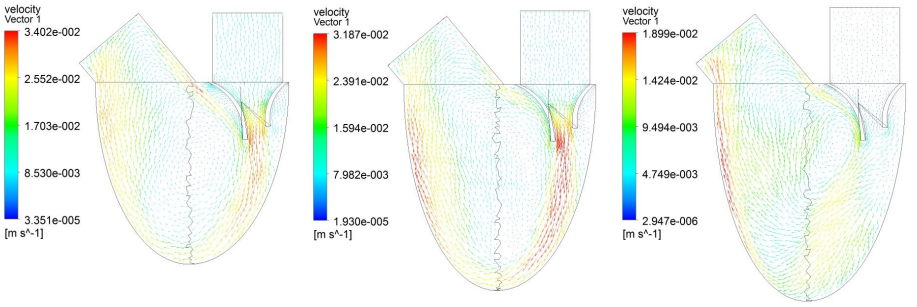

(25) t=0.550 Sec (26) t=0.600 Sec (27) t=0.650 Sec

Figure 3.28: Velocity contours in the long axis (symmetry) Plane. SV=60 ml, HR=60 bpm (cont).

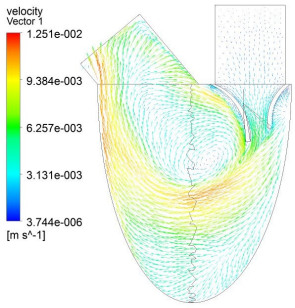

(28) t=0.700 Sec

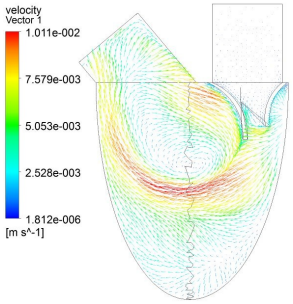

(29) t=0.750 Sec

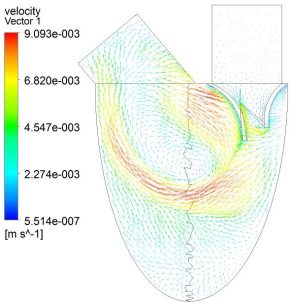

(30) t=0.800 Sec

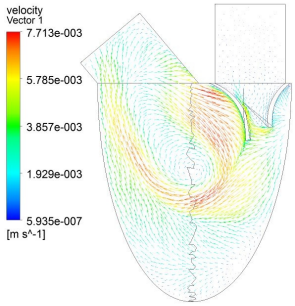

(31) t=0.850 Sec

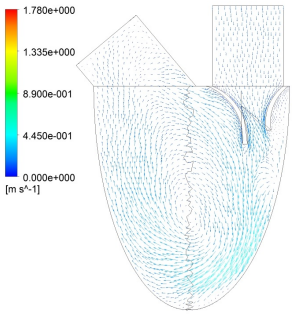

(32) t=0.8875 Sec

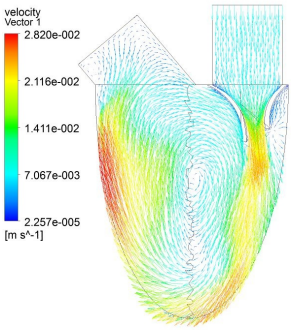

(33) t=0.925 Sec

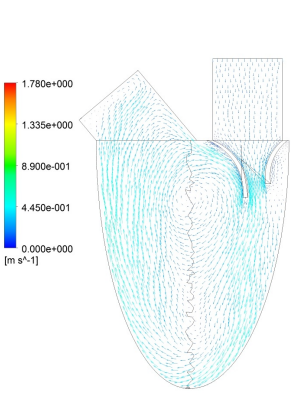

(34) t=0.9625 Sec

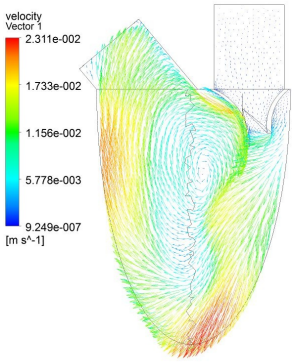

(35) t=0.1000 Sec

Figure 3.28: Velocity contours in the long axis (symmetry) Plane. SV=60 ml, HR=60 bpm(cont).

Chapter 4

FSI Simulation of The Mitral Valve In A Diseased Left Ventricle with Obstructive Hyperthrophic Cardiomyopathy

4.1 Introduction

Hypertrophic cardiomyopathy (HCM) is a genetic cardiac disease in which the septum is thickened (hypertrophied) creating a narrow passage (left ventricular out flow tract: LVOT) for blood flow out of the left ventricle [71]. The blood flow accelerates in the narrow passage and consequently the blood pressure drops down which causes the mitral valve open and consequently regurgitation occurs in the systole. In this disease,the anterior leaflet of the mitral valve moves toward the thickened septum and contacts the opposing bulged septum. This phenomena is called Systolic Anterior Motion (SAM) which causes the obstruction of the blood flow out of the LV in systole [70, 78, 39, 85, 103]. The purpose of this work is to model and investigate the SAM by means of computational fluid dynamics and fluid-structure interaction.

4.2 Geometry of The Left Ventricle With OHCM and Boundary Conditions

The geometry of the left ventricle with OHCM was constructed by subtracting two half ellipsoids from the normal left ventricle. Figure 4.1 presents assembly of the diseased left ventricle and mitral valve. In this case the end diastolic left ventricular volume (EDLVV) is 70 mL which is 41.6 percent less than its normal counterpart used in the chapter 3. We introduced the left ventricular and atrial pressures to the normal parts of the left ventricular walls and mitral aperture respectively. Also, the left ventricular flow rate was applied to the aortic aperture.

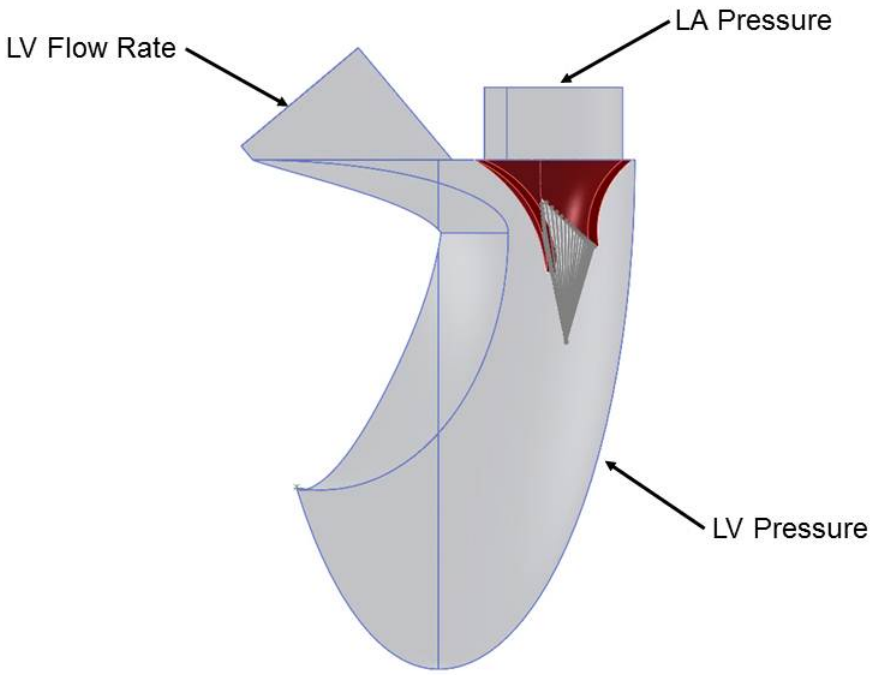

Figure 4.1: Assembly of LV with OHCM and Mitral Valve with chordaes

4.3 Results and Discussion

Early studies suggested the Venturi effect as the mechanism of SAM ([9], [77]). In the Venturi mechanism: (1) the thickened septum creates a narrow passage for outflow in systole, (2) the velocity of blood flow in systole increases in the narrow tract, (3) consequently, the pressure holding the anterior leaflet in place drops causing (5) the anterior leaflet deform into the LVOT and eventually have contact with the bulged septum. Our simulation demonstrates this mechanism (figures 4.8(1) to 4.8(28)).

4.3.1 Mitral valve Closure

We began the simulation at end of diastole when the mitral valve starts to close. Figures 4.8(1) to 4.8(9) present the closure phase of the mitral valve. In this phase we applied the left ventricular and atrial pressures to the normal walls of the left ventricle and mitral aperture respectively. Also, the aortic aperture is closed. In this phase the blood flow is initiated from high pressure regions (the left ventricular walls) and

converges toward the mitral valve opening. As the left ventricular pressure rises the mitral leaflet deform toward the left atrium. Coaptation of the mitral leaflets begins at $t = 15\,ms$ when the leaflets contact at the symmetry plane (long axis plane). The coaptation progresses until the $t = 30\,ms$ when the mitral valve completely closes.

4.3.2 Systolic Anterior Motion Analysis

At the beginning of systole ($t = 40\,ms$), we open the aortic orifice by applying systolic left ventricular flow rate to the aortic aperture. Figures 4.8(9) to 4.8(28) show that in this phase the blood flows into the left ventricle through the left ventricular walls and converges toward the outflow track where the pressure begin to drop down between the anterior leaflet and thickened septum. Figure 4.2 presents the average pressure on the left ventricular sides of the anterior and posterior leaflets. This graph shows that at the onset of systole ($t = 40\,ms$) the pressure on the left ventricular side of the anterior leaflet stop rising and approximately remains constant until $t = 70\,ms$. Between $t = 40\,ms$ to $t = 70\,ms$ the anterior leaflet continue to deform toward the left atrium with a slower rate than before and the pressure drop in the narrow passage is not high enough to reverse its deformation. At the $t = 70\,ms$ the anterior leaflet starts to deform back toward the left ventricle. Figure 4.2 show that while the pressure behind the anterior leaflet keeps dropping down, the pressure behind the posterior leaflet continue raising therefore, from $t = 70\,ms$ to $t = 100\,ms$, although the anterior leaflet deforms toward the thickened septum it keeps its contact with the posterior leaflet since the posterior leaflet deforms toward the left atrium (figure 4.8(13) to 4.8(17)). Figure 4.2 depicts the average contact pressure between the anterior leaflet and posterior/septum with respect to time. After the beginning of coaptation the average contact pressure fluctuates until the full contact ($t = 40\,ms$, start of systole). After this point the contact pressure stabilizes until $t = 70\,ms$. From $t = 70\,ms$ to $t = 100\,ms$ the contact pressure reduces since the anterior leaflet begin to deform back while keeping its contact with the posterior leaflet. At $t = 100\,ms$ the pressure on the left ventricular side of the anterior leaflet drops bellow the pressure on the atrial side (see figure 4.2) and anterior leaflet suddenly separates from posterior leaflet (see figure 4.8(17)). After this point the contact pressure is zero until $t = 110\,ms$ from which the contact between the anterior leaflet and thickened septum starts. Figures 4.8(17) to 4.8(20) show that between $t = 100\,ms$ to $t = 110\,ms$ the anterior leaflet deforms toward the septum and creates an opening for the blood to flow to the left atrium. Figures 4.6(1) to 4.6(3) display flow streamlines from $t = 105\,ms$ to $t = 110\,ms$. The

streamlines show a small vortex is formed from $t = 105\,ms$ besides the atrial side of the posterior leaflet and as the flow rate increases this vortex becomes larger. Also, the vorticity contours confirms the formation of this vortex (4.6(1) to 4.6(3)). The shear stress on the surfaces of the mitral leaflets were displayed in the figure 4.4. From the beginning of the SAM ($t = 100\,ms$), the shear stress on the LV and LA sides of the anterior leaflet (ALV and ALA) increases and becomes maximum at the peak systole ($t = 130\,ms$). The graph (figure 4.4) show that the order of shear stress on the ALV is at least 2.5 times larger than the shear stress on the rest of surfaces. This is due to high magnitude of velocity in the outflow track. The shear stress on the LV side of the posterior leaflet (PLV) remains almost constant while the shear stress on its atrial (PLA) side initially increases and reaches the maximum at $t = 107.5\,ms$ and decreases afterward. As we mentioned earlier at $t = 107.5\,ms$ a vortex is formed besides the PLA which contributes to the reduction of the shear stress on this surface. Figure 4.5 presents the maximum velocity in the outflow track with respect to time. As expected, the maximum velocity increases and reaches its maximum at the peak systole ($t = 130\,ms$).

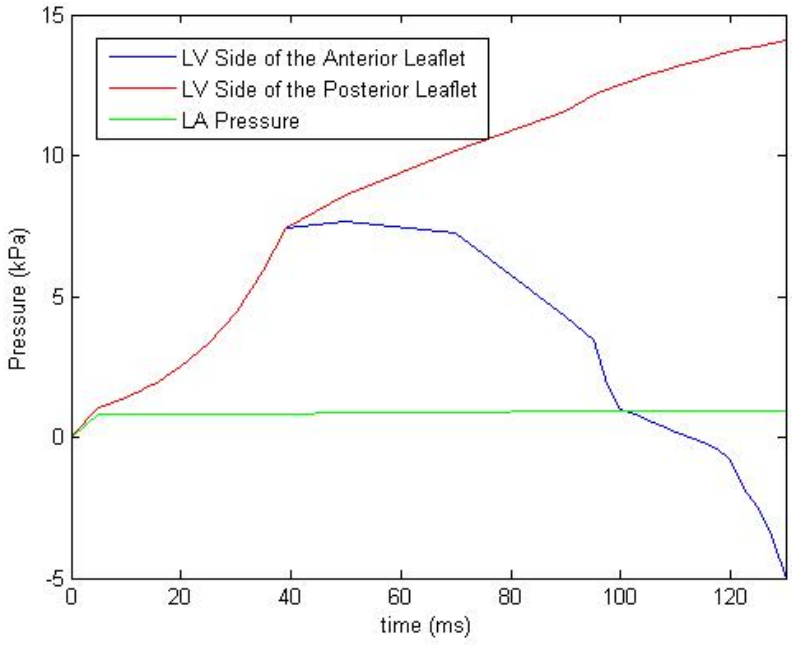

Figure 4.2: Average pressures on the surfaces of mitral valve.

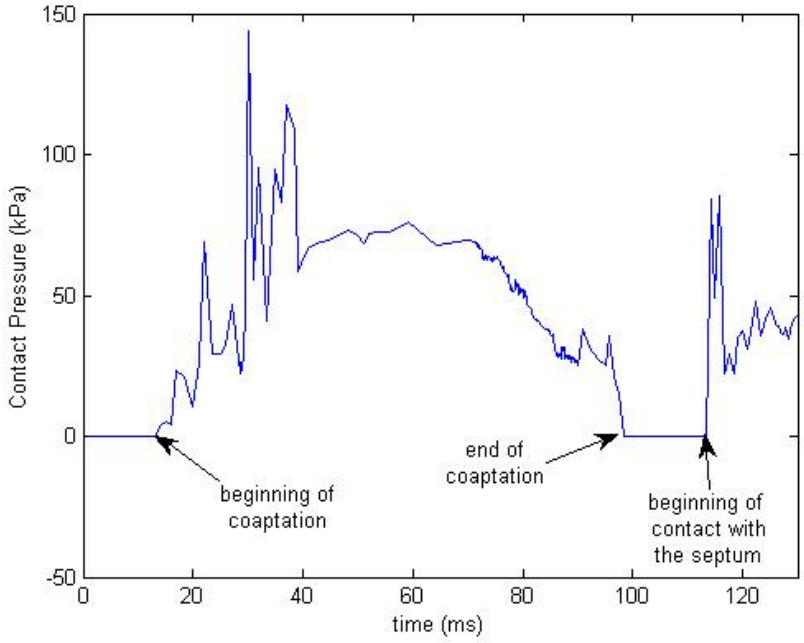

Figure 4.3: Average contact pressure during systole

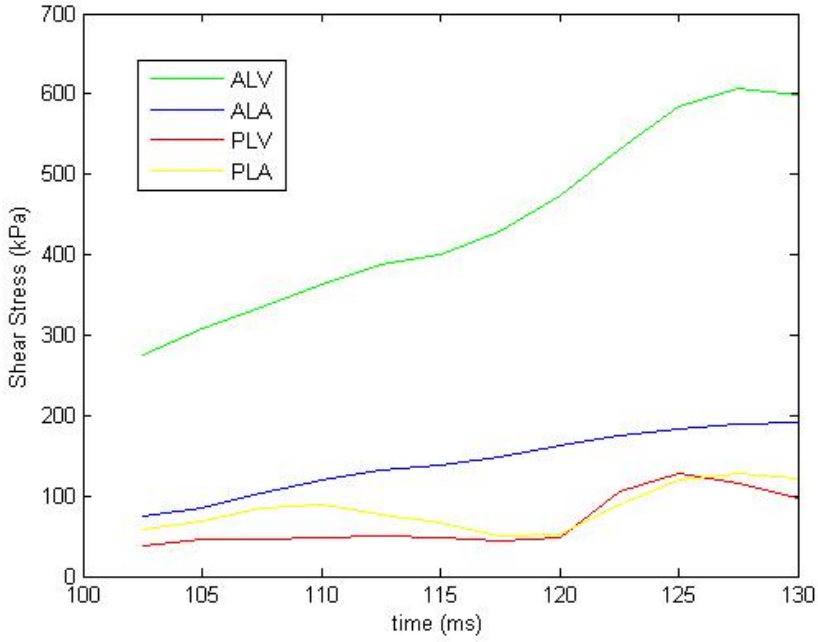

Figure 4.4: Shear stress. ALV: LV side of anterior leaflet, ALA: Atrial side of anterior leaflet, PLV: LV side of posterior leaflet, PLA: Atrial side of posterior leaflet

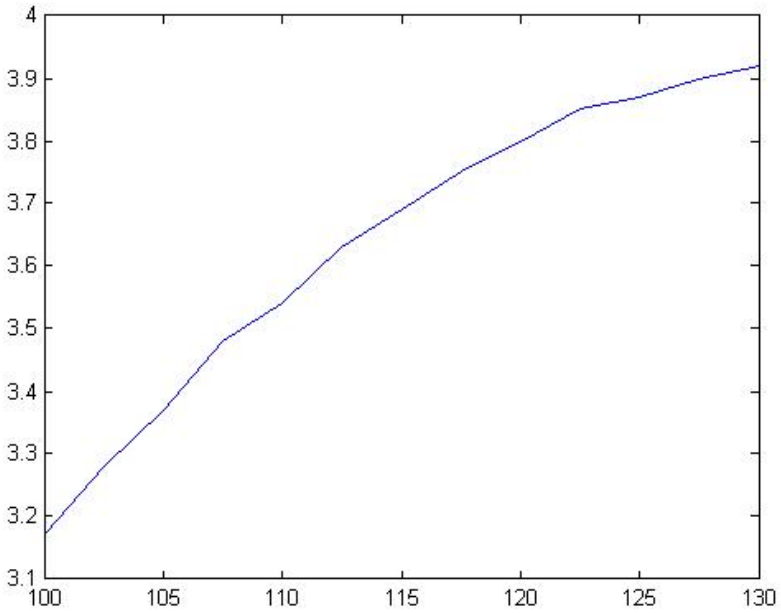

Figure 4.5: Maximum velocity in the outflow track.

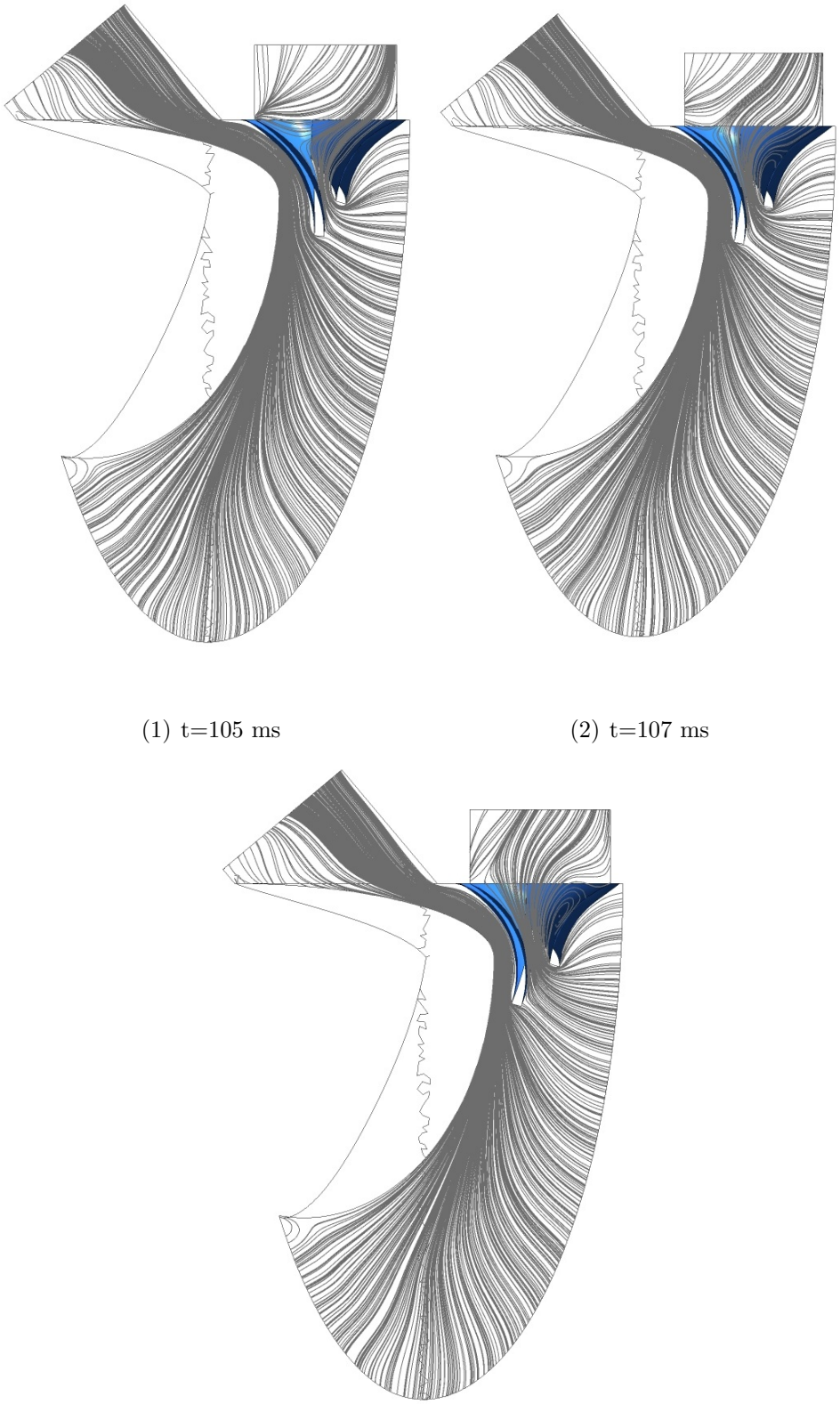

(1) t=105 ms

(2) t=107 ms

(3) t=110 ms

Figure 4.6: Streamlines at symmetry plane

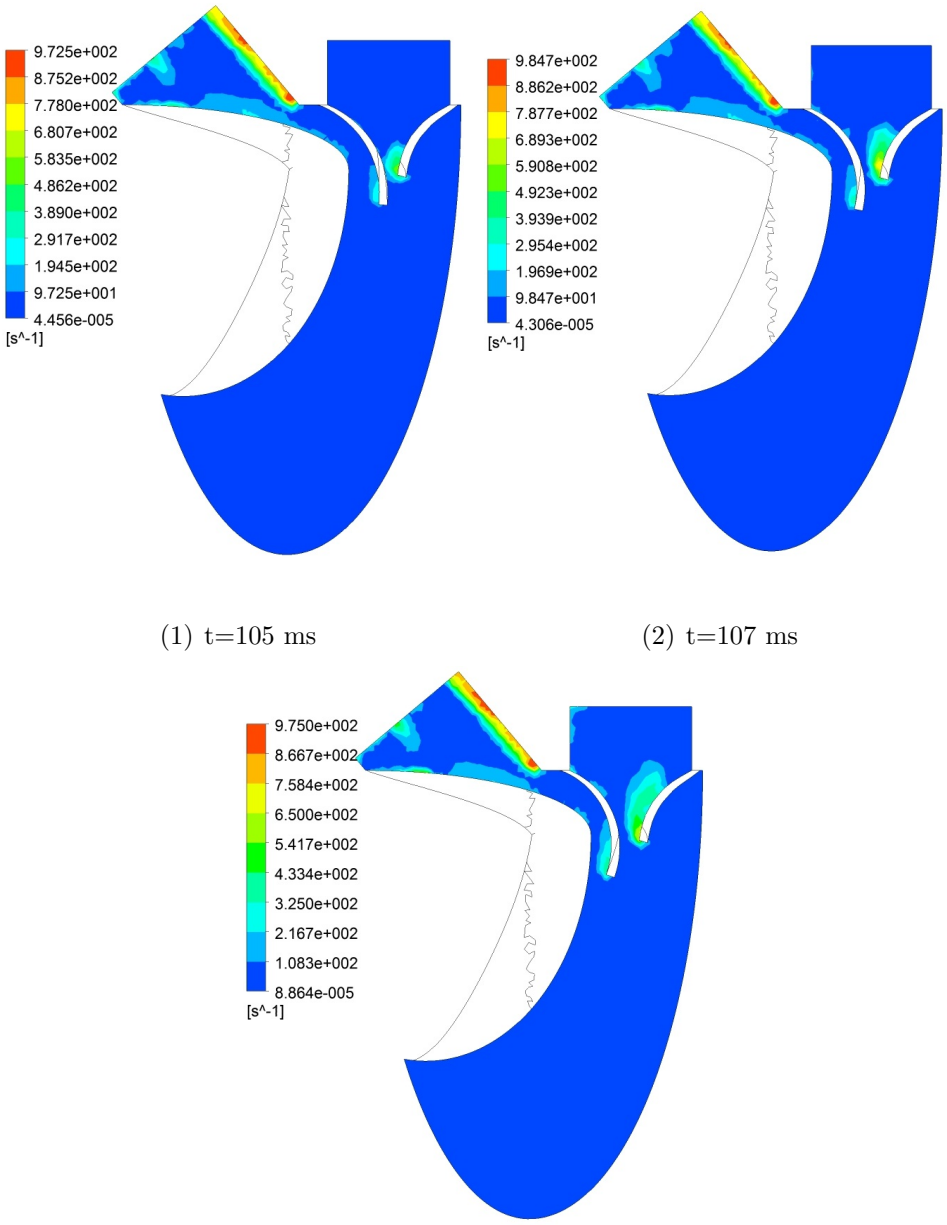

(1) t=105 ms (2) t=107 ms

(3) t=110 ms

Figure 4.7: Vorticity contours at symmetry plane

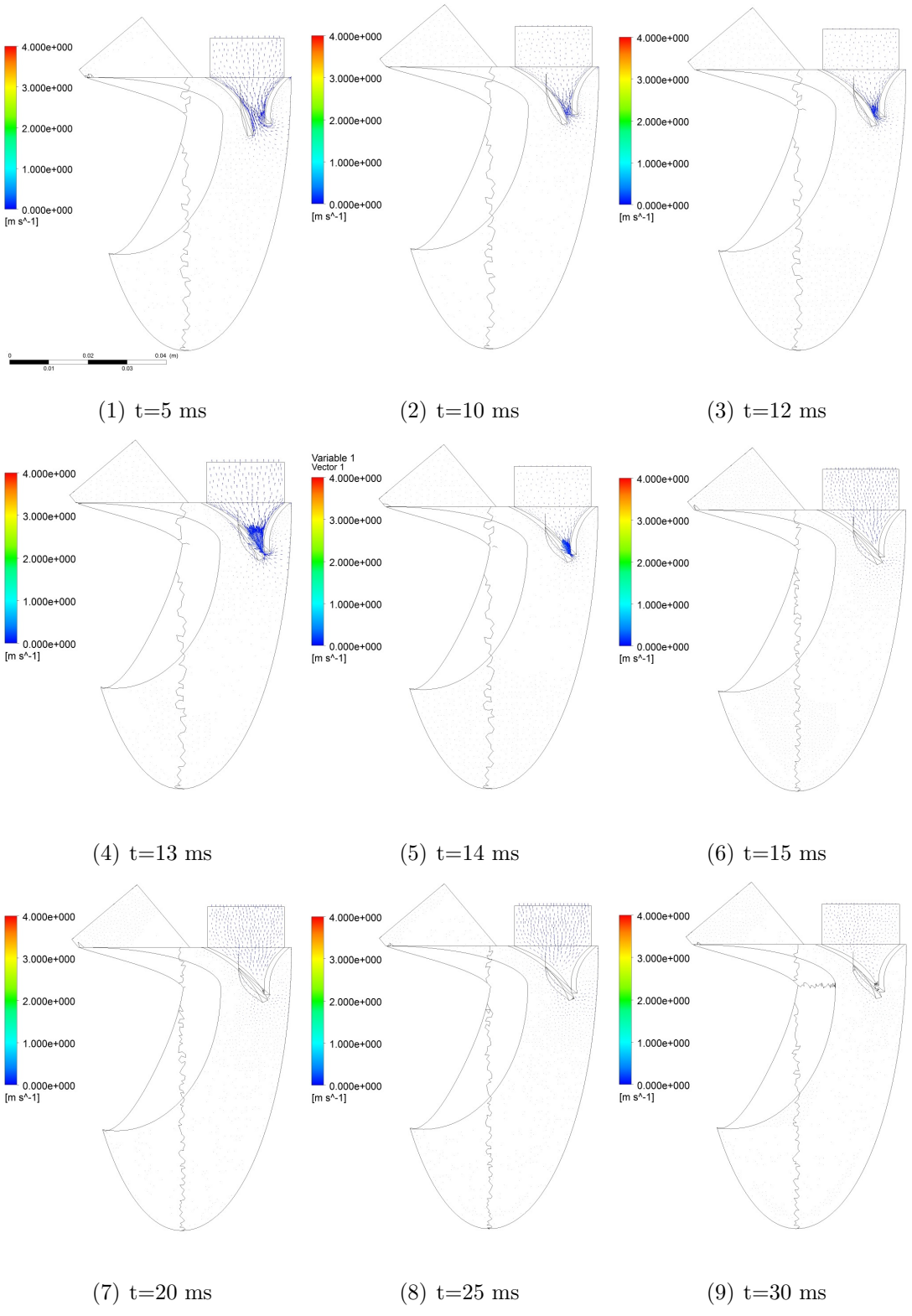

(1) t=5 ms (2) t=10 ms (3) t=12 ms

(4) t=13 ms (5) t=14 ms (6) t=15 ms

(7) t=20 ms (8) t=25 ms (9) t=30 ms

Figure 4.8: Velocity vectors at different time steps during systole

.

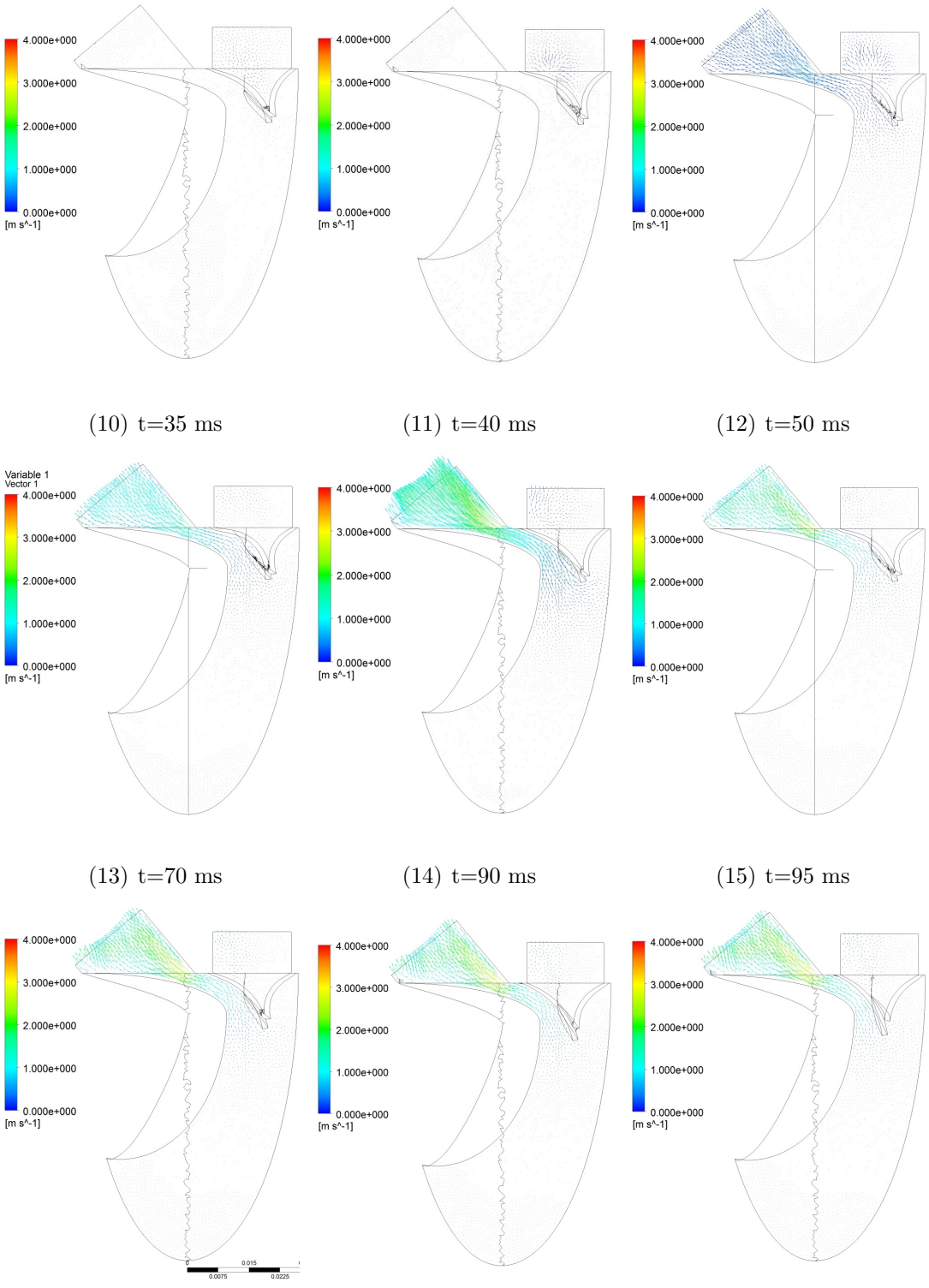

(10) t=35 ms (11) t=40 ms (12) t=50 ms

(13) t=70 ms (14) t=90 ms (15) t=95 ms

(16) t=97 ms (17) t=100 ms (18) t=102 ms

Figure 4.8: Velocity vectors at different time steps during systole (cont).

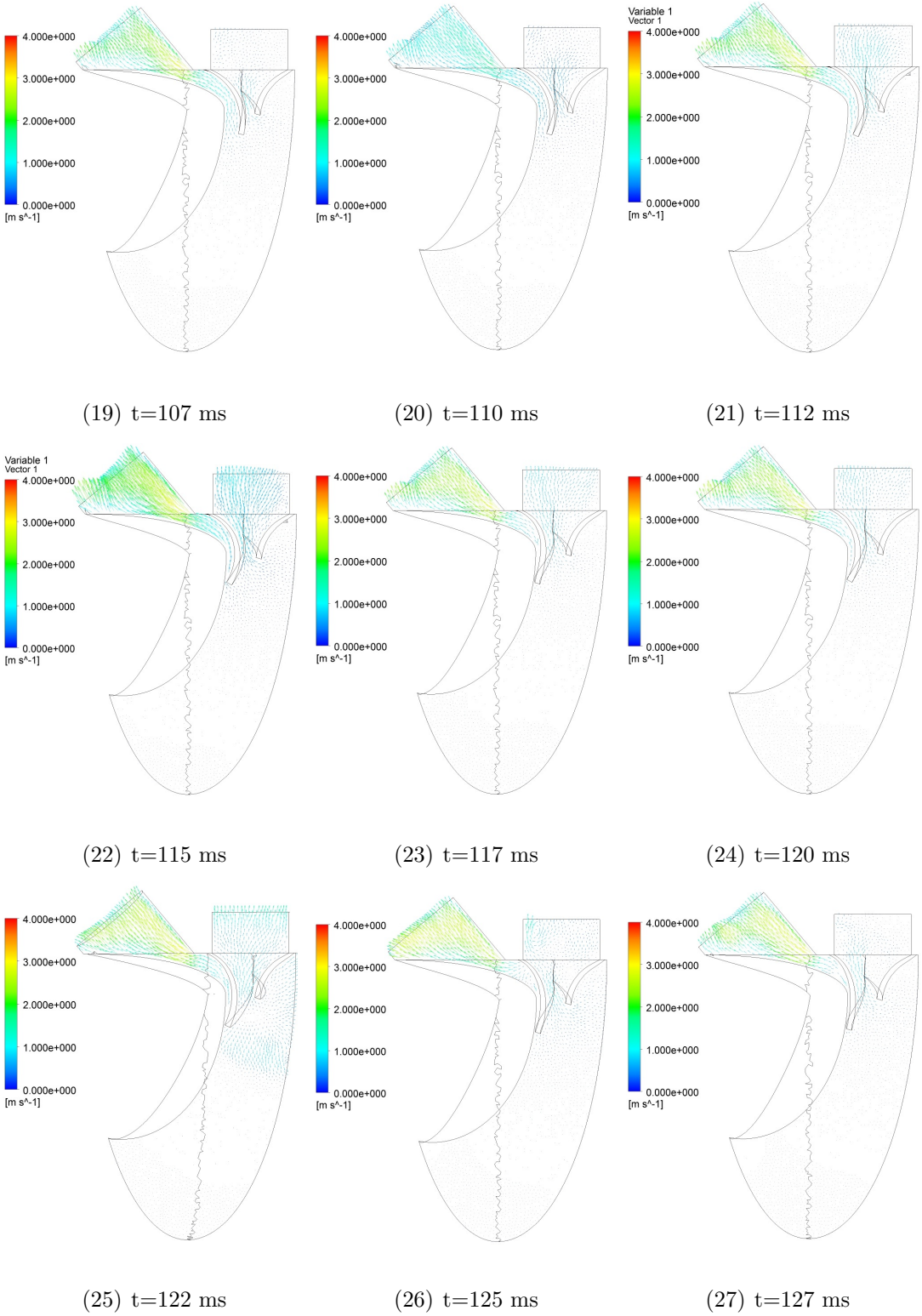

(19) t=107 ms (20) t=110 ms (21) t=112 ms

(22) t=115 ms (23) t=117 ms (24) t=120 ms

(25) t=122 ms (26) t=125 ms (27) t=127 ms

Figure 4.8: Velocity vectors at different time steps during systole (cont).

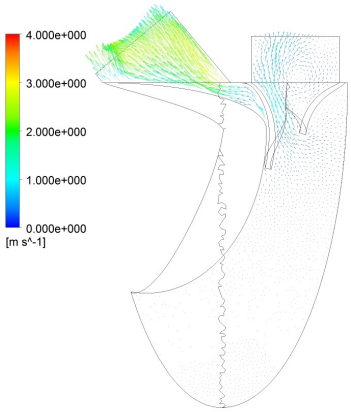

(28) t=130 ms

Figure 4.8: Velocity vectors at different time steps during systole

Chapter 5

Fluid-Structure Interaction Analysis of a New Accelerated Durability Tester for Prosthetic Heart Valves

5.1 Introduction

Prosthetic Heart Valve (PHV)s are unique in essence that, they must be durable for over millions of cycles and failure to do so, may cause the user's death. To ensure the durability requirements, PHV's must undergo several cycles of vitro tests prior to implantation. Also, durability data is used by heart valve manufacturers to improve their PHV designs [19]. The durability of prosthetic heart valves is assessed by accelerated fatigue testing apparatus. Throughout the years, several concepts of accelerated testers have been developed, including hydraulic cycling, pneumatic cycling, variations of mechanical cycling and combinations of them. Among the ones mentioned earlier, the hydraulic method is the primary method of conducting durability tests [30]. The test must complete a full cycle which means that the valve opens and closes completely [104]. The main challenge is that by increasing the cycling frequency the chance reaching full valve cycle decreases [25]. In other words, increasing the cycling rate reduces the accumulation of the strain applied to the valve in a cycle. According to [30], the accelerated test produces severe conditions for PHVs (comparing to real clinical conditions) due to imposing extra pressure in order to achieve full valve cycle. There are various standards for the fatigue test of MHV, among them the International Standard Organization (ISO) 5840 [79], Food and Drug Administration (FDA) Replacement Heart Valve Guidance [29] and CEN Proposed Standard EN 12006-1 [34] are the most used ones where, the expected material property and accelerated fatigue test features were covered. Up today, the main models of accelerated fatigue

testers which meet the above standards are: Rowan Ash (Rowan Ash Ltd. Sheffield, UK), Helmholtz (Helmholtz Institute, Aachen, Germany), Dynatek (Dynatek Laboratories, Inc., Galena, MO, USA) and Shelhigh (Shelhigh Inc., Hartsdale, NY, USA). None of these models simulate the real physiological conditions [25]. According to ISO 5840 [79], a tester should be able to examine the durability of a mechanical valve for 400 million cycles and a biological valve for 200 million cycles. Tests should be performed between 8 to 15 hertz with the target differential pressure of higher than 100 mmHg for aortic valve. Furthermore, the tester should be capable of testing at least 5 valves simultaneously. The aim of the present proposal is developing a Computational Fluid Dynamics (CFD) model to simulate the flow inside the durability tester and thought the valve. The results of this simulation will be used to improve the current design.

5.2 Objectives

A new concept of accelerated durability tester was developed by ViVitro Labs and the objective of this project is to simulate the fluid flow inside the tester and through the PHV. The results of this simulation will be used to improve the initial conceptual design and also this will be an attempt to examine if we can use results of CFD instead of hydrodynamic experiments for submission to FDA.

5.3 Conceptual Design of the Apparatus

As we said earlier, the ViVtro Labs has developed a new concept for accelerated durability tester which includes a impeller to flow the fluid bidirectional through the PHV (Figure 5.1). The impeller (which is driven by a servomotor) spins clock wise in half period to close the valve (the red vectors demonstrate the direction of the fluid) and counter clock wise in the other half to open the valve (the blue vectors).

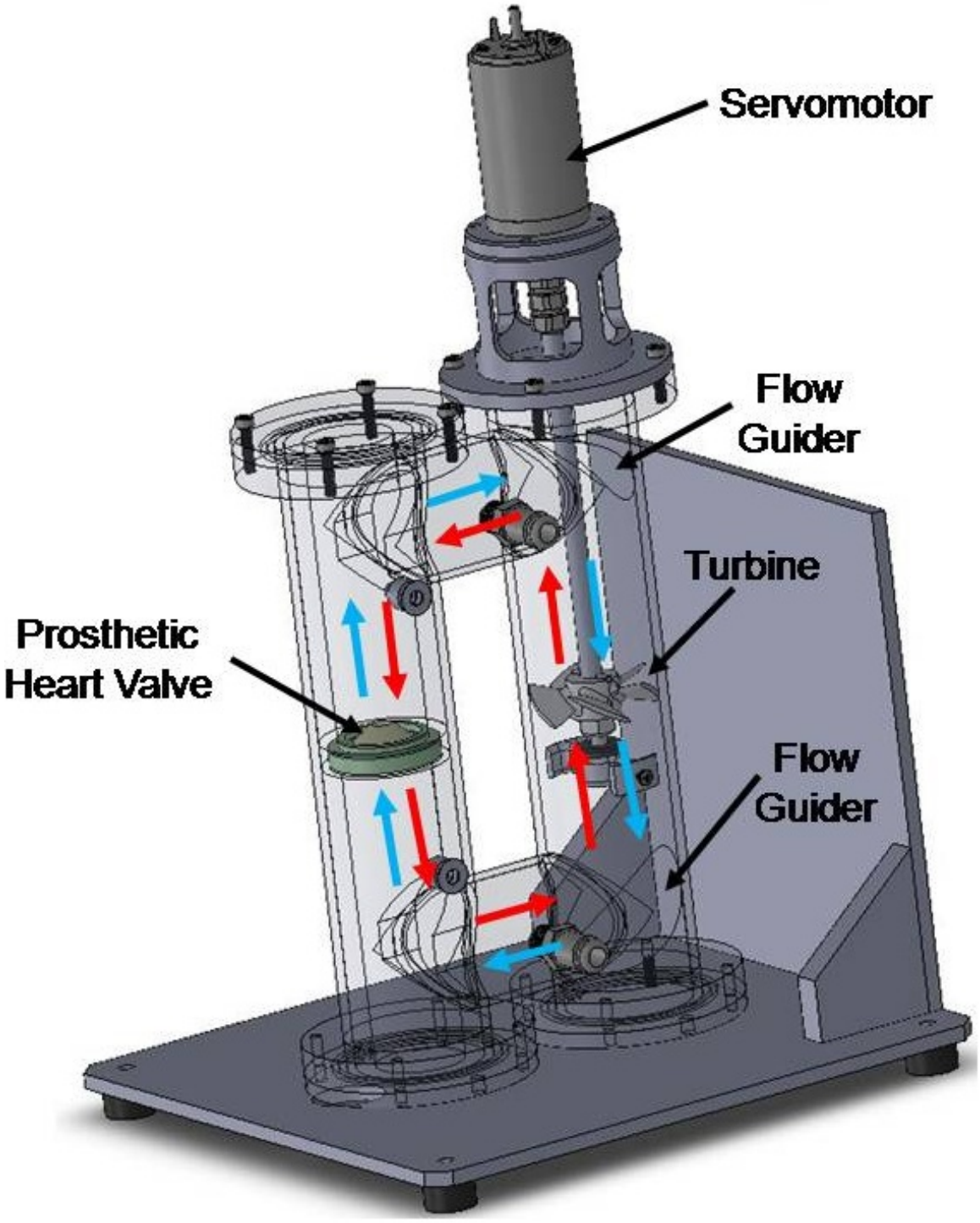

Figure 5.1: Assembly of the new accelerated durability equipment

5.4 Geometry of the Valve

Figure 5.2 shows the geometry of the bi-leaflet prosthetic valve which will be used for CFD analysis. The valve includes inner and outer rings and leaflets.

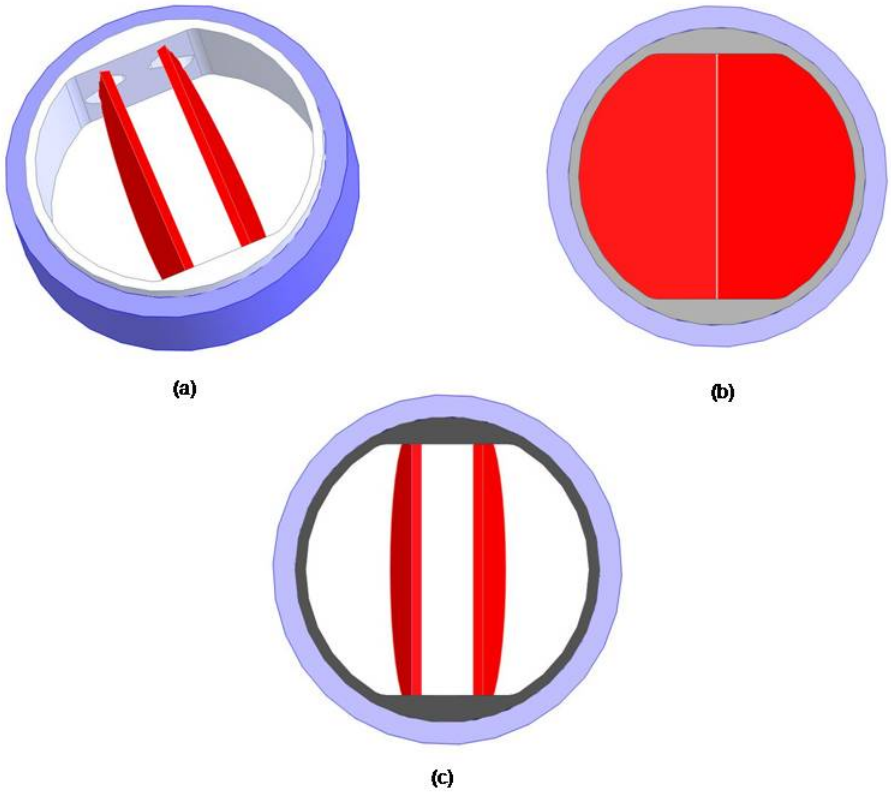

Figure 5.2: (a) Oblique view of the geometry of the bi-leaflet prosthetic valve, (b) and (c) valve closed and open respectively.

5.5 Fluid-Solid Interaction Procedure

Weak coupling of fluid-solid interaction (FSI) will be employed to transfer the motion of the impeller to the fluid and also the pressure of the fluid to the valve. Figure 5.3 demonstrated the FSI algorithm briefly.

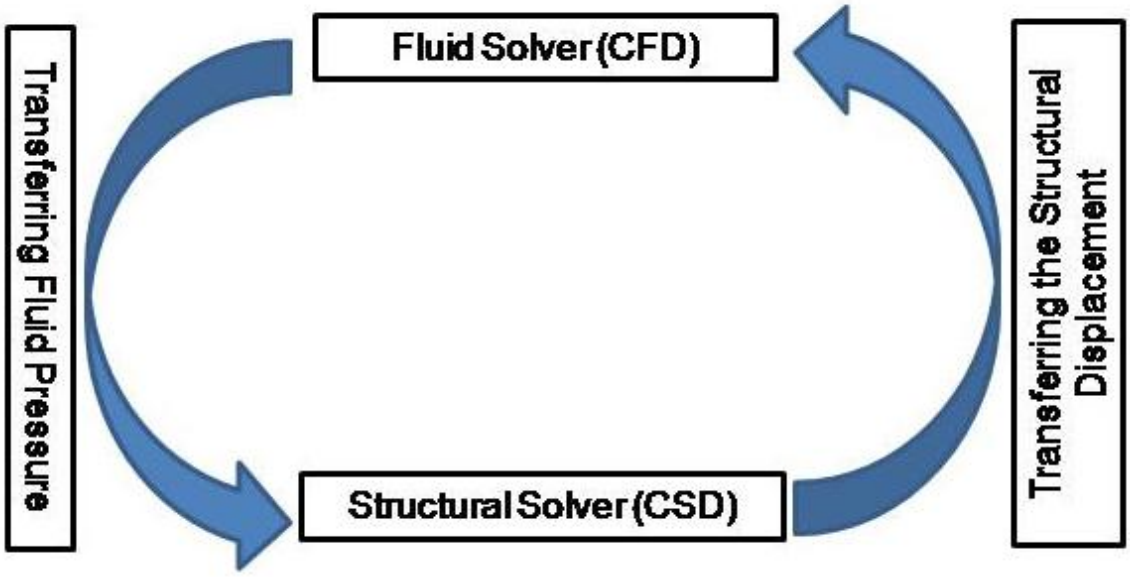

Figure 5.3: Weak Coupling Fluid-Structure Interaction Procedure.

In this procedure, the fluid and structural models are solved by two separate solvers and pressure is transfered to the structure and deformation of the structure is transfered to the fluid domain and the fluid mesh is moved accordingly. For this study we will use ANSYS CFX package for fluid solver and mesh movement and we will write a program to calculate the dynamic rigid body motion of the valve.

5.6 Computational Fluid Dynamics (CFD)

Continuity and Navier-Stokes equations (equations 5.1 to 5.4) in unsteady, incompressible, laminar and Newtonian form will be solved with Finite Element method using ANSYS CFX package.

ANSYS ICEM package will be employed for discretization of the spatial domain using mixture of hexahedral and tetrahedral elements for meshing (see figure 5.4).

$$\frac{\partial \rho}{\partial \mathrm{t}} + \frac{\partial(\rho \mathrm{u_x})}{\partial \mathrm{x}} + \frac{\partial(\rho \mathrm{u_y})}{\partial \mathrm{y}} + \frac{\partial(\rho \mathrm{u_z})}{\partial \mathrm{z}} = 0 \tag{5.1}$$

$$\rho\left(\frac{\partial \mathrm{u_x}}{\partial \mathrm{t}}+\mathrm{u_x}\frac{\partial \mathrm{u_x}}{\partial \mathrm{x}}+\mathrm{u_y}\frac{\partial \mathrm{u_x}}{\partial \mathrm{y}}+\mathrm{u_z}\frac{\partial \mathrm{u_x}}{\partial \mathrm{z}}\right)= -\frac{\partial \mathrm{p}}{\partial \mathrm{x}}+\mu\left(\frac{\partial^2 \mathrm{u_x}}{\mathrm{x}^2}+\frac{\partial^2 \mathrm{u_x}}{\mathrm{y}^2}+\frac{\partial^2 \mathrm{u_x}}{\mathrm{z}^2}\right) \tag{5.2}$$

$$\rho\left(\frac{\partial \mathrm{u_y}}{\partial \mathrm{t}}+\mathrm{u_x}\frac{\partial \mathrm{u_y}}{\partial \mathrm{x}}+\mathrm{u_y}\frac{\partial \mathrm{u_y}}{\partial \mathrm{y}}+\mathrm{u_z}\frac{\partial \mathrm{u_y}}{\partial \mathrm{z}}\right)= -\frac{\partial \mathrm{p}}{\partial \mathrm{y}}+\mu\left(\frac{\partial^2 \mathrm{u_y}}{\mathrm{x}^2}+\frac{\partial^2 \mathrm{u_y}}{\mathrm{y}^2}+\frac{\partial^2 \mathrm{u_y}}{\mathrm{z}^2}\right) \tag{5.3}$$

$$\rho\left(\frac{\partial \mathrm{u_z}}{\partial \mathrm{t}}+\mathrm{u_x}\frac{\partial \mathrm{u_z}}{\partial \mathrm{x}}+\mathrm{u_y}\frac{\partial \mathrm{u_z}}{\partial \mathrm{y}}+\mathrm{u_z}\frac{\partial \mathrm{u_z}}{\partial \mathrm{z}}\right)= -\frac{\partial \mathrm{p}}{\partial \mathrm{z}}+\mu\left(\frac{\partial^2 \mathrm{u_z}}{\mathrm{x}^2}+\frac{\partial^2 \mathrm{u_z}}{\mathrm{y}^2}+\frac{\partial^2 \mathrm{u_z}}{\mathrm{z}^2}\right) \tag{5.4}$$

Where u_x, u_y and u_z are components of velocity, p pressure, ρ and μ are density and viscosity of the testing fluid which are 1060 kg/m^3 and 4 $mPa.s$

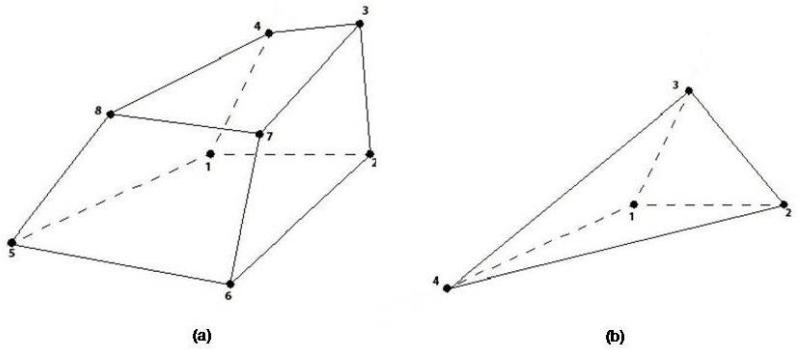

Figure 5.4: (a) Hexahedral and (b) Thetrahedral elements will be used to mesh the fluid domain.

5.7 Mesh Movement

According to the FSI procedure (figure 5.7) the fluid mesh must move according to the solid (valve leaflets) displacement at each time step. This is performed by employing dynamic mesh model of the ANSYS CFX package. In this model, the position of each node will be determined by calculating the displacement diffusion. The displacements

applied on the boundaries are diffused to other mesh nodes by solving the diffusion equation:

$$\nabla \left(\mathrm{K_{dis}} . \nabla \lambda \right) = 0 \tag{5.5}$$

In this equation, λ is the displacement relative to the previous mesh locations and K_{dis} is the mesh stiffness, which determines the degree to which nodes move together. The displacement diffusion model is designed to preserve the relative mesh distribution of the initial mesh. For example, if the initial mesh is relatively fine in certain regions of the domain, then it will remain relatively fine after solving the displacement diffusion equation.

5.8 Boundary Conditions

We have two types boundary conditions: Wall and fluid-solid interaction (FSI). Figure 5.6 presents the boundary conditions for CFD analysis. The fluid velocity will be set to zero at the surfaces with no-slip wall. The angular velocity of the impeller obeys the following equations:

$$\omega = \omega_{\max} \sin \left(\pi \mathrm{ft} \right) \tag{5.6}$$

Where, ω, $\omega_{\max}$, f are the angular velocity, amplitude and frequency of the impeller. We cab obtain the angular displacement of the impeller from:

$$\theta = \int \omega \mathrm{dt} \tag{5.7}$$

Substituting ω from 5.6 into 5.7 we will calculate the angular displacement as:

$$\theta = -\pi \mathrm{f} \omega_{\max} \cos \left(\pi \mathrm{ft} \right) + \mathrm{C} \tag{5.8}$$

Including the initial boundary condition of $\theta \left(\mathrm{t} = 0 \right) = 0$ we will have: $\mathrm{C} = \pi \mathrm{f} \omega_{\max}$. Therefore:

$$\theta = \pi \mathrm{f} \omega_{\max} \left[1 - \cos \left(\pi \mathrm{ft} \right) \right] \tag{5.9}$$

From equations 5.6 and 5.9 we conclude that:

$$\omega_{\max} = \frac{\theta_{\max}}{2 \pi \mathrm{f}} \tag{5.10}$$

Figure 5.5 presents the angular velocity and displacement of the impeller.

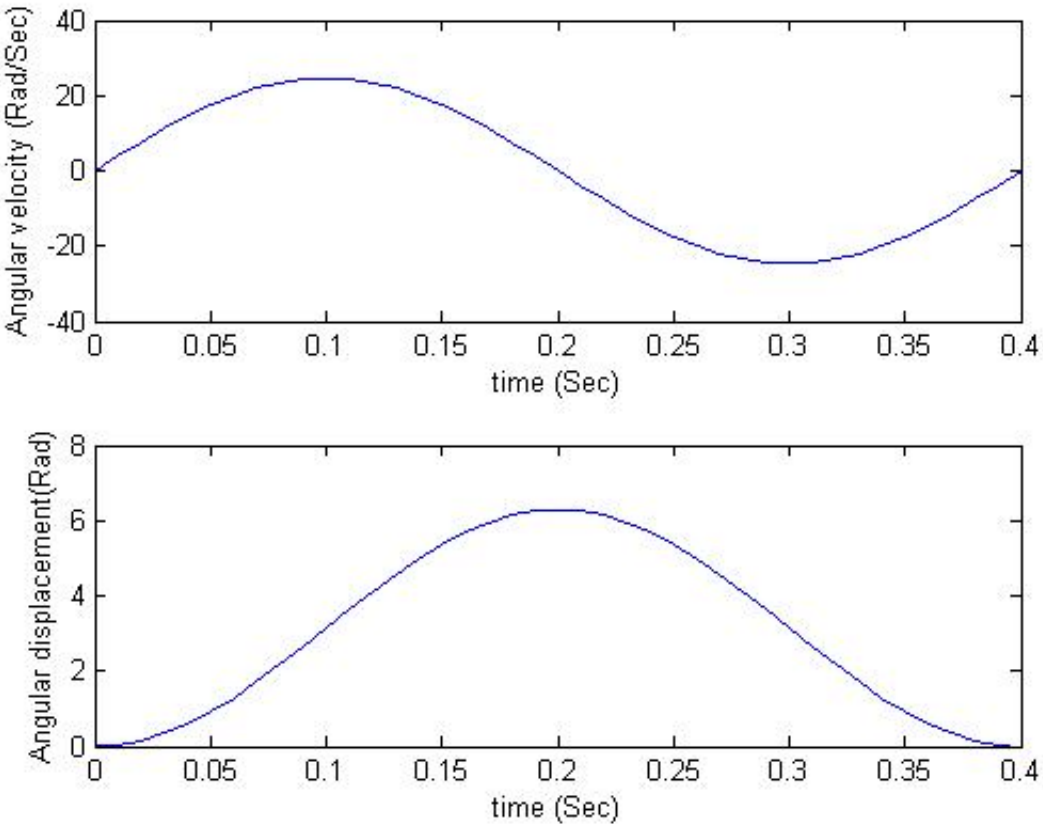

Figure 5.5: Angular velocity and displacement of the impeller during one period with the frequency of 5 Hz.

5.9 Immersed Solid Method for Modeling the Interaction impeller with Fluid

The Immersed Solid (IS) methodology is used to model the interaction of a solid which is immersed inside a fluid ([81] and [82]). In this project, we will use the IS model of the ANSYS CFX to transfer the motion of the impeller to the fluid. The IS model of the ANSYS CFX adds a momentum source term to the NS equations to make the fluid velocity equal to the solid velocity (impeller blades in this case). According to CFX manual, the size of source term is controlled by the "Momentum Source Scaling Factor" which can be changed in the "Solver Control" menu. The default value of the Momentum Source Scaling Factor is 10 which is suitable for most

cases.

5.10 Computational Structural Dynamics (CSD) for Modeling the Interaction of the Valve Leaflets with Fluid

The fluid pressure causes the valve leaflet rotate about its hinges. One dimensional dynamic equation for leaflets needs to be solved to determine the new angle of the leaflets at each time step:

$$\mathrm{M} = \mathrm{I}\,\ddot{\theta} \tag{5.11}$$

Where, M is the moment which pressure applies to the leaflet, I is the angular moment of inertia of the leaflet about the hinge and θ is the angle of the leaflet.

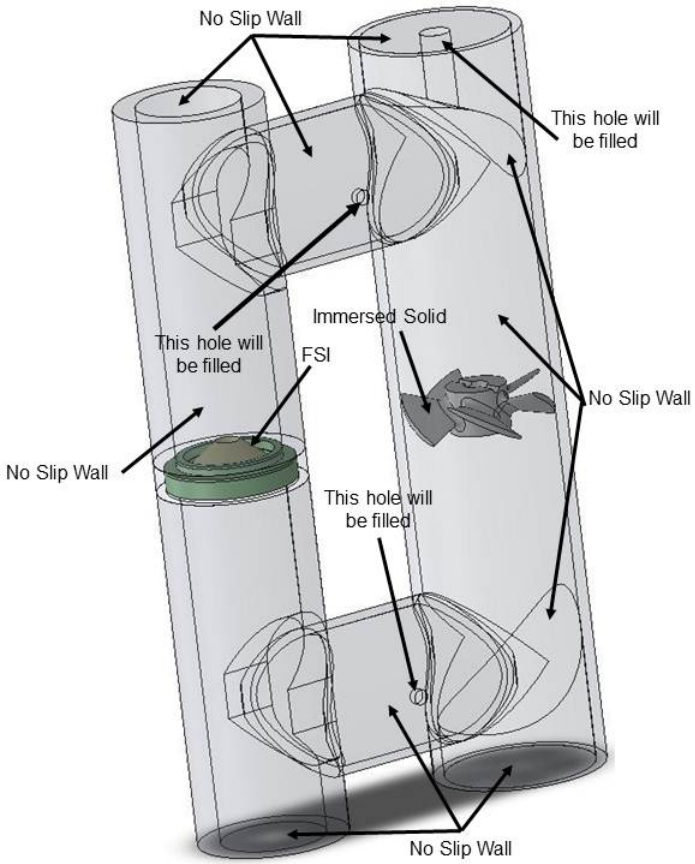

Figure 5.6: Boundary conditions for CFD simulation.

5.11 Proposed Algorithm

For this problem, we will use the algorithm which was successfully implemented and validated against experimental results by Jan Vierendeels *et al.* [99] for a tilting valve. Figure 5.7 presents the proposed algorithm. A program will be written (in FORTRAN) and coupled to the CFD package (ANSYS CFX) to implement this algorithm.

The following time integration scheme will be used for valve:

$$\dot{\theta}^{\mathrm{n+1}} = \dot{\theta}^{\mathrm{n}} + (1-\beta)\ \Delta\mathrm{t}\ \ddot{\theta}^{\mathrm{n}} + \beta\Delta\mathrm{t}\ \ddot{\theta}^{\mathrm{n+1}} \tag{5.12}$$

$$\theta^{\mathrm{n+1}} = \theta^{\mathrm{n}} + \Delta\mathrm{t}\ \dot{\theta}^{\mathrm{n}} + \gamma\ \Delta\mathrm{t}^2\ \ddot{\theta}^{\mathrm{n}} + \alpha\ \Delta\mathrm{t}^2\ \ddot{\theta}^{\mathrm{n+1}} \tag{5.13}$$

Where, n and $n+1$ corresponds to time steps of t and $t+\Delta t$ respectively.

In this algorithm, the derivative of $dM/d\ddot{\theta}$ is estimated at the beginning of each time step. To estimate the $\theta^{n+1,k=0}$ (k is the iteration number), we use the equation 5.13 with the old value of acceleration: $\dot{\theta}^{n}$. Then, mesh is moved using dynamic mesh model of the ANSYS CFX. Next, Navier-Stocks equations (5.1 to 5.4) will be solved by ANSYS CFX and $M^{n+1,k=0}$ will be computed. Second iteration ($k=1$) starts with calculating $\theta^{n+1,k=1}$ by increasing the $\dot{\theta}^{n}$ to $\dot{\theta}^{n}+\delta$ ($\delta = 0.1 rad/s^2$) in the equation 5.13. Next, mesh is moved and NS equations are solved and $M^{n+1,k=1}$ is calculated for the second iteration. At this point, we will compute the $dM/d\ddot{\theta}$ as followed:

$$\ddot{\theta}^{\mathrm{n+1,k=0}} = \ddot{\theta}^{\mathrm{n}} \tag{5.14}$$

and

$$\ddot{\theta}^{\mathrm{n+1,k=1}} = \ddot{\theta}^{\mathrm{n}} + \delta \tag{5.15}$$

$$\frac{\mathrm{dM}}{\mathrm{d}\ddot{\theta}} = \frac{\mathrm{M}^{\mathrm{n+1,k=1}} - \mathrm{M}^{\mathrm{n+1,k=0}}}{\ddot{\theta}^{\mathrm{n+1,k=1}} - \ddot{\theta}^{\mathrm{n+1,k=0}}} \tag{5.16}$$

Therefore, a better estimation of the $\ddot{\theta}^{n+1,k=1}$ will be calculated as followed:

$$\mathrm{M}^{\mathrm{n+1,k=1}} = \mathrm{I}\ \ddot{\theta}^{\mathrm{n+1,k=1}} \implies \tag{5.17}$$

$$\mathrm{M}^{\mathrm{n+1,k}}\ \frac{\mathrm{dM}}{\mathrm{d}\ddot{\theta}}\ \left(\ddot{\theta}^{\mathrm{n+1,k+1}} - \ddot{\theta}^{\mathrm{n+1,k}}\right) = \mathrm{I}\ \ddot{\theta}^{\mathrm{n+1,k+1}} \implies \tag{5.18}$$

$$\ddot{\theta}^{\mathrm{n+1,k+1}} = \frac{\mathrm{M}^{\mathrm{n+1,k}} - \frac{\mathrm{dM}}{\mathrm{d}\ddot{\theta}}\ddot{\theta}^{\mathrm{n+1,k}}}{\mathrm{I} - \frac{\mathrm{dM}}{\mathrm{d}\ddot{\theta}}} \tag{5.19}$$

With this better estimation of the acceleration we will calculate the $\theta^{n+1,k}$ and consequently, the mesh will be updated and NS equations will be solved and $M^{n+1,k}$ will be computed. The convergence is checked with:

$$\mathrm{M}^{\mathrm{n+1,k}} \approx \mathrm{I}\ \ddot{\theta}^{\mathrm{n+1,k}} \tag{5.20}$$

The k-loop will be repeated until we reach the convergence. Then, we will move to the next time step and repeat the algorithm until the end of computational time.

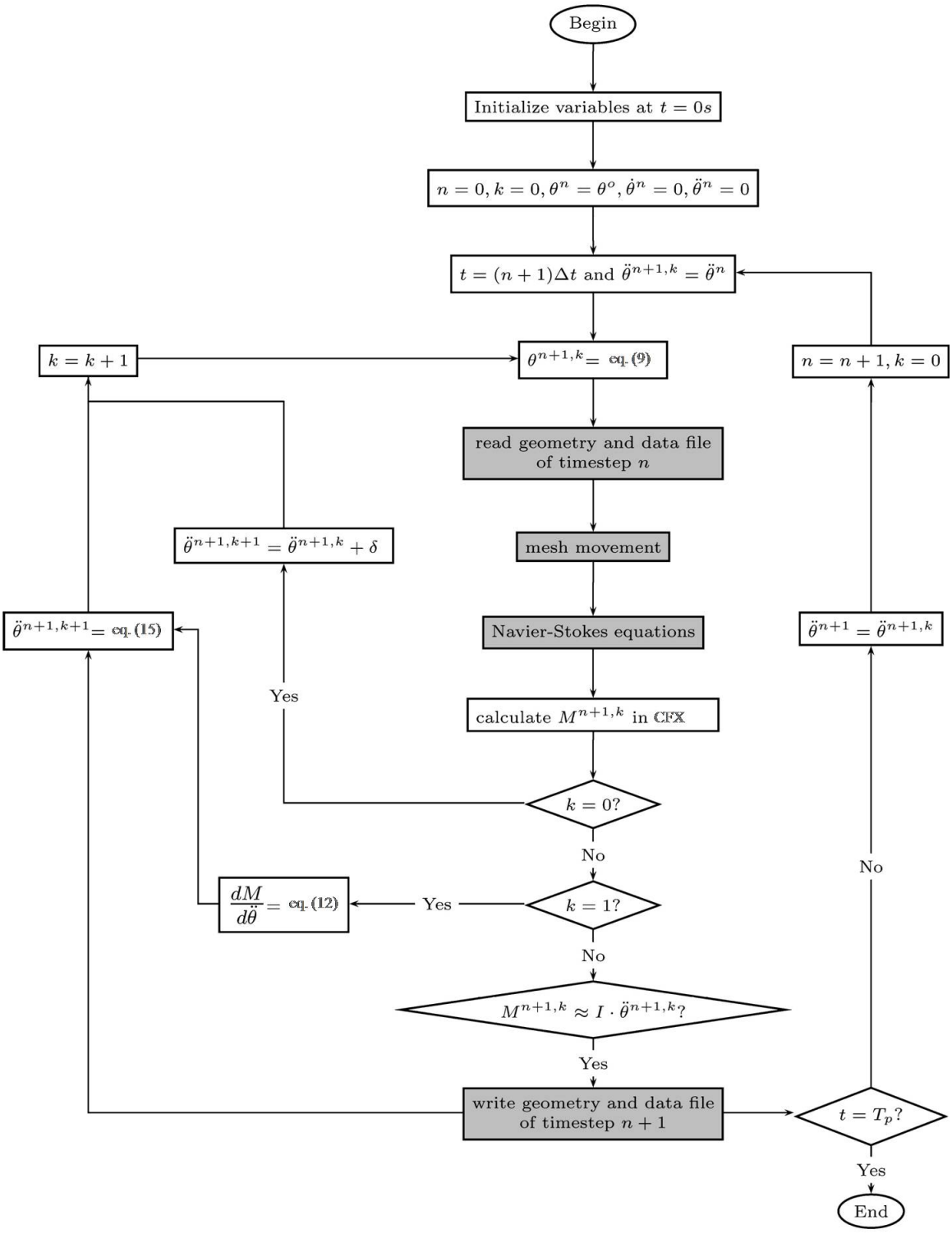

Figure 5.7: Proposed algorithm extracted from [99].

5.12 Results and Discussion

Our first objective is simulating different design configurations without FSI to evaluate which one creates higher back pressure for the valve. Therefore, we simulated three configurations in sections 5.12.1, 5.12.2, 5.12.3. The following operating conditions were used for all the simulations for consistency purposes.

- Frequency (f): 5 Hz
- Maximum angular displacement of the impeller (θ_{max}): π rad
- Angle of the leaflets of the valve: 45°
- Time step (Δt): 0.02 Sec

5.12.1 Initial configuration

The first case which was simulated is the system with the valve fixed in its position. Figure C.1 shows the 3D streamlines, colored with velocity at $\Delta t = 0.1$ in which the impeller is at its pick velocity. In this picture we observe that each blade of the impeller creates vortices. Also, the velocity of the fluid close to the blades are much higher than the entire system, therefore in order to evaluate the velocity and pressure near the valve we need to show the results in an area near the valve and isolated from the rest of the system. Also, we predicted that some vortices are created in the corners. Figure C.1 show that theses vortices are small and their effect are insignificant. Figures C.2(1) to C.2(20) and C.4(1) to C.4(20) present the streamlines(colored with velocity) and z component of velocity on the symmetrical plane with respect to the valve respectively. The general objective of this simulation is to understand the structure of the flow inside the apparatus. The streamlines show that the the impeller's blades create vortices which are elongated above and bellow the impeller from the blades root to the tip. These vortices cause the stagnation flow on the side of the impeller which the flow is being pushed. For example, in the figures C.2(1) to C.2(14) the vortices are formed and as the velocity of the impeller goes higher the vortices are developed more. In these figures the fluid is flowing clockwise i.e. fluid is being pushed downward by the impeller and the vortics are spinning anticlockwise (see figure C.3) therefore the we have a very low velocity region with stagnation pint just bellow the impeller. Also, we observe that when the impeller changes the direction of its rotation the flow on the valve side does not change immediately and has a delay.

In the figure C.2(14), when the flow direction starts to change two symmetric vortices are formed above the valve holder. Further down, these two vortices move toward the center of the valve (figure C.2(15)) and finally create a low velocity region on top of the valve (figures C.2(16) and C.4(16)).

Figure 5.15 presents the average pressure on the top and bottom surfaces of the valve. As it was expected the in half of the cycle the the pressure on bottom surfaces are higher than the one on the top surfaces (closing phase) and it becomes opposite in the next half cycle. Figure 5.15 shows that the pressure fluctuates which is interpreted that the valve does not close smoothly but it has flutter speed.

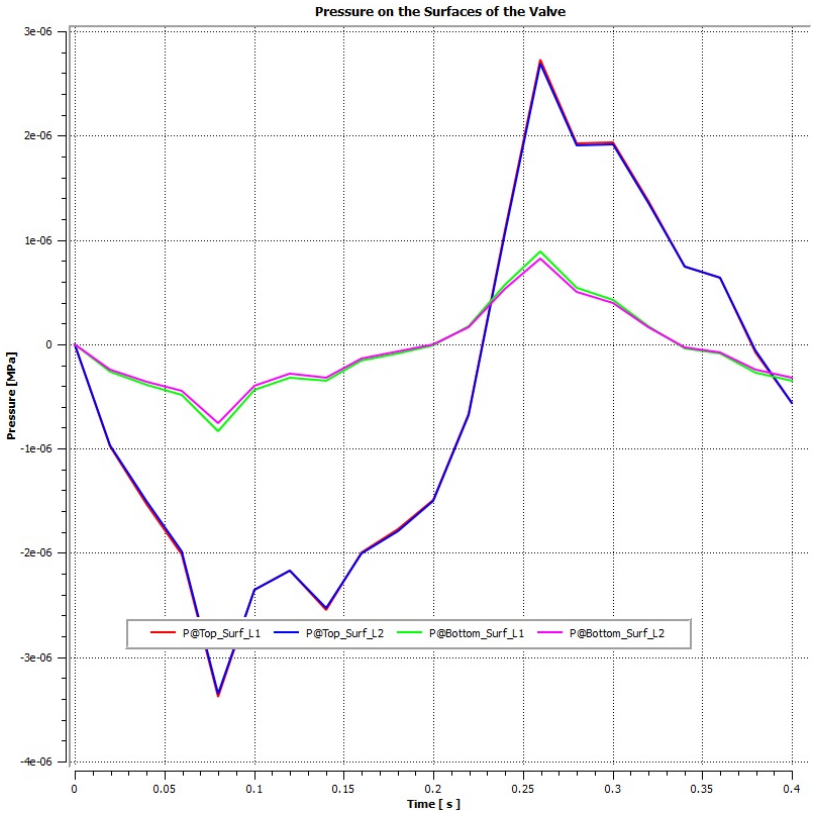

Figure 5.8: Pressure on the surfaces of the valve in one cycle(0.4 Sec). P1: pressure on the top surface of the leaflet 1, P2: pressure on the top surface of the leaflet 2, P3: pressure on the bottom surface of the leaflet 1, P4: pressure on the bottom surface of the leaflet 2.

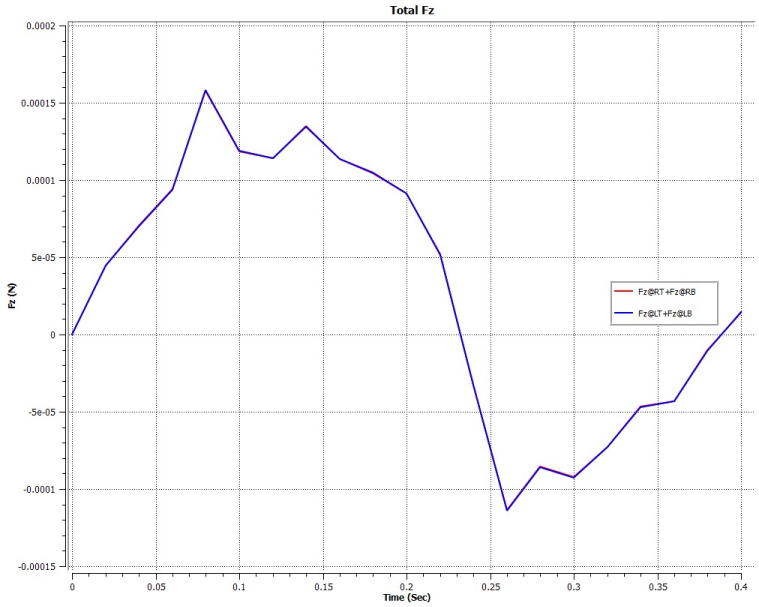

Figure 5.9: Sum of Fz on the leaflets in one cycle(0.4 Sec).RT: top surface of right leaflet, RB: bottom surface of right leaflet, LB: bottom surface of left leaflet, LT: top surface of left leaflet

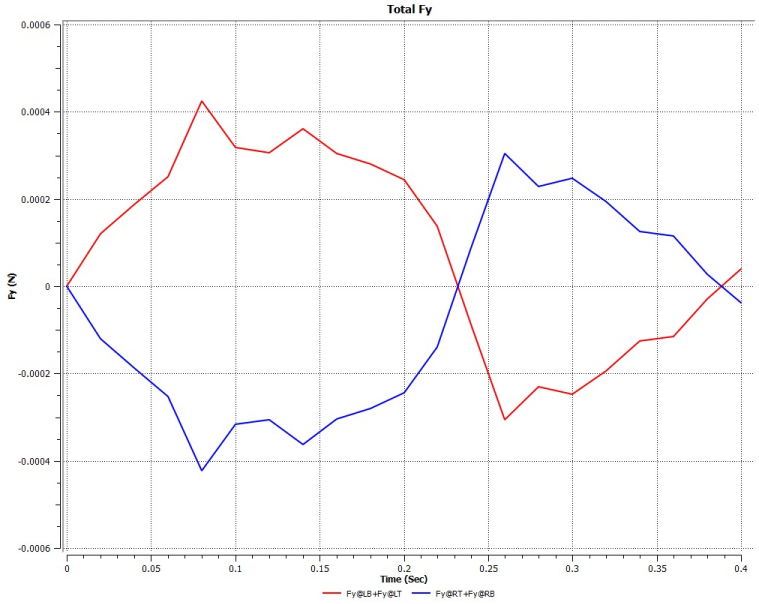

Figure 5.10: Sum of Fy on the leaflets in one cycle(0.4 Sec).RT: top surface of right leaflet, RB: bottom surface of right leaflet, LB: bottom surface of left leaflet, LT: top surface of left leaflet

5.12.2 Effect Having More Impellers

In this case study we installed three impellers in the system and calculated the net force applied to the leaflets. Figures C.5(1) to C.5(20) show the velocity contours (z component) near the valve. Theses results show that the maximum velocity with three impellers is about 122 mm/sec while the maximum velocity for the system with one impeller is about 67 mm/sec. Figure 5.13 and 5.14 show the net z and y component of forces applied to the leaflets. Figure 5.13 show that the maximum net z component of force is 0.4 mN while the same parameter with one impeller is 0.16 mN (see figure 5.9). Also, the maximum net Fy for three impellers system is about 1 mN while for one impeller is 0.4 mN.

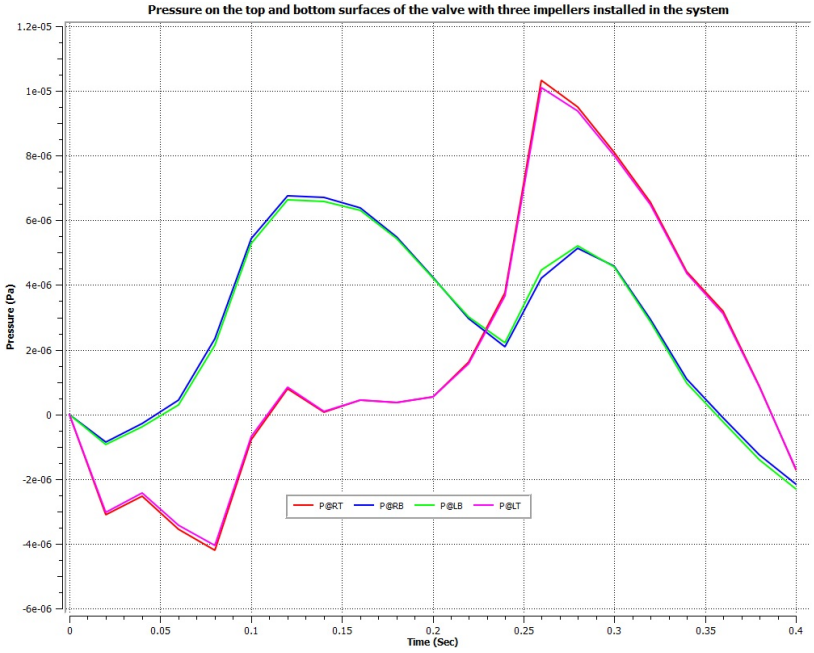

Figure 5.11: Pressure on the surfaces of the valve in one cycle(0.4 Sec). RT: right top, RB: right bottom, LB: left bottom, LT: left top

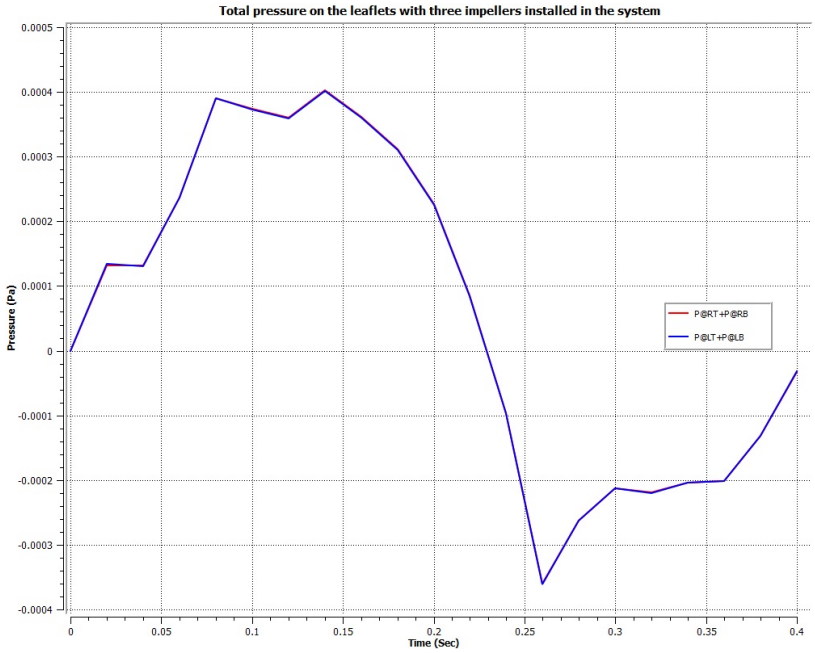

Figure 5.12: Total Pressure on the surfaces of the valve in one cycle(0.4 Sec). RT: right top, RB: right bottom, LB: left bottom, LT: left top

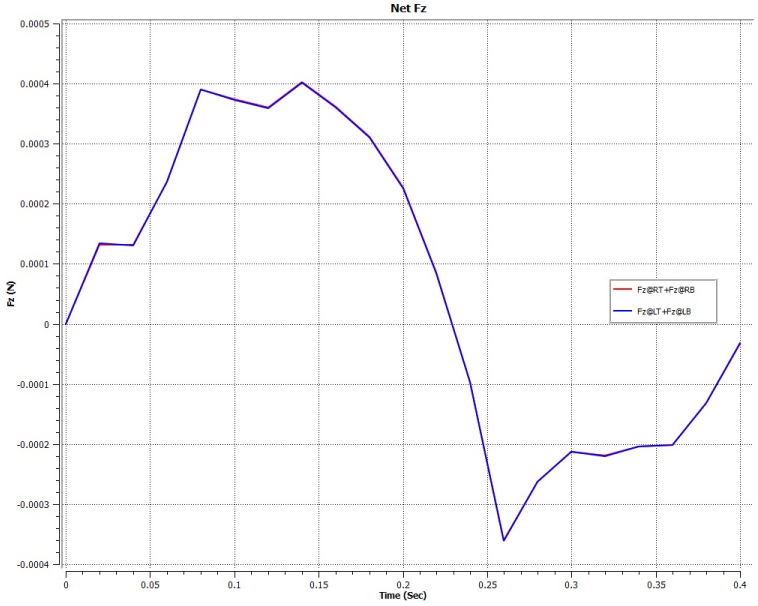

Figure 5.13: Sum of Fz on the leaflets in one cycle(0.4 Sec) in the system with 3 impellers installed.RT: top surface of right leaflet, RB: bottom surface of right leaflet, LB: bottom surface of left leaflet, LT: top surface of left leaflet

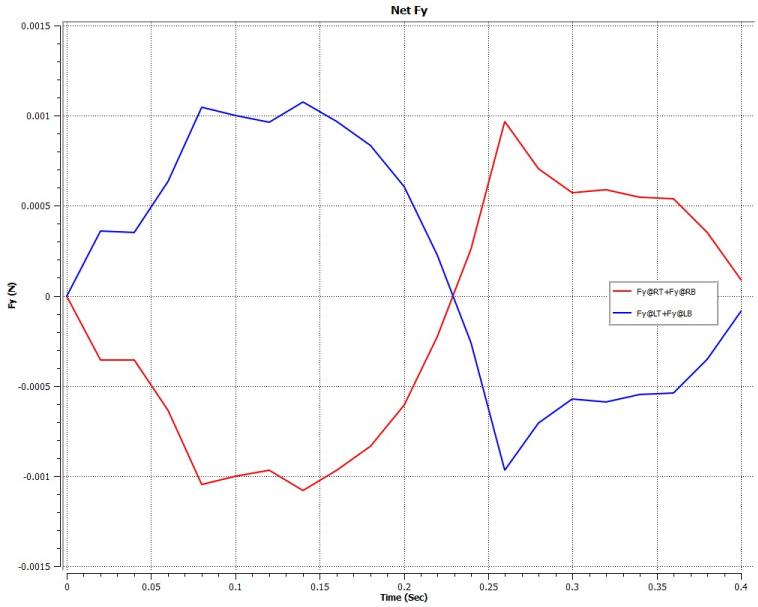

Figure 5.14: Sum of Fy on the leaflets in one cycle(0.4 Sec) in the system with 3 impellers installed.RT: top surface of right leaflet, RB: bottom surface of right leaflet, LB: bottom surface of left leaflet, LT: top surface of left leaflet

5.12.3 Effect Installing the Impeller Close to the Valve

We also investigated the effect of installing the impeller closer to the valve. In this case the impeller was accommodated 25 mm bellow the valve. Figure C.6(1) to C.6(20) show the velocity (z component) contours. The maximum velocity is about 90 mm/sec which is about %33 more than the system with one impeller. Also, figure 5.16 show that the maximum net Fz is 0.2 mN which is %20 more than the system with one impeller. Moreover, figure 5.17 show that the maximum Fy for the right leflet is 0.6 mN and for the left one is 0.4 mN which means the right leaflet should close sooner.

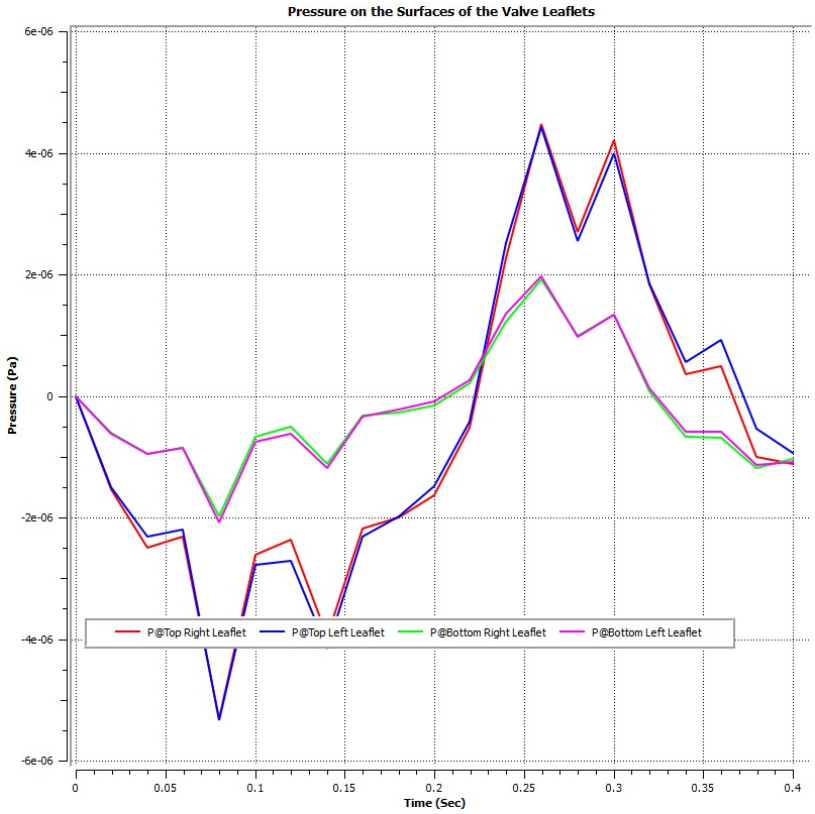

Figure 5.15: Pressure on the surfaces of the valve in one cycle(0.4 Sec).

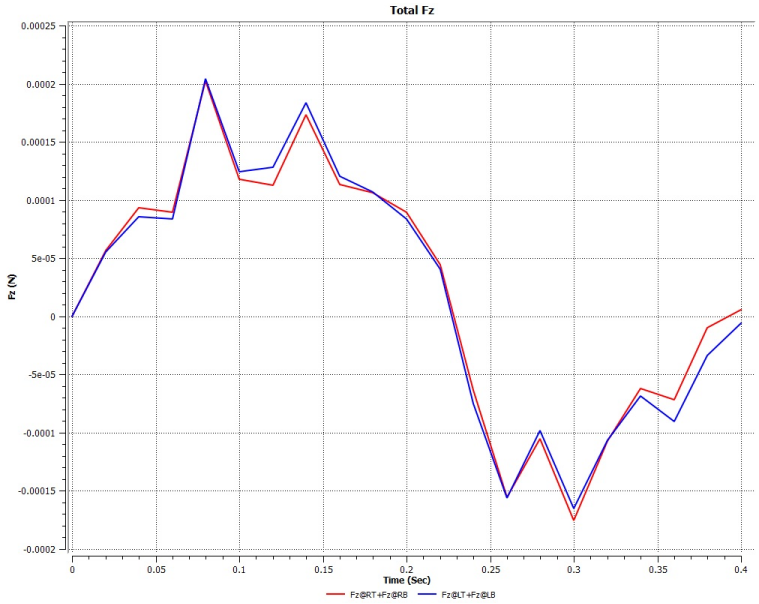

Figure 5.16: Sum of Fz on the leaflets in one cycle(0.4 Sec).RT: top surface of right leaflet, RB: bottom surface of right leaflet, LB: bottom surface of left leaflet, LT: top surface of left leaflet

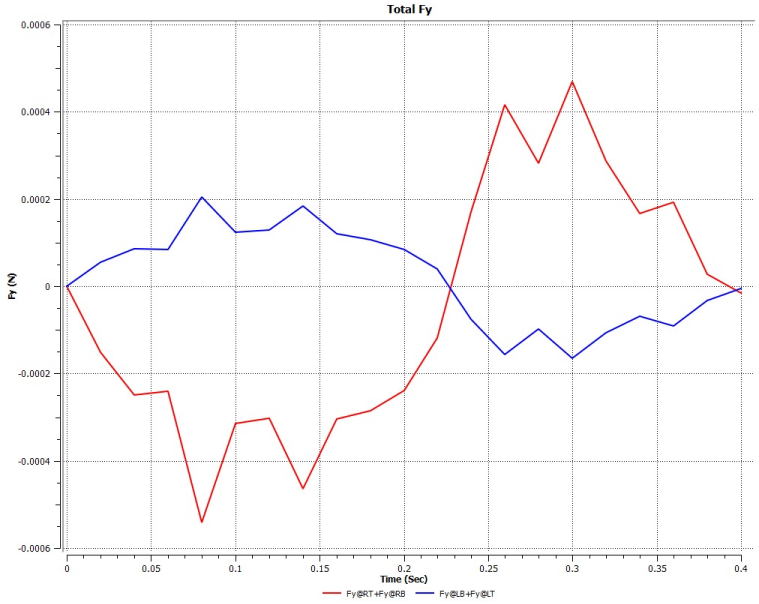

Figure 5.17: Sum of Fy on the leaflets in one cycle(0.4 Sec).RT: top surface of right leaflet, RB: bottom surface of right leaflet, LB: bottom surface of left leaflet, LT: top surface of left leaflet

5.12.4 Full FSI Simulation

In this chapter we presented the results of the full FSI simulation of the system for the operating conditions mentioned earlier in the section: 5.12. In this simulation we followed the algorithm, described in the section: 5.11. Figures C.7(1) to C.7(20) show the streamline of the flow during a cycle. In these figures the fluid is flowing clockwise and a stagnation region is created bellow the impeller from the beginning to 0.24 Sec (figure C.7(12)). At $t = 0.2\ Sec$ the impeller changes the direction but it takes about 0.06 Sec for the fluid to become fully inversed. At $t = 0.26\ Sec$ (figure C.7(13)) we have many vortices in the system. After this point the stagnation area is moved above the impeller. Also, if we look at the pressure contours across the valve (figures C.8(1) to C.8(20)) we see that the pressure across the valve becomes reversed after $t = 0.26\ Sec$. Figures 5.18 to 5.38 present the velocity contours around the valve during a cycle. at the beginning (figure 5.18), we see high velocity at the edge of the valve holder. As the pressure builds up bellow the valve, valve starts to close and the open area reduces causing the increase in jet flow at the edge of valve holder as well as the middle of the valve. From $t = 0.06\ Sec$ to $t = 0.12\ Sec$ (figures 5.18 to 5.24), the velocity contours are not symmetric and the flow with higher velocity flows from right bellow toward the valve and going out toward above right. Figure 5.39 presents the angle of the leaflets during a cycle. This chart shows that the left leaflet closes 0.02 Sec sooner than the right one. Figure C.9(9) to C.9(12) show that once the left leaflet closes two vortices are developed above the valve holder. Also, at the onset of both leaflet closing two other vortices are developed bellow the leaflets (see figures C.9(12) to C.9(15)). Another aspect of the flow is the high velocity on the top surface of the right leaflet. Figure 5.27 to 5.38 show that this high velocity region starts at the edge of the right leaflet (figure 5.27) and moves up during the cycle. Also, if we look at the pressure contours (figures C.8(9) to C.8(15)), we see low pressure in the same high velocity area where there is high chance of cavitation.

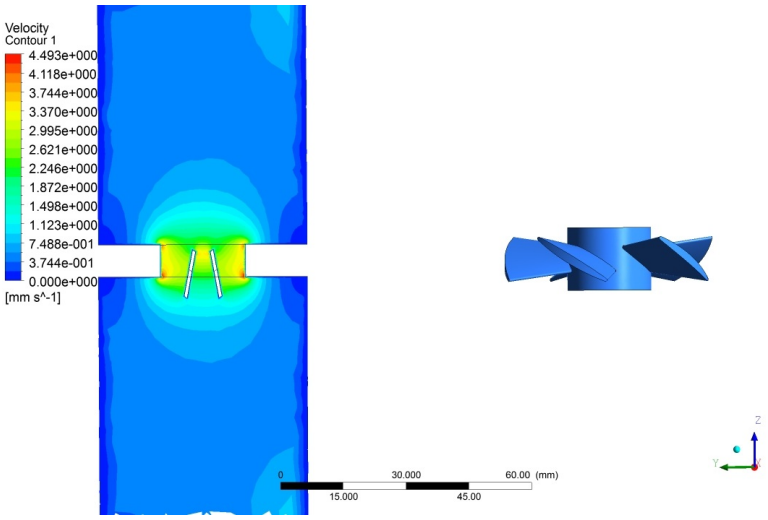

Figure 5.18: Velocity contours at mid surface(0.02 Sec).

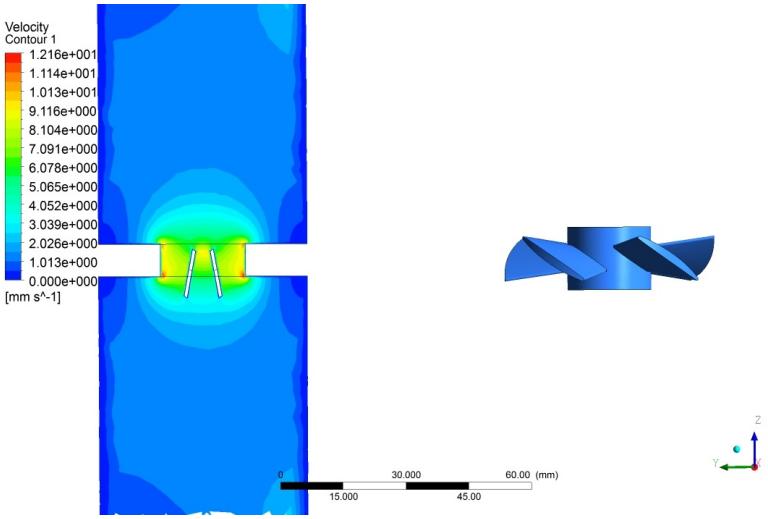

Figure 5.19: Velocity contours at mid surface(0.04 Sec).

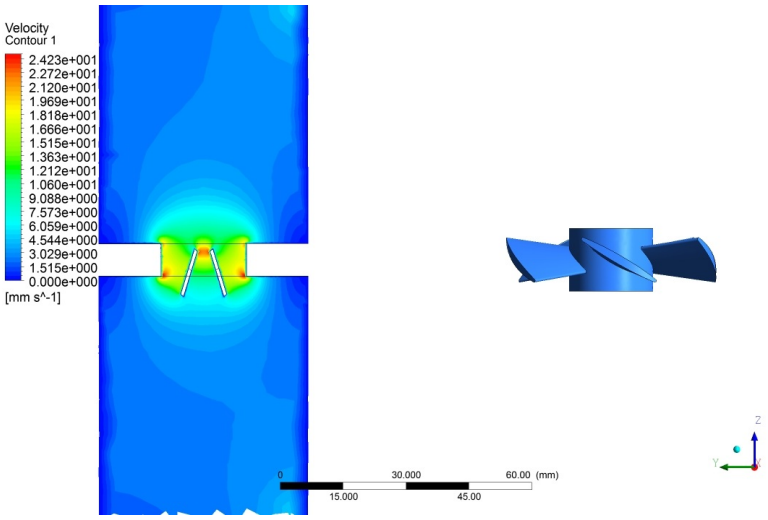

Figure 5.20: Velocity contours at mid surface(0.06 Sec).

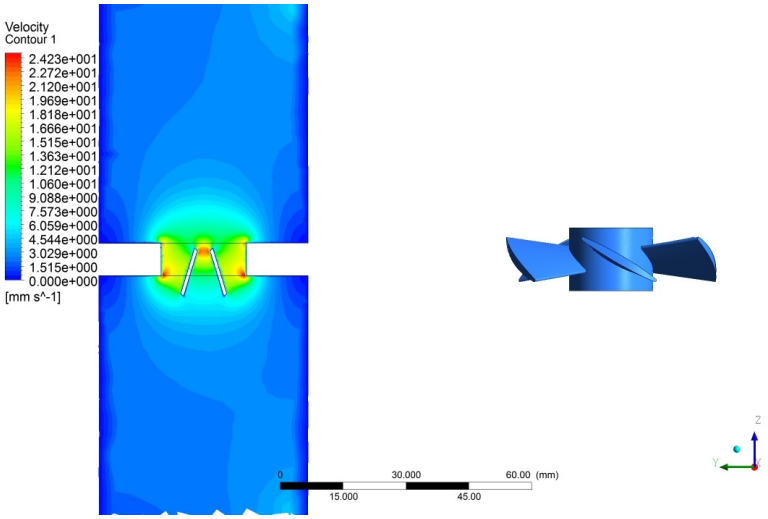

Figure 5.21: Velocity contours at mid surface(0.06 Sec).

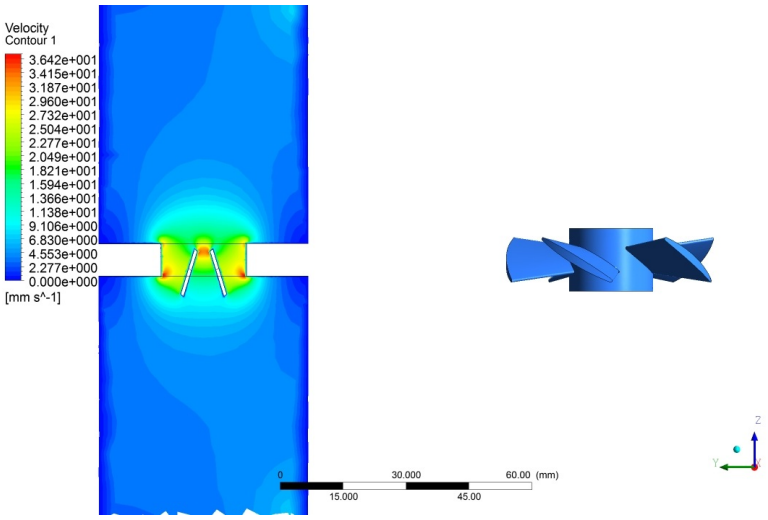

Figure 5.22: Velocity contours at mid surface(0.08 Sec).

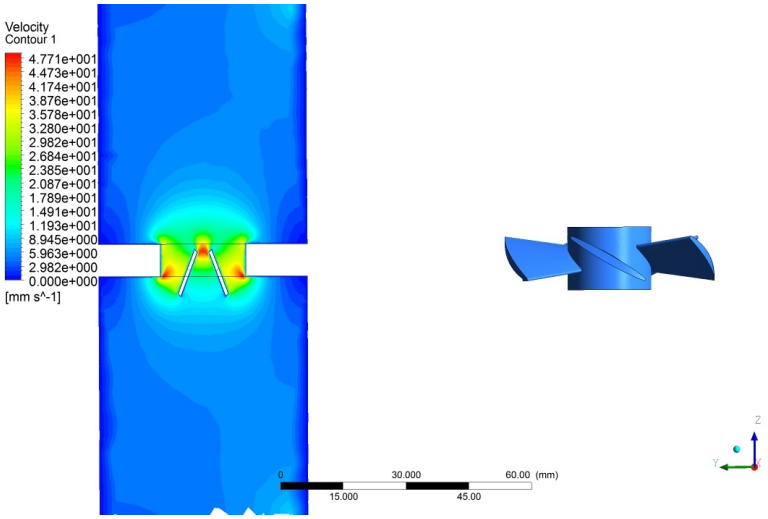

Figure 5.23: Velocity contours at mid surface(0.1 Sec).

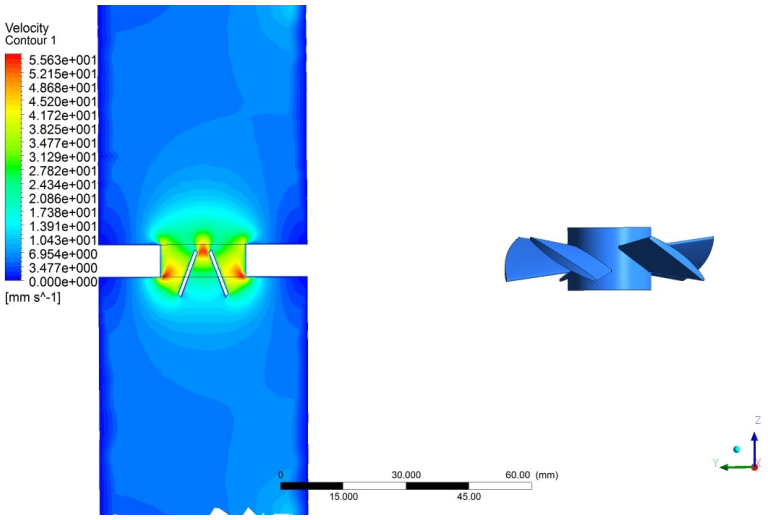

Figure 5.24: Velocity contours at mid surface(0.12 Sec).

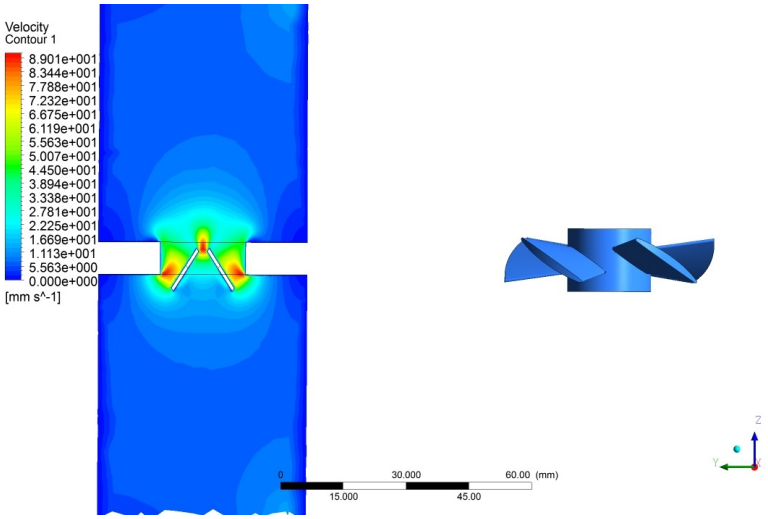

Figure 5.25: Velocity contours at mid surface(0.14 Sec).

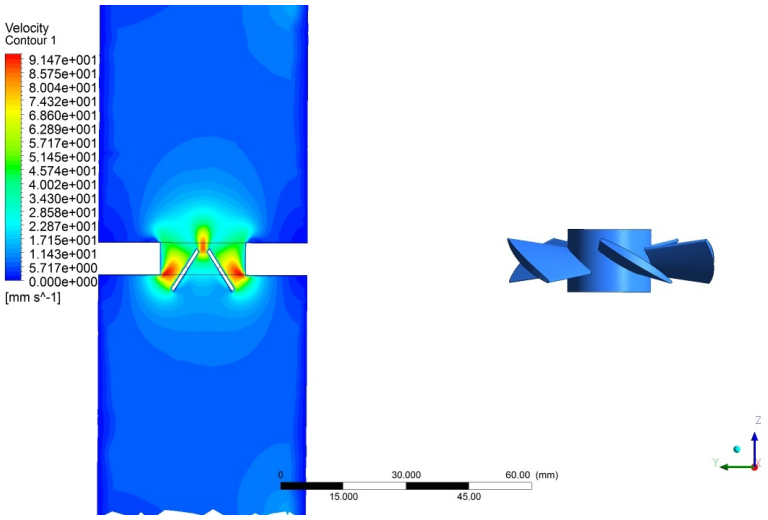

Figure 5.26: Velocity contours at mid surface(0.16 Sec).

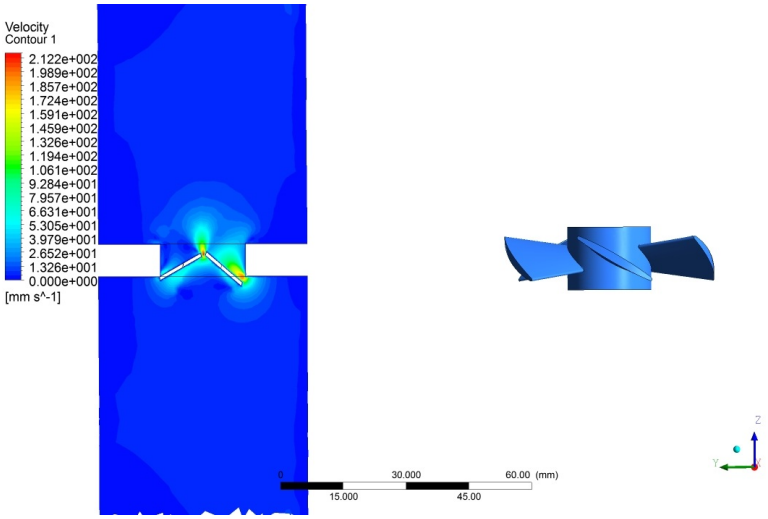

Figure 5.27: Velocity contours at mid surface(0.18 Sec).

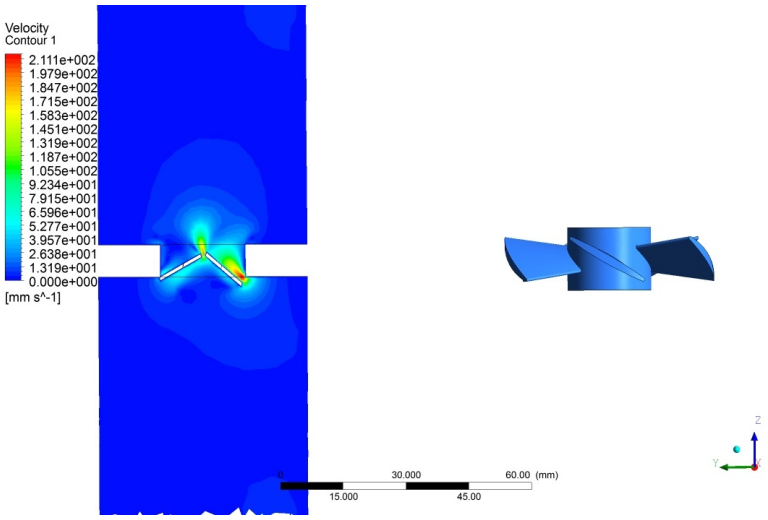

Figure 5.28: Velocity contours at mid surface(0.2 Sec).

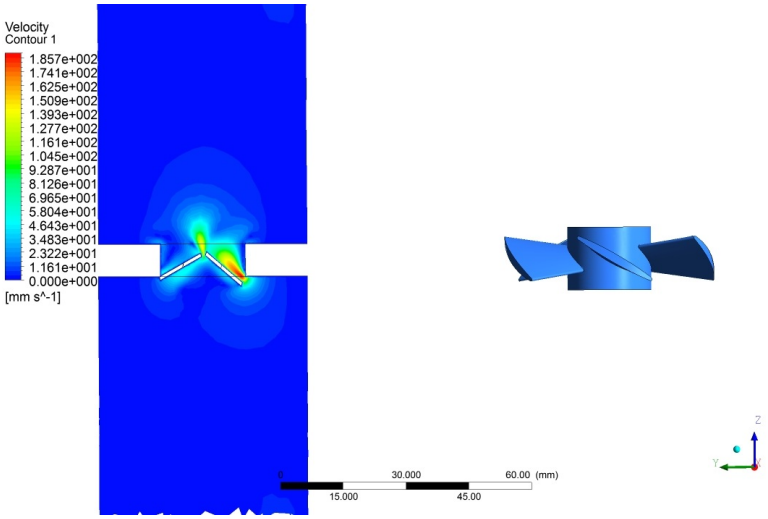

Figure 5.29: Velocity contours at mid surface(0.22 Sec).

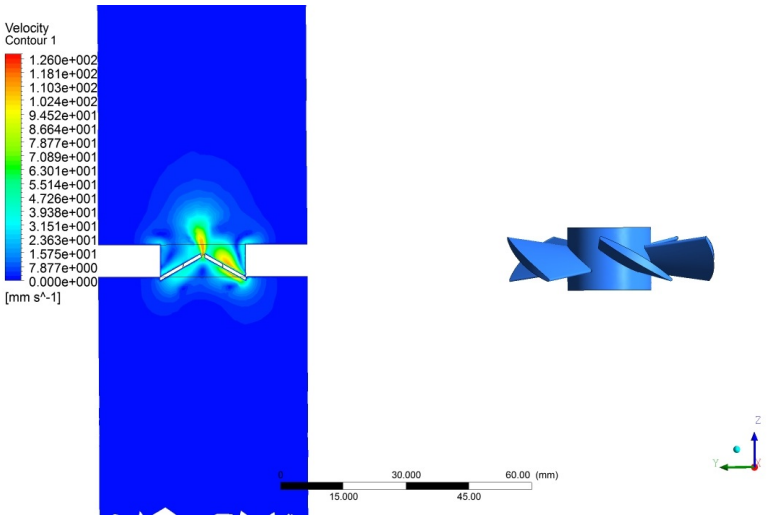

Figure 5.30: Velocity contours at mid surface(0.24 Sec).

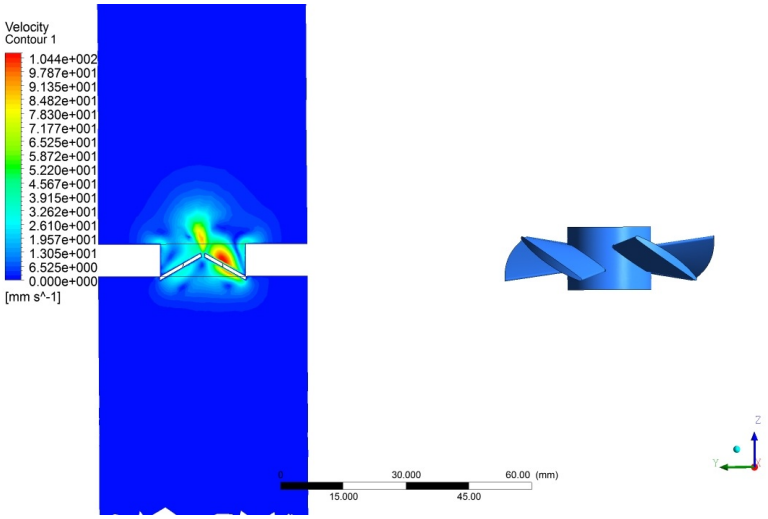

Figure 5.31: Velocity contours at mid surface(0.26 Sec).

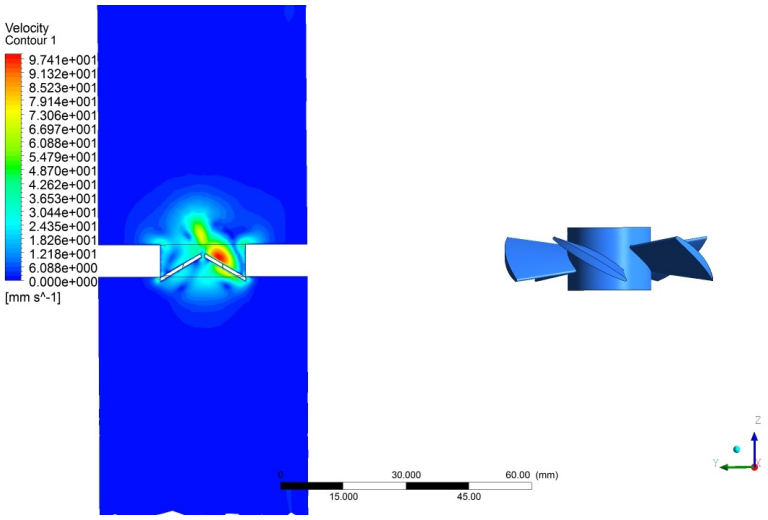

Figure 5.32: Velocity contours at mid surface(0.28 Sec).

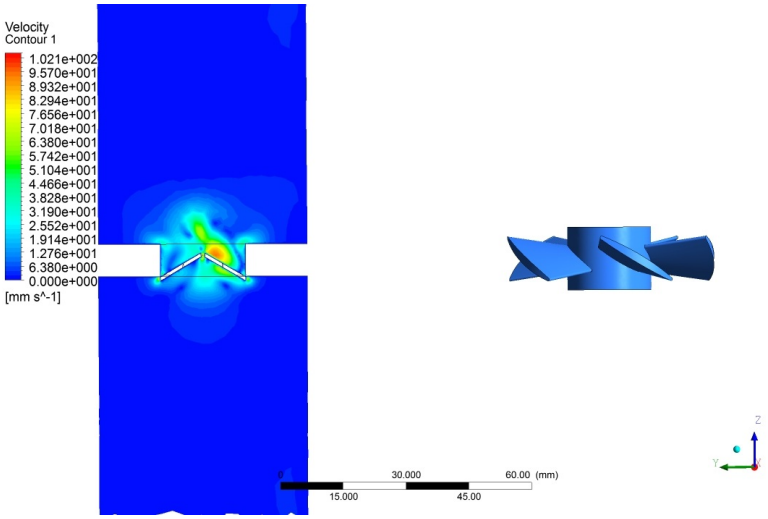

Figure 5.33: Velocity contours at mid surface(0.30 Sec).

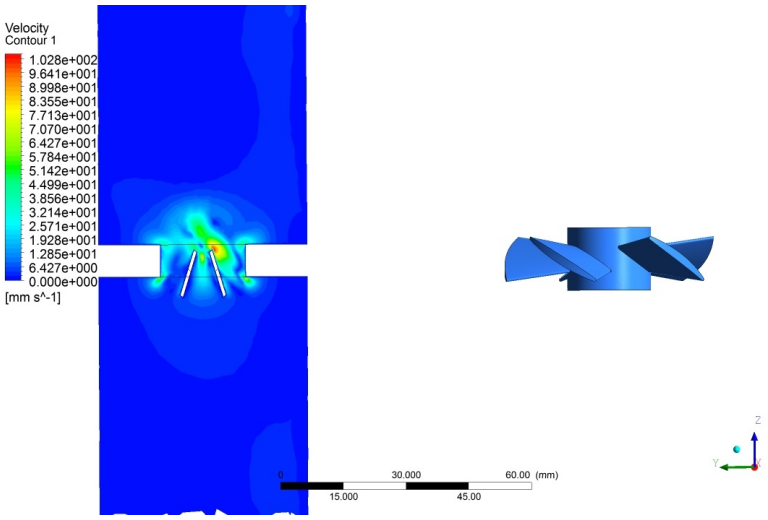

Figure 5.34: Velocity contours at mid surface(0.32 Sec).

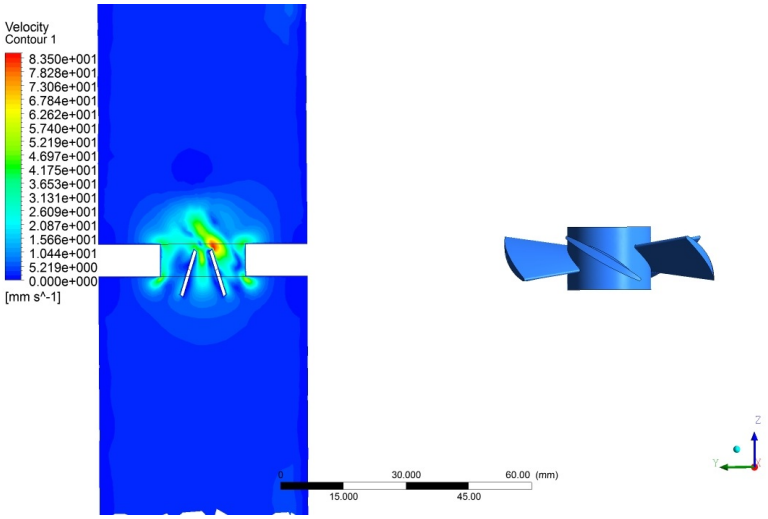

Figure 5.35: Velocity contours at mid surface(0.34 Sec).

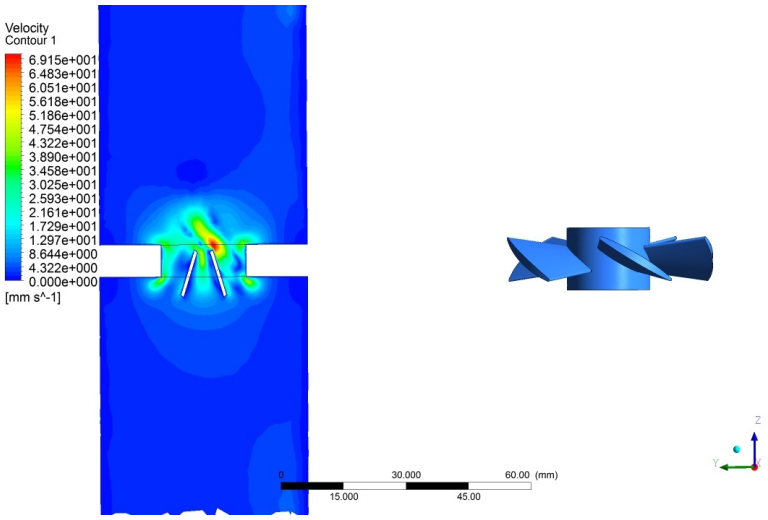

Figure 5.36: Velocity contours at mid surface(0.36 Sec).

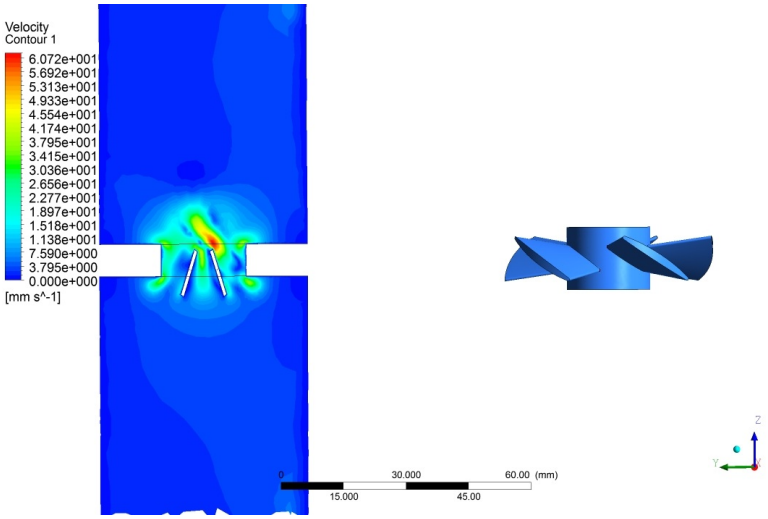

Figure 5.37: Velocity contours at mid surface(0.38 Sec).

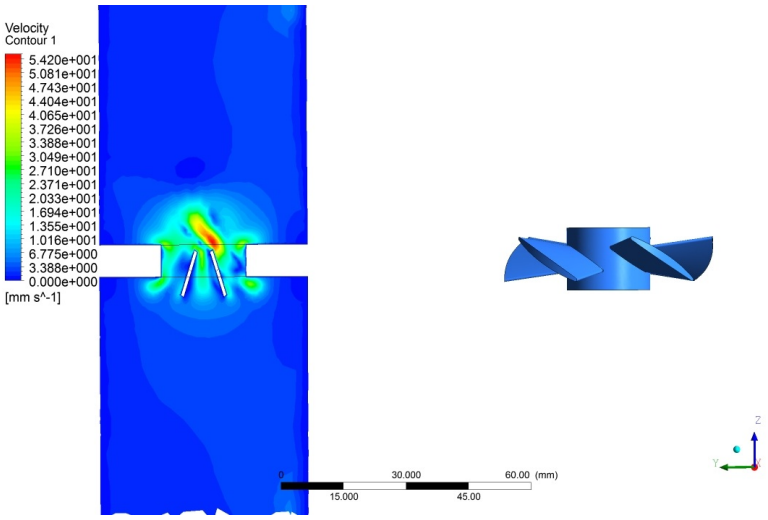

Figure 5.38: Velocity contours at mid surface(0.4 Sec).

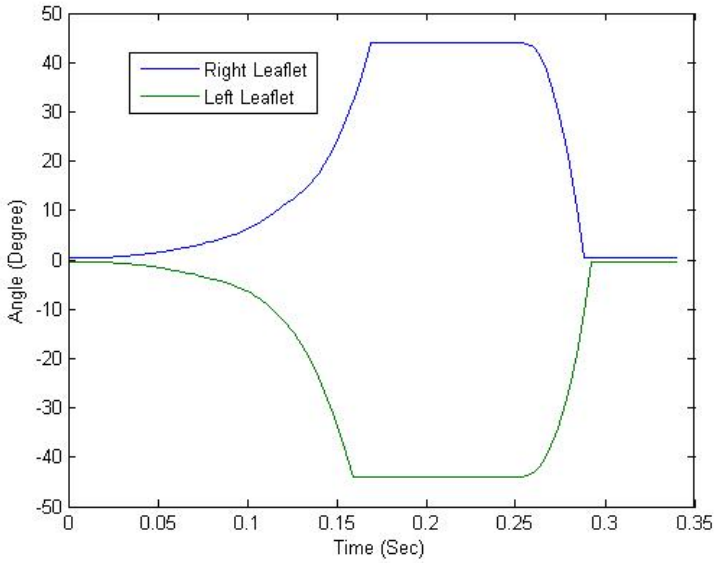

Figure 5.39: Leaflet angle during a period. The left leaflet closes slightly sooner than the right one.

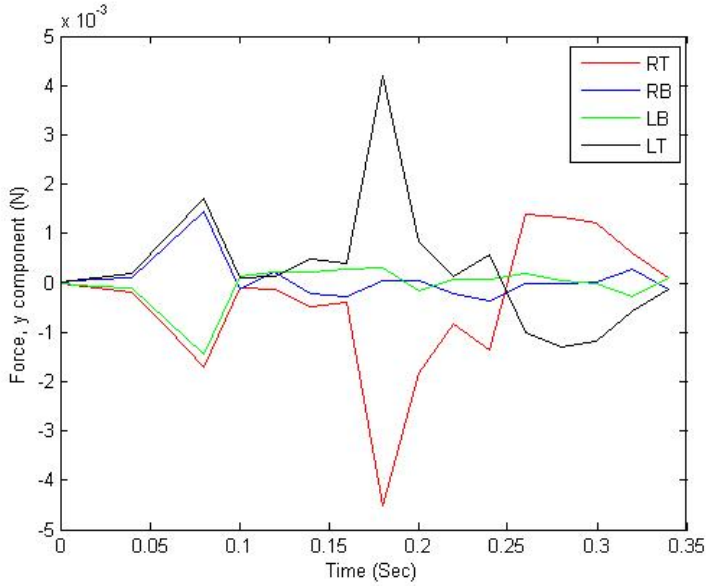

Figure 5.40: Y component of the force applied by fluid to the top and bottom surfaces of the leaflets during a period. RT: right top, RB: right bottom, LB: left bottom, LT: left top

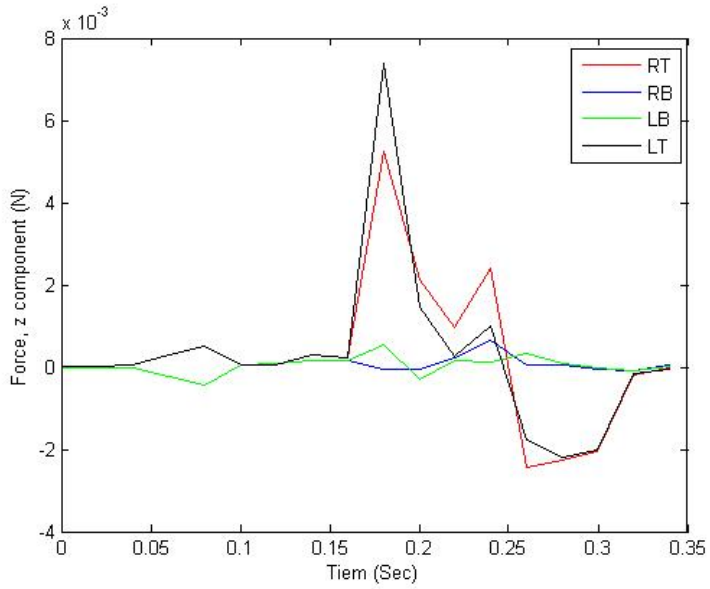

Figure 5.41: Z component of the force applied by fluid to the top and bottom surfaces of the leaflets during a period. RT: right top, RB: right bottom, LB: left bottom, LT: left top

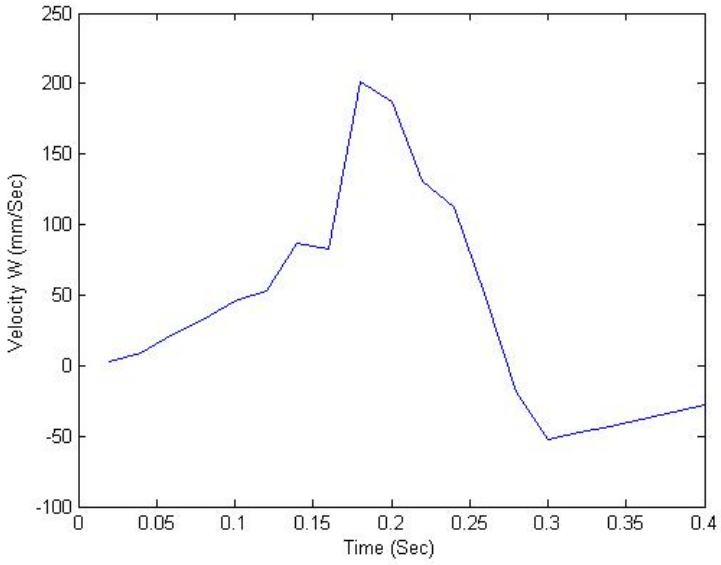

Figure 5.42: Z component of the velocity (w) at the mid point of the valve

5.13 Conclusion

In this project we used CFD to investigate the fluid flow inside the new accelerated heart valve fatigue tester which was developed by ViVitro Labs Inc. We used IS

and FSI methods to simulate the impeller and PHV respectively. We first fixed the valve's leaflets at the 45 degree angle (no FSI) and ran three cases to understand the flow characteristics without getting into the complications of FSI. In the first case we used one impeller rotating according to sin wave with frequency if 5 Hz. In the second case two more impellers was added to the system and finally in the third case we positioned the impeller close to the valve. We showed the net y and z force being applied to the leaflets in the figures 5.10, 5.9, 5.14, 5.13, 5.17 and 5.16. Table 5.1 compares the maximum force in the three cases:

Table 5.1: y and z component of forces applied to the leaflets. case 1: one impeller, case 2: three impellers, case 3: impeller installed close to the valve.

Case	Fy@Right Leaflet	Fy@Left Leaflet	Fz@Right Leaflet	Fz@Left Leaflet
1	0.4 mN	0.4 mN	0.16 mN	0.16 mN
2	1 mN	1 mN	0.4 mN	0.4 mN
3	0.6 mN	0.4 mN	0.2 mN	0.2 mN

The results show that Fy in the case of three impellers is %250 and Fz is %40 higher than one impeller system. Also, the Fy and Fz in case 3 (impeller closer to the valve) is %150 (for the right leaflet) %125 higher than the case 1.

The full FSI simulation was conducted using the algorithm which was described in the section 5.11. We studied the flow pattern near the valve and we described the vortices created pre and post closure of the valve. We observed that the closure phase is longer than the opening phase. (see figure 5.39). Also, the valve opens much faster than the valve closing which can be due the column water above the valve. Another phenomena which we noticed is that the right leaflet closes with delay and this creates a high velocity region with low pressure above the valve which is a chance for cavitation. Based on the case studies we did, in order to be able to afford higher frequency of the opening-closing of the valve we suggest to install more impellers (if we would like to use the same type of impeller) or a screw type of impeller right bellow the valve. This helps the fluid to have a higher and faster force on the valve.

Chapter 6

Conclusions and Future Work

6.1 Conclusions

The thesis research proposed a fluid-structure modeling and simulation framework based on a commercial software ANSYS-CFX. Several subroutines have been designed and implemented to accurately model the complex cardiovascular dynamics related to large deformations of the left ventricle and the mitral valve. Thus, parametric geometric models for the left ventricle and natural mitral valve have been developed and structural characterization of the mitral valve has been accomplished. These models have been applied to investigate the blood flow in the diastole phase of the cardiac cycle, the venturi effect on the septal-anterior motion in the obstructive hypertrophic cardiomyopathy and finally the fluid flow was characterized for a novel conceptual device for accelerated fatigue testing of prosthetic heart valves. Figure 6.1 summarizes the various stages of the thesis development.

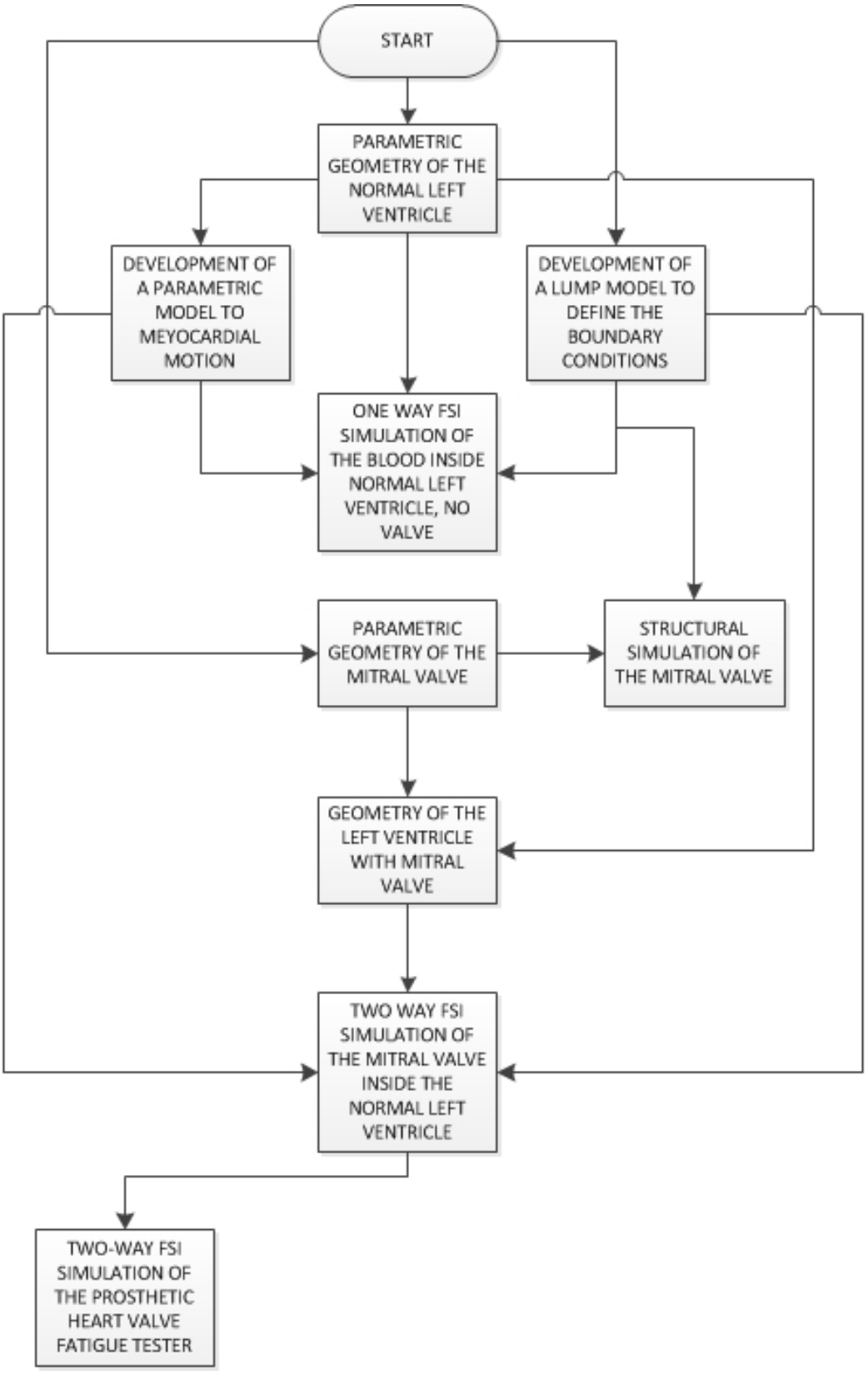

Figure 6.1: Overview of the project.

We began by building a mathematical model representing the geometry of a healthy left ventricle. A simplified semi-elliptical model was implemented using dimensions extracted from medical imaging techniques. In order to provide pressure boundary conditions for the aortic and mitral apertures, the Windkessel and Alexander lump models were used to simulate the arterial and pulmonary circulations. In order to simulate the effect of myocardium motion on the flow, we created a mathematical model for the left ventricular wall. This model was designed to satisfy the predefined volume profile of the left ventricle as a function of time. In this model, the maximum displacement is observed at the apex while the left ventricular base has no displacements.

The first fluid dynamics model was created including only the left ventricle with moving walls coupled with the arterial and pulmonary circuits of the aortic and mitral orifices. In this simulation, the left ventricular wall motion is the driving force on the fluid domain. At the beginning of the diastole phase, a non asymmetric vortex ring initiates from the mitral orifice with a larger diameter in the septal side of the left ventricle. As the left ventricle becomes larger and the incoming flow increases, the vortex ring becomes larger and rotates faster until the end of E-wave. The vortex ring slows down between the E and A-waves and picks up speed with the emergence of the A wave.

The model complexity was further increased by creating a parametric geometrical model for the mitral valve using pathology data available in the literature. This model allows us to conduct studies for different valve dimensions. It is noted that an orthotropic structural model was used to accurately represent the effect of the fibers in the valve material properties.

6.1.1 Two-Way Fluid-Structure Interaction Simulation of the Mitral Valve

The mitral valve undergoes large deformations. The partitioned fluid-structure interaction algorithm is not able to accommodate large deformations and also is not capable to model the complete closing of the valve and simulate the coaptation of the leaflets. In order to accommodate these features, a hybrid architecture has been used that allows the mesh displacement and subsequent re-meshing of the grid. In this framework, when the mesh becomes distorted due to large deformations of the mitral leaflets, a new geometry is created based on the previous step and re-meshing is carried out based on the new geometry while conserving the boundary conditions.

Next, we interpolate the old solution (including fluid velocity, fluid pressure, structural stress, velocity and acceleration) to the new mesh and the FSI simulation is thus continued. For this special purpose, a software program was developed in Fortran to create a precise geometry from the mesh. Also, another program was developed to interpolate the old solution to the new mesh at re-meshing points of simulations. One of the advantages related to this approach is the increased computational efficiency since it is possible to use larger time steps during the simulations. More importantly, this approach allows the model to accurately represent the coaptation of the mitral valve.

The computational model consists of an assembly of the mitral valve and the left ventricular models and these in turn are coupled with arterial, pulmonary and wall motion models. Using the hybrid fluid-structure interaction framework, we conducted a full two-way fluid-structure interaction simulation of the mitral valve within a beating left ventricle. The simulation was initiated at the beginning of the systole phase by moving the left ventricular wall inward to increase the pressure which causes the closing of the mitral valve. We continued the simulation until the complete closure of the mitral valve. At this point, we opened the aortic aperture and let the blood flows out of the left ventricle. The simulation was carried out until the end of systole when we began to move the left ventricular wall outward causing the left ventricular pressure dropped bellow the left atrial pressure rapidly. At this point the mitral valve began to open and let the blood flows into the left ventricle. The resulting jet recoiled back and created a vortex ring.

The original theory of the vortex ring (Gharib *et. al.* [35]) showed that the energy expended on a vortex ring after the critical formation number does not increase the vortex ring energy. Instead, the extra energy makes the vortex ring pinch off. In this study, for the first time, the vortex ring formation for the natural mitral valve was quantified using a fluid-structure interaction model.

From this study, it is concluded that in a healthy LV working under normal conditions (HR=60 bpm and SV=60 mL), the vortex ring pinch off does not take place due to the break between the E and A waves in the diastole phase. This conclusion is consistent with experimental studies conducted by Pierrakos *et. al.* [84] on the prosthetic mitral trileaflet valve. It is also concluded that the energy being exerted to the vortex ring during the E wave increases the circulation of the vortex ring up to the end of the E wave with no local maximum. Then, in the break between the E and A, the vortex ring circulation reduces due to the shear stress and finally, during

the A wave, vortex ring circulation increases up to the end of diastole. For the larger stroke volumes, if we had the stroke volume in one wave, the pinch off would happen around formation number 4, as observed in other reported studies ([84] and [53]). Since the vortex ring is an important factor in the diastolic efficiency, the results of this model can be used for optimum design mitral valve repair such as edge-to-edge operation to preserve the vortex ring energy at the most.

6.1.2 Two-Way Fluid-Structure Interaction Simulation of Septal-Anterior Motion of the Mitral Valve in Obstructive Hypertrophic Cardiomyopathy

Systolic Anterior Motion of the mitral valve (SAM) in hypertrophic cardiomyopathy was studied next. The diseased left ventricle was constructed by making the septal wall thicker, thus occupying 40 percent of the left ventricular volume. In this study, the left ventricular motion was not simulated due the complexity and lack of medical data. Instead, a systolic mass flow to the lateral ventricular wall was applied. This is an acceptable approximation since in hyperthrophic cardiomyopathy, the thick septum does not contribute to the pumping motion of the heart. The simulation was initiated with the mitral valve fully relaxed. The flow started from the lateral wall slowly converging toward the mitral valve opening thus causing it to close. At this point, the aortic orifice was opened and the flow rushed out. Since the outflow track is partially blocked by the thickened septum, a pressure drop was observed resulting in a high velocity flow between the thickened septum and the anterior leaflet. As the systole progressed, the pressure continues to drop and the coaptation of the anterior leaflet decreased due to loss of back pressure until it opened partially. At this point, the flow rushes into the left atrium causing further opening of the mitral valve. This simulation accurately described the malfunctioning of the left ventricle and mitral valve for a diseased left ventricle. One of the clinical solutions for the OHCM is myotomy-myectomy (septal myectomy) surgery [73] in which a part of thickened septum is removed to provide wider outflow track and consequently avoiding the SAM. Normally, this cut begins from near aortic annulus to just bellow the tip of anterior mitral leaflet. The length and depth of the resected tissue are important factors since the excessive depth increase the risk of left ventricular-septal defects and shortage of depth and length resected tissue will decrease the chance of removing the SAM. The FSI model of the OHCM can provide a computational tool to optimize septal myectomy prior the operation.

6.1.3 Accelerated Heart Valve Durability Tester

In the context of an industrial collaboration with Vivitro Inc., a novel accelerated durability and fatigue artificial valve tester was evaluated using the computational framework. This device consists of an impeller to drive the flow back and forth through the mechanical heart valve. The geometry was constructed to simulate the impeller propulsion as an immersed solid with angular momentum sources. This is accurate since the fluid does not have any effect on the rotation of the impeller. A rigid body dynamic model of the mechanical heart valve was included. The impeller rotated back and forth according to a sinusoidal function. The performance of the equipment was evaluated with three impellers and one impeller installed close to the valve. The evolution of the flow pattern during a full cycle was quantified and design decisions have been made on the performance of the device.

6.2 Study Limitations

Although the fluid-structure interaction framework developed in this thesis represents an accurate global representation of the hemodynamics of the left ventricle with the mitral valve, the model needs to be improved near the localized regions where singular discontinuities exist. The lack of physiological data further complicated the evaluation and verification of results. Finally, while the simulations were carried out in a personal computer, the complexity of the model for a parametric study would require the use of super-computers, especially in the regions of sharp geometrical discontinuities such as the leaflet ends of the mitral valve.

6.3 Future Work

- **Experimental Validation with In-vivo MRI or Ecocardiographic Data:** The FSI framework results will be required to be evaluated and verified against physiological data. To this end, the following future work is proposed:

    1. Replace the left ventricular ellipsoidal model with a time series of 3D wire frame geometry of left ventricle extracted from clinical images.
    2. Develop a model to calculate the momentum which the left ventricular wall applies to the blood at each time step.
    3. Measure the pressure for the inflow/outflow data and impose as boundary conditions on the mitral and aortic orifices respectively.
    4. Perform the FSI simulation with the real left ventricular beating geometry.

5. Compare the computational results with clinical data

A brief literature review of the available imaging data regarding the hemodynamics of left ventricular flow is presented and these papers would provide the basis for the evaluation and verification framework.

Kerwin *et. al.* [52] visualized the vortex ring streamlines and calculated vorticity using MR images. They used 6 to 9 MR images at equal angular distance about the MV center-apex axis. They presented the asymmetric diastolic vortex ring in these series of images which are similar to our work. Also, they presented the graph of circulation as a function of diastolic time. Similar to our work this shows to local maximum belonging to the E and A waves.

Saber *et. al.* [89, 90] developed a combined CFD and MRI methodology to simulate blood flow in the left ventricle. In his framework he used time-resolved left ventricular MR images to construct 3D geometry of the left ventricle and then he used this geometry in the CFD model. They calculated the left ventricular momentum between the consecutive images and imposed it to the blood in the CFD model. Similar to our work, their results show that the diastolic inflow jet forms an asymmetric vortex ring in the left ventricle which becomes larger as the diastole progresses. They also noted that their calculated diastolic velocities are overestimated because of underestimation of mitral valve orifice.

Schenkel *et. al.* [93] constructed 3D left ventricular geometry using time dependent left ventricular MR images and used these geometries in his CFD model as moving boundary condition. Similarly, they were able to capture the formation of asymmetric diastolic vortex ring but they noted that the vortex ring is extremely sensitive to the change in the inflow (mitral orifice) boundary conditions.

Geest et. al. [98] developed and implemented an algorithm for automatic detection of left ventricular wall using time series of MR images based on active appearance motion model. Also, Codreanu *et. al.* [15] used tissue phase mapping MR to detect twisting and longitudinal movement of left ventricle in systole. Moreover, Kvitting *et. al.* [58] implemented a phase contrast technique to create time series of 3D left ventricular geometry.

Markl *et. al.* [69] used phase contrast cardiovascular MR to measure and visualize the three components of left ventricular velocity at any time in the cardiac

cycle. They visualized the systolic velocity streamlines in the left ventricle and aorta. They showed that the systolic streamlines begin from left ventricular wall and straighten toward the aorta which shows that our systolic flow pattern is consistent with their report. They also visualized the diastolic vortex ring in both left and right ventricle.

Long *et. al.* [63] attempted to simulate the left ventricular blood flow using a patient specific model using MR images. Similar to other works, they extracted the time series of left ventricular geometry from MR images and used them as moving wall boundary conditions in his CFD model. They reported that when the diastolic blood jet reaches two-third of the mitral-apex distance, it starts to recoil and form a vortex ring.

Bolger *et. al.* [27] used time resolved phase contrast velocity mapping to measure and visualize the velocity profile and kinetic energy of diastolic inflow blood into the left ventricle. These data can be used as accurate boundary conditions for the mitral aperture in our FSI framework.

- **New prosthetic mitral valve:** Currently, the FDA has approved the implementation of artificial mitral valves such as tri-leaflet prosthetic valves. However, due to the surgical complexity, FDA has not approved bileaflet prosthetic mitral valves. The computational tool developed here can be used to characterize the hemodynamics of bileaflet chordaeless prosthetic mitral valves;

- **Edge to Edge Mitral Valve Repair:** Edge to edge mitral valve repair is one of the surgical procedure used to fix the malfunction of the mitral valve. The fluid-structure framework can also be used by practitioners to properly plan the procedure by having a-priori knowledge of the physiological parameters of the patient;

- **Left ventricular geometry and motion:** A semi-ellipsoidal model for the geometry of the left ventricle was used in this research. Real geometry of the LV based on the time history provided by medical images could be used to improve the accuracy of the model;

- **Structure of myocardium:** The structural representation of the myocardium can be improved by implementing a fiber composite hyperelastic structural model;

- **Boundary conditions:** The circuit analogy of the arterial and pulmonary circuits can be customized for patients using measured medical data.
- **Aortic valve:** The complete model of the cardiovascular cycle can be further improved by the aortic model instead of prescribing a set of boundary conditions.
- **Flexible Mitral Annulus:** For the sake of simplicity, we considered the mitral annulus rigid while in reality the mitral annulus is flexible and deforms during the cardiac cycle. This feature can be included by applying elastic boundary conditions to the to the mitral annulus in the structural solver and applying the geometrical changes to the left ventricular base in every FSI coupling step.
- **Motion of the Papillary Muscles:** In this model, we fixed the end points of the mitral chordaes (cables) to two stationary points. In reality, the chordaes are connected to the papillary muscles which expand and contract during a cardiac cycle. This can be included by implementing a lump model to calculate the motion of the papillary muscles and displacing the two points according to the lump model.

Bibliography

[1] N J Tustison D Abendschein and A A Amini. Biventricular myocardial kinematics based on tagged mri from anatomical nurbs models. In *IEEE Computer Society Conference on Computer Vision and Pattern Recognition*, pages 124–131, San Francisco, CA, USA, 2004.

[2] Au AD and Greenfield HS. Computer prediction of thrombogenic sites for a tilting-disc prosthetic heart valve. *Comput. Biomed. Res.*, 10:165–182, 1977.

[3] J. Alexander, Jr. Sunagawa, K. Chang, and K. Sagawa. Instanous pressure-volume relation of the ejecting canine left atrium. *Circ. Res.*, 61:209–219, 1987.

[4] S. Aluri and K. B. Chandran. Numerical simulation of mechanical mitral heart valve closure. *Annals of Biomedical Engineering*, 29.

[5] Bernardo Baccani, Federico Domenichini, and Gianni Pedrizzettib. Model and influence of mitral valve opening during the left ventricular filling. *Journal of Biomechanics*, 36:355–361, 2003.

[6] Bernardo Baccani, Federico Domenichini, Gianni Pedrizzettib, and Giovanni Tontic. Fluid dynamics of the left ventricular fillingin dilated cardiomyopathy. *Journal of Biomechanics*, 35:665–671, 2002.

[7] B. J. Bellhouse. Fluid mechanics of a model mitral valve and left ventricle. *Cardiovascular Research*, 6:199–210, 1972.

[8] Rafael Beyar and Samuel Sideman. A model of left ventricular contraction and transmural ventricular deformation. *IEEE*.

[9] R. Cannon, C. L. McIntosh, W. H. Schenke, B. J. Maron, R. Bonow, and S. E. Epstein. "elfect of surgical reduction of left ventricular outflow obstruction on hemodynamics, coronary flow, and myocardial metabolism in hypertrophic cardiomyopathy". *Circulation*, 79:766–775, 1989.

[10] Burriesci Carmody, C., G., Howard I.C., and E.A. Patterson. An approach to the simulation of fluid-structure interaction in the aortic valve. *J. Biomech.*, 96:256–263, 2005.

[11] Ling Chen and Karen May-Newman. Effect of strut chordae transection on mitral valve leaflet biomechanics. *Annals of Biomedical Engineering*, 34(6):917–926, June 2006.

[12] Ling Chen, Andrew D Mcculloch, and Karen May-Newman. Relationship between collagen fibrils, glycosaminoglycans, and stress relaxation in mitral valve chordae tendineae. *Annals of Biomedical Engineering*, 32(12):1599–1606, Dec 2004.

[13] C. S. Chung and M. Karamanoglu. "duration of diastole and its phases as a function of heart rate during supine bicycle exercise". *Am. J. Physiol. Heart. Circ. Physiol.*, 287:H2003–H2008, 2004.

[14] R. P. Cochran, K. S. Kunzelman, C. J. Choung, M. S. Sacks, and R. C. Eberhart. Nondestructive analysis of mitral valve collagen fiber orientation. *The Annals of thoracic surgery*, 37(3):447–450, May 1991.

[15] I. Codreanu, M. D. Robson, S. J. Golding, B. A. Jung, K. Clarke, and C. J. Holloway. "longitudinally and circumferentially directed movements of the left ventricle studied by cardiovascular magnetic resonance phase contrast velocity mapping". *Journal of Cardiovascular Magnetic Resonance*, 12(48):1–8, 2010.

[16] Peskin CS and McQueen DM. A three dimensional computational method for blood flow in the heart. i. immersed elastic fibers in a viscous incompressible fluid. *J. Comput. Phys.*, 81:372–405, 1989.

[17] Peskin CS and McQueen DM. A three dimensional computational method for blood flow in the heart. ii. contractile fibers. *J. Comput. Phys.*, 82:289–297, 1989.

[18] Peskin CS and McQueen DM. Fluid dynamics of the heart and its valves.", in case studies in mathematical modeling-ecology, physiology, and cell biology. *J. Comput. Phys.*, 86:410–415, 1997.

[19] T.E. David, R. Pusdunarm, J. Ivanov, and et al. "aortic valve replacement with stentless and stented porcine valves: A case-match study". *J Thorac Cardiovasc Surg*, 116:236–241, 1998.

[20] de Hart J, Peters GWM, Schreurs PJG, and Baaijens FPT. A computational fluid-structure interaction analysis of a fiber-reinforced stentless aortic valve. *J. Biomech.*, 36:699–712, 2003.

[21] Stevenson DM, Yoganathan AP, and Williams FP. Numerical simulation of steady turbulent flow through trileaflet aortic heart valves - ii. results on five models. *J. Biomech.*, 18:909–926, 1985.

[22] Stevenson DM and AP. Yoganathan. Numerical simulation of steady turbulent flow through trileaflet aortic heart valves - i. computational scheme and methodology. *J. Biomech.*, 18:899–907, 1985.

[23] F. Domenichini, G Pedrizzetti, and B Baccani. Three-dimensional filling flow into a model left ventricle. *J. Fluid Mech.*, 539:179–198, 2005.

[24] Rumei Dong, Ying Sun, Frederick J Vetter, , and Salvatore A Chiaramida. Time-varying left ventricular elastance determined by a finite element model. *IEEE*.

[25] S. S. D'Souza, M. Butterfield, and J. Fisher. "kinematics of synthetic flexible leaflet heart valves during accelerated testing". *The Journal of Heart Valve Disease*, 12:110–120, 2003.

[26] J G Dumesnil and J L Laurenceau. A mathematical model of the dynamic geometry of the intact left ventricle and its application to clinical data. *Circulation*, 59(5), 1979.

[27] Bolger A. F., E. Heiberg, M. Karlsson, M. Wigstrom, J. Engvall, A. Sigfridsson, T. Ebbers, J. P. E. Kvitting, C. J. Carlhall, and B. and Wranne. "transit of blood flow through the human left ventricle mapped by cardiovascular magnetic resonance". *Journal of Cardiovascular Magnetic Resonance*, 9:741–747, 2007.

[28] C. Farhat, C. Degand, B. Koobus, , and M. Lesoinne. "torsional springs for two-dimensional dynamic unstructured fluid meshes". *Computer Methods in Applied Mechanics and Engineering*, 163:231–245, 1998.

[29] FDA, Rockville, Maryland, and USA. FDA - replacement heart valve guidance, 1994.

[30] B. E. Fettel, D. R. Johnston, and P. E. Morris. "accelerated life testing of prosthetic heart valves". *Medical Instrumentation*, 14(4):161–164, May-June 1980.

[31] Underwood FN and Mueller TJ. Numerical analysis of blood flow in the heart. *J. Comput. Phys.*, 25:220–252, 1977.

[32] Underwood FN and Mueller TJ. Numerical study of the steady axisymmetric flow through a disk-type prosthetic heart valve in a constant diameter chamber. *J. Biomech. Eng.*, 99:91–97, 1977.

[33] Underwood FN and Mueller TJ. Numerical study of the steady axisymmetric flow through a disk-type prosthetic heart valve in an aortic-shaped chamber. *J. Comput. Phys.*, 101:198–204, 1979.

[34] European Committee for Standardization. CEN prop. standard en 12006-1, 1995.

[35] M. Gharib, E. Rambod, and K Shariff. "a universal time scale for vortex ring formation". *J. Fluid. Mech.*, 360:121–140, 1998.

[36] Jonathan S Grashow, Ajit P Yoganathan, and Michael S Sacks. Biaixal stress–stretch behavior of the mitral valve anterior leaflet at physiologic strain rates. *Annals of Biomedical Engineering*, 34(2):315–325, Feb 2006.

[37] E. Hayek, C.N. Gring, and B.P. Griffin. Mitral valve prolapse. *Lancet*, 365(9458):507–518, Feb 2005.

[38] Heart and Stroke Foundation of Canada, June 2009. http://www.heartandstroke.com/site/c.ikIQLcMWJtE/b.2796497/k.BF8B/Home.htm?src=h

[39] B. Hiot, E. Pionen, and N Dalton. Doppler color flow mapping studies of jet formation and spatial orientation in obstructive hypertrophic cardiomyopathy. *Am Heart J*, 117:1119–1126, 1989.

[40] S. Hirschfeld and R. Meyer. "the isovolumic contraction time of the left ventricle. an echographic study". *Circulation*, 54:751–756, 1976.

[41] Zhenhua Hu, Dimitris Metaxas, and Leon Axel. Computational modeling and simulation of heart ventricular mechanics with tagged mri. *ACM.*

[42] Merkle C L Huang Z J, Abdallah S, and Tarbell J M. Numerical simulation of steady turbulent flow through trileaflet aortic heart valves - i. computational scheme and methodology. *J. Biomech.*, 27:391–402, 1994.

[43] Jacques M Huyghe, Theo Arts, Dick H Van Campen, and Robert S Reneman. Porous medium finite element model of the beating left ventricle. *Am. J. Physiol.*, 262.

[44] A Bosnjak Is, G Montilla, V Torrealba B Solaiman, and C Row. 3d segmentation of the left ventricle in echocardiographic images using deformable model based on the geometric evolution shapes. *Computers in Cardiology*, 27.

[45] Streeter D D J and W T Hanna. Engineering mechanics for successive states in canine left ventricular myocardium. 1. cavity and wall geometry. *Circ. Res.*, 33.

[46] Ronald F Janz and Arthur F Grimm. Finite-element model for the mechanical behavior of the left ventricle: Prediction of deformation in the potassium-arrested rat heart. *Circulation Research*, 30.

[47] Morten O J Jensen, Arnold A Fontaine, and Ajit P Yoganathan. Improved in vitro quantification of the force exerted by the papillary muscle on the left ventricular wall: Three-dimensional force vector measurement system. *Annals of Biomedical Engineering*, 29.

[48] Jorge Hernan Jimenez, Dennis Dam Soerensen, Zhaoming He, Jennifer Ritchie, , and Ajit P Yoganathan. Mitral valve function and chordal force distribution using a flexible annulus model: An in vitro study. *Annals of Biomedical Engineering*, 33(5):557–566, May 2005.

[49] Meisner J.S., Keren G., Pajaro O.E., and Mani A. Atrial contribution to ventricular filling in mitral stenosis. *Circulation*, 84:1469–1480, 1991.

[50] Elie H. Karam and Antoine B. Abche. Left ventricular model using second order electromechanical coupling: Effects of viscoelastic damping. *Transactions On Engineering, Computing And Technology*, 11.

[51] Michael R Kaus, Jens Von Berg, Jurgen Weese, Wiro Niessen, and Vladimir Pekar. Automated segmentation of the left ventricle in cardiac mri. *Medical Image Analysis*, 8.

[52] W. S. Kerwin, D. Owens, J. Hertzberg, R. Shandas, and E. Gill. "vortex ring formation in diastolic dysfunction: Phase contrast mri of left ventricular filling". *Proc. Intl. Soc. Mag. Reson. Med.*, 16, 2008.

[53] A. Kherdavar and M. Gharib. "influence of ventricular pressure drop on mitral annulus dynamics through the process of vortex ring formation". *Annals of Biomedical Engineering*, 35(12):2050–2064, December 2007.

[54] Kwak D Kiris C, Rogers SE, and Chang ID. Computational approach for probing the flow through artificial heart devices. *Med. Eng. Phys.*, 119:452–460, 1997.

[55] K. S. Kunzelman, R. P. Cochran, W. Steves Ring, Choung C., E. D. Verrier, and R. C. Eberhart. Stress/strain characteristics of porcine mitral valve tissue: Parallel versus perpendicular collagen orientation. *Journal of Cardiac Surgery*, 7(1):71–78, May 1992.

[56] K. S. Kunzelman, R. P. Cochran, W. Steves Ring, Choung C., E. D. Verrier, and R. C. Eberhart. Finite element analysis of the mitral valve. *J. Heart Valve Dis.*, 2(3):326–340, May 1993.

[57] K. S. Kunzelman, R. P. Cochran, E. D. Verrier, and R. C. Eberhart. Anatomical basis for mitral valve modeling. *J. Heart Valve Dis.*, 3(5):491–496, Sep 1994.

[58] J. P. E. Kvitting, T. Ebbers, J. Engvall, G. R. S. Sutherland, B. Wranne, and L. Wigstrom. "three-directional myocardial motion assessed using 3d phase contrast mri". *Journal of Cardiovascular Magnetic Resonance*, 6(3):627–636, 2004.

[59] Chandran KB Lai YG and Lemmon J. A numerical simulation of mechanical heart valve closure fluid dynamics. *J. Biomech.*, 35:881–892, 2002.

[60] V. Q. Lance and H. Spodik. "heart rate left ventricular ejection time relations". *British Heart Journal*, 38:1332–1338, 1976.

[61] Lei, Ming, Parthasarathy, V, Makhijani, and V B. Flow in an integrated model of heart and aorta. In *Proceeding of ASME Bioengineering Conference*, volume 50, pages 123–129, Warsaw, Poland, Aug 2001.

[62] Jun Liao and Ivan Vesely. Nonhomogeneous deformation in the anterior leaflet of the mitral valve. *Annals of Biomedical Engineering*, 32(7):977–983, Jul 2004.

[63] Q. Long, R. Merrifield, X. Y. Xu, P. Kilner, D. N. Firmin, and G. Z. Yang. "subject-specific computational simulation of left ventricular flow based on magnetic resonance imaging". *J. Engineering in Medicine*, 222:475–485, 2008.

[64] Cristian Lorenz and Jens Von Berg. A comprehensive shape model of the heart"; medical image analysis. *Medical Image Analysis*, 10.

[65] Dieuddonne J M. Left ventricle as confocal prolate spheroids. *Bull Math Biophys*, 31.

[66] Krafczyk M, Cerrolaza M, Schulz M, and Rank E. Analysis of 3d transient blood flow passing through an artificial aortic valve by lattice-boltzmann methods. *Med. Eng. Phys.*, 31:453–462, 1998.

[67] Nakamura M, Wada S, and Yokosawa S. Flow in an integrated model of heart and aorta. In *XXIICTAM*, volume 2, pages 124–131, Warsaw, Poland, Aug 2004.

[68] Norberto Malpica, Mara Ledesma-Carbayo, Andrs Santos, Esther Prez, M Angel Garca-Fernandez, and Manuel Desco. A coupled active contour model for myocardial tracking in contrast echocardiography. *Image understanding and analisys.*

[69] M. Markl, P. J. Kilner, and T. Ebbers. "comprehensive 4d velocity mapping of the heart and great vessels by cardiovascular magnetic resonance". *Journal of Cardiovascular Magnetic Resonance*, 13(7):1–22, 2011.

[70] B. Maron and J. Gottdiener. Dynamic subaortic obstruction in hypertrophic cardiomyopathy: analysis by pulse duppler echocardiography. *J Am Col Cardiol*, 6:1–15, 1985.

[71] B. J. Maron. "hypertrophic cardiomyopathy a systematic review". *JAMA*, 287:1308–1320, 2002.

[72] Peskin C S. McCracken M F. A vortex method for blood flow through heart valves. *J. Comput. Phys.*, 35:183–205, 1980.

[73] C.L. McIntosh and B.J. Maron. "current operative treatment of obstructive hypertrophic cardiomyopathy". *Circulation*, 78:487–495, 1988.

[74] King MJ, Corden J, David T, and Fisher J. A three-dimensional, time-dependent analysis of flow through a bileaflet mechanical heart valve: comparison of experimental and numerical results. *J. Biomech.*, 29:609–618, 1996.

[75] King MJ, David T, and Fisher J. An initial parametric study on fluid flow through bileaflet mechanical heart valves using computational fluid dynamics. *J. Eng. Med.*, 208:63–72, 1994.

[76] King MJ, David T, and Fisher J. Three dimensional study of the effect of two leaflet opening angles on the time-dependent flow through a bileaflet mechanical heart valve. *Med. Eng. Phys.*, 29:235–241, 1997.

[77] Sherrid M.V., Chu C.K., and Delia E. Echocardiographic study of the fluid mechanics of obstruction in hypertrophic cardiomyopathy. *JACC*, 22:816–825, 1993.

[78] R. Nishimura, A. Tajik, and G. Reeder. Evaluation of hypertrophic cardiomyopathy by doppler color flow imaging. *Myo Clin Proc*, 61:631–639, 1986.

[79] The International organization for Standardization. "ISO standard 5840", 2005.

[80] Patterson, E.A., I.C. Howard, Thornton, and M.A. Comparative study of linear and nonlinear simulations of the leaflets in a bioprosthetic heart valve during the cardiac cycle. *J. Biomech.*, 24:549–562, 1991.

[81] C. S. Peskin. "numerical analysis of blood flow in the heart". *J. Comput. Phys.*, 25:220–252, 1977.

[82] C. S. Peskin. "the immersed boundary method". *Acta Numerica*, 11:1–39, 2002.

[83] McQueen DM. Peskin CS. Modeling prosthetic heart valves for numerical analysis of blood flow through the heart. *J. Comput. Phys.*, 37:113–132, 1980.

[84] O. Pierrakos and P. P. Vlachos. "the effect of vortex formation on left ventricular filling and mitral valve efficiency". *J. Biomech. Eng.*, 128(4):527–540, August 2006.

[85] C. Polick, H. Rakowaski, and E Wigle. Muscular subaortic stenosis: the quantitative relatioship between systolic anterior motion and the pressure gradient. *Circulation*, 69:43–49, 1984.

[86] M. Rosenfeld, E. Rambod, and Gharib M. "circulation and formation number of laminar vortex rings". *J. Fluid. Mech.*, 376:297–318, 1998.

[87] Aluri S and Chandran KB. Numerical simulation of mechanical mitral heart valve closure. *Ann. Biomed. Eng.*, 29:665–676, 2001.

[88] Peskin C S. Flow patterns around heart valves: a numerical method. *J. Comput. Phys.*, 10:252–271, 1972.

[89] N. R. Saber, A. D. Gosman, N. B. Wood, P. J. Kilner, C. L. Charrier, and D. N. Firmin. "computational flow modeling of the left ventricle based on in vivo mri data: Initial experience". *Annals of Biomedical Engineering*, 29:275–283, 2001.

[90] N. R. Saber, A. D. Gosman, N. B. Wood, P. J. Kilner, C. L. Charrier, and D. N. Firmin. "progress towards patient-specific computational flow modeling of the left heart via combination of magnetic resonance imaging with computational fluid dynamics". *Annals of Biomedical Engineering*, 31:42–52, 2003.

[91] M S Sacks, Z He, L Baijens, S Wanant, P Shah, H Sugimoto, , and A P Yoganathan. Surface strains in the anterior leaflet of the functioning mitral valve. *Annals of Biomedical Engineering*, 30.

[92] J Sainte-Marie, D Chapelle, R Cimrman, and M Sorine. Modeling and estimation of the cardiac electromechanical activity. *Computers and Structures*, 84:1743–1759, 2006.

[93] T. Schenkel, M. Malve, M. Reik, M. Markl, B. Jung, and H. Oertel. "mri-based cfd analysis of flow in a human left ventricle: Methodology and application to a healthy heart". *Annals of Biomedical Engineering*, 37(3):503–515, 2009.

[94] M. Shusser and M. Gharib. "energy and velocity of a forming vortex ring". *Physics of Fluids*, 12(3):618–622, 2000.

[95] Helene A Simon, Hwa-Liang Leo, Josie Carberry, and Ajit P Yoganathan. Comparison of the hinge flow fields of two bileaflet mechanical heart valves under aortic and mitral conditions. *Annals of Biomedical Engineering*, 32(12):1607–1617, Dec 2004.

[96] Idelsohn SR, Costa LE, and Ponso R. A comparative computational study of blood flow through prosthetic heart valves using the finite element method. *J. Biomech.*, 37:97–115, 1985.

[97] Mario G Tapia, Karyn S Kunzelman, Per G Reinhall, and Richard P Cochran. A three-dimensional coupled fluid-structure computational model of mitral valve function. In *Proceedings of The First Joint BMES/EMBS Conference Serving Humanity and Advancing Technology*, pages 144–150, Atlanta, GA, USA, July 1999.

[98] R. J. van der Geest, B. P. F. Lelieveldt, E. Angelie, M. Danilouchkine, C. Swingen, M. Sonka, and J. H. C. Reiber. "evaluation of a new method for automated detection of left ventricular boundaries in time series of magnetic resonance images using an active appearance motion model". *Journal Of Cardiovascular Magnetic Resonance*, 6(3):609–617, 2004.

[99] J. Vierendeels, K. Dumont, E. Dick, and P. Verdonck. "analysis and stabilization of fluidstructure interaction algorithm for rigid-body motion". *AIAA Journal*, 43(12):2549–2557, Dec 2005.

[100] Hiroshi Watanabe, Seiryo Sugiura, Hidenobu Kafuku, , and Toshiaki Hisada. Multiphysics simulation of left ventricular filling dynamics using fluid-structure interaction finite element method. *Biophysical Journal*, 87:2074–2085, 2004.

[101] P N Watton, X Y Luo, R Singleton, X Wang, G M Bernacca, P Molloy, and D J Wheatley. Modelling chorded prosthetic mitral valves using the immersed boundary method. In *Proceedings of the 26th Annual International Conference of the IEEE EMBS*, pages 124–131, San Francisco, CA, USA, Sep 2004.

[102] N. Westerhof, G. Elzinga, and P. Sipkema. An artificial arterial system for pumping hearts. *J. Appl. Physiol.*

[103] E. Wigle. hypertrophic cardiomyopathy: a 1987 viewpoint. *Circulation*, 75:311–322, 1987.

[104] H. E. Wilson and H. D. Stokes. "an accelerated fatigues tester for flexible heart valve prostheses". *Dis. Chest.*, 45:528–532, 1964.

[105] Richard G Wise, Christopher L-H Huang, Ahmed I M Al-Shafei, T Adrian Carpenter, and Laurance D Hall. Geometrical models of left ventricular contraction from mri of the normal and spontaneously hypertensive rat heart. *Phys. Med. Biol.*, 44.

[106] Ling Xia, Meimei Huo, Qing Wei, Feng Liu, and Stuart Crozier. Analysis of cardiac ventricular wall motion based on a three-dimensional electromechanical biventricular model. *Phys. Med. Biol.*, 50.

[107] Cheng Y, Oertel H, and Schenkel T. Fluid-structure coupled cfd simulation of the left ventricular flow during filling phase. *Annals of Biomedical Engineering*, 33:567–576, May 2005.

[108] Liang Zhong, Dhanjoo N Ghista, Eddie Y K Ng, Soo T Lim, Terrance S J Chua, and Chuen N Lee. Left ventricular shape-based contractility index. *Journal of Biomechanics*, 39:2397–2409, 2006.

Appendix A

Time History Results of Chapter 2

In this appendix we presented selected time history results of chapter 2. Figure A.1 depicts the velocity vectors on the long axis (symmetry plane) for the stroke volume of 60 mL, heart rate of 60 bpm. Figure A.2 presents the velocity vectors in the anterio-posterior plane. Figure A.3 displays the 3D velocity streamlines in the symmetry plane. Figures A.4 and A.5 depicts the velocity contours in the symmetry and anterio-posterior planes respectively. Figure A.6 presents pressure contours in the symmetry plane. Figures A.7 and A.8 depicts the vorticity contours in the symmetry and anterio-posterior planes. The figure A.9 displays the velocity contours on the mitral orifice plane. Finally figures A.10 and A.11 show the velocity vectors in the symmetry and anterio-posterior planes for the stroke volume of 30 mL and heart rate of 60 bpm.

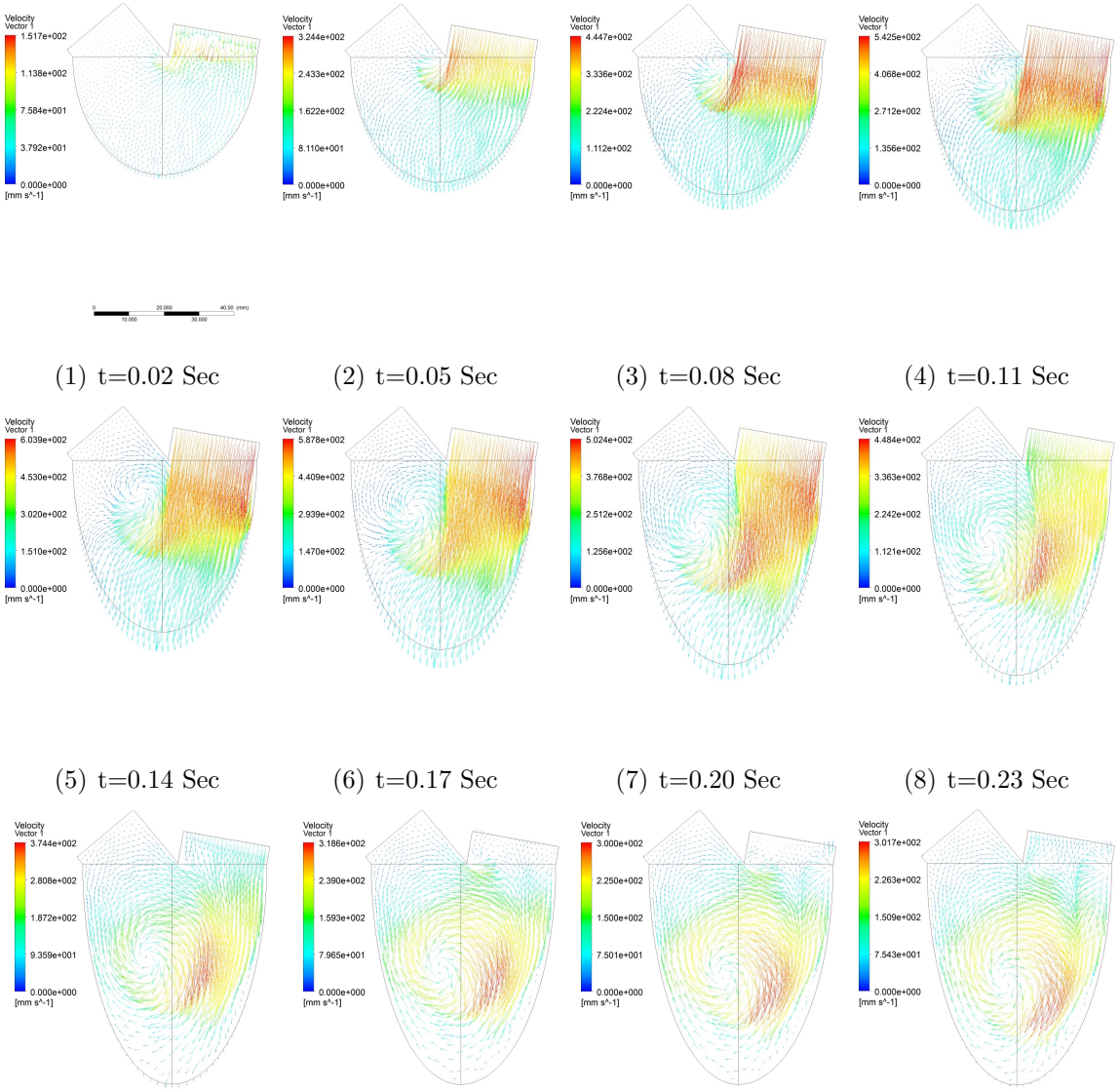

(1) t=0.02 Sec (2) t=0.05 Sec (3) t=0.08 Sec (4) t=0.11 Sec

(5) t=0.14 Sec (6) t=0.17 Sec (7) t=0.20 Sec (8) t=0.23 Sec

(9) t=0.26 Sec (10) t=0.29 Sec (11) t=0.32 Sec (12) t=0.35 Sec

Figure A.1: Velocity vectors in the long axis (symmetry) view. SV=60 ml, HR=60 bpm.

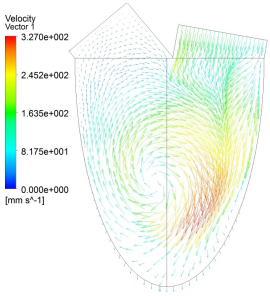

(13) t=0.36 Sec

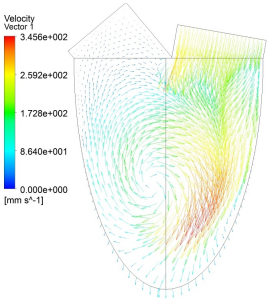

(14) t=0.37 Sec

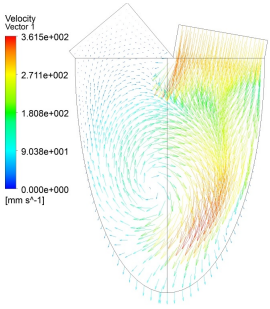

(15) t=0.38 Sec

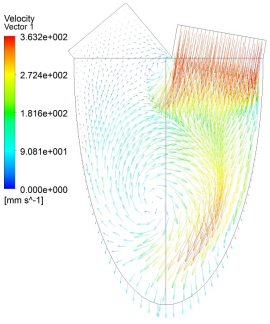

(16) t=0.41 Sec

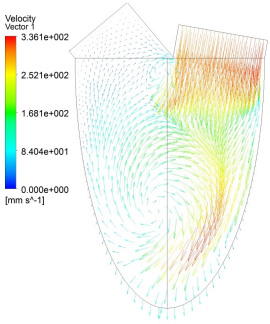

(17) t=0.42 Sec

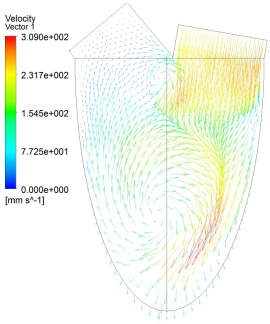

(18) t=0.43 Sec

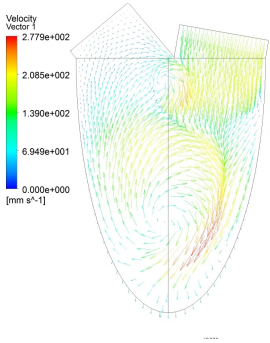

(19) t=0.44 Sec

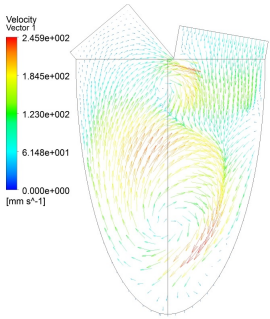

(20) t=0.45 Sec

Figure A.1: Velocity vectors in the long axis (symmetry) view. SV=60 ml, HR=60 bpm(cont).

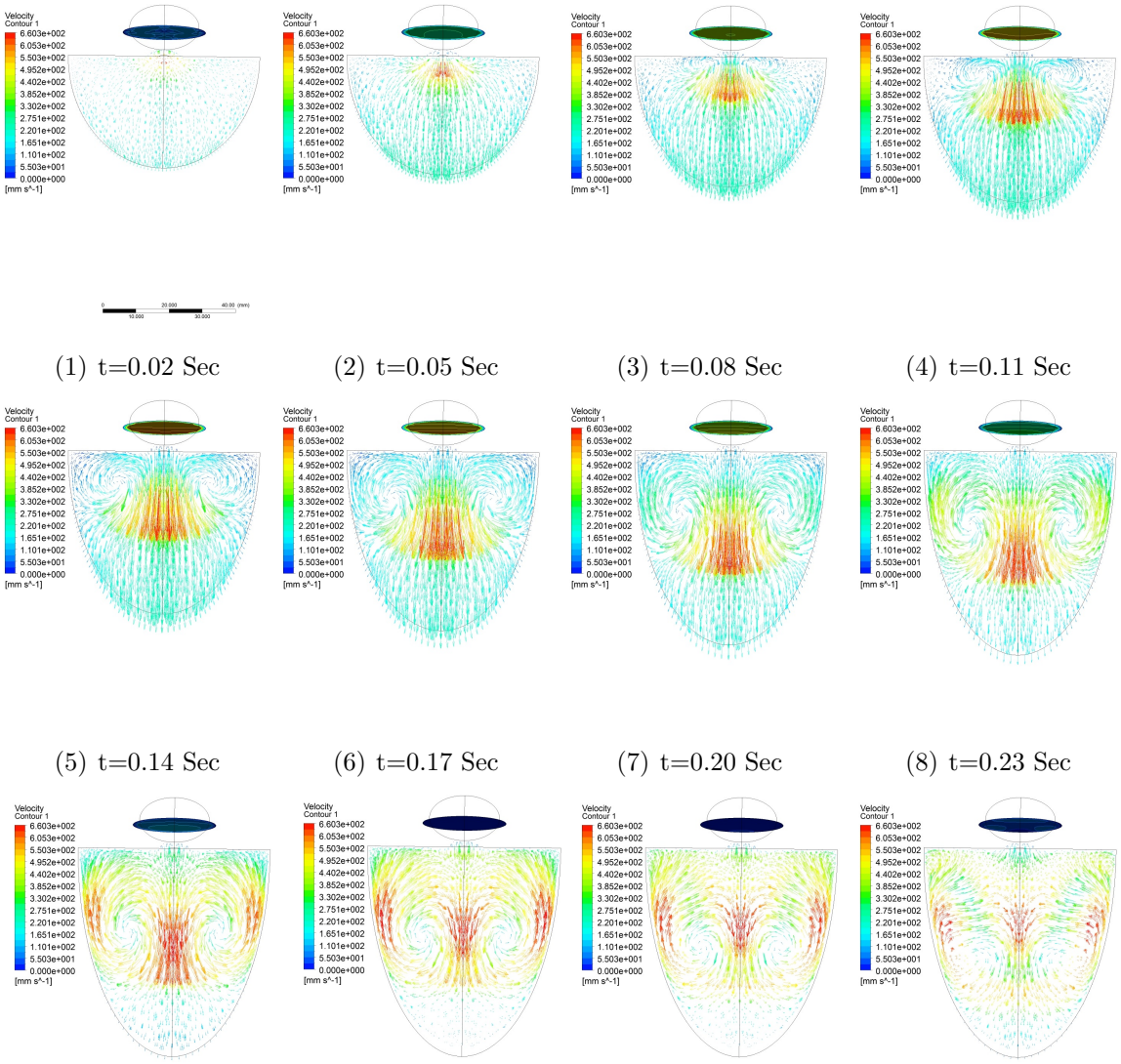

(1) t=0.02 Sec (2) t=0.05 Sec (3) t=0.08 Sec (4) t=0.11 Sec

(5) t=0.14 Sec (6) t=0.17 Sec (7) t=0.20 Sec (8) t=0.23 Sec

(9) t=0.26 Sec (10) t=0.29 Sec (11) t=0.32 Sec (12) t=0.35 Sec

Figure A.2: Velocity vectors in the Anterio-Posterior view. SV=60 ml, HR=60 bpm.

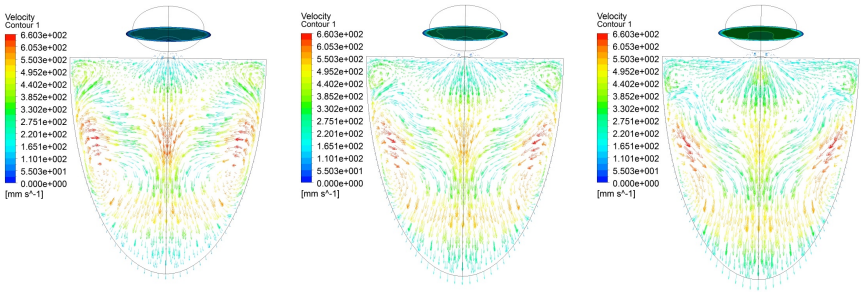

(13) t=0.36 Sec (14) t=0.37 Sec (15) t=0.38 Sec

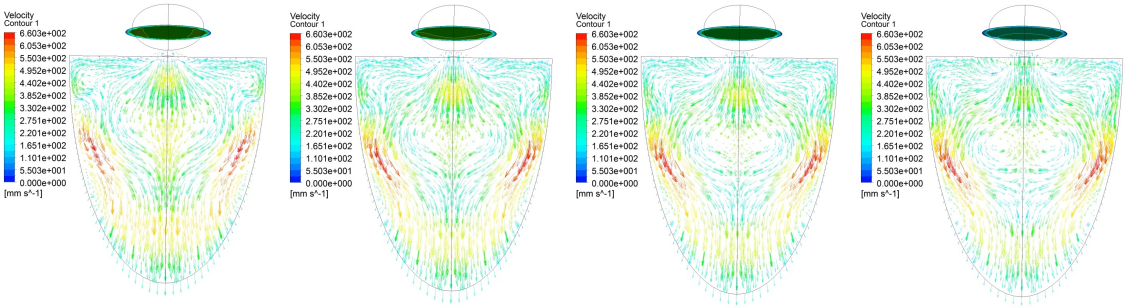

(16) t=0.39 Sec (17) t=0.41 Sec (18) t=0.42 Sec (19) t=0.43 Sec

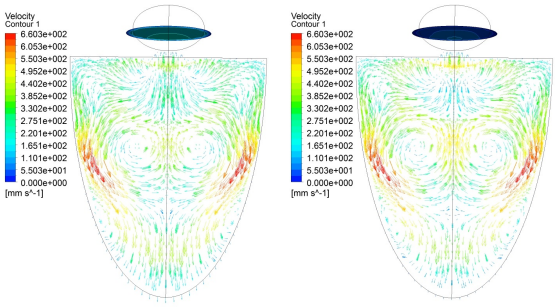

(20) t=0.44 Sec (21) t=0.45 Sec

Figure A.2: Velocity vectors in the Anterio-Posterior view. SV=60 ml, HR=60 bpm(cont).

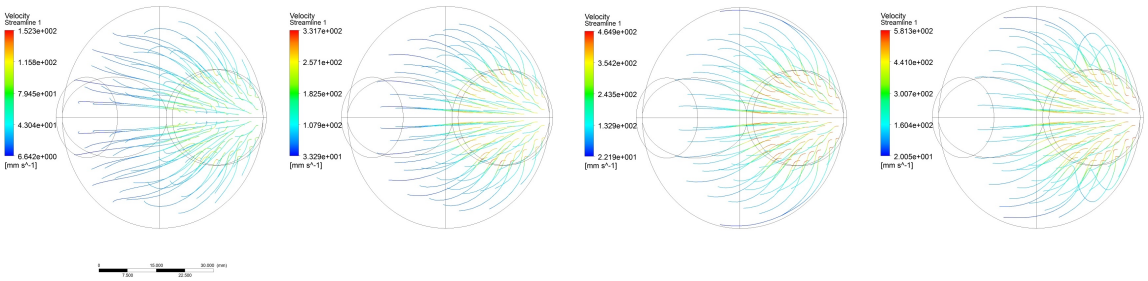

(1) t=0.02 Sec (2) t=0.05 Sec (3) t=0.08 Sec (4) t=0.11 Sec

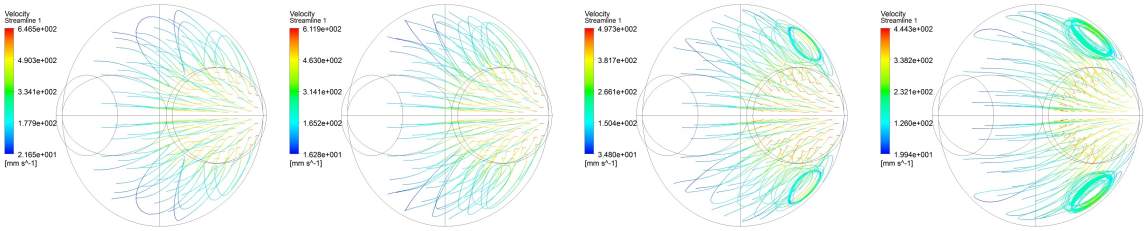

(5) t=0.14 Sec (6) t=0.17 Sec (7) t=0.20 Sec (8) t=0.23 Sec

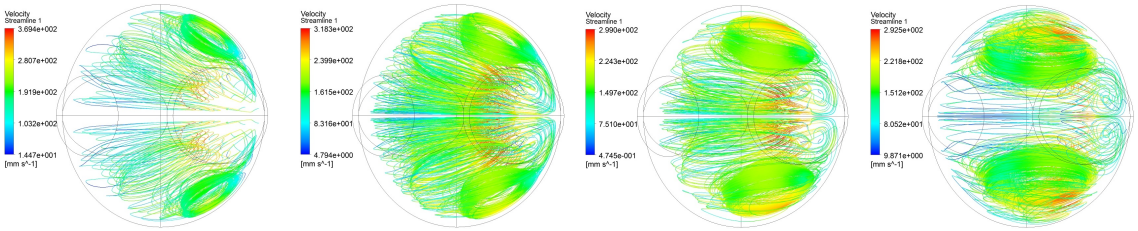

(9) t=0.26 Sec (10) t=0.29 Sec (11) t=0.32 Sec (12) t=0.35 Sec

Figure A.3: Streamlines of the flow in the Basal view. SV=60 ml, HR=60 bpm.

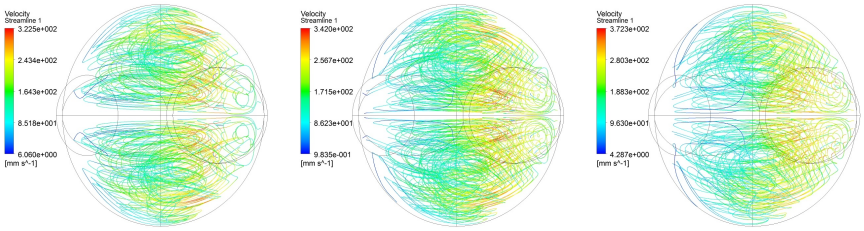

(13) t=0.36 Sec (14) t=0.37 Sec (15) t=0.38 Sec

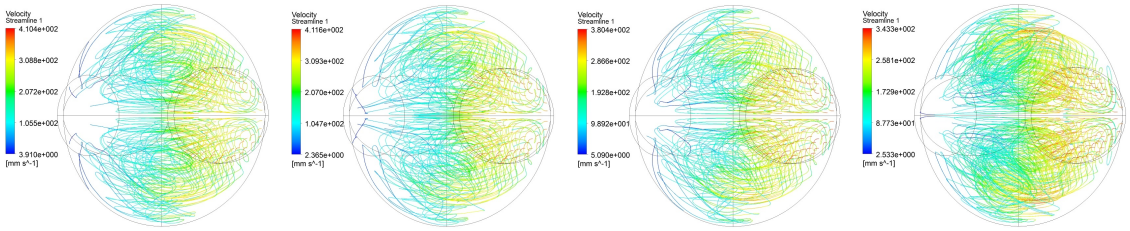

(16) t=0.39 Sec (17) t=0.40 Sec (18) t=0.41 Sec (19) t=0.42 Sec

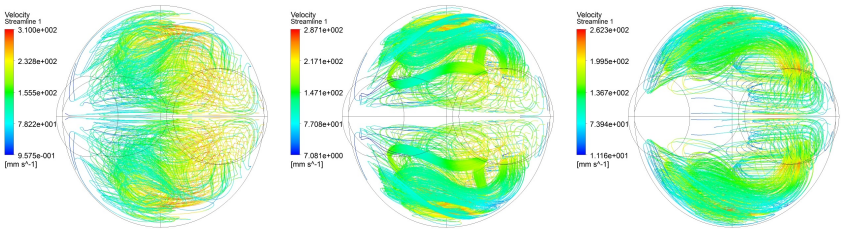

(20) t=0.43 Sec (21) t=0.44 Sec (22) t=0.45 Sec

Figure A.3: Streamlines of the flow in the Basal view. SV=60 ml, HR=60 bpm(cont).

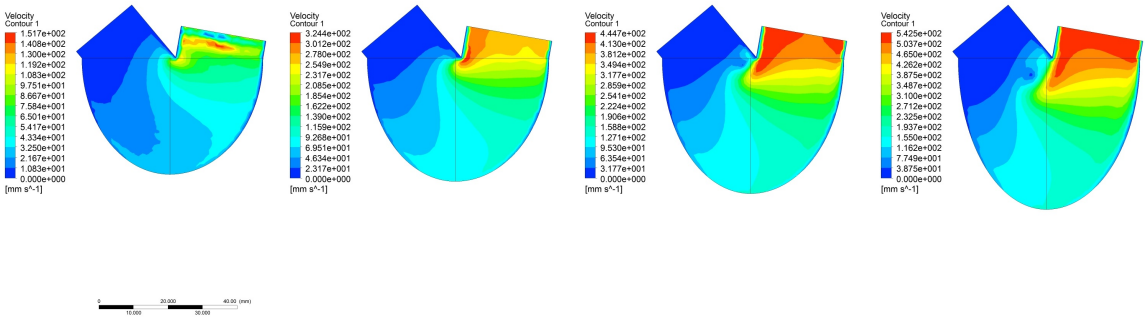

(1) t=0.02 Sec (2) t=0.05 Sec (3) t=0.08 Sec (4) t=0.11 Sec

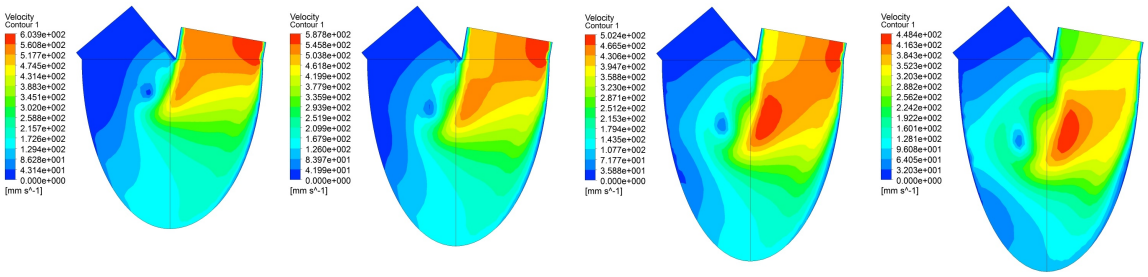

(5) t=0.14 Sec (6) t=0.17 Sec (7) t=0.20 Sec (8) t=0.23 Sec

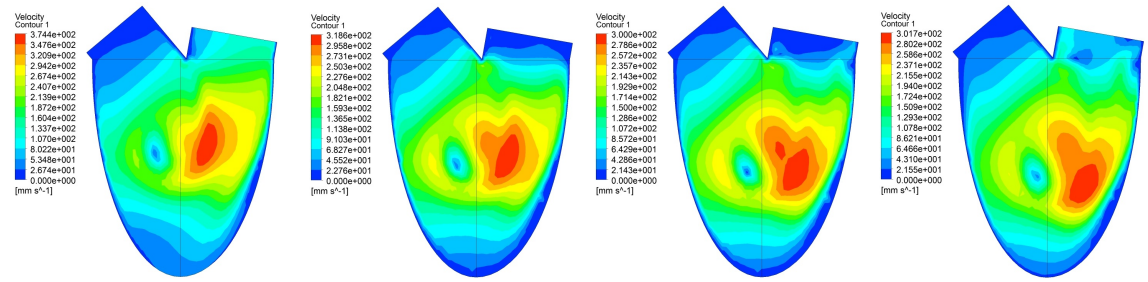

(9) t=0.26 Sec (10) t=0.29 Sec (11) t=0.32 Sec (12) t=0.35 Sec

Figure A.4: Velocity contours in the long axis (symmetry) view. SV=60 ml, HR=60 bpm.

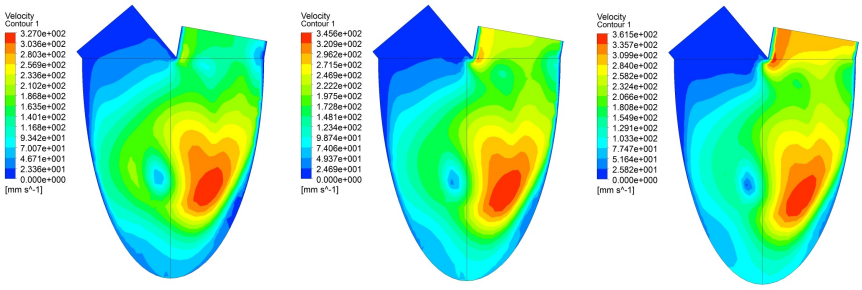

(13) t=0.36 Sec (14) t=0.37 Sec (15) t=0.38 Sec

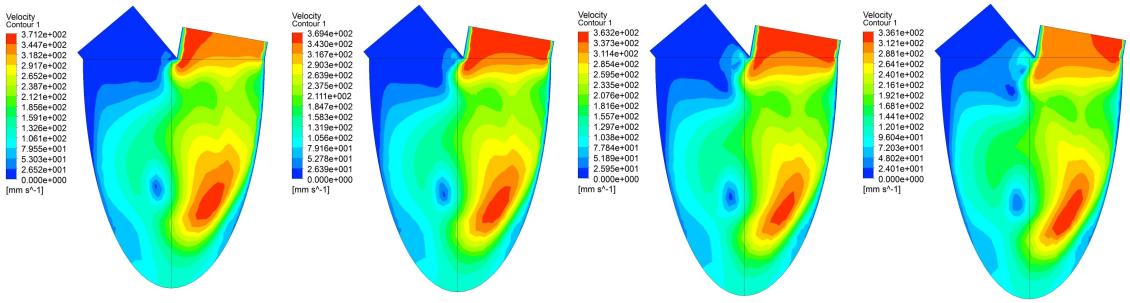

(16) t=0.39 Sec (17) t=0.40 Sec (18) t=0.41 Sec (19) t=0.42 Sec

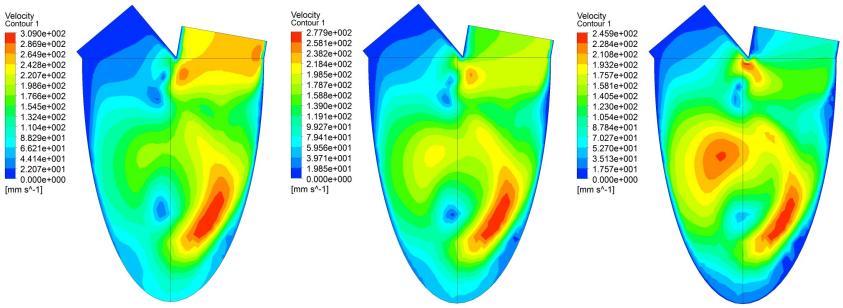

(20) t=0.43 Sec (21) t=0.44 Sec (22) t=0.45 Sec

Figure A.4: Velocity contours in the long axis (symmetry) view. SV=60 ml, HR=60 bpm(cont).

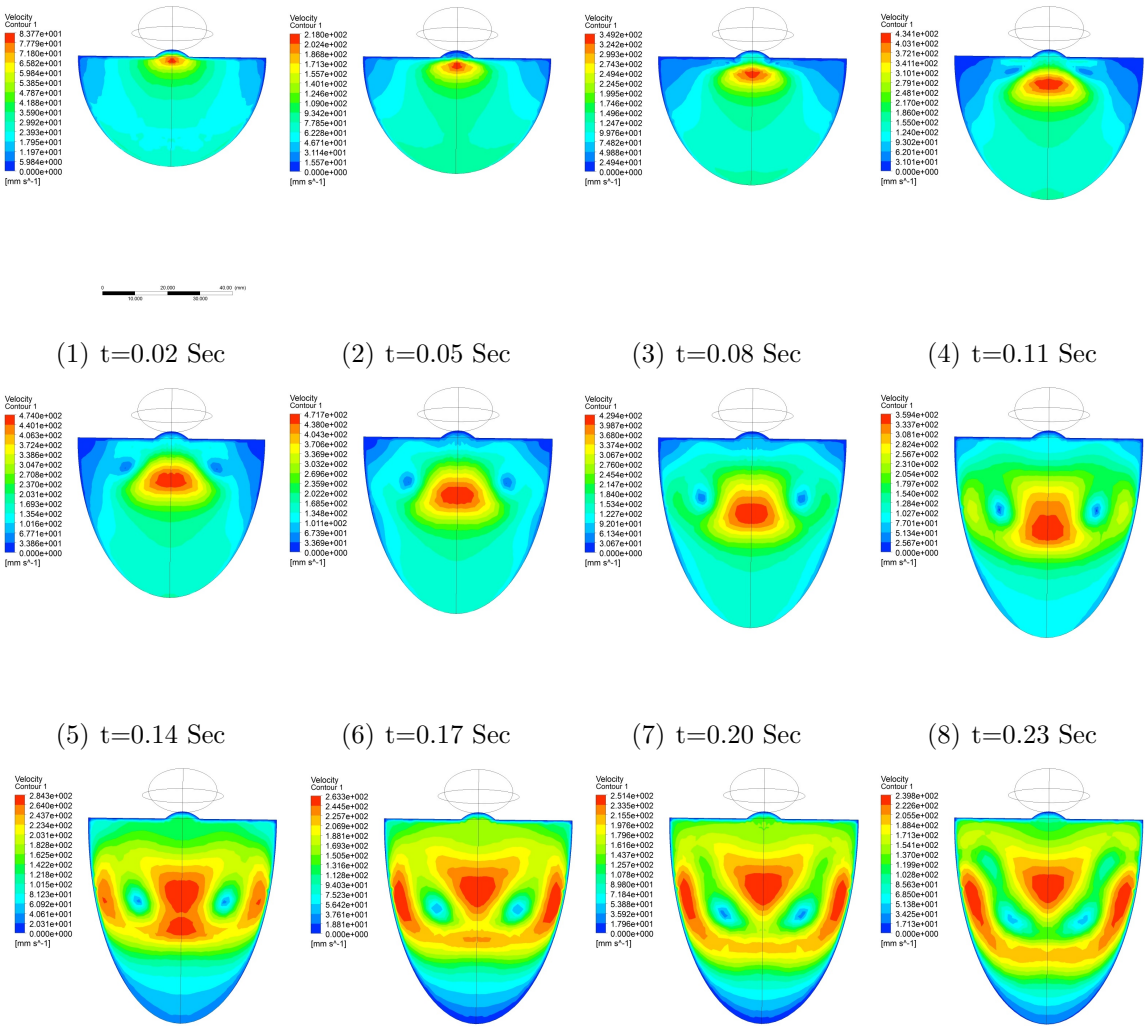

(1) t=0.02 Sec (2) t=0.05 Sec (3) t=0.08 Sec (4) t=0.11 Sec

(5) t=0.14 Sec (6) t=0.17 Sec (7) t=0.20 Sec (8) t=0.23 Sec

(9) t=0.26 Sec (10) t=0.29 Sec (11) t=0.32 Sec (12) t=0.35 Sec

Figure A.5: Velocity contours in the Antrio-Posterior view. SV=60 ml, HR=60 bpm.

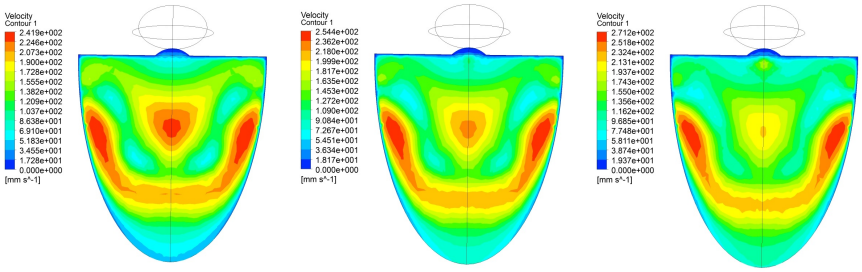

(13) t=0.36 Sec (14) t=0.37 Sec (15) t=0.38 Sec

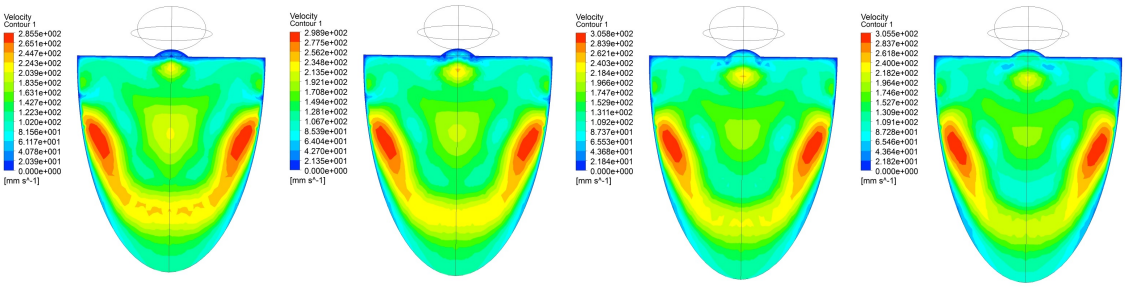

(16) t=0.39 Sec (17) t=0.40 Sec (18) t=0.41 Sec (19) t=0.42 Sec

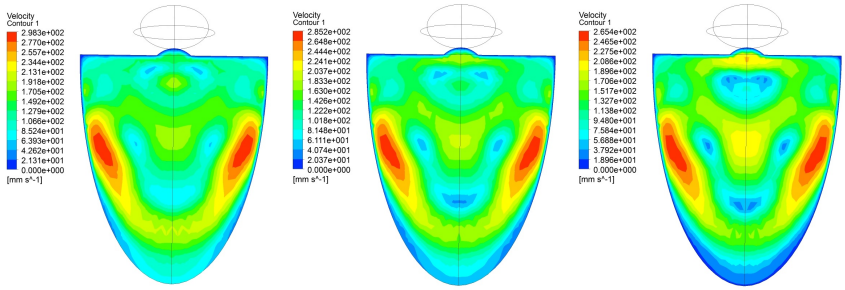

(20) t=0.43 Sec (21) t=0.44 Sec (22) t=0.45 Sec

Figure A.5: Velocity contours in the Antrio-Posterior view. SV=60 ml, HR=60 bpm(cont).

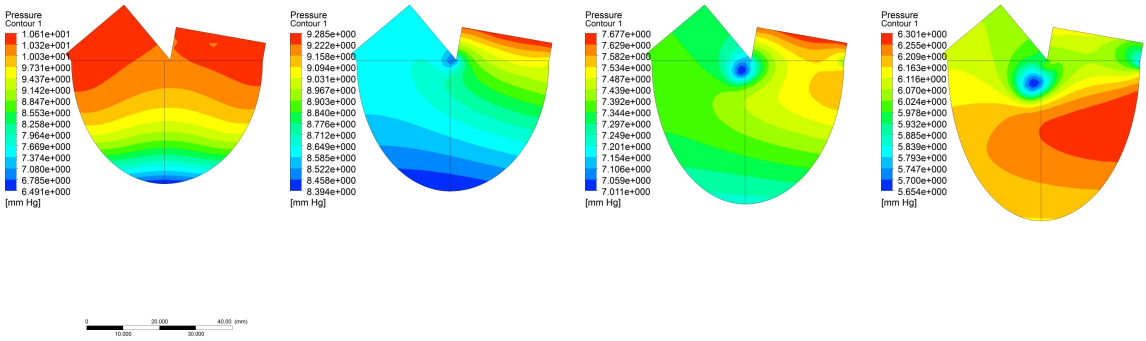

(1) t=0.02 Sec (2) t=0.05 Sec (3) t=0.08 Sec (4) t=0.11 Sec

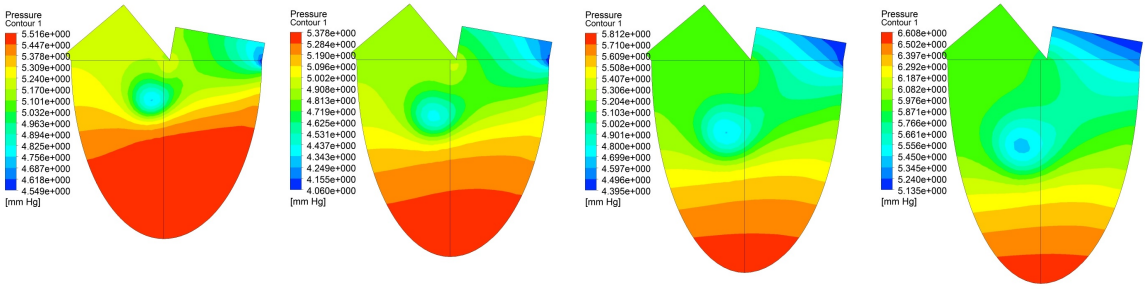

(5) t=0.14 Sec (6) t=0.17 Sec (7) t=0.20 Sec (8) t=0.23 Sec

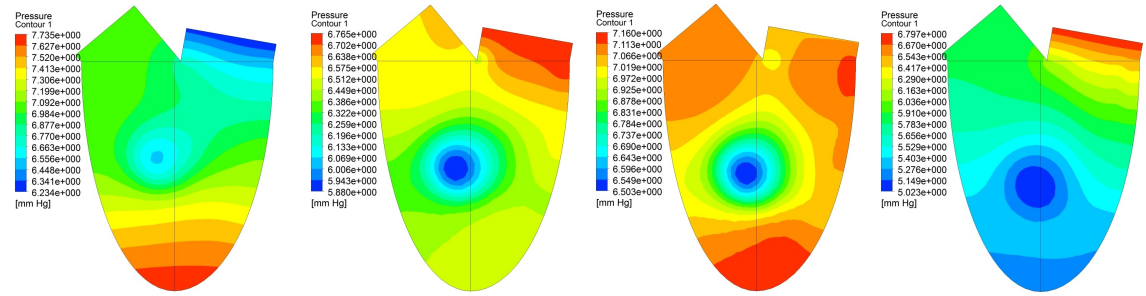

(9) t=0.26 Sec (10) t=0.29 Sec (11) t=0.32 Sec (12) t=0.35 Sec

Figure A.6: Pressure contours in the long axis view. SV=60 ml, HR=60 bpm.

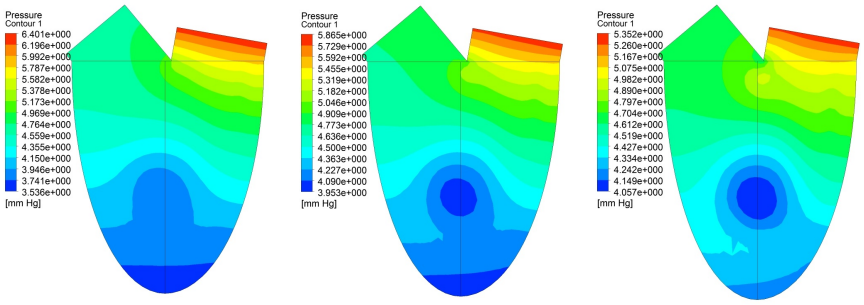

(13) t=0.36 Sec (14) t=0.37 Sec (15) t=0.38 Sec

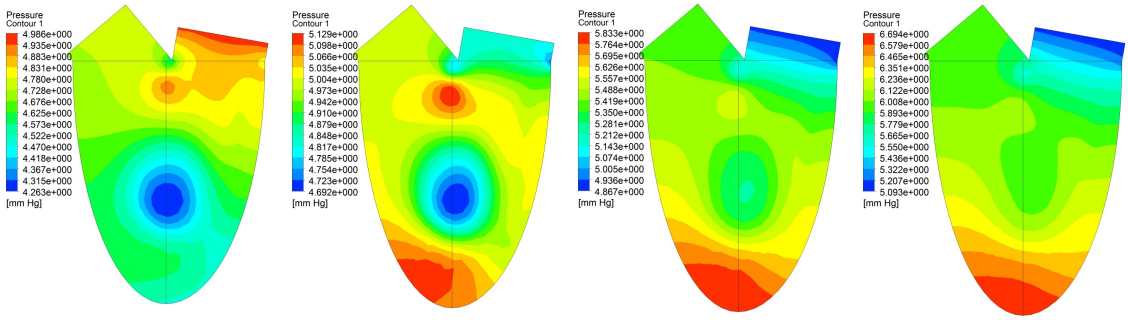

(16) t=0.39 Sec (17) t=0.40 Sec (18) t=0.41 Sec (19) t=0.42 Sec

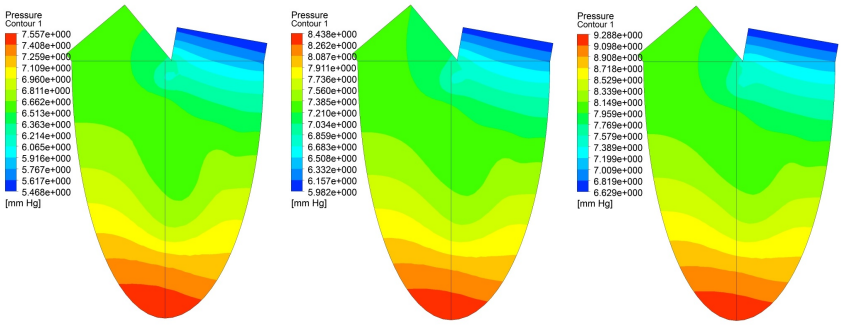

(20) t=0.43 Sec (21) t=0.44 Sec (22) t=0.45 Sec

Figure A.6: Pressure contours in the long axis view. SV=60 ml, HR=60 bpm(cont).

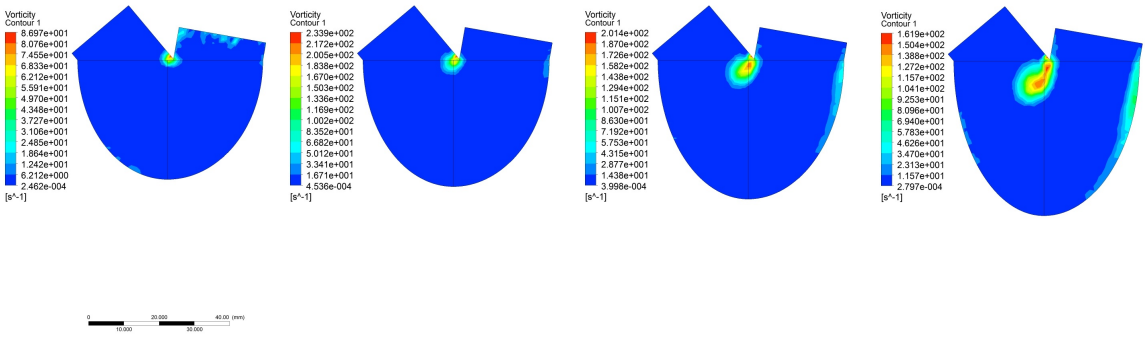

(1) t=0.02 Sec (2) t=0.05 Sec (3) t=0.08 Sec (4) t=0.11 Sec

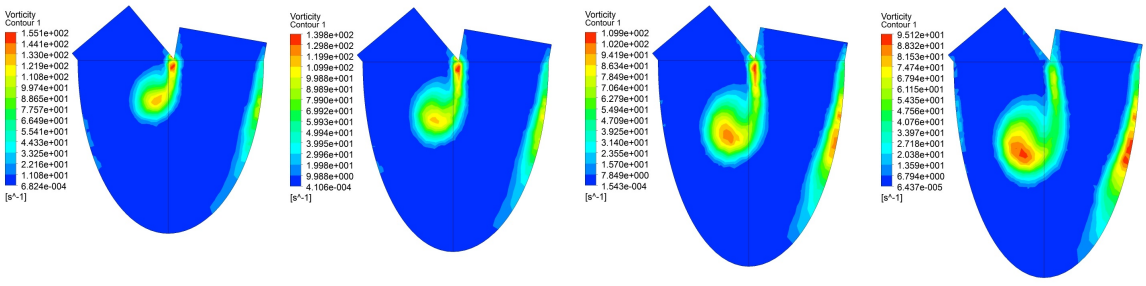

(5) t=0.14 Sec (6) t=0.17 Sec (7) t=0.20 Sec (8) t=0.23 Sec

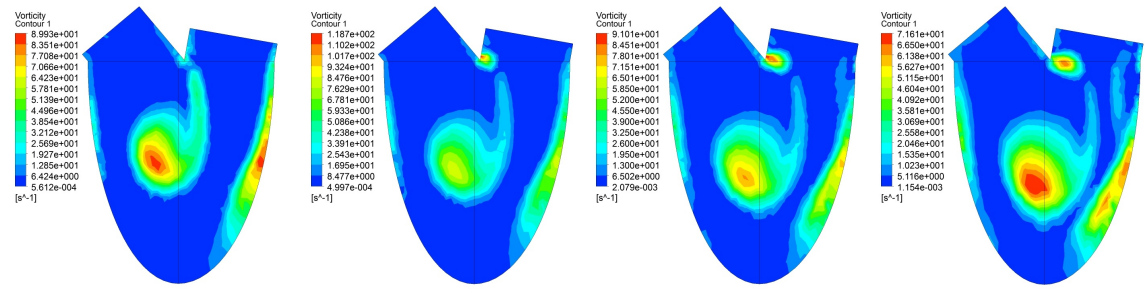

(9) t=0.26 Sec (10) t=0.29 Sec (11) t=0.32 Sec (12) t=0.35 Sec

Figure A.7: Vorticity contours in the long axis (symmetry) view. SV=60 ml, HR=60 bpm.

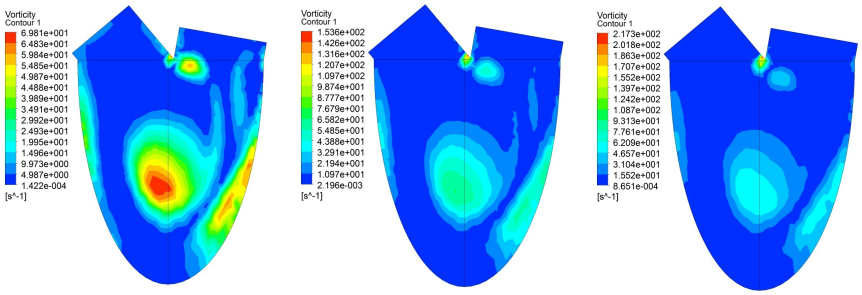

(13) t=0.36 Sec (14) t=0.37 Sec (15) t=0.38 Sec

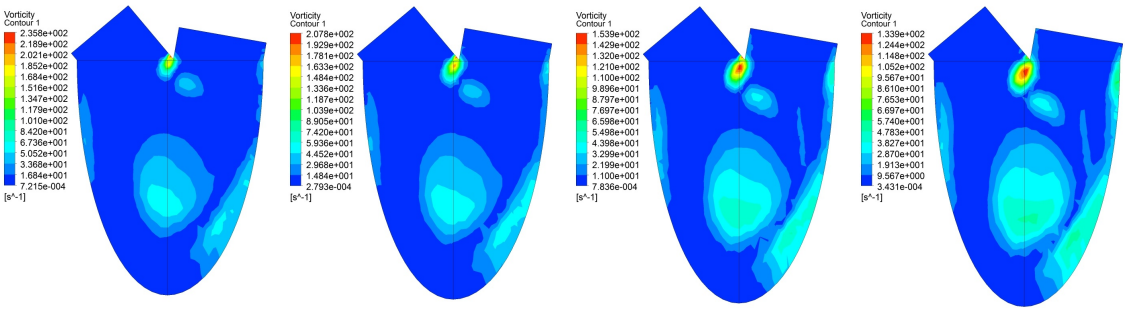

(16) t=0.39 Sec (17) t=0.40 Sec (18) t=0.41 Sec (19) t=0.42 Sec

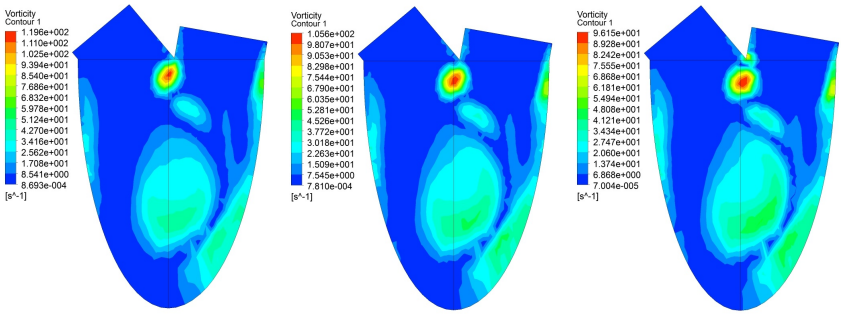

(20) t=0.43 Sec (21) t=0.44 Sec (22) t=0.45 Sec

Figure A.7: Vorticity contours in the long axis (symmetry) view. SV=60 ml, HR=60 bpm(cont).

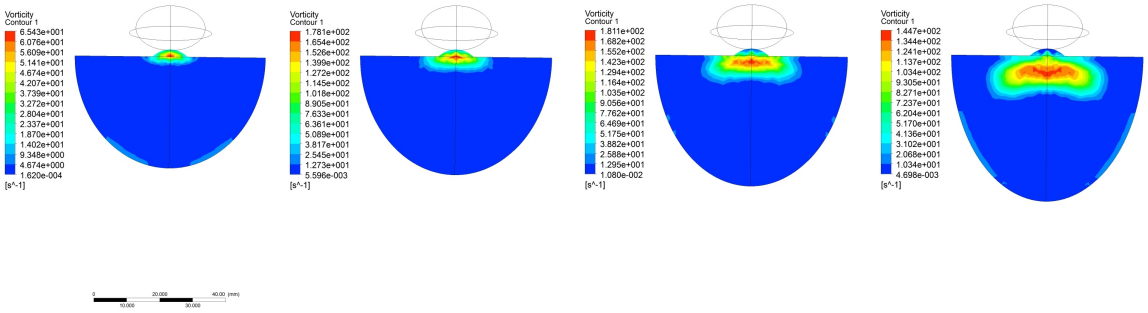

(1) t=0.02 Sec (2) t=0.05 Sec (3) t=0.08 Sec (4) t=0.11 Sec

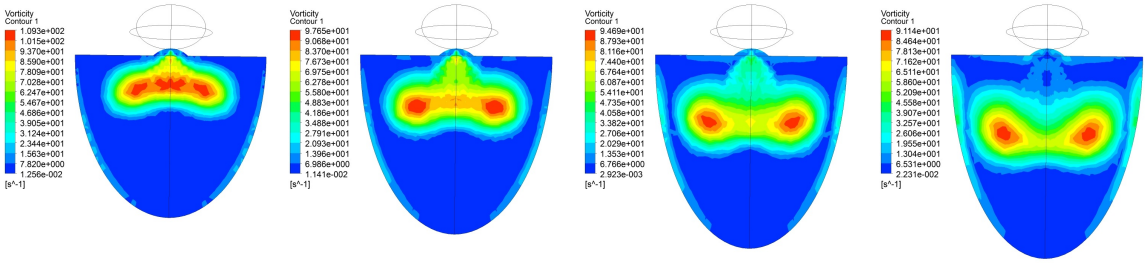

(5) t=0.14 Sec (6) t=0.17 Sec (7) t=0.20 Sec (8) t=0.23 Sec

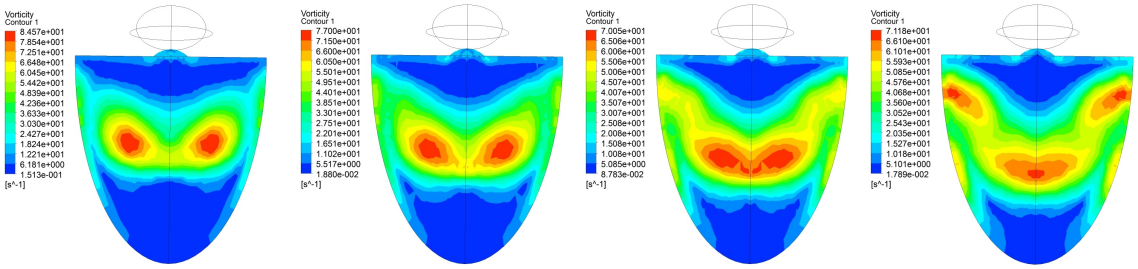

(9) t=0.26 Sec (10) t=0.29 Sec (11) t=0.32 Sec (12) t=0.35 Sec

Figure A.8: Vorticity contours in the Antrio-Posterior view. SV=60 ml, HR=60 bpm.

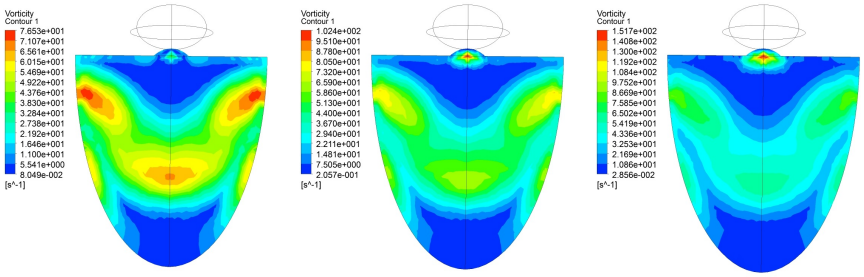

(13) t=0.36 Sec (14) t=0.37 Sec (15) t=0.38 Sec

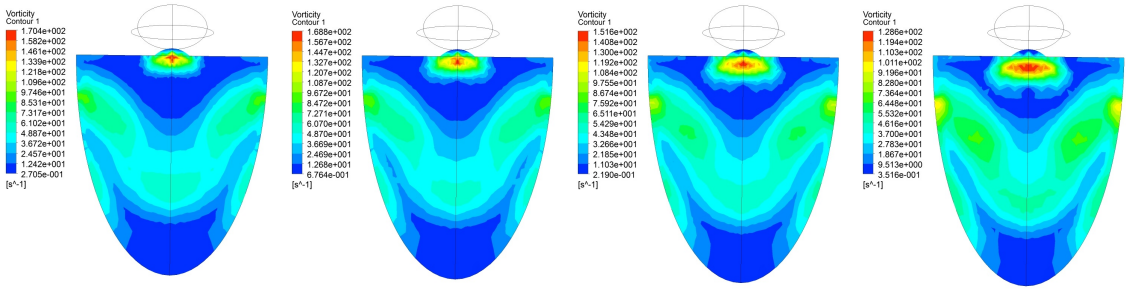

(16) t=0.39 Sec (17) t=0.40 Sec (18) t=0.41 Sec (19) t=0.42 Sec

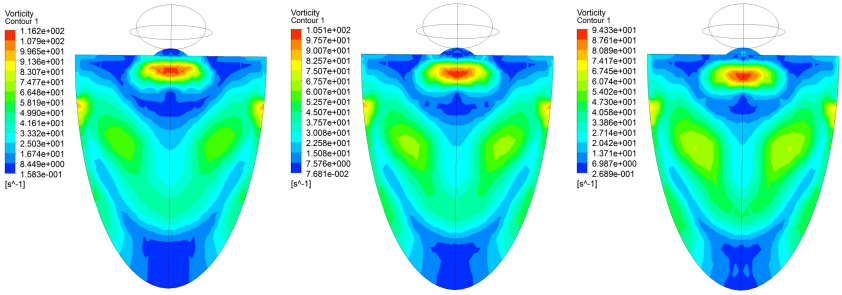

(20) t=0.43 Sec (21) t=0.44 Sec (22) t=0.45 Sec

Figure A.8: Vorticity contours in the Antrio-Posterior view. SV=60 ml, HR=60 bpm(cont).

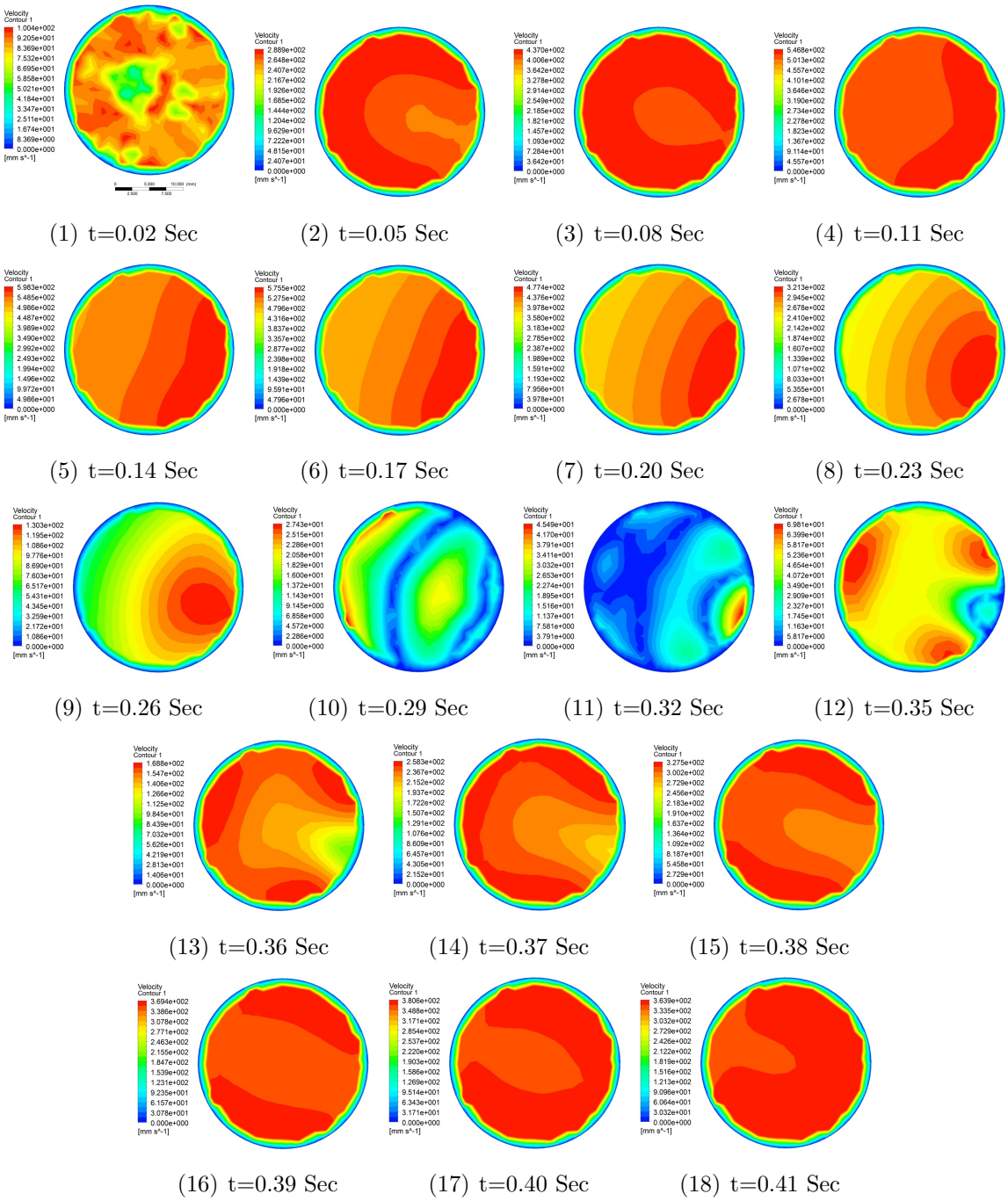

(1) t=0.02 Sec (2) t=0.05 Sec (3) t=0.08 Sec (4) t=0.11 Sec

(5) t=0.14 Sec (6) t=0.17 Sec (7) t=0.20 Sec (8) t=0.23 Sec

(9) t=0.26 Sec (10) t=0.29 Sec (11) t=0.32 Sec (12) t=0.35 Sec

(13) t=0.36 Sec (14) t=0.37 Sec (15) t=0.38 Sec

(16) t=0.39 Sec (17) t=0.40 Sec (18) t=0.41 Sec

Figure A.9: Velocity contours in the mitral valve orifice. SV=60 ml, HR=60 bpm.

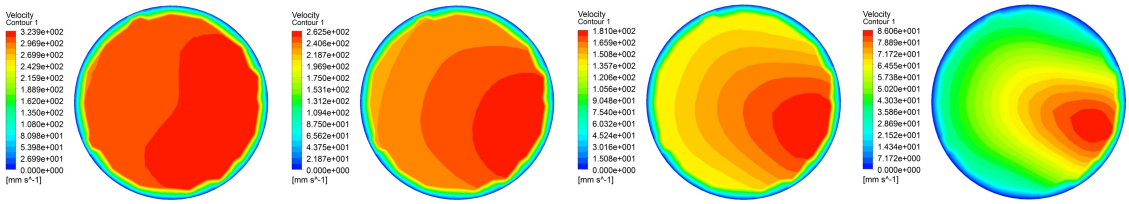

(19) t=0.42 Sec (20) t=0.43 Sec (21) t=0.44 Sec (22) t=0.45 Sec

Figure A.9: Velocity contours in the mitral valve orifice. SV=60 ml, HR=60 bpm(cont).

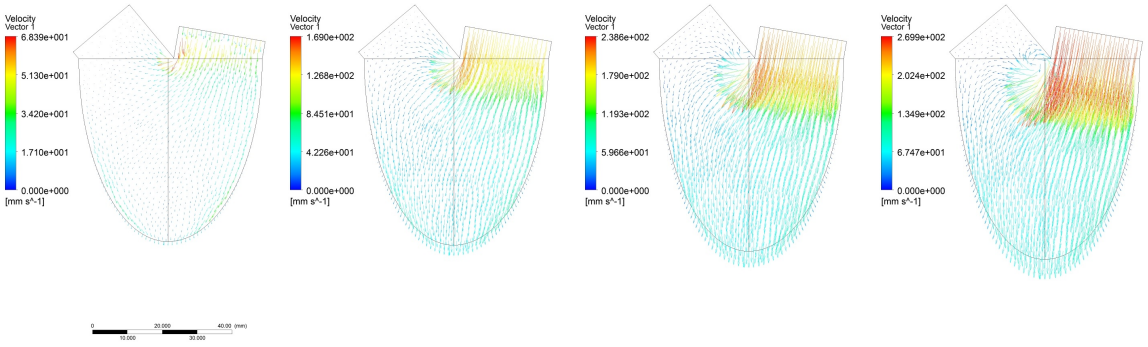

(1) t=0.02 Sec (2) t=0.05 Sec (3) t=0.08 Sec (4) t=0.11 Sec

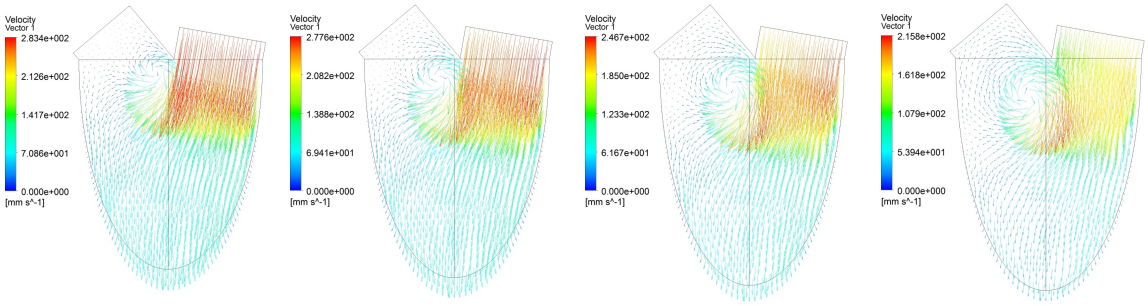

(5) t=0.14 Sec (6) t=0.17 Sec (7) t=0.20 Sec (8) t=0.23 Sec

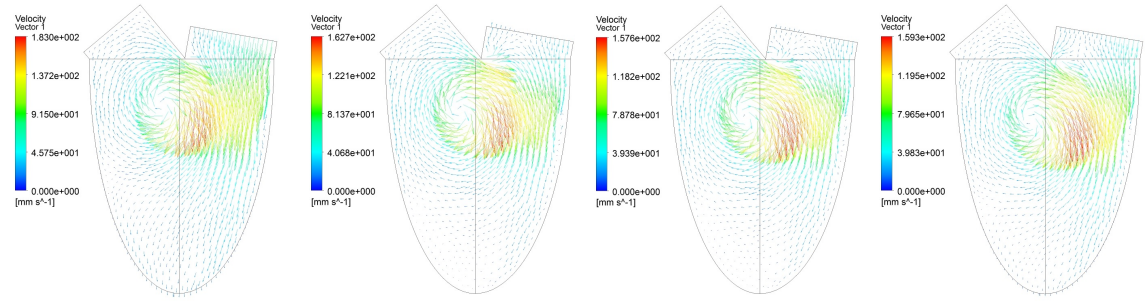

(9) t=0.26 Sec (10) t=0.29 Sec (11) t=0.32 Sec (12) t=0.35 Sec

Figure A.10: Velocity vectors in the long axis (symmetry) view. SV=30 ml, HR=60 bpm.

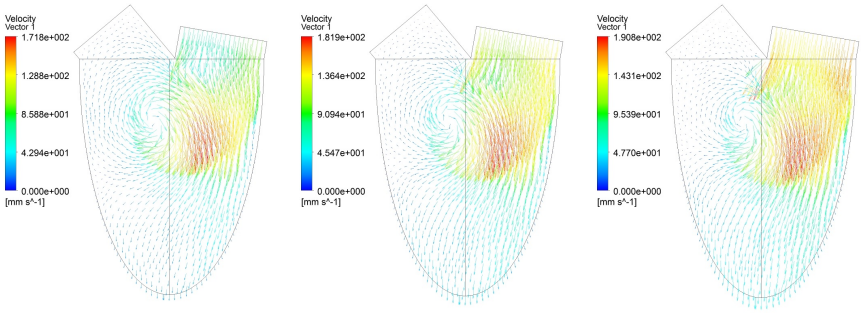

(13) t=0.36 Sec (14) t=0.37 Sec (15) t=0.38 Sec

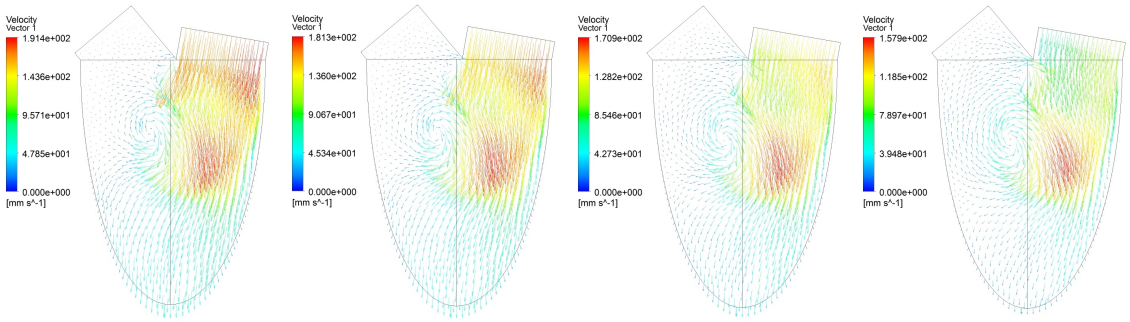

(16) t=0.41 Sec (17) t=0.42 Sec (18) t=0.43 Sec (19) t=0.44 Sec

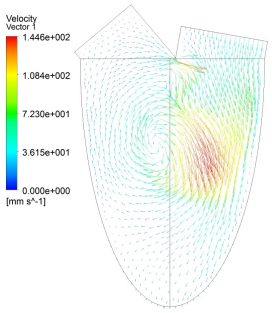

(20) t=0.45 Sec

Figure A.10: Velocity vectors in the long axis (symmetry) view. SV=30 ml, HR=60 bpm(cont).

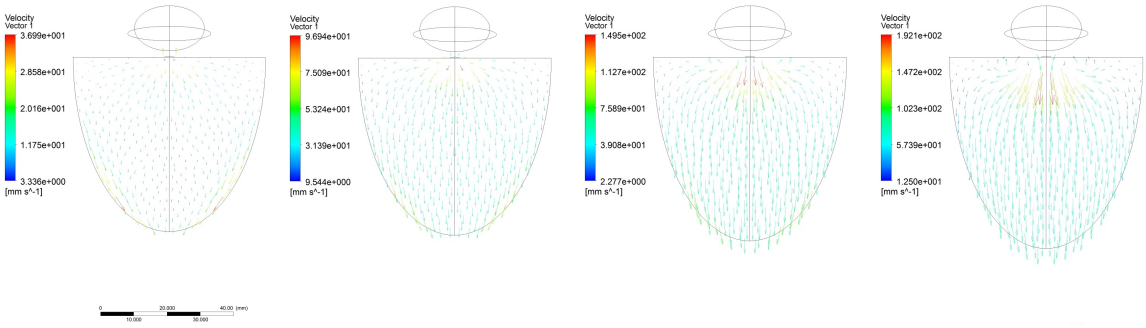

(1) t=0.02 Sec (2) t=0.05 Sec (3) t=0.08 Sec (4) t=0.11 Sec

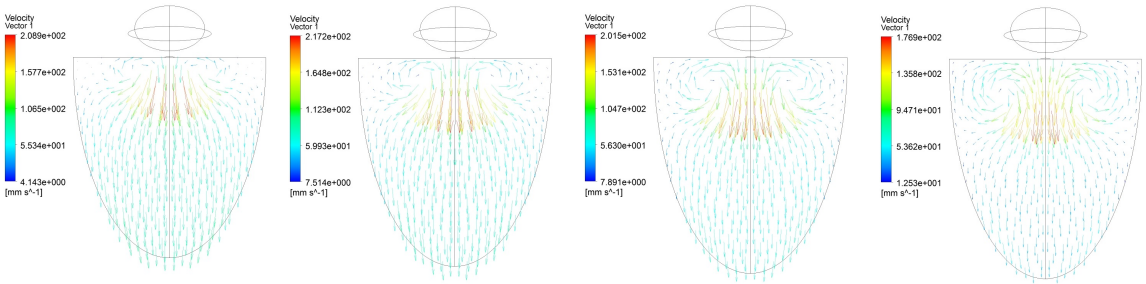

(5) t=0.14 Sec (6) t=0.17 Sec (7) t=0.20 Sec (8) t=0.23 Sec

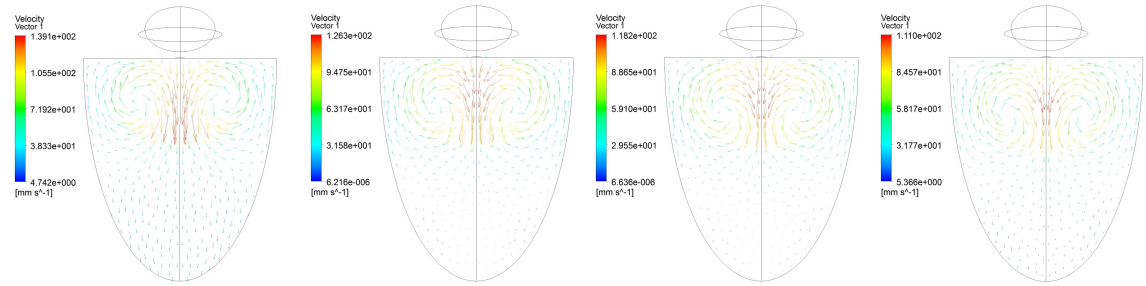

(9) t=0.26 Sec (10) t=0.29 Sec (11) t=0.32 Sec (12) t=0.35 Sec

Figure A.11: Velocity vectors in the Anterio-Posterior view. SV=30 ml, HR=60 bpm.

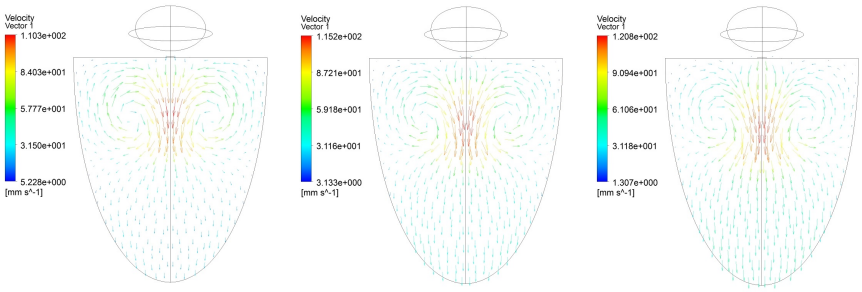

(13) t=0.36 Sec (14) t=0.37 Sec (15) t=0.38 Sec

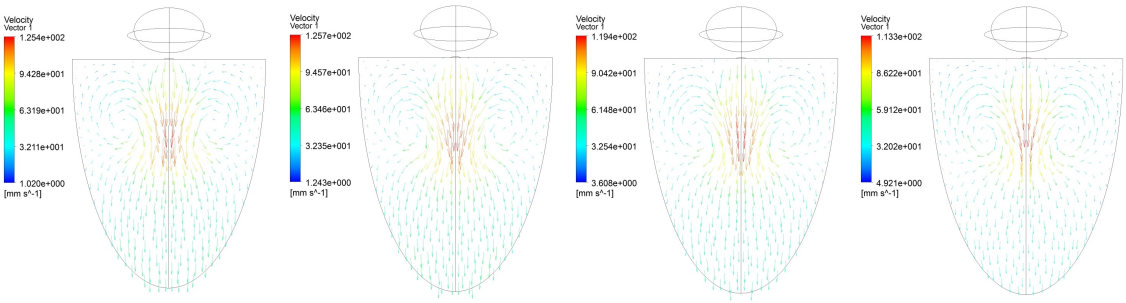

(16) t=0.39 Sec (17) t=0.41 Sec (18) t=0.42 Sec (19) t=0.43 Sec

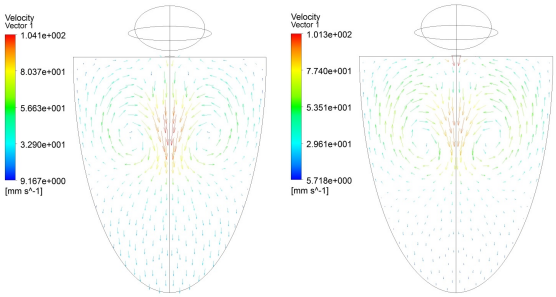

(20) t=0.44 Sec (21) t=0.45 Sec

Figure A.11: Velocity vectors in the Anterio-Posterior view. SV=30 ml, HR=60 bpm(cont).

Appendix B

Time History Results of Chapter 3

In this appendix we presented selected time history results of chapter 3. Figures B.1 and B.2 present the first principal stresses of the mitral valve in the basal and symmetry planes respectively. Figure B.3 shows the velocity contours in the left ventricle at symmetry plane. Figure B.4 depicts the 2D streamlines in the symmetry plane. Finally, figure B.5 displays the vorticity contours in the symmetry plane.

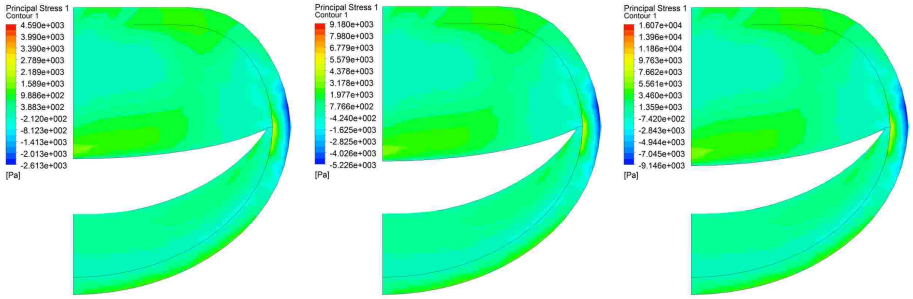

(1) t=0.001 Sec (2) t= Sec (3) t=0.003 Sec

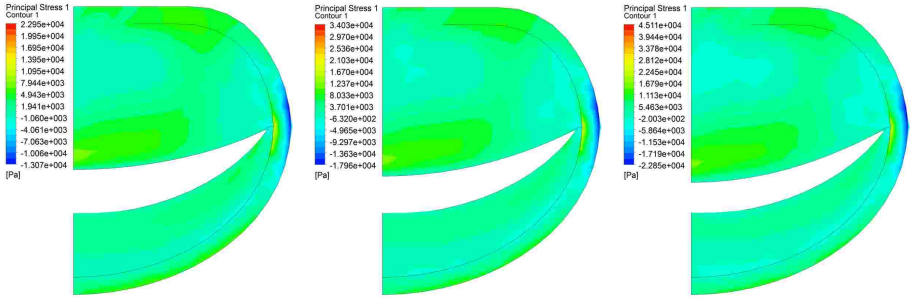

(4) t=0.005 Sec (5) t=0.006 Sec (6) t=0.007 Sec

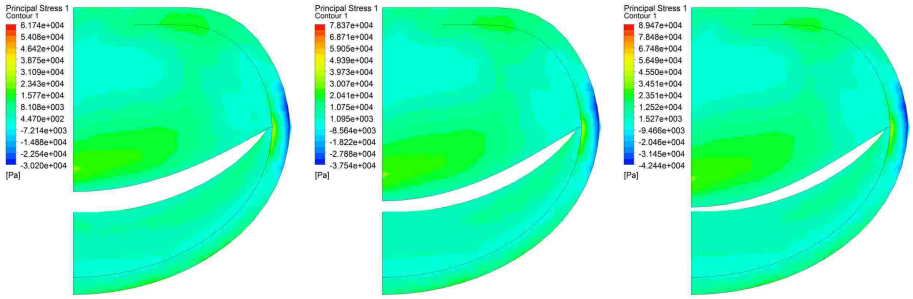

(7) t=0.008 Sec (8) t=0.010 Sec (9) t=0.011 Sec

Figure B.1: First principal stress, view: basal Plane. SV=60 ml, HR=60 bpm.

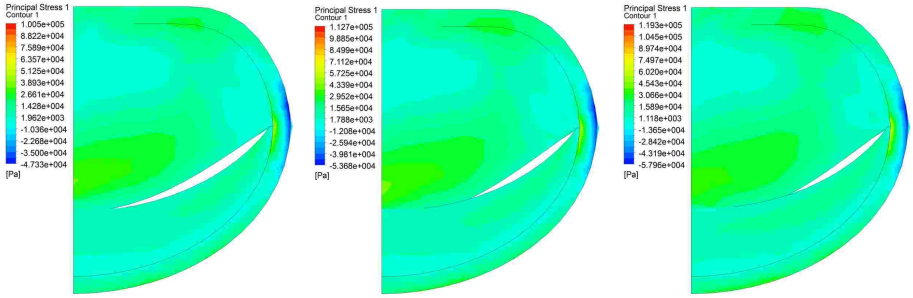

(10) t=0.012 Sec (11) t=0.013 Sec (12) t=0.015 Sec

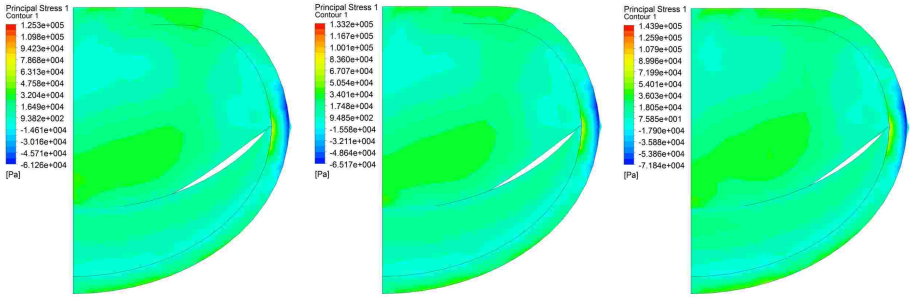

(13) t= Sec (14) t=0.017 Sec (15) t=0.018 Sec

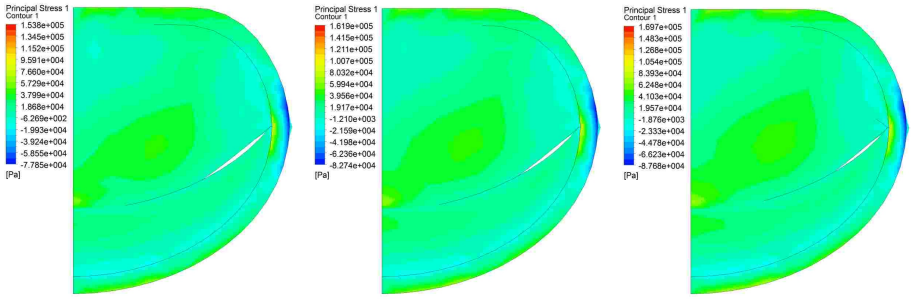

(16) t=0.020 Sec (17) t=0.021 Sec (18) t=0.022 Sec

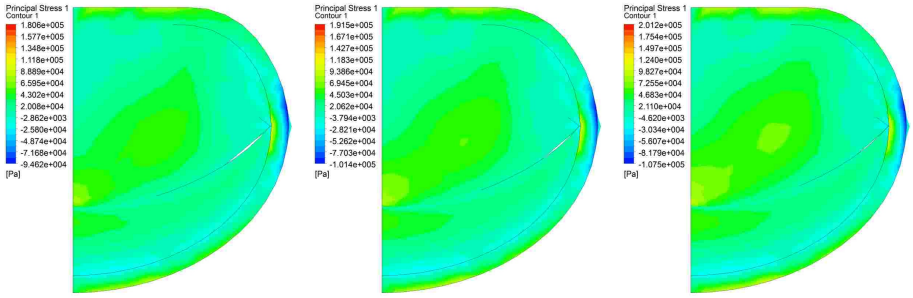

(19) t=0.023 Sec (20) t=0.025 Sec (21) t=0.026 Sec

Figure B.1: First principal stress, view: basal Plane. SV=60 ml, HR=60 bpm (cont).

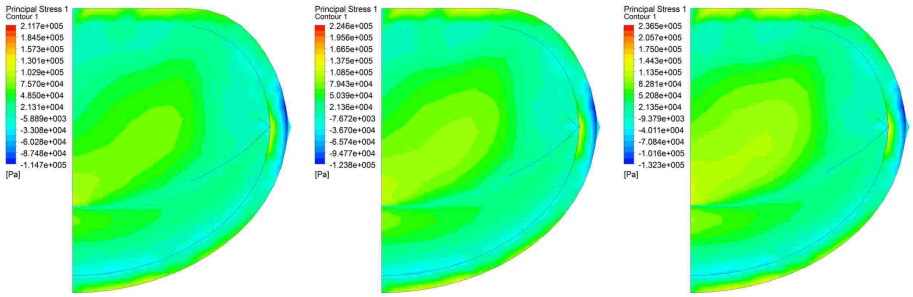

(22) t=0.027 Sec (23) t=0.028 Sec (24) t=0.030 Sec

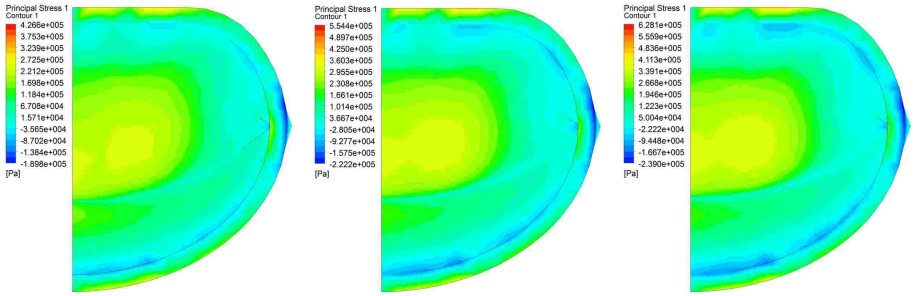

(25) t=0.039 Sec (26) t=0.065 Sec (27) t=0.080 Sec

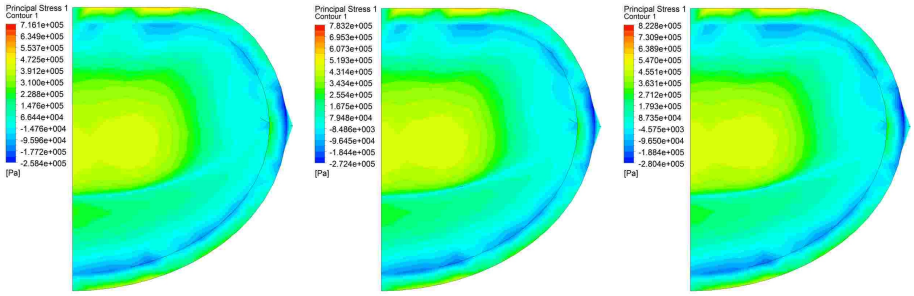

(28) t=0.100 Sec (29) t=0.120 Sec (30) t=0.140 Sec

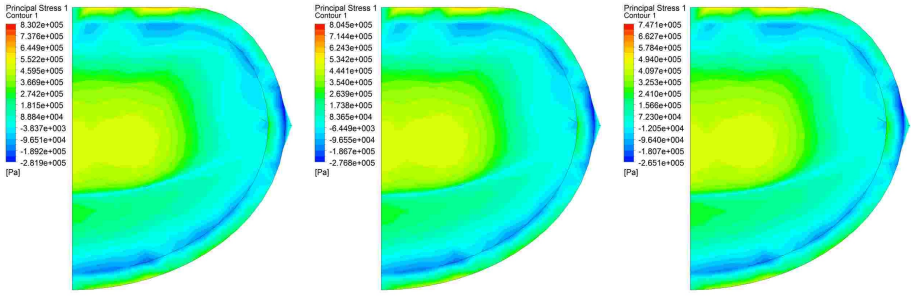

(31) t=0.160 Sec (32) t=0.180 Sec (33) t=0.200 Sec

Figure B.1: First principal stress, view: basal Plane. SV=60 ml, HR=60 bpm (cont).

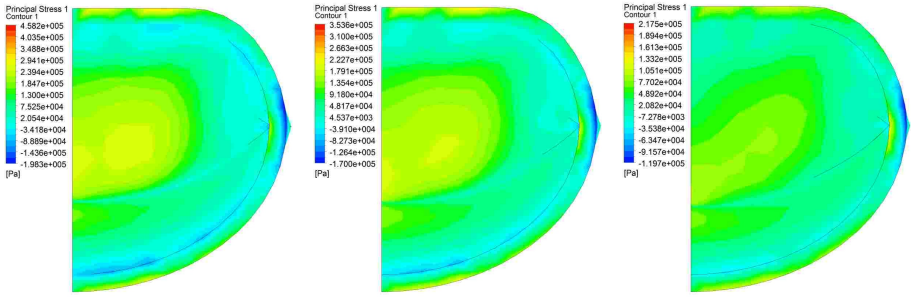

(34) t=0.250 Sec

(35) t=0.400 Sec

(36) t=0.406 Sec

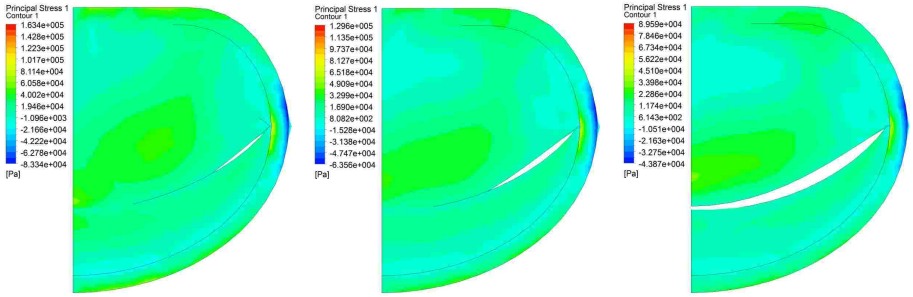

(37) t=0.412 Sec

(38) t=0.418 Sec

(39) t=0.421 Sec

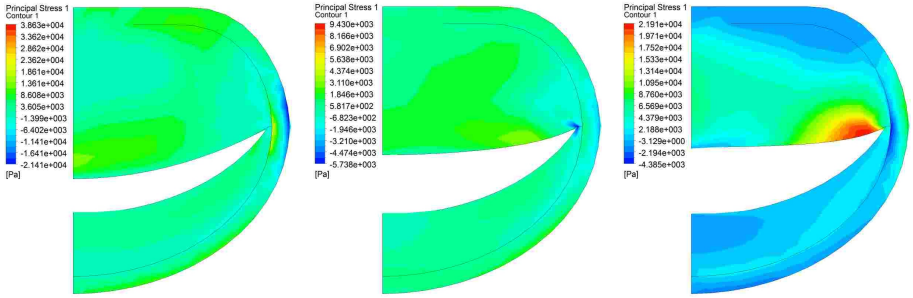

(40) t=0.424 Sec

(41) t=0.427 Sec

(42) t=0.430 Sec

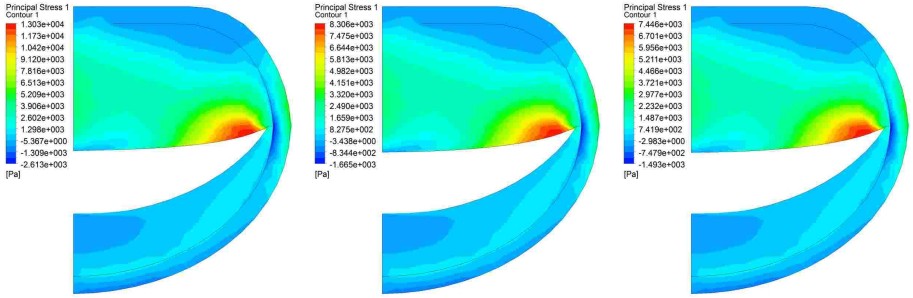

(43) t=0.500 Sec

(44) t=0.550 Sec

(45) t=0.600 Sec

Figure B.1: First principal stress, view: basal Plane. SV=60 ml, HR=60 bpm (cont).

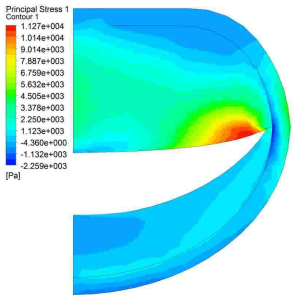

(46) t=0.650 Sec

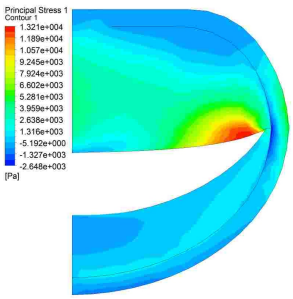

(47) t=0.400 Sec

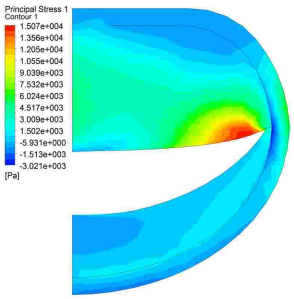

(48) t=0.750 Sec

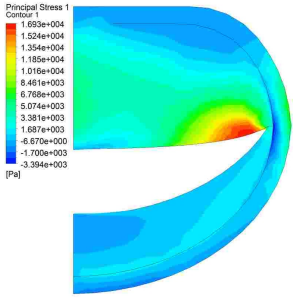

(49) t=0.800 Sec

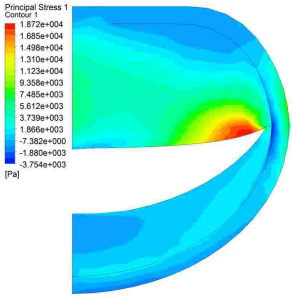

(50) t=0.850 Sec

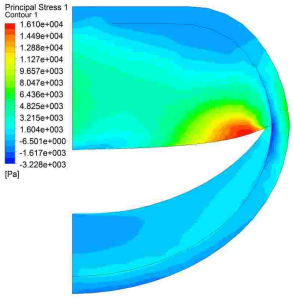

(51) t=0.887 Sec

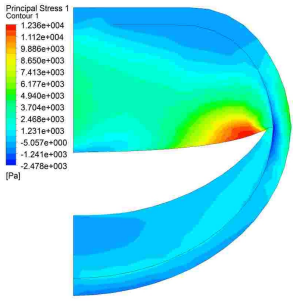

(52) t=0.925 Sec

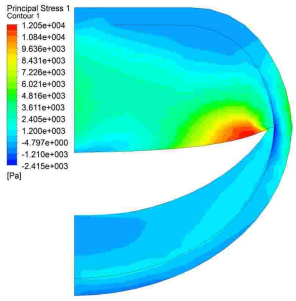

(53) t=0.962 Sec

Figure B.1: First principal stress, view: basal Plane. SV=60 ml, HR=60 bpm (cont).

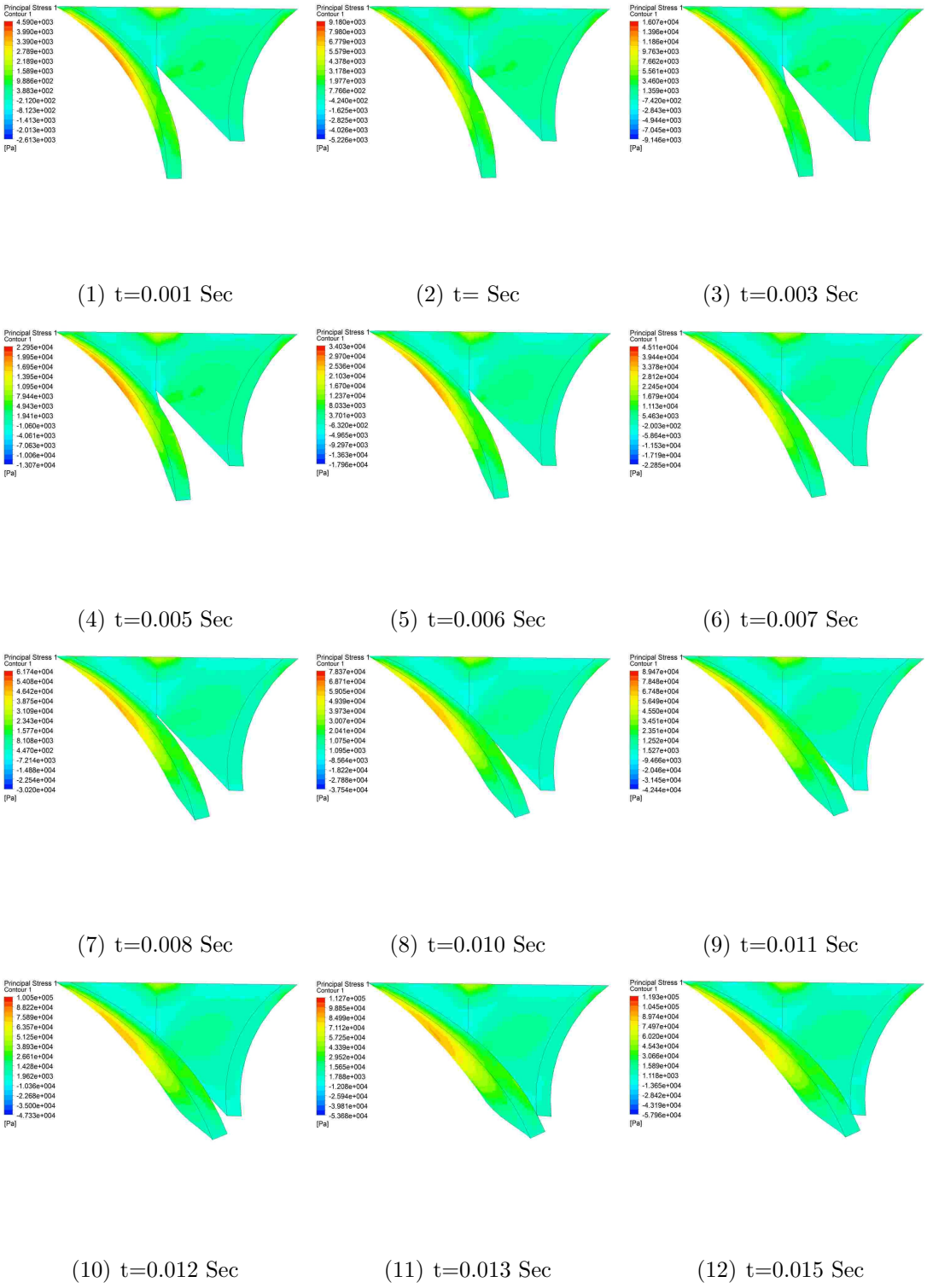

Figure B.2: First principal stress, view: Symmetry Plane. SV=60 ml, HR=60 bpm.

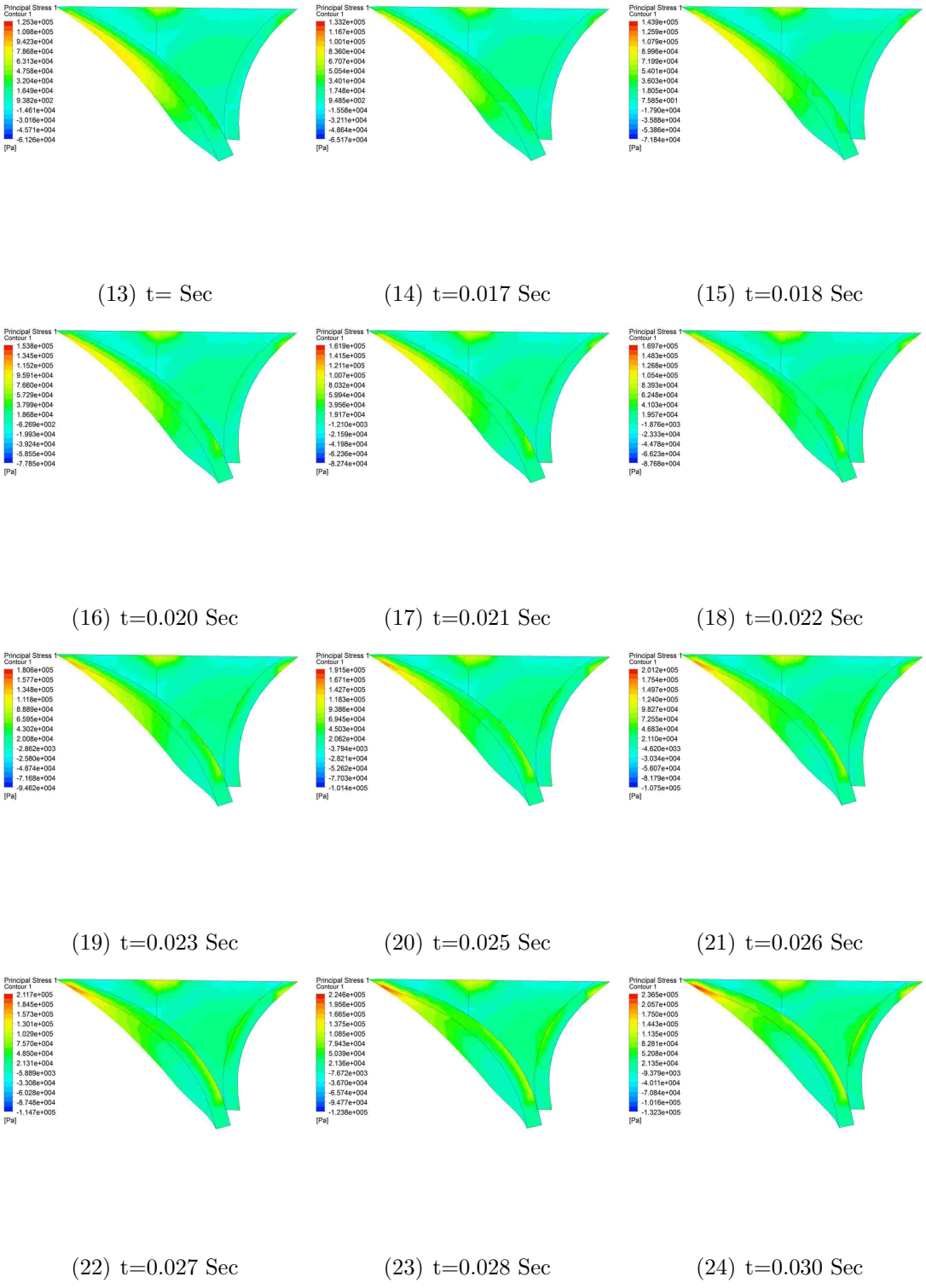

(13) t= Sec (14) t=0.017 Sec (15) t=0.018 Sec

(16) t=0.020 Sec (17) t=0.021 Sec (18) t=0.022 Sec

(19) t=0.023 Sec (20) t=0.025 Sec (21) t=0.026 Sec

(22) t=0.027 Sec (23) t=0.028 Sec (24) t=0.030 Sec

Figure B.2: First principal stress, view: Symmetry Plane. SV=60 ml, HR=60 bpm (cont).

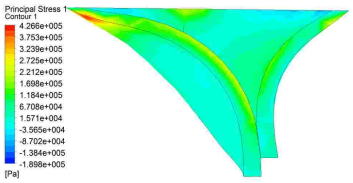

(25) t=0.039 Sec

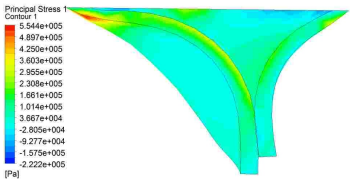

(26) t=0.065 Sec

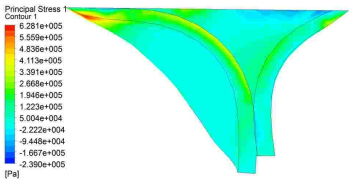

(27) t=0.080 Sec

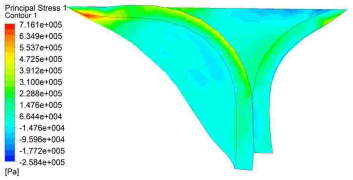

(28) t=0.100 Sec

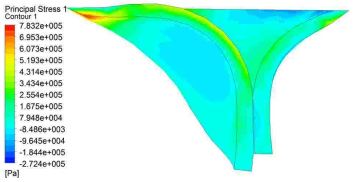

(29) t=0.120 Sec

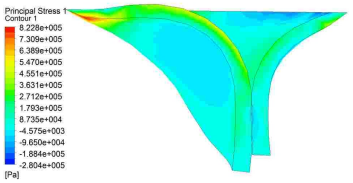

(30) t=0.140 Sec

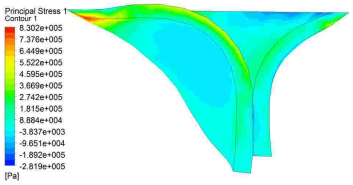

(31) t=0.160 Sec

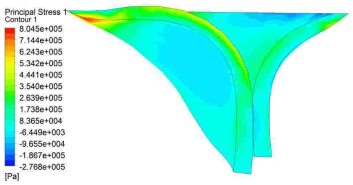

(32) t=0.180 Sec

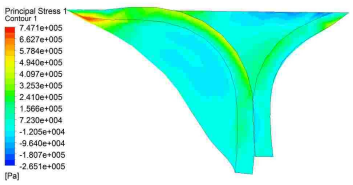

(33) t=0.200 Sec

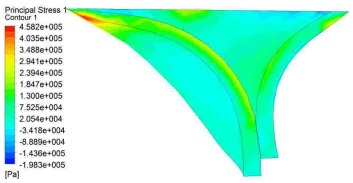

(34) t=0.250 Sec

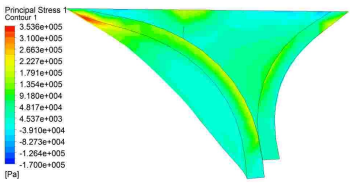

(35) t=0.400 Sec

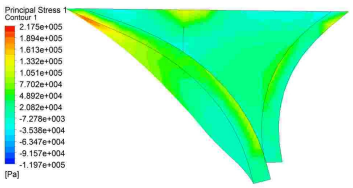

(36) t=0.406 Sec

Figure B.2: First principal stress, view: Symmetry Plane. SV=60 ml, HR=60 bpm (cont).

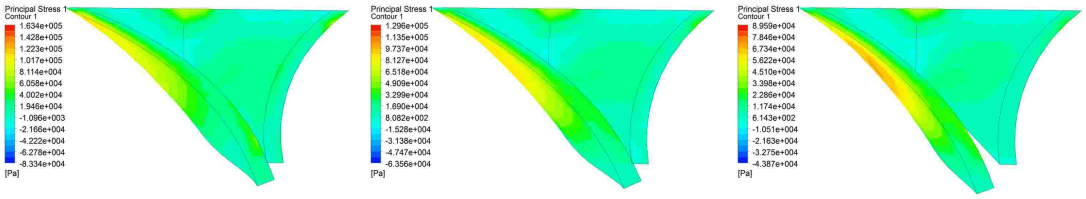

(37) t=0.412 Sec (38) t=0.418 Sec (39) t=0.421 Sec

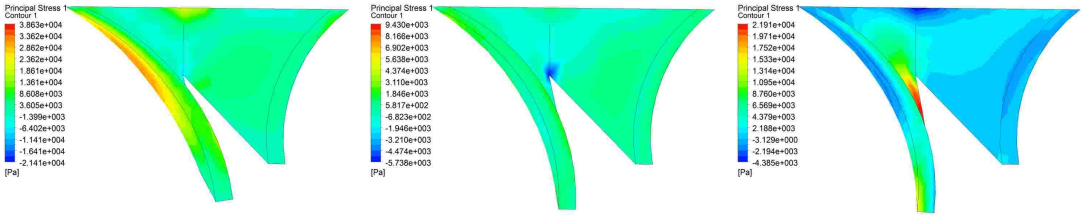

(40) t=0.424 Sec (41) t=0.427 Sec (42) t=0.430 Sec

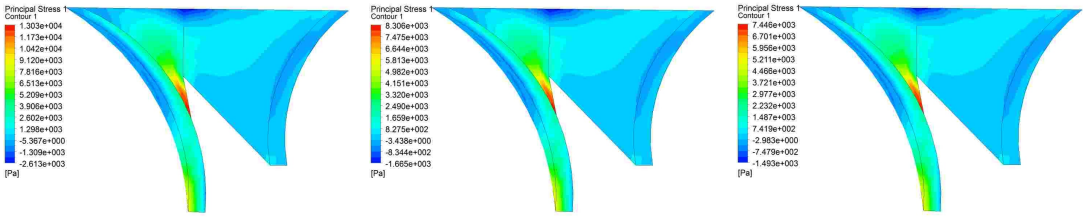

(43) t=0.500 Sec (44) t=0.550 Sec (45) t=0.600 Sec

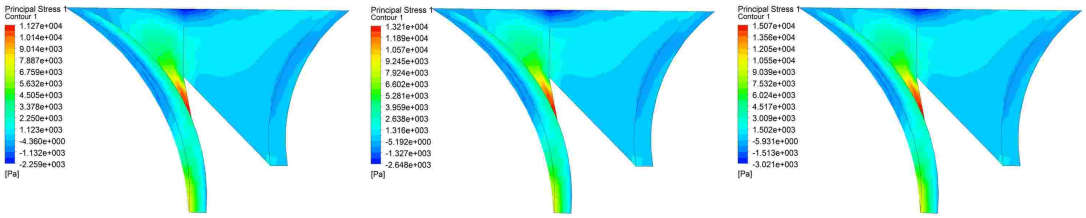

(46) t=0.650 Sec (47) t=0.400 Sec (48) t=0.750 Sec

Figure B.2: First principal stress, view: Symmetry Plane. SV=60 ml, HR=60 bpm (cont).

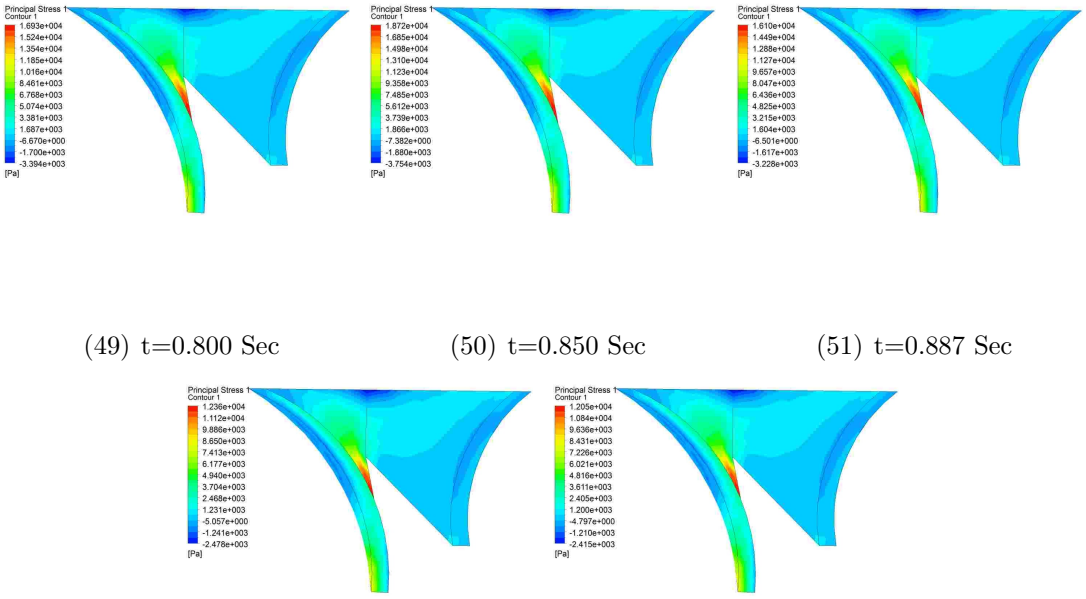

(49) t=0.800 Sec (50) t=0.850 Sec (51) t=0.887 Sec

(52) t=0.925 Sec (53) t=0.962 Sec

Figure B.2: First principal stress, view: Symmetry Plane. SV=60 ml, HR=60 bpm (cont).

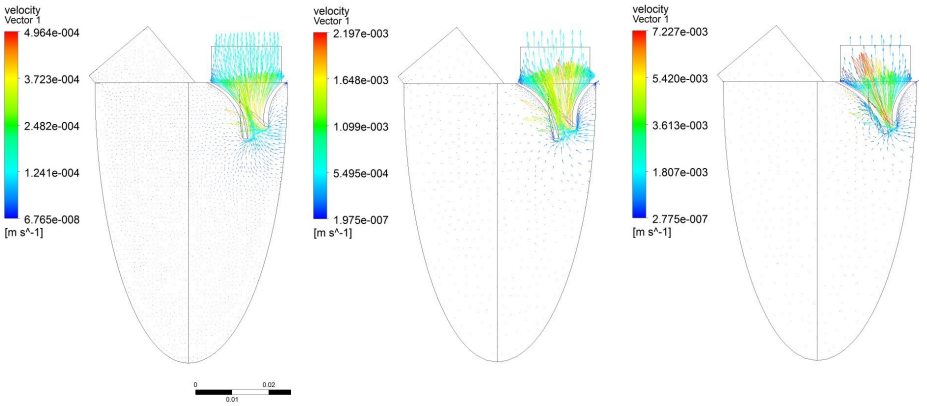

(1) t=0.005 Sec (2) t=0.010 Sec (3) t=0.015 Sec

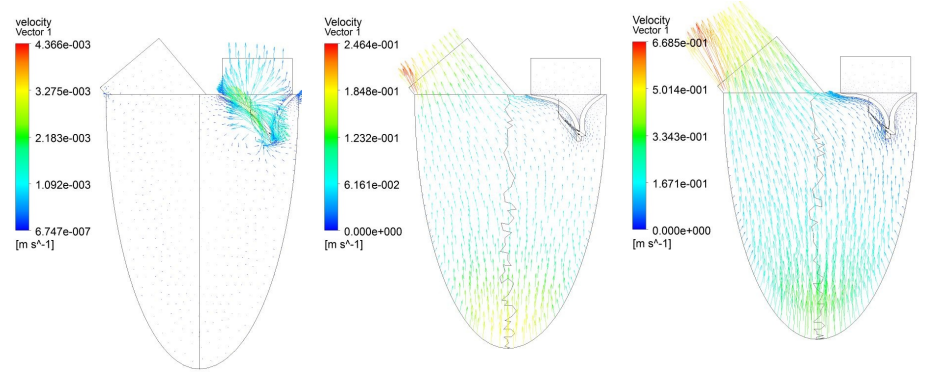

(4) t=0.030 Sec (5) t=0.065 Sec (6) t=0.080 Sec

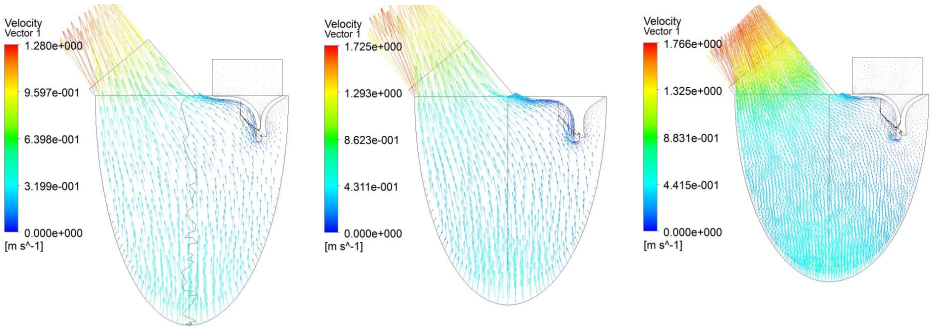

(7) t=0.100 Sec (8) t=0.120 Sec (9) t=0.140 Sec

Figure B.3: Velocity contours in the long axis (symmetry) Plane. SV=60 ml, HR=60 bpm.

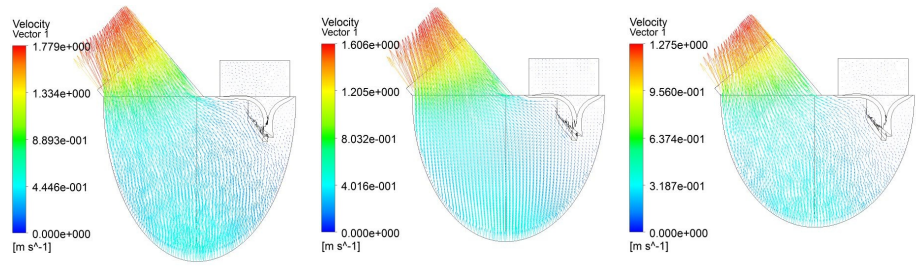

(10) t=0.160 Sec (11) t=0.180 Sec (12) t=0.200 Sec

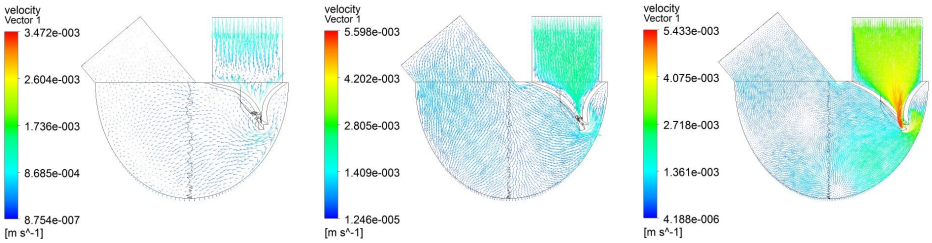

(13) t=0.406 Sec (14) t=0.412 Sec (15) t=0.418 Sec

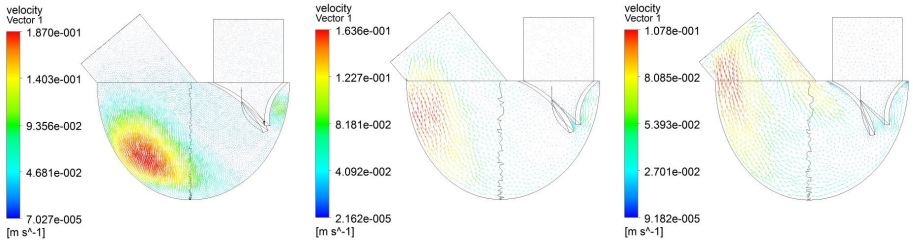

(16) t=0.421 Sec (17) t=0.424 Sec (18) t=0.427 Sec

Figure B.3: Velocity contours in the long axis (symmetry) Plane. SV=60 ml, HR=60 bpm (cpnt).

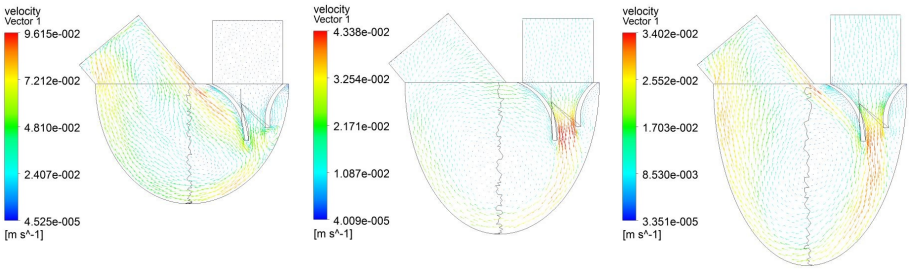

(19) t=0.430 Sec (20) t=0.500 Sec (21) t=0.550 Sec

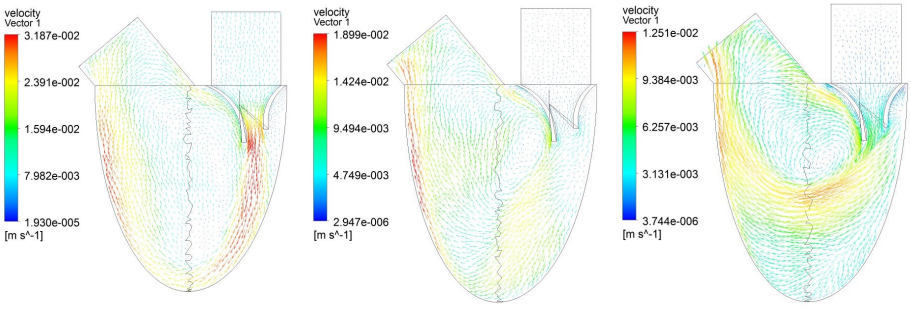

(22) t=0.600 Sec (23) t=0.650 Sec (24) t=0.700 Sec

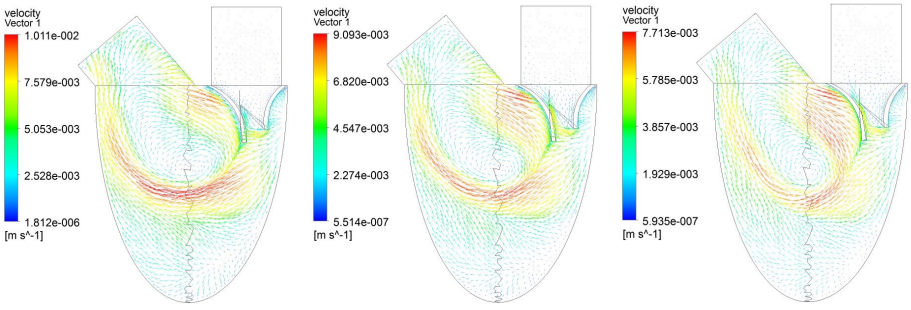

(25) t=0.750 Sec (26) t=0.800 Sec (27) t=0.850 Sec

Figure B.3: Velocity contours in the long axis (symmetry) Plane. SV=60 ml, HR=60 bpm (cpnt).

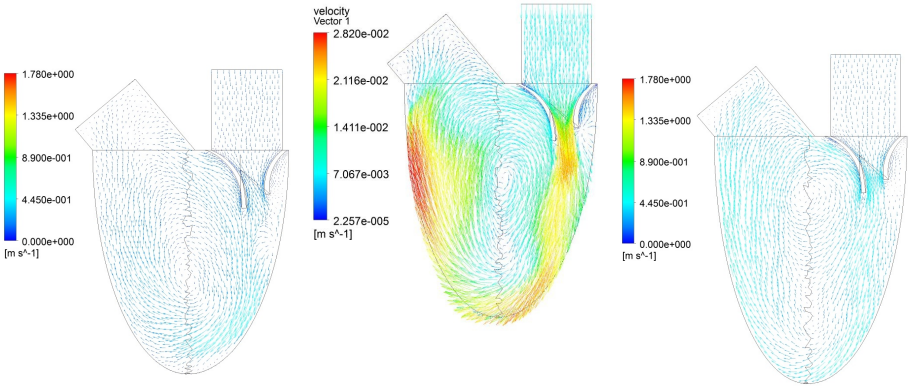

(28) t=0.887 Sec (29) t=0.925 Sec (30) t=0.962 Sec

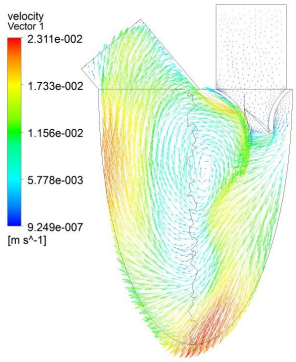

(31) t=1 Sec

Figure B.3: Velocity contours in the long axis (symmetry) Plane. SV=60 ml, HR=60 bpm (cont).

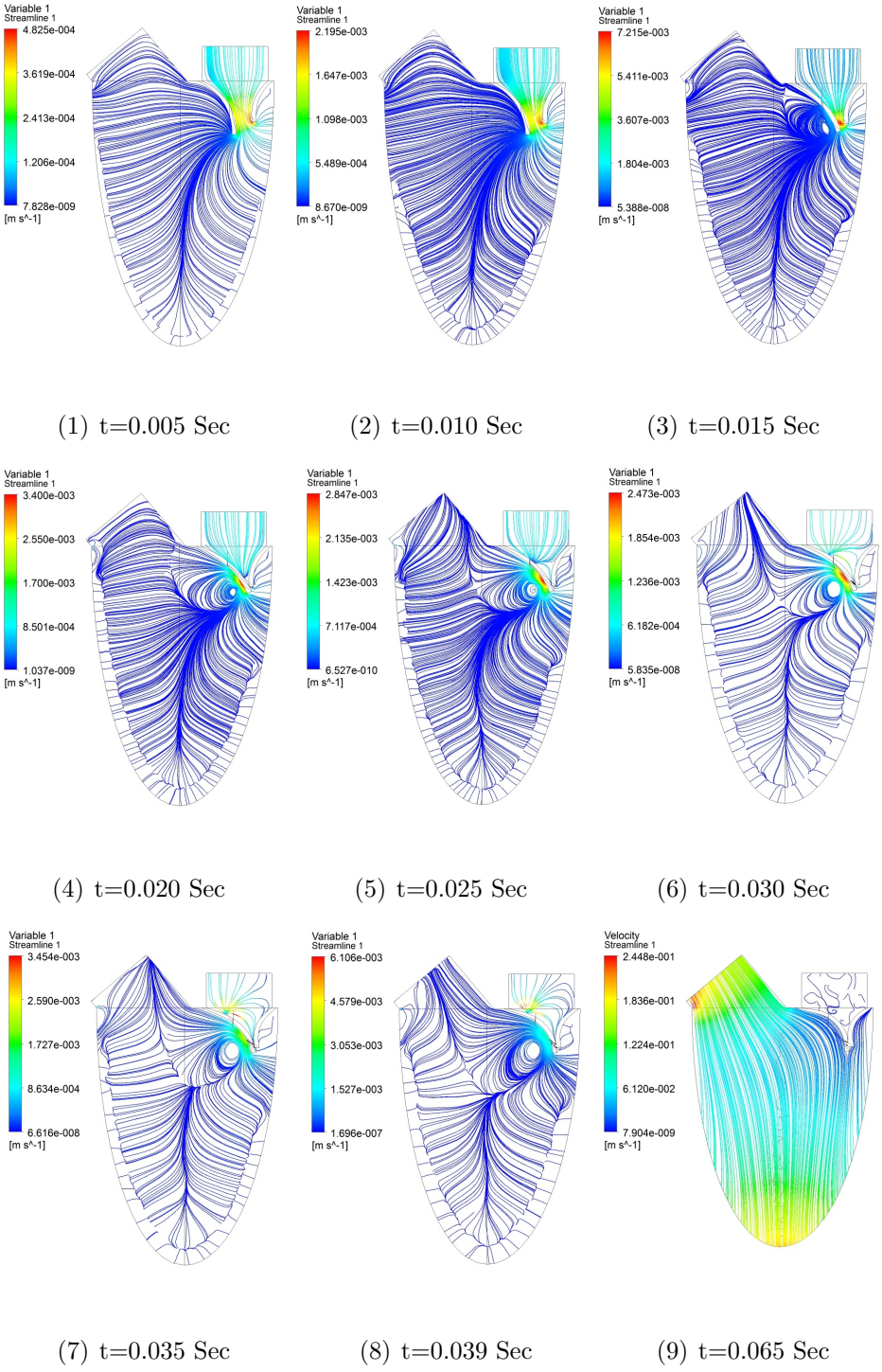

(1) t=0.005 Sec (2) t=0.010 Sec (3) t=0.015 Sec

(4) t=0.020 Sec (5) t=0.025 Sec (6) t=0.030 Sec

(7) t=0.035 Sec (8) t=0.039 Sec (9) t=0.065 Sec

Figure B.4: Velocity contours in the long axis (symmetry) Plane. SV=60 ml, HR=60 bpm.

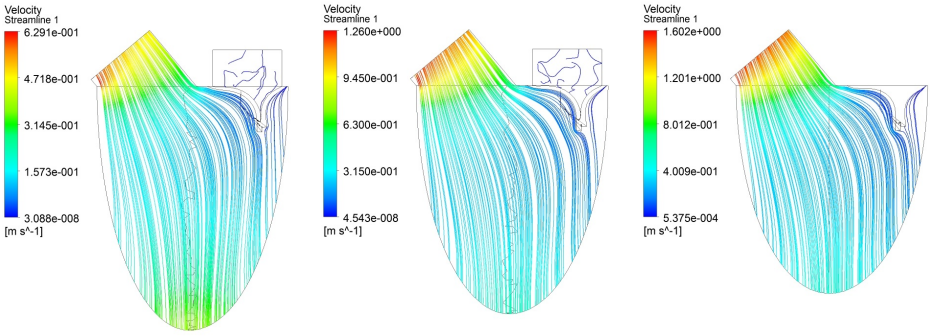

(10) t=0.080 Sec (11) t=0.100 Sec (12) t=0.120 Sec

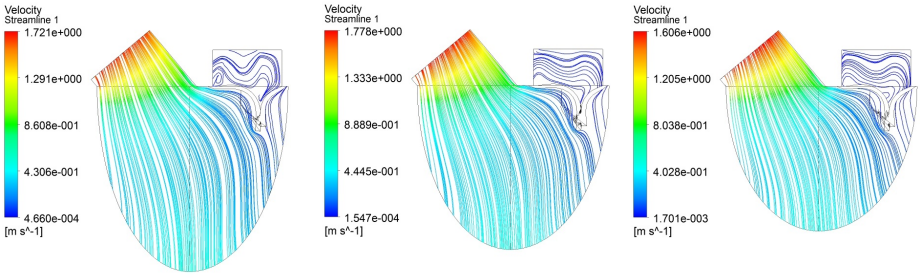

(13) t=0.140 Sec (14) t=0.160 Sec (15) t=0.180 Sec

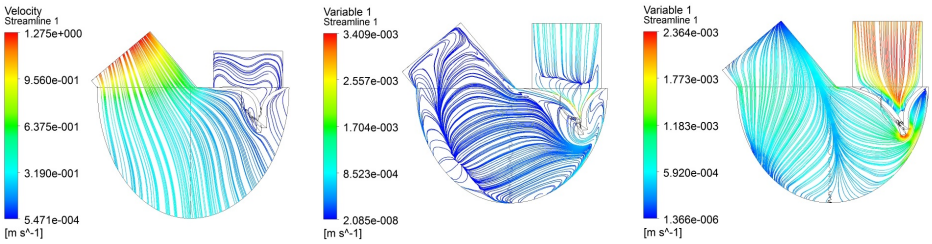

(16) t=0.200 Sec (17) t=0.406 Sec (18) t=0.412 Sec

Figure B.4: Velocity contours in the long axis (symmetry) Plane. SV=60 ml, HR=60 bpm (cont).

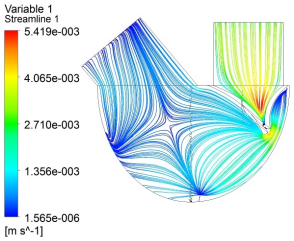

(19) t=0.418 Sec

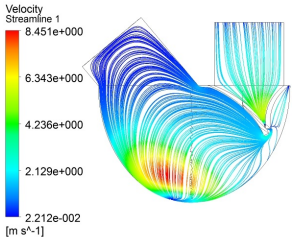

(20) t=0.419 Sec

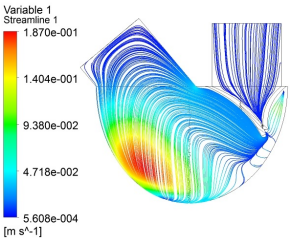

(21) t=0.421 Sec

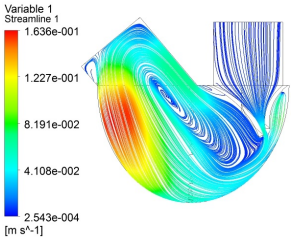

(22) t=0.424 Sec

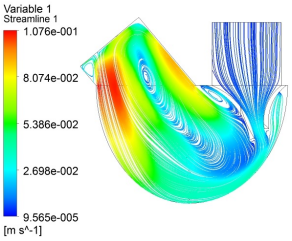

(23) t=0.427 Sec

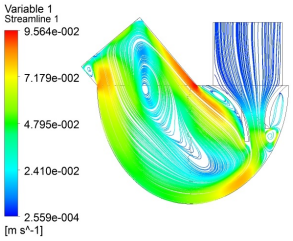

(24) t=0.430 Sec

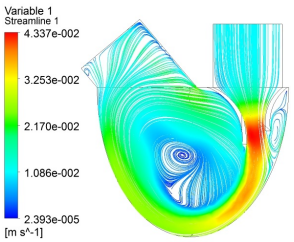

(25) t=0.500 Sec

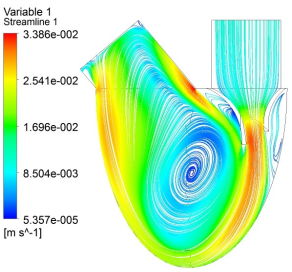

(26) t=0.550 Sec

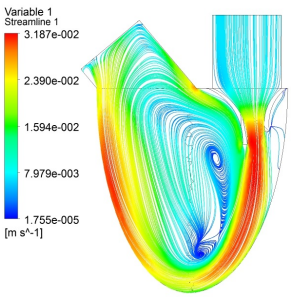

(27) t=0.600 Sec

Figure B.4: Velocity contours in the long axis (symmetry) Plane. SV=60 ml, HR=60 bpm (cont).

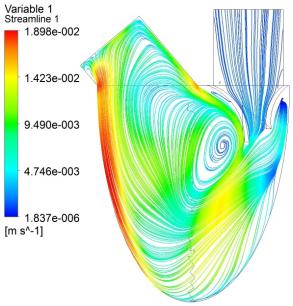

(28) t=0.650 Sec

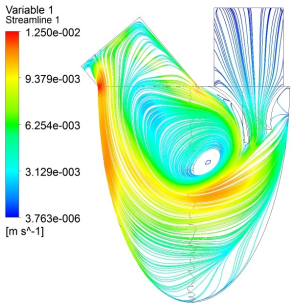

(29) t=0.700 Sec

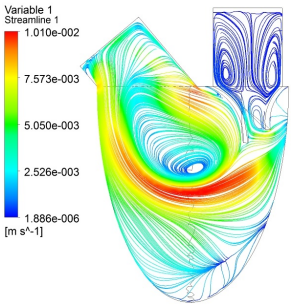

(30) t=0.750 Sec

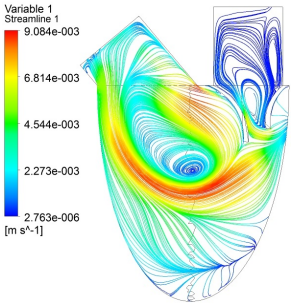

(31) t=0.800 Sec

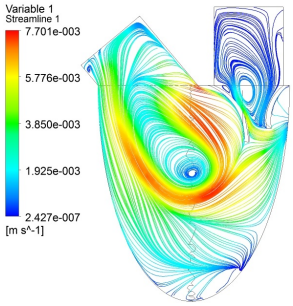

(32) t=0.850 Sec

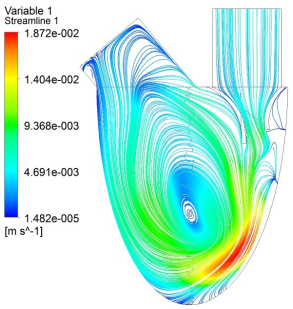

(33) t=0.8875 Sec

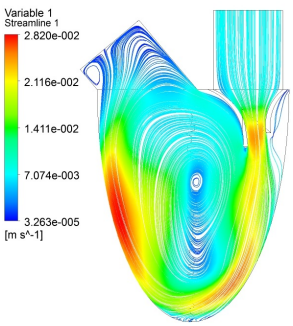

(34) t=0.925 Sec

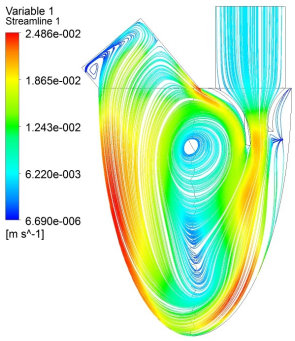

(35) t=0.9625 Sec

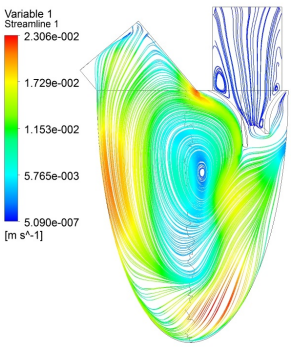

(36) t=0.1000 Sec

Figure B.4: Velocity contours in the long axis (symmetry) Plane. SV=60 ml, HR=60 bpm(cont).

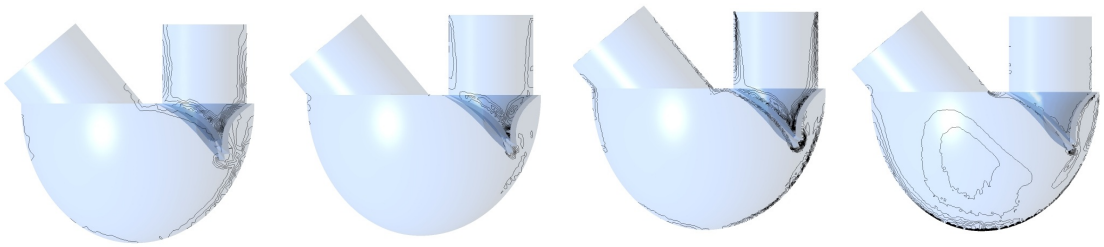

(1) t=0.406 Sec (2) t=0.412 Sec (3) t=0.418 Sec (4) t=0.421 Sec

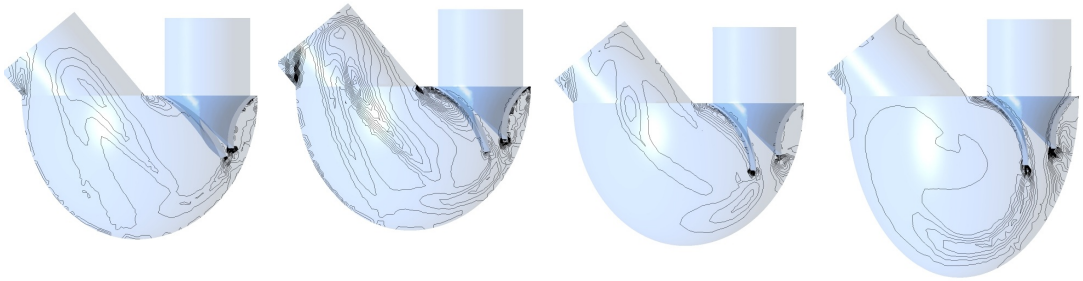

(5) t=0.424 Sec (6) t=0.427 Sec (7) t=0.430 Sec (8) t=0.500 Sec

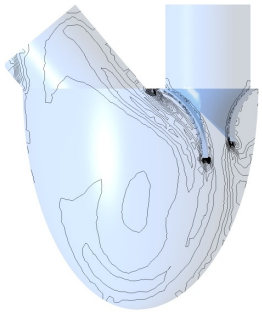

(9) t=0.550 Sec

Figure B.5: Vorticity contours in the long axis (symmetry) Plane. SV=60 ml, HR=60 bpm (cont.).

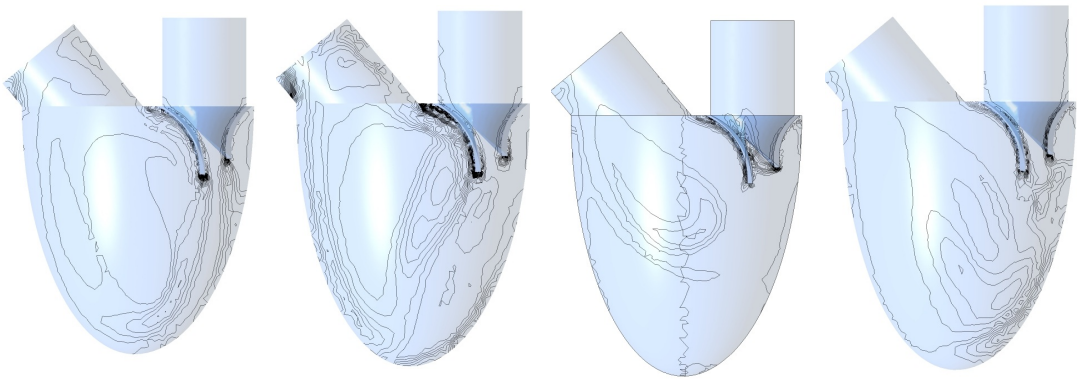

(10) t=0.600 Sec (11) t=0.650 Sec (12) t=0.850 Sec (13) t=0.887 Sec

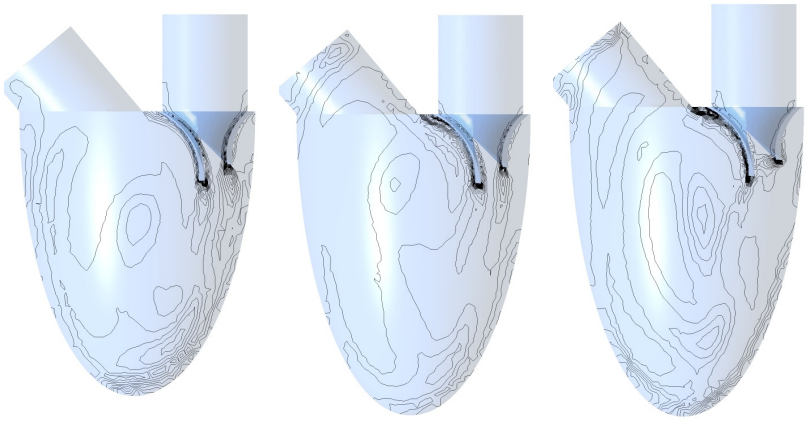

(14) t=0.925 Sec (15) t=0.962 Sec (16) t=1 Sec

Figure B.5: Vorticity contours in the long axis (symmetry) Plane. SV=60 ml, HR=60 bpm(cont).

Appendix C

Time History Results of Chapter 5

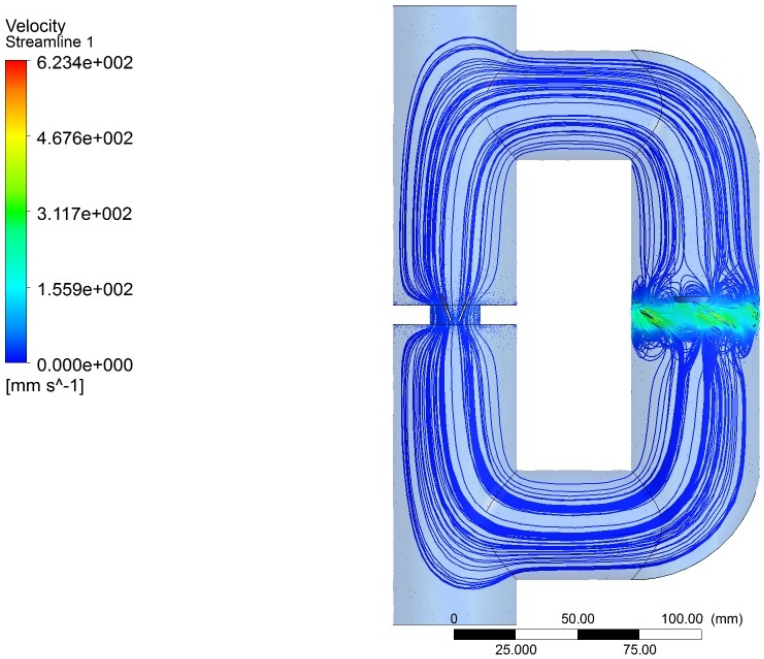

Figure C.1: 3D streamlines, colored with velocity at $t = 0.1$ Sec in which the impeller is at its pick velocity.

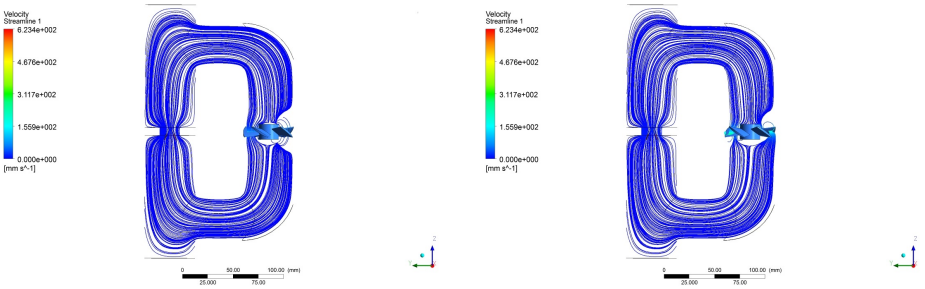

(1) t=0.7 Sec

(2) t=0.04 Sec

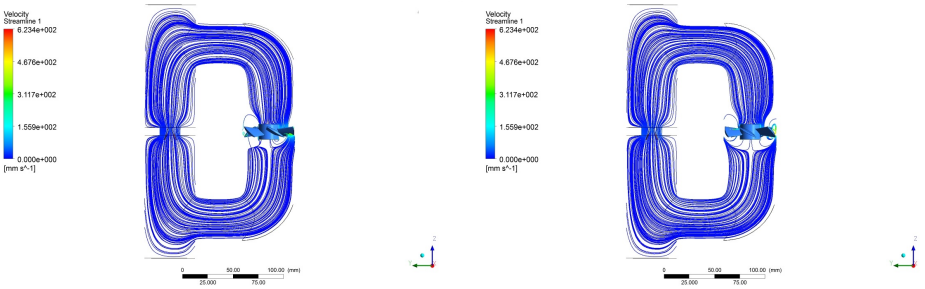

(3) t=0.06 Sec

(4) t=0.08 Sec

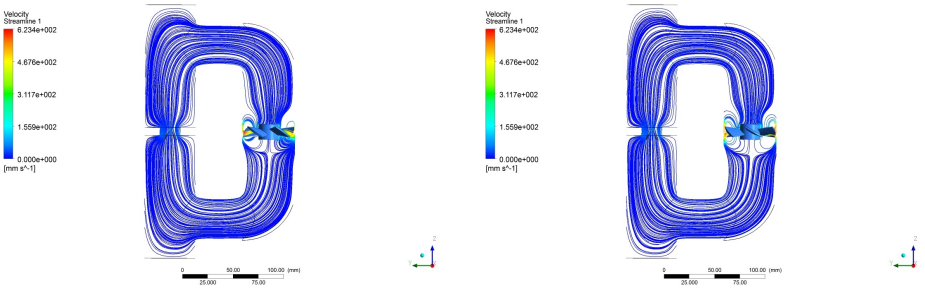

(5) t=0.1 Sec

(6) t=0.12 Sec

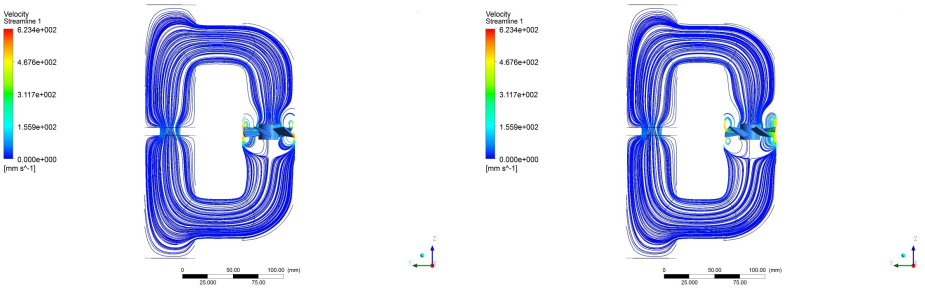

(7) t=0.14 Sec

(8) t=0.16 Sec

Figure C.2: 2D streamlines, colored with velocity at different time steps.

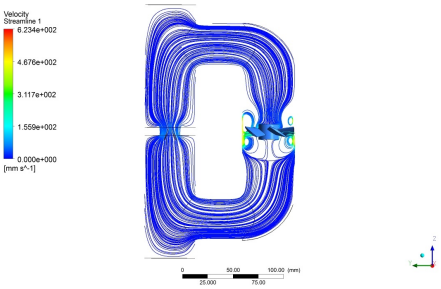

(9) t=0.18 Sec

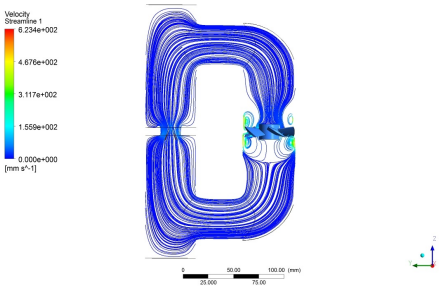

(10) t=0.20 Sec

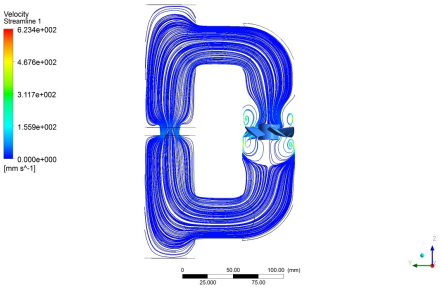

(11) t=0.22 Sec

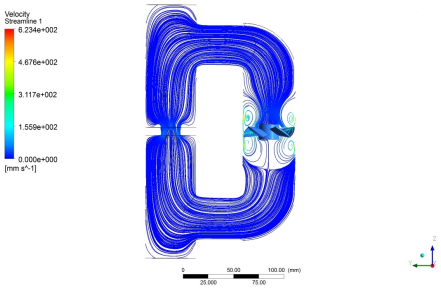

(12) t=0.24 Sec

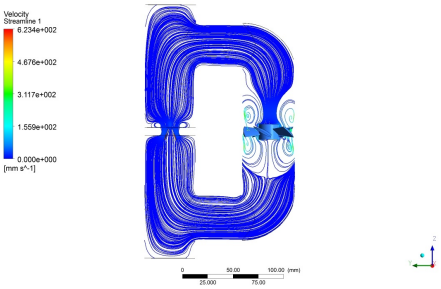

(13) t=0.26 Sec

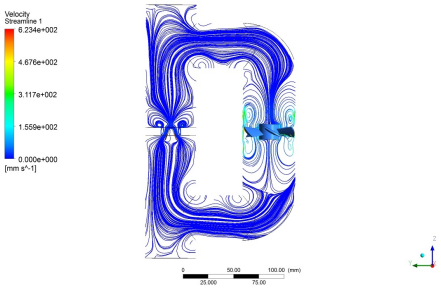

(14) t=0.28 Sec

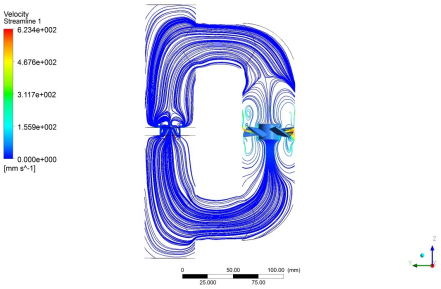

(15) t=0.30 Sec

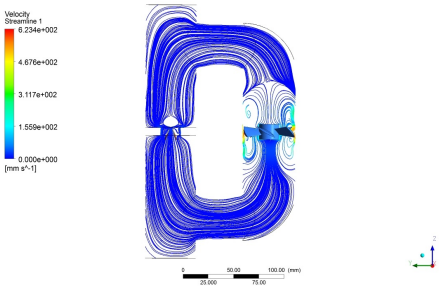

(16) t=0.32 Sec

Figure C.2: 2D streamlines, colored with velocity at different time steps (cont).

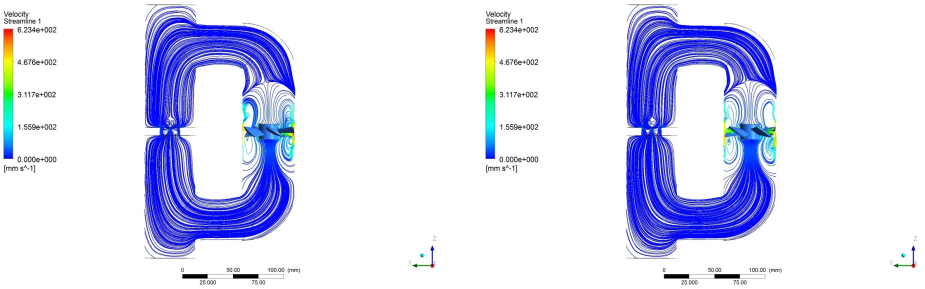

(17) t=0.34 Sec (18) t=0.36 Sec

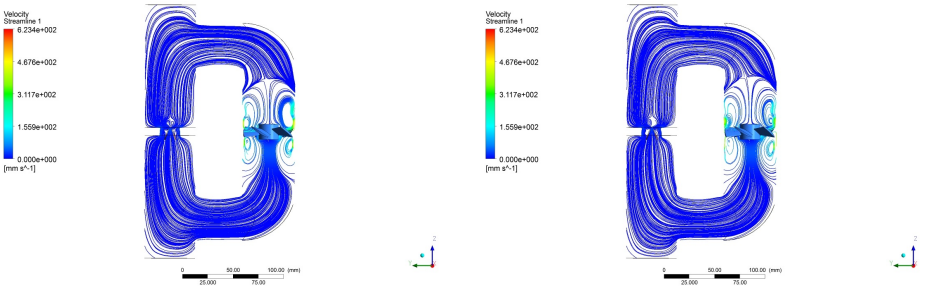

(19) t=0.38 Sec (20) t=0.40 Sec

Figure C.2: 2D streamlines, colored with velocity at different time steps (cont).

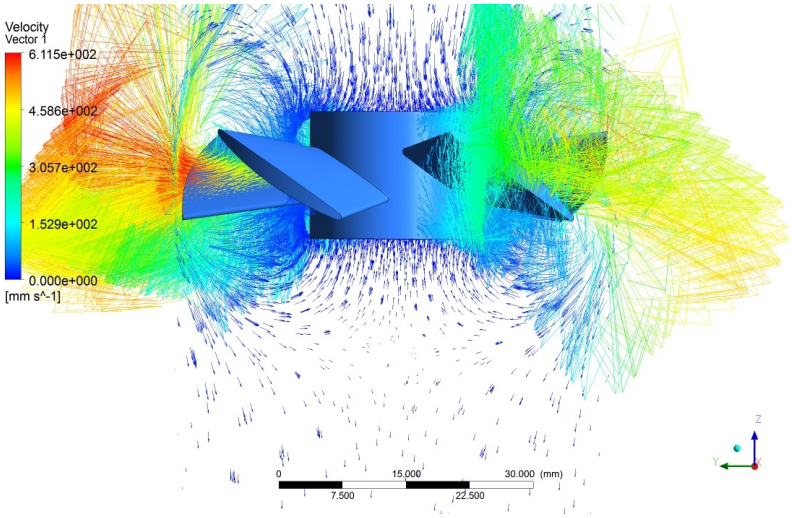

Figure C.3: Velocity vectors at $t = 0.1$ Sec.

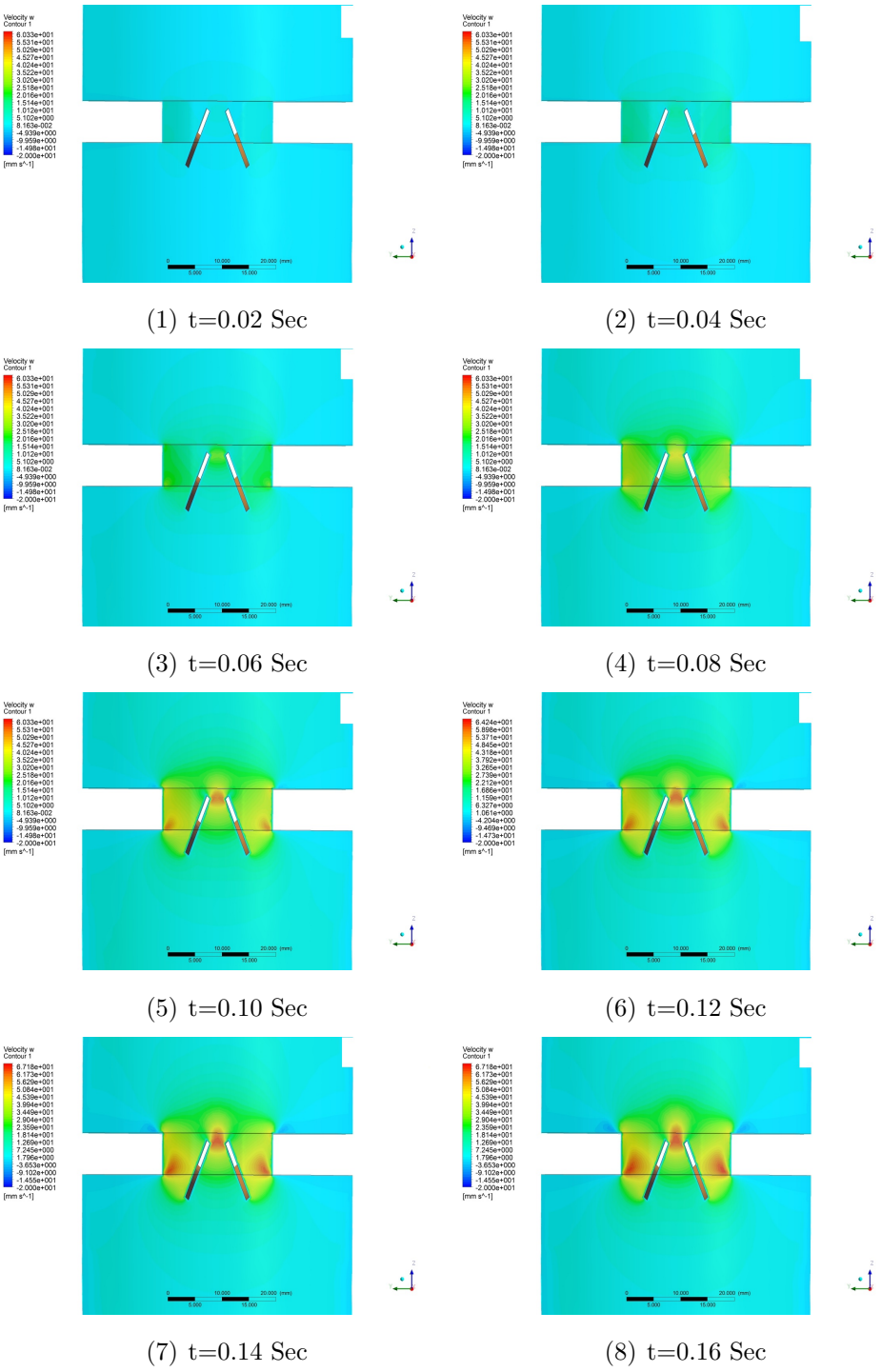

(1) t=0.02 Sec (2) t=0.04 Sec

(3) t=0.06 Sec (4) t=0.08 Sec

(5) t=0.10 Sec (6) t=0.12 Sec

(7) t=0.14 Sec (8) t=0.16 Sec

Figure C.4: Velocity contours at different time steps.

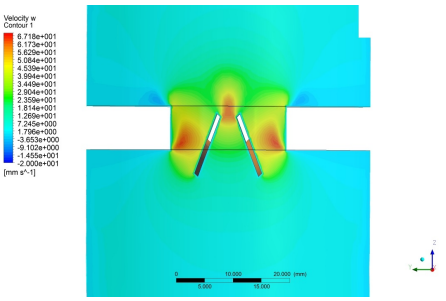

(9) t=0.18 Sec

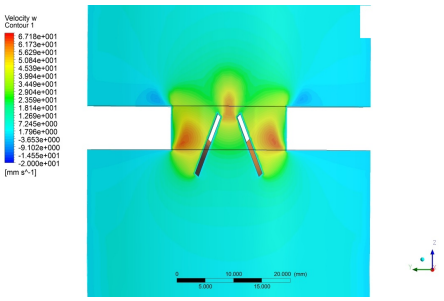

(10) t=0.20 Sec

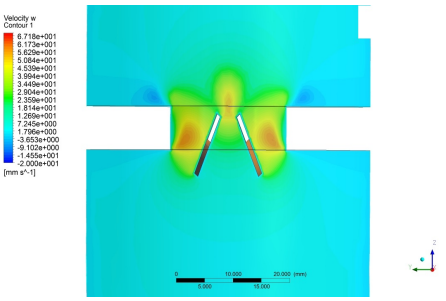

(11) t=0.22 Sec

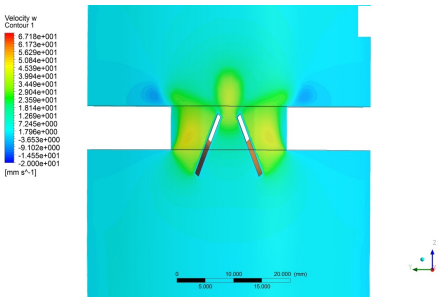

(12) t=0.24 Sec

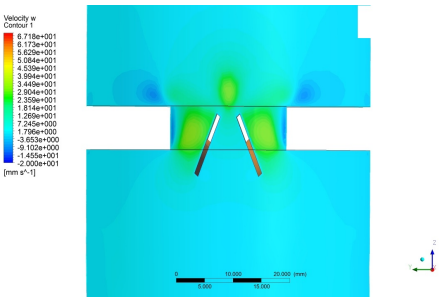

(13) t=0.26 Sec

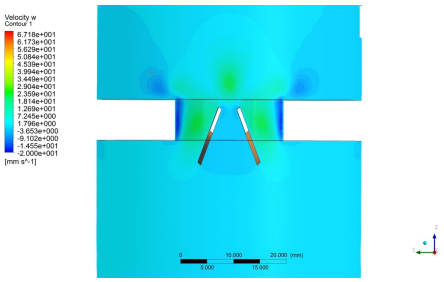

(14) t=0.28 Sec

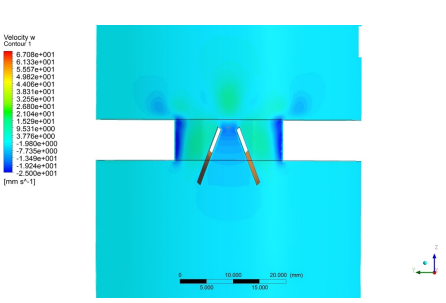

(15) t=0.30 Sec

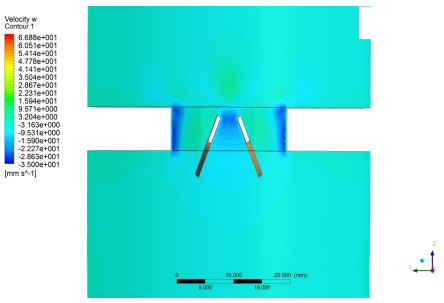

(16) t=0.32 Sec

Figure C.4: Velocity contours at different time steps (cont).

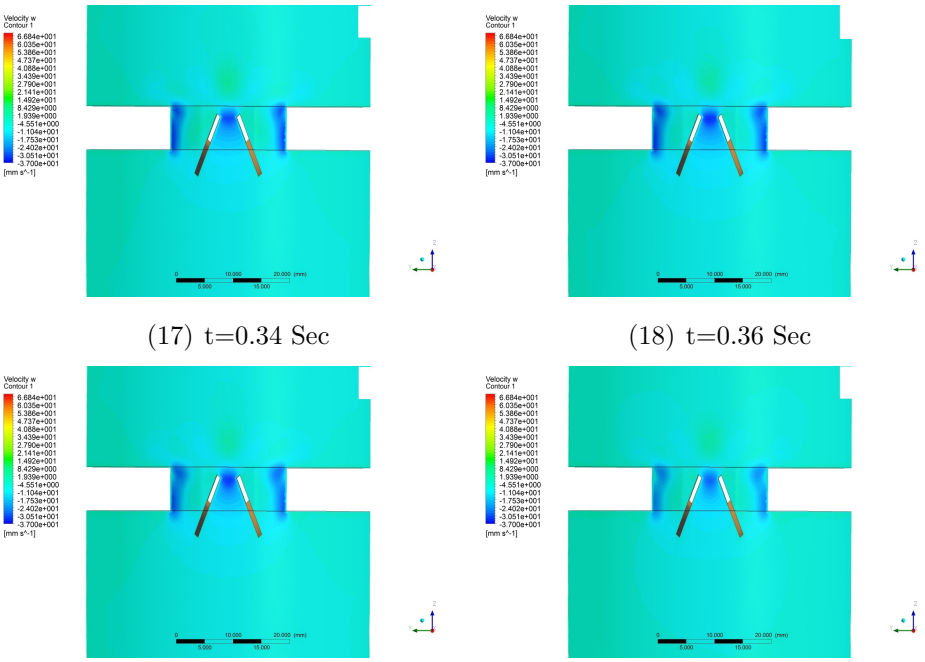

(17) t=0.34 Sec

(18) t=0.36 Sec

(19) t=0.38 Sec

(20) t=0.40 Sec

Figure C.4: Velocity contours at different time steps(cont).

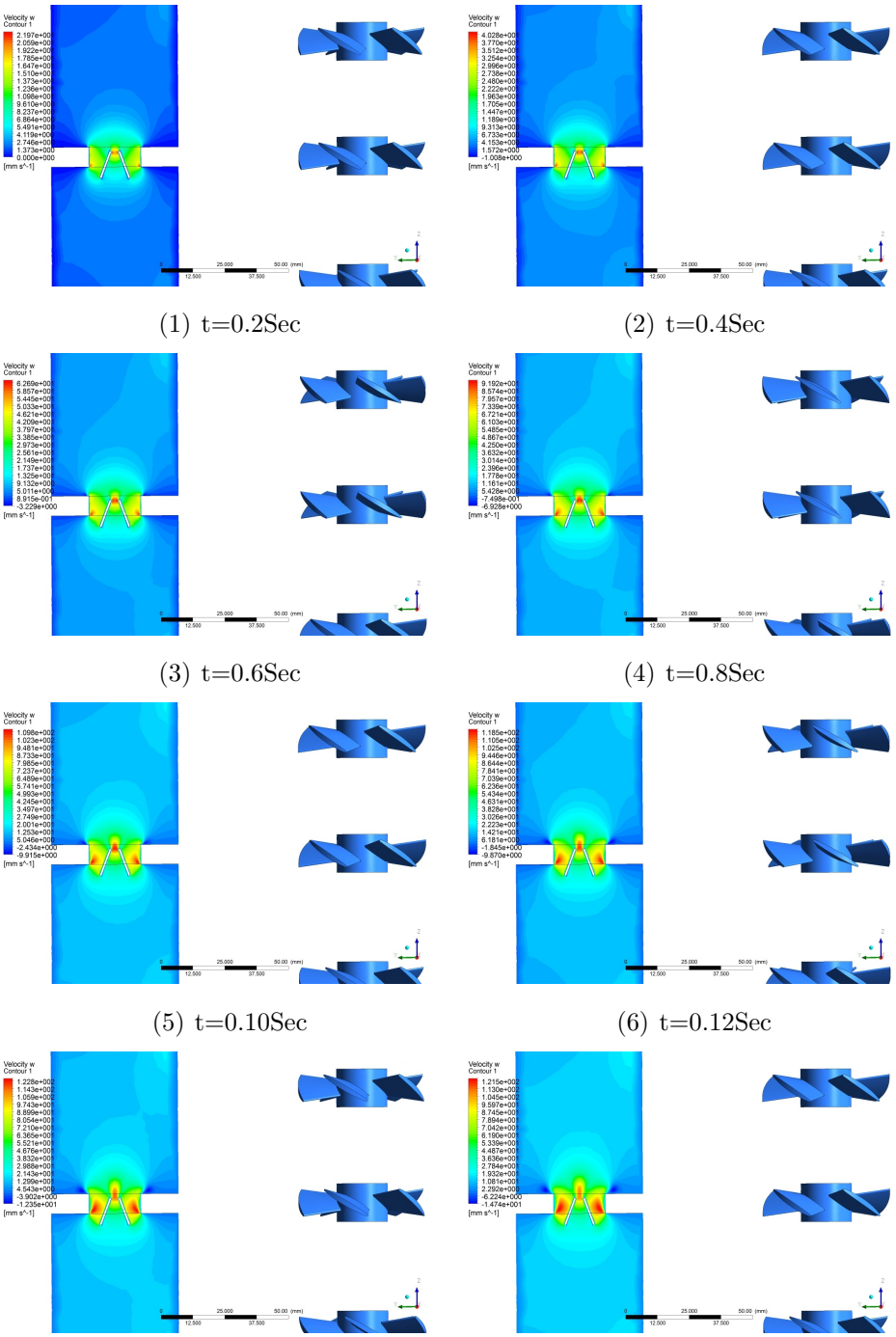

(1) t=0.2Sec (2) t=0.4Sec

(3) t=0.6Sec (4) t=0.8Sec

(5) t=0.10Sec (6) t=0.12Sec

(7) t=0.14Sec (8) t=0.16Sec

Figure C.5: Velocity contours at different time steps.

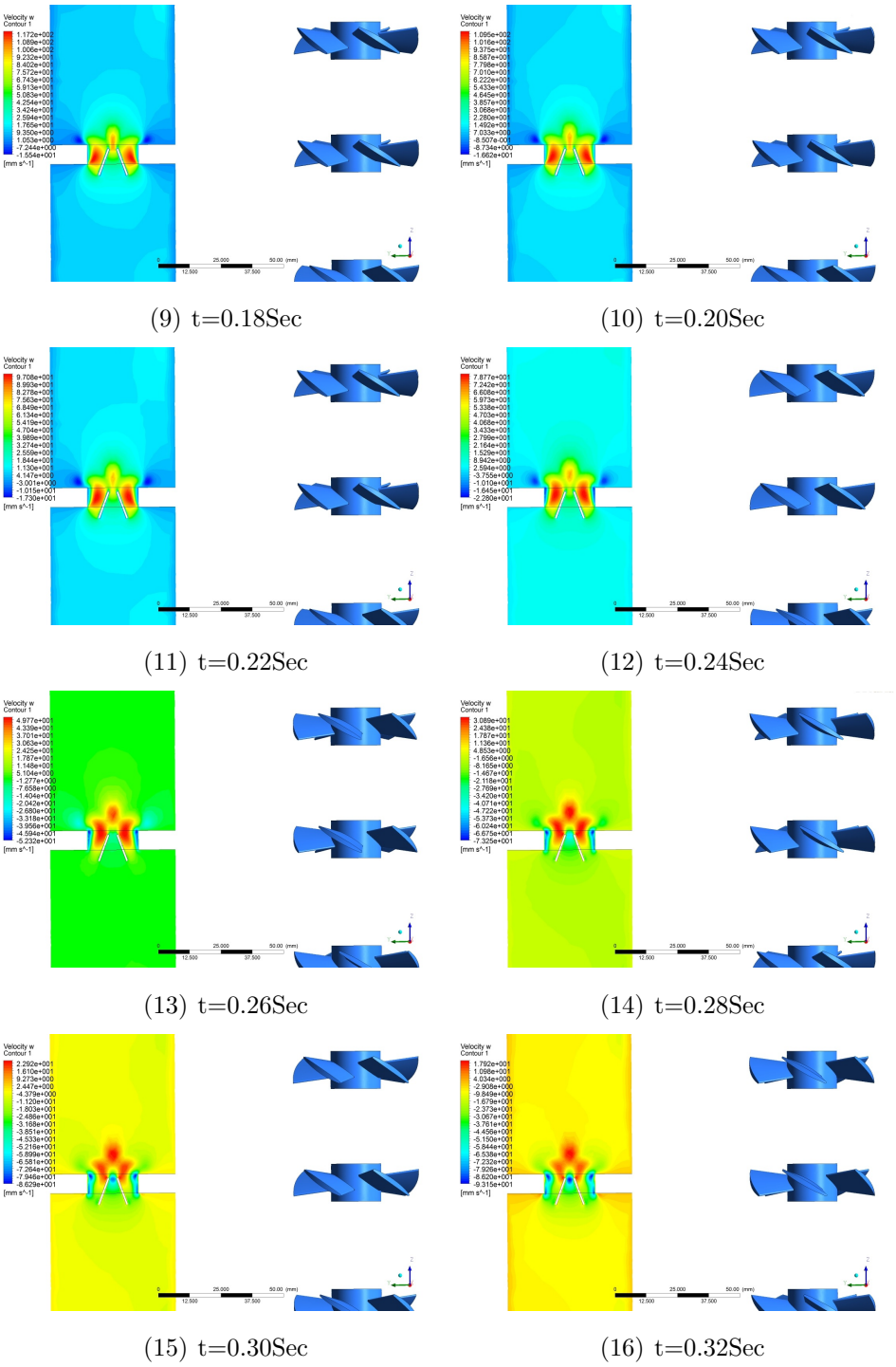

(9) t=0.18Sec (10) t=0.20Sec

(11) t=0.22Sec (12) t=0.24Sec

(13) t=0.26Sec (14) t=0.28Sec

(15) t=0.30Sec (16) t=0.32Sec

Figure C.5: Velocity contours at different time steps (cont).

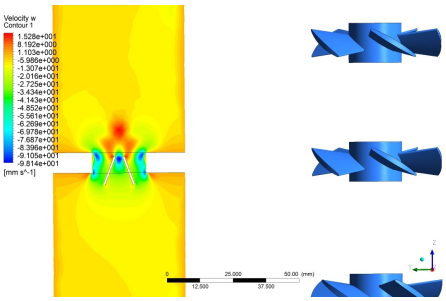

(17) t=0.34Sec

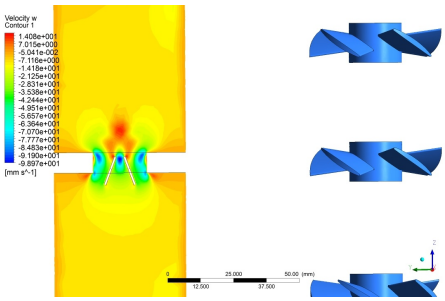

(18) t=0.36Sec

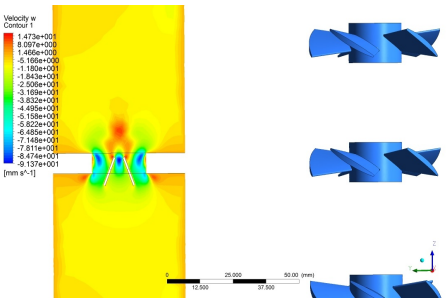

(19) t=0.38Sec

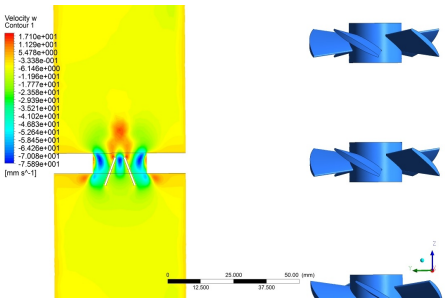

(20) t=0.40Sec

Figure C.5: Velocity contours at different time steps (cont).

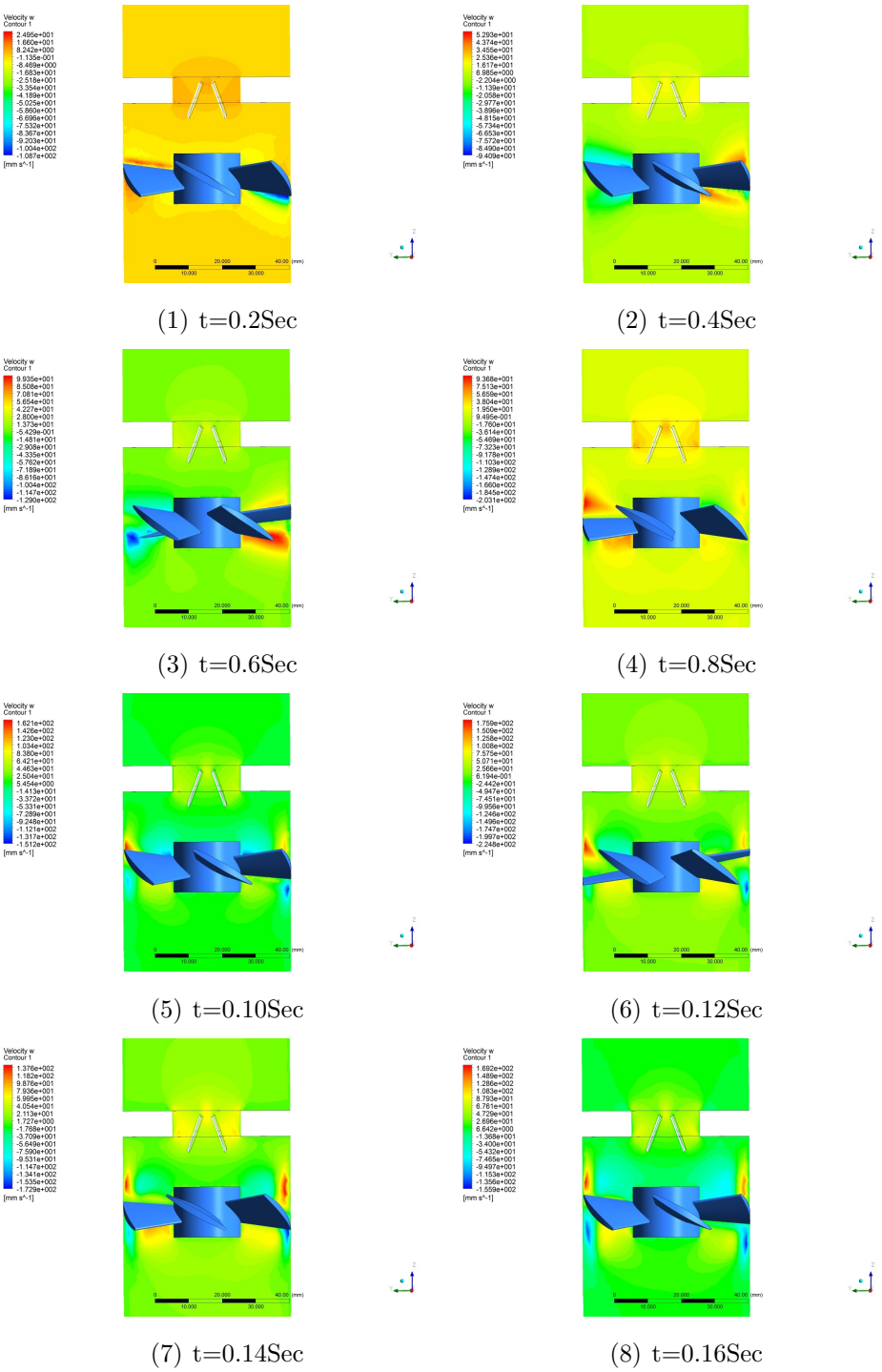

(1) t=0.2Sec (2) t=0.4Sec

(3) t=0.6Sec (4) t=0.8Sec

(5) t=0.10Sec (6) t=0.12Sec

(7) t=0.14Sec (8) t=0.16Sec

Figure C.6: Velocity contours at different time steps for the case of installing the impeller close to the valve.

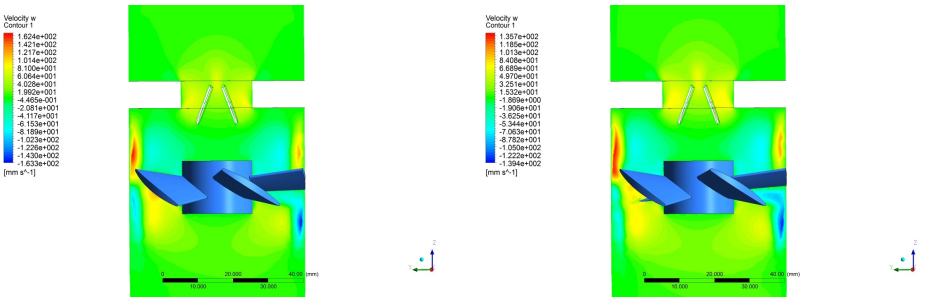

(9) t=0.18Sec (10) t=0.20Sec

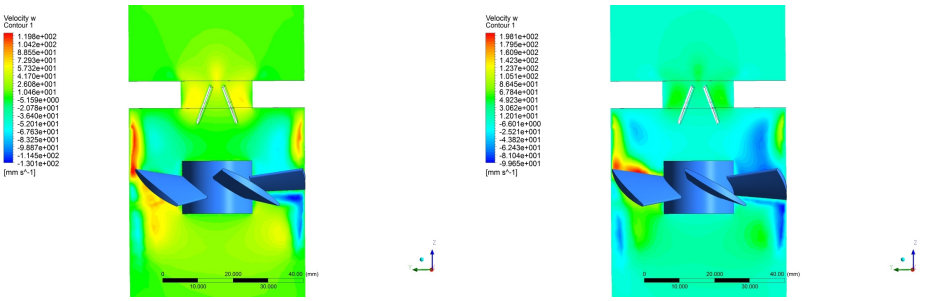

(11) t=0.22Sec (12) t=0.24Sec

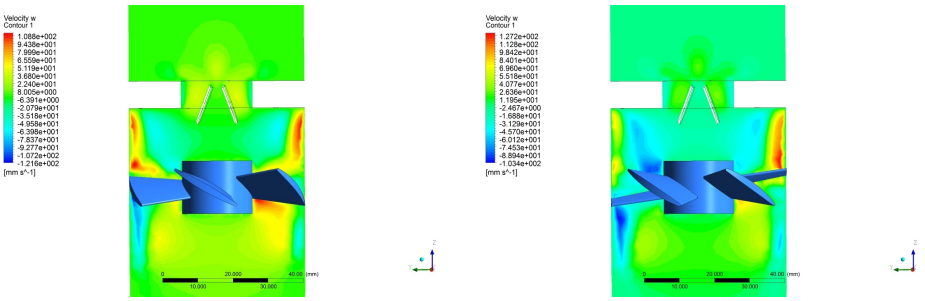

(13) t=0.26Sec (14) t=0.28Sec

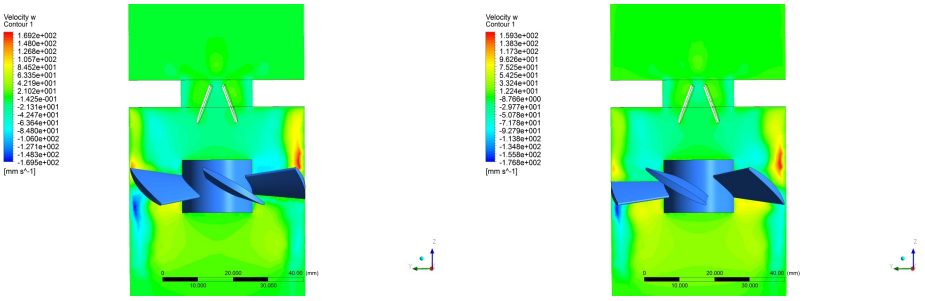

(15) t=0.30Sec (16) t=0.32Sec

Figure C.6: Velocity contours at different time steps for the case of installing the impeller close to the valve (cont).

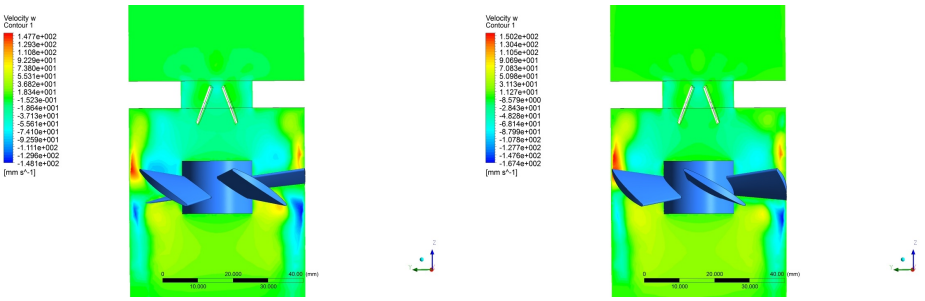

(17) t=0.34Sec (18) t=0.36Sec

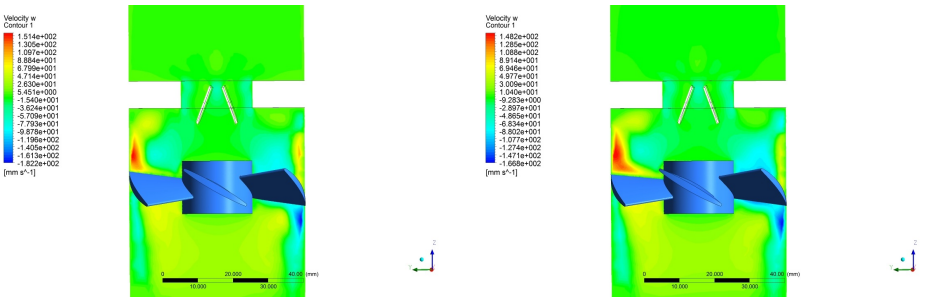

(19) t=0.38Sec (20) t=0.40Sec

Figure C.6: Velocity contours at different time steps for the case of installing the impeller close to the valve (cont).

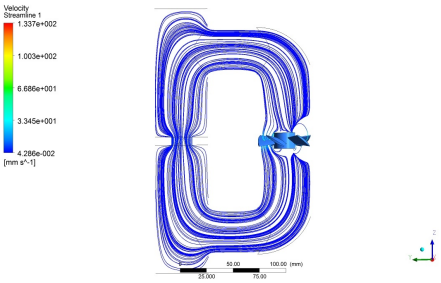

(1) t=0.2 Sec

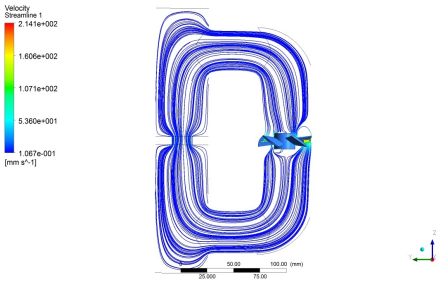

(2) t=0.4 Sec

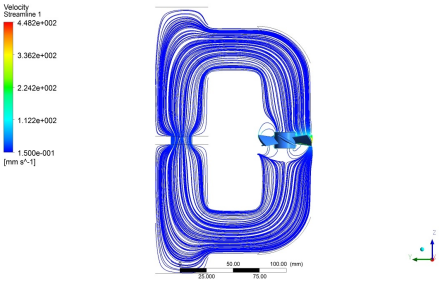

(3) t=0.6 Sec

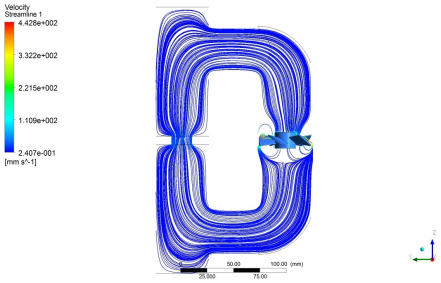

(4) t=0.8 Sec

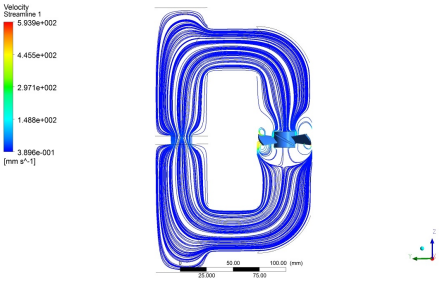

(5) t=0.10 Sec

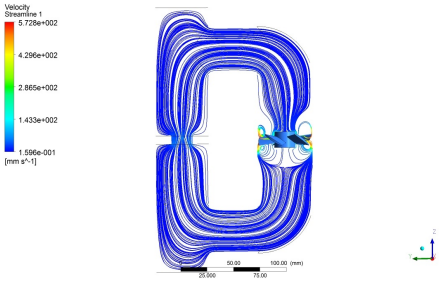

(6) t=0.12 Sec

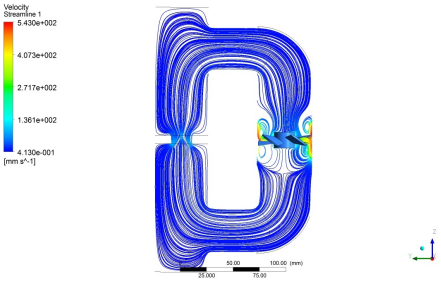

(7) t=0.14 Sec

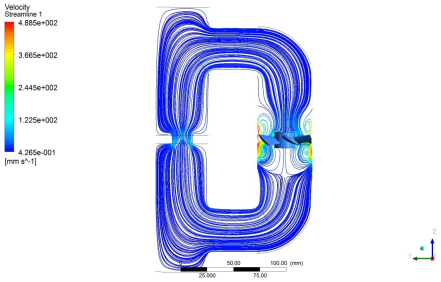

(8) t=0.16 Sec

Figure C.7: Streamlines for the case of full FSI.

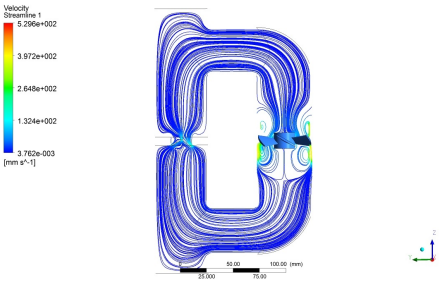

(9) t=0.18 Sec

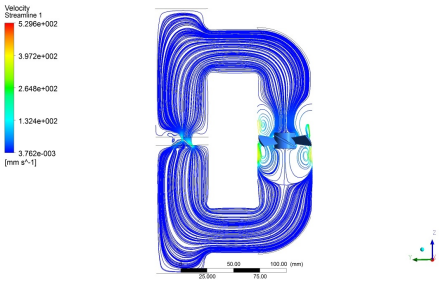

(10) t=0.20 Sec

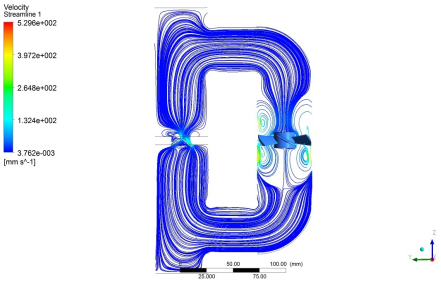

(11) t=0.22 Sec

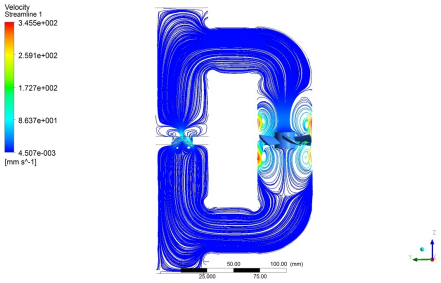

(12) t=0.24 Sec

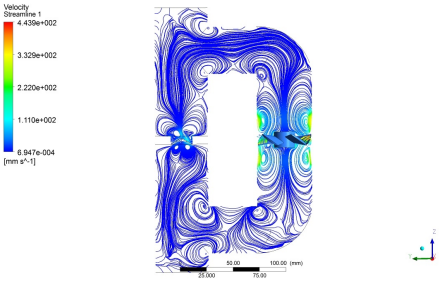

(13) t=0.26 Sec

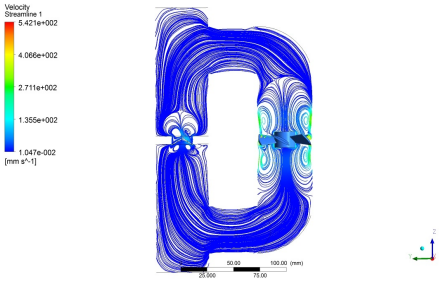

(14) t=0.28 Sec

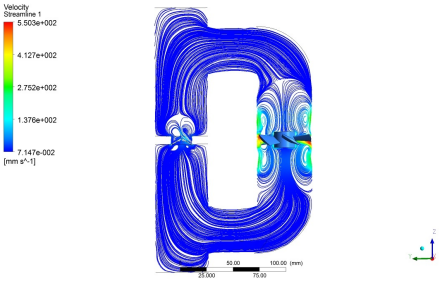

(15) t=0.30 Sec

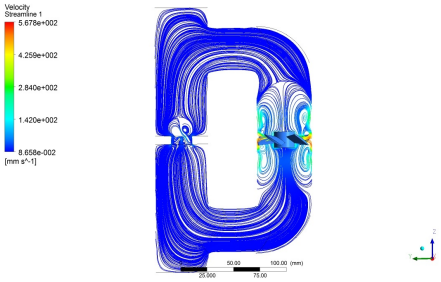

(16) t=0.32 Sec

Figure C.7: Streamlines for the case of full FSI (cont).

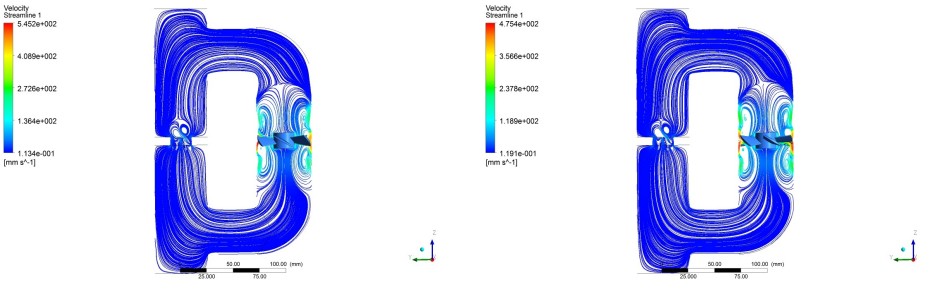

(17) t=0.34 Sec (18) t=0.36 Sec

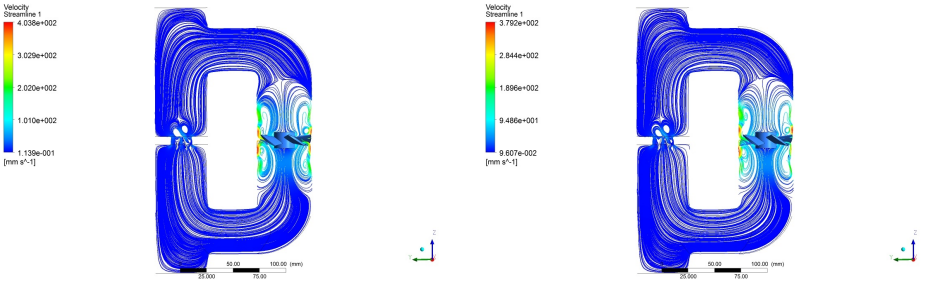

(19) t=0.38 Sec (20) t=0.40 Sec

Figure C.7: Streamlines for the case of full FSI (cont).

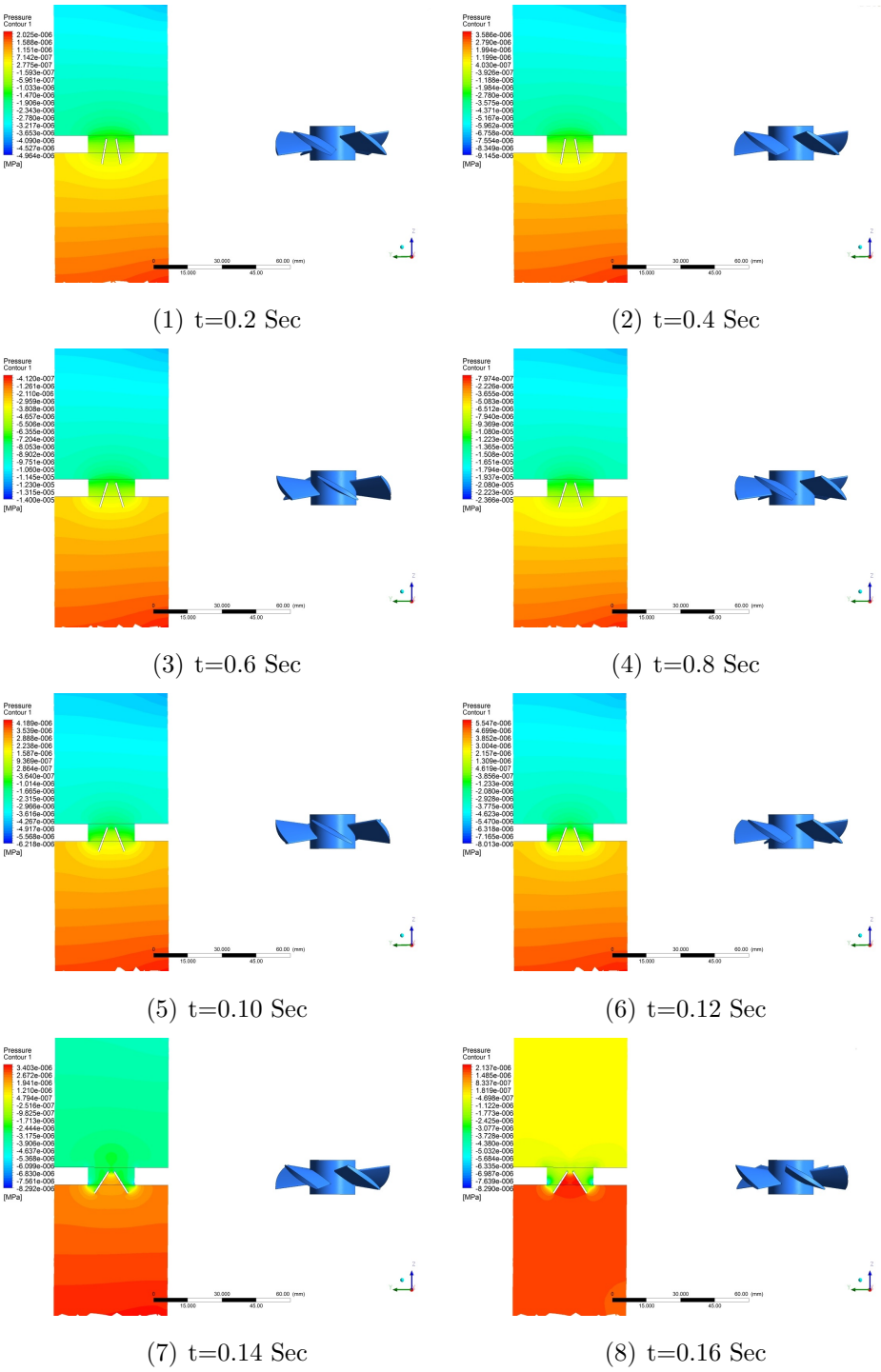

(1) t=0.2 Sec (2) t=0.4 Sec

(3) t=0.6 Sec (4) t=0.8 Sec

(5) t=0.10 Sec (6) t=0.12 Sec

(7) t=0.14 Sec (8) t=0.16 Sec

Figure C.8: Pressure contours for the case of full FSI.

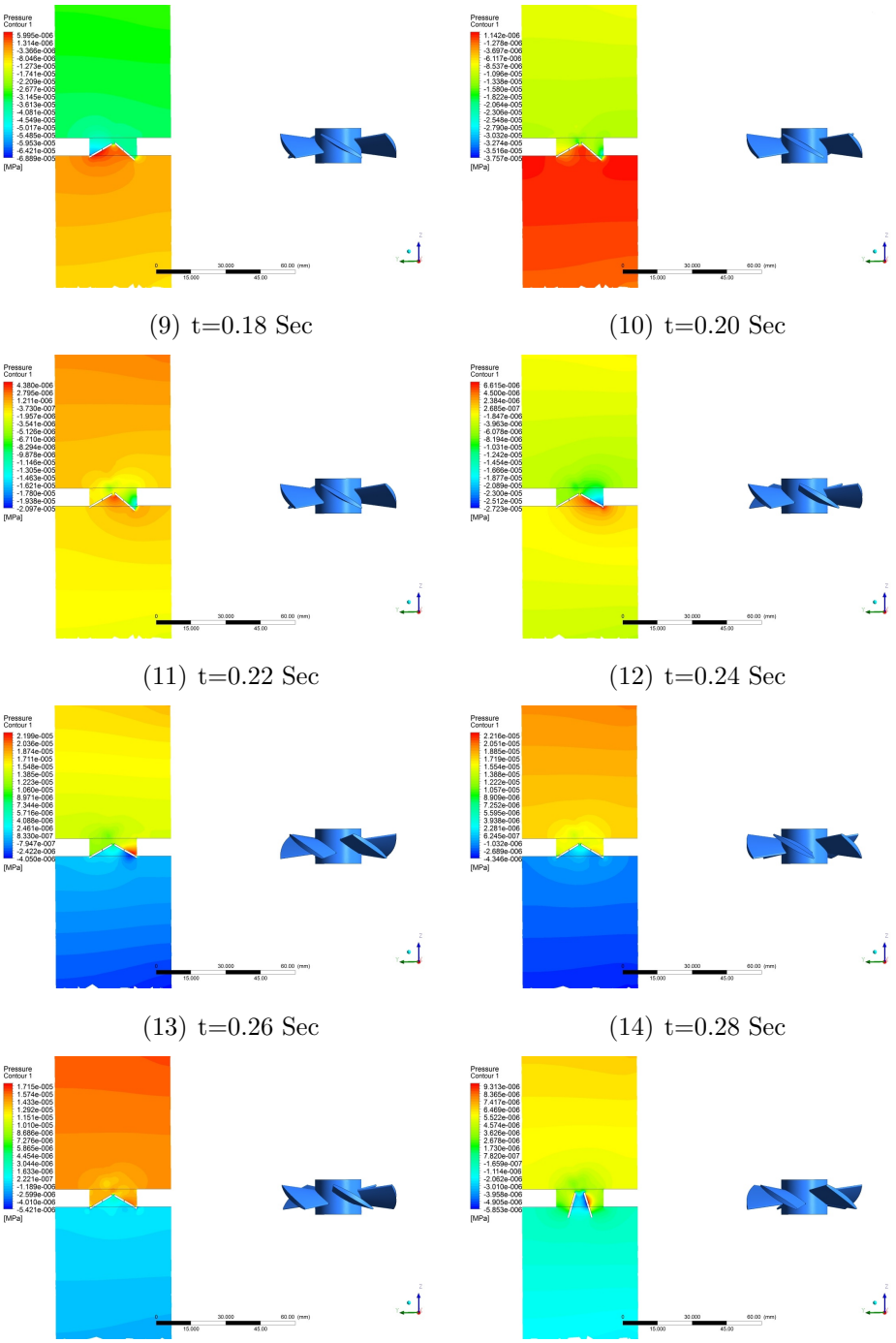

(9) t=0.18 Sec (10) t=0.20 Sec

(11) t=0.22 Sec (12) t=0.24 Sec

(13) t=0.26 Sec (14) t=0.28 Sec

(15) t=0.30 Sec (16) t=0.32 Sec

Figure C.8: Pressure contours for the case of full FSI (cont).

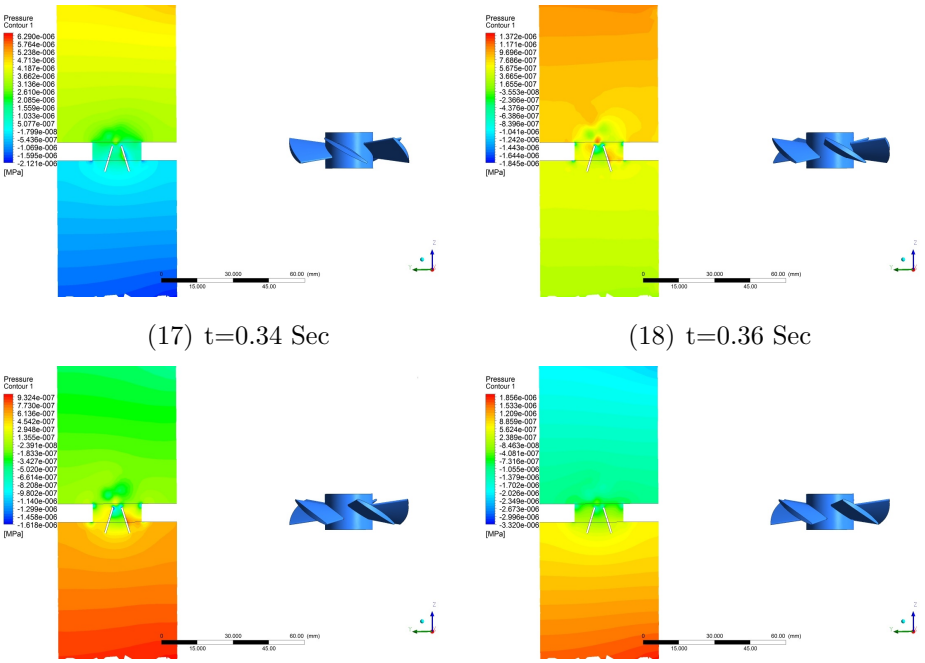

(17) t=0.34 Sec (18) t=0.36 Sec

(19) t=0.38 Sec (20) t=0.40 Sec

Figure C.8: Pressure contours for the case of full FSI (cont).

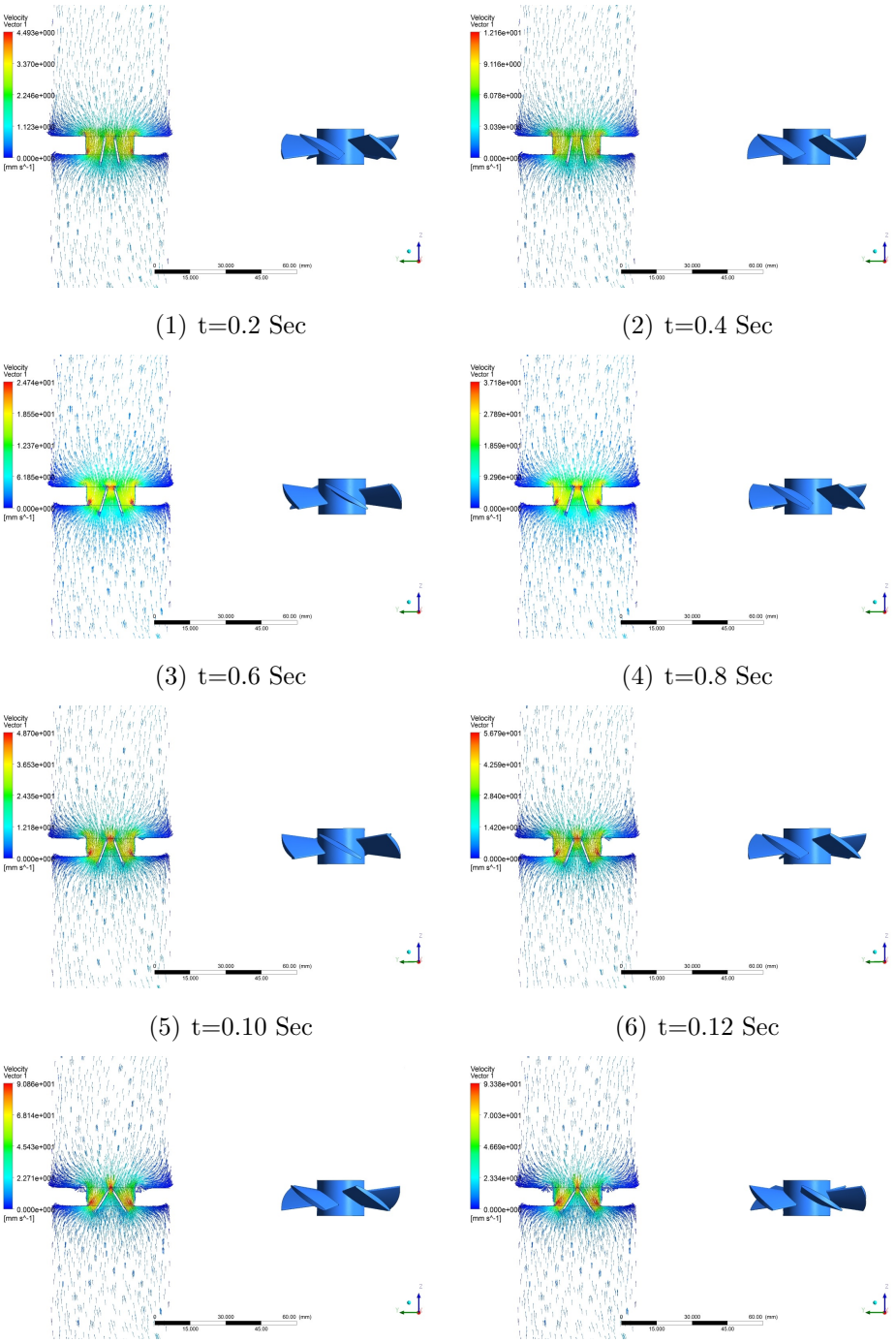

(1) t=0.2 Sec (2) t=0.4 Sec

(3) t=0.6 Sec (4) t=0.8 Sec

(5) t=0.10 Sec (6) t=0.12 Sec

(7) t=0.14 Sec (8) t=0.16 Sec

Figure C.9: Velocity vectors for the case of full FSI.

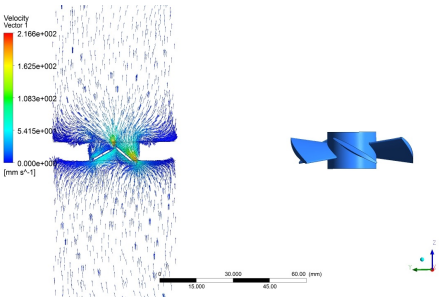

(9) t=0.18 Sec

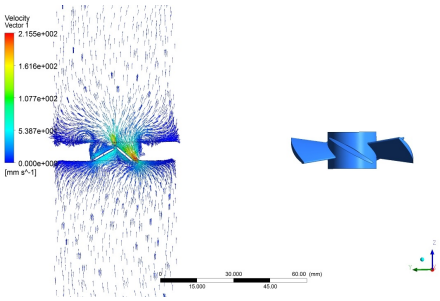

(10) t=0.20 Sec

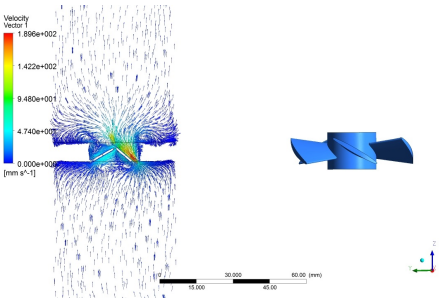

(11) t=0.22 Sec

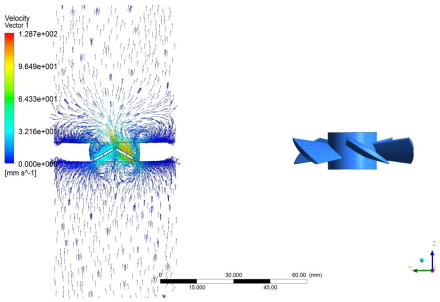

(12) t=0.24 Sec

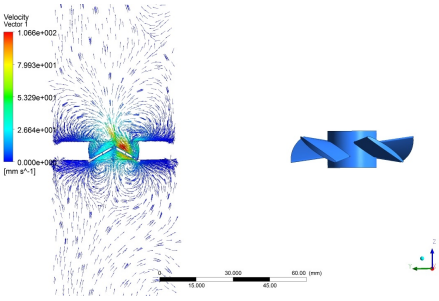

(13) t=0.26 Sec

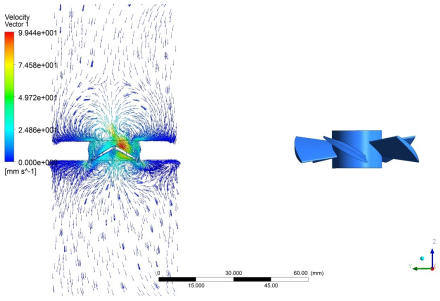

(14) t=0.28 Sec

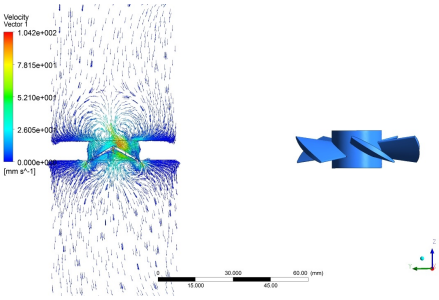

(15) t=0.30 Sec

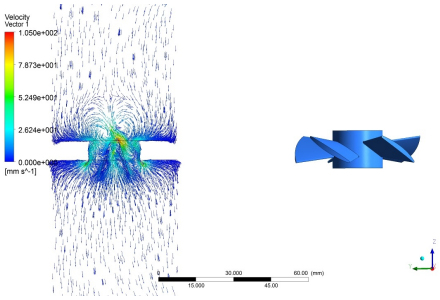

(16) t=0.32 Sec

Figure C.9: Velocity vectors for the case of full FSI (cont).

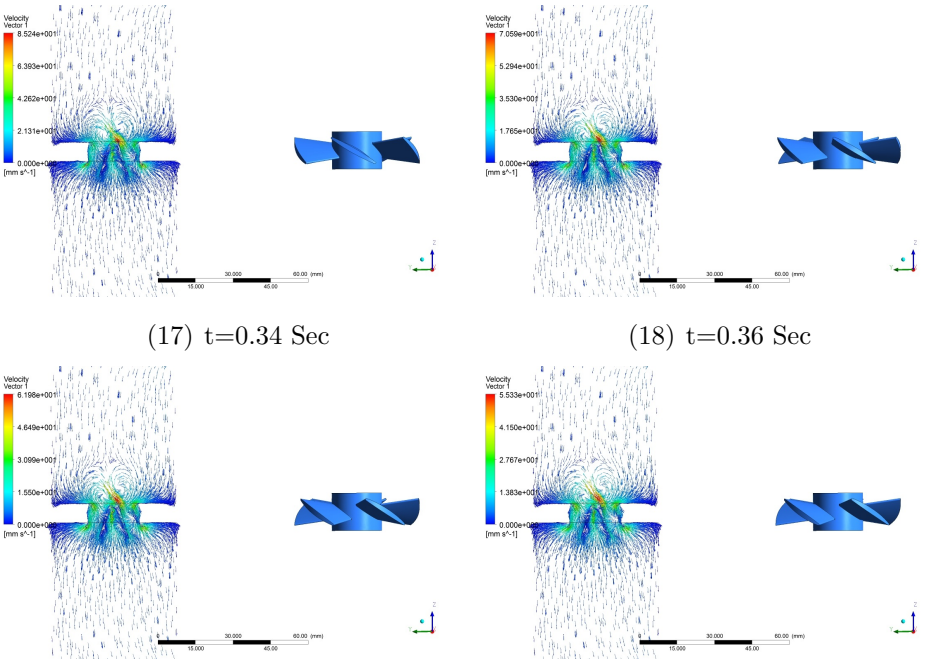

(17) t=0.34 Sec (18) t=0.36 Sec

(19) t=0.38 Sec (20) t=0.40 Sec

Figure C.9: Velocity vectors for the case of full FSI (cont).

Appendix D

Permission Letter For Copyright Material

Dear Ahmad M. Kermani,

You are authorized to include in your thesis the project you conduct in ViVitro Labs Inc under MITACS program.

I am aware that you are granting an irrevocable, non-exclusive license allowing the National Library of Canada to reproduce, loan, distribute, or sell copies of this thesis by any means and in any form or format to make it available to interested persons.

David Mester
General Manager
ViVtro Labs, Inc.